# *Coherent Manipulation of Rydberg Polaritons*

NICHOLAS LEONARD ROBERT SPONG

**How to cite:**

SPONG, NICHOLAS LEONARD ROBERT (2022) Coherent Manipulation of Rydberg Polaritons. Doctoral thesis, Durham University.

# COHERENT MANIPULATION OF RYDBERG POLARITONS

**Nicholas Leonard Robert Spong**

## Abstract

This thesis contains a statistical analysis of the resonant transmission of photons through an ensemble of cold Rubidium 87 atoms *in-vacuo*, where the resonant excited state is coupled to one or two highly-excited Rydberg states via optical and microwave fields. Transient emission with decay rates far below the excited state decay rate $\Gamma_e$ are observed. Analysis of the second-order auto-correlation statistic reveals Rydberg-mediated anti-bunching of transient photons, a signature of Rydberg blockade. The application of resonant microwave fields creates strong resonant interactions between Rydberg atoms. This presents a new, transient regime for the study of interaction-induced dephasing and blockade physics in cold atomic ensembles. A demonstration of a collective Rydberg qubit is presented. Quantum information is encoded into a superposition of Rydberg polariton states with a direct photonic interface suitable for applications in quantum networking. The coherence of Rydberg qubits is demonstrated through Ramsey interferometry. Sensitivity to AC and DC electric fields through differential Stark shifts of the qubit states is confirmed through a study of interferometric fringe shifts and dephasing. Controlled removal of atoms from the collective qubit under the action of a resonant scattering beam is shown to diminish readout fidelity but have little effect upon coherence due to the collective nature of the encoding. Theoretical models of the effect of photon scattering and electrical noise on the Rydberg qubit are confirmed experimentally. Ramsey fringe visibility is observed to scale with the fourth power of an applied noise field, matching a theoretical model.

# COHERENT MANIPULATION OF RYDBERG POLARITONS

**Nicholas Leonard Robert Spong**

A thesis submitted in partial fulfilment
of the requirements for the degree of
Doctor of Philosophy

Quantum Light & Matter (QLM) Group
Department of Physics
University of Durham
England

2022

# Contents

# List of Tables

# List of Figures

# Declaration

I confirm that the work in this thesis is based on research carried out at the Quantum Light & Matter research group in Durham, England. No part of this thesis has been submitted elsewhere for any other degree or qualification. Where material has been generated through joint work, the work of others has been indicated.

Nicholas Spong,
February 22, 2022

*Dedicated to*

Amy Joyce

For endless love & support.

And to my parents,

who placed me where I am.

# Acknowledgements

It is difficult to understate the impact of seven years in Durham. I would thank everyone that has invested in me, invested in themselves, or just been around to enjoy the fun. And we did have fun. Some names, experiences, and events are more easily recalled than others and for that part, I remember the following.

I would first like to thank my supervisor, who invited me into the EQOP group at a time in my life when I was very much in need of guidance. Charles' interest and enthusiasm in his subject are catching. Charles has succeeded in guiding me through the development of a skill set that allows me to continue on, and for that I am grateful. Charles' patience, kindness, and skill will live with me for a long time. Busy people are happy people, and I expect to be busy for quite some time.

I must also thank my co-supervisor Matt Jones. Matt's counseling helped me at a time when I needed it, and without this help, I might never have reached the end. I would also like to give special thanks to Ifan Hughes for giving excellent advice at opportune moments. Ifan was kind, understanding, and pastoral throughout my time in QLM. His clarity of explanation when relating foreign concepts was supremely valuable. Honestly, I'm blown away.

I must also thank the other members of my project, without whom, as with any Ph.D. student, I would not have had any success at all. I found Simon Ball the most relatable when I first arrived. Simon was calm and patient with me. This is especially clear in hindsight. Shortly after I arrived several lasers died at the peak of his Ph.D. How he managed to take his time with me is beyond my comprehension. Teodora Ilieva gave me experimental time and space, and made me feel like part of the team. Paul Huillery was instrumental in teaching me basic optics and experimental methods. Many times he would stay in the lab late into the night disassembling and reassembling optical imaging systems, or measuring the temperature of our ensemble. Paul, If you are reading this, thank you! Chris (Yuechun) Jiao was an absolute joy to work with. Joining the group as a post-doc when the experiment would not work at all, his experience helped nurse the experiment back to life, and together we had several months of excellent experimental uptime. This was an exciting time and I am glad to have shared it with Chris. Finally, I would particularly like to thank Hannes Busche. Although our relationship was often fraught, Hannes intellect and respect for his subject were inspiring and something I carry with me. I consider myself privileged to have worked alongside him. I leave the experiment in the capable hands of Oliver Hughes, and wish him every success in taking hold of a fascinating project.

I must also pay tribute to the excellent atmosphere that exists within the Quantum Light & Matter group at Durham University. I must thank Rob Bettles for patience in explaining the most simple of concepts when I had just arrived. Dan Whiting's flurry of technological gizmos encouraged me to be confident in applying technology to my experiments. I found James Keaveny open and supportive, especially in sharing PCB designs and experimental apparatus before I had any capital of my own and with no reasonable expectation of reciprocation. Chris Wade and I would destress by running up hills during the odd lunch break. Danielle Pizzey was always helpful. Elizabeth Bridge helped me couple my first optical cavity. Alistair Bounds was always a calming influence and made time in the lab fly by. Benjamin Beswick would always cheer me up. Lucy Downes would helpfully challenge my opinions. My wonderful academic relationship with Renju Matthew brought me much joy and philosophical debate. Oliver Wales was understanding and kind. Chloe So was easygoing and passionately interested in her work. Charles Moehl was driven and his energy for the subject was boundless. Ana Rakonjac was upbeat and occasionally imitating some Star Wars character or other. I had some wonderful days cycling to Seaham with Joschka Roffe for a full English breakfast. To round off team QLM, A special thanks goes to Will Hamlyn. Will showed me the pleasure of waking at 6 am to hit the river, giving me some of my most valued memories of Durham. He confirmed to me that physics could be fun and accessible. There was never a group meeting that Will Hamlyn did not have a question for. Amongst this tapestry of people, diversity of opinions, and pursuit of physics, I find some of my most treasured experiences and most productive and advantageous years. There must be a $\sqrt{N}$ speedup.

And of course, my gratitude goes to my family. Their immaculate support over the longest time is a testament to their good nature. Without their support, I would never have been in a position to approach higher education. I would also like to thank my wonderful partner Amy for allowing me the space to complete my thesis and pursue my career whilst never losing warmth. Academia is psychologically challenging, but Amy has always encouraged me. Our conversations were all I ever needed.

**February 22, 2022**

# Chapter 1

# Introduction

> Now is a privileged time in the history of science and technology, as we are witnessing the opening of the NISQ era
>
> - John Preskill - 2018

Photons - the fundamental bosonic quanta of the electromagnetic field - fulfill five out of the seven DiVincenzo criteria [1] for constructing a quantum computer[1]. The remaining two criteria, those of universal gates and conversion to stationary qubits, are more challenging to achieve [2]. Photons have a tiny cross section for photon-photon scattering events, negligible under most experimental conditions [3, 4][2]. Interactions between photons and the environment are generally weak. In many cases this is useful. Careful control of environmental conditions can be used to suppress interactions, effectively decoupling the photon from environmentally-induced decoherence. The lack of self-interaction combined with suppression of environmental interactions makes photons useful information carriers [7]. Encoded photonic quantum information is robust and can retain coherence during propagation over long distances, realising a useful ‘flying qubit’ and

---

[1] The first criterea, scalability, has recently been satisfied by the advent of multiplexed quantum memories [106].

[2] Proposals to observe photon-photon scattering test the limits of available laser power [5, 6].

securing applications in quantum networking and interfacing [8, 9]. The ability to transmit photons over huge distances without loss-inducing interactions using optical fibers underpin the global telecoms industry [10]. Proposals to realise similar quantum networks carrying photonic *quantum information* exist, with authors recently heralding the imminent birth of the quantum internet [11].

Conversely, the implementation of quantum computation relies upon *interacting* qubits supporting two-qubit logic [12]. Thus photonic isolation from the environment limits the scope of photonic quantum computing [2, 13], and makes photons poorly suited for *processing* quantum information. The Knill-Laflamme-Milburn (KLM) scheme[14, 15] provides a route towards universal all-optical quantum computation without relying on photonic interactions, relying instead upon *effective* interactions implemented through post-selection of photon detection events. However the KLM scheme is resource-heavy. Fabrication of silicon waveguide circuits have improved the overhead [16, 17] and lead to experimental demonstrations of Shor's algorithm [18] and Grover's algorithm [19]. However, the technique scales poorly and requires application-specific, prefabricated custom waveguide circuits.

To move beyond KLM restrictions, there is scientific research interest in the development of photonic interactions and nonlinear materials that work at the single-photon level. Interactions between photons and their environment can be strong under specific experimental conditions, as with resonant interaction with atomic systems [20]. The atomic cross-section for resonant absorption can be enhanced by confining an atom within an optical cavity [21] spawning the field of cavity quantum electrodynamics (CQED) [22]. Early demonstrations of nonlinear materials were based on the intrinsic 'blockade' phenomena of a single atomic emitter [23]. CQED has since yielded optical non-linearities [24] leading to the successful implementation of blockade [25] and controlled phase gates [26] which might form

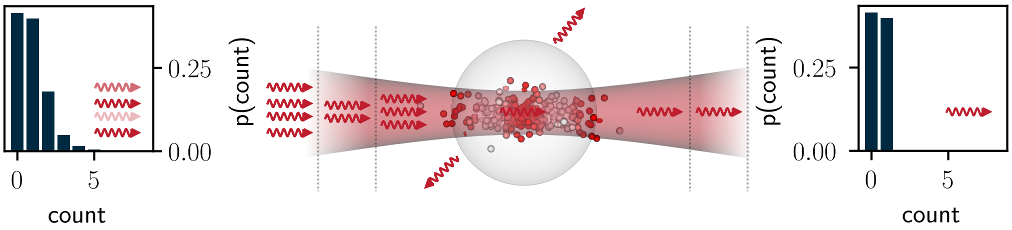

Figure 1.1: **Left** a coherent probe pulse enters an atomic medium in a superposition of number states. **center** A probe pulse propagates under Rydberg electronically induced transparency (EIT) conditions. Upon absorption of a single photon, Rydberg Blockade destroys the EIT condition. Subsequent photons are scattered by the medium, rendering an effective two-level system, termed a Rydberg *Superatom* implementing free space CQED [27]. Strong suppression of occupation numbers of the outgoing photon field $N > 1$ is observed leading to photon anti-bunching in the outgoing light field. **Right** the probe pulse exits the medium in a superposition of Fock states $|0\rangle$, $|1\rangle$.

the building blocks of a quantum computer as specified by DiVincenzo.

## 1.1 Rydberg Systems

The field of Rydberg physics concerns atoms promoted to highly excited quantum ‘Rydberg states’, with large principal quantum numbers $n$ and exaggerated atomic properties. Pairs or ensembles of Rydberg atoms possess strong dipole-dipole interactions [28–30]. These interactions can extend over distances larger than typical interatomic spacings in cold atomic ensembles or atomic arrays and thus lends many-body character to dense Rydberg gases. The presence of a single Rydberg excitation in an atomic medium can dramatically alter its optical properties. This can be leveraged to turn an ultra-cold ensemble of Rubidium 87 into an effective superatom [27, 31–34], a phenomenon known as ‘Rydberg blockade’ [35]. Superatoms possess enhanced light matter coupling with Rabi frequencies $\propto \sqrt{N}$ intrinsic to dense systems of atomic dipoles, [36, 37]. Thus superatoms can circumvent some technical complexities of CQED implementation whilst retaining useful light-matter coupling and blockade, effectively simulating the Jaynes-Cummings Hamiltonian [38, 39].

In traditional CQED devices, the state of a single atom interacting with a cavity mode can modify the propagation of a second cavity photon due to the enhanced light-matter coupling afforded by small accessible mode volumes [**Zubairy2003**]. A blockaded superatom can similarly modify the propagation of photons in free space. A conceptual picture is given in Figure 1.1. Photons traveling under Rydberg electromagnetically induced transparency (EIT) [40] experience resonant transmission for low incident photon rates. If the incident photon rate is increased, blockade limits the degree of EIT coherence that can build in the medium. Thus resonant transmission is reduced. Suppression of resonant transmission in an interacting EIT system was first observed in Durham [41]. The quantum nonlinear nature of this phenomenon has since been demonstrated [42–45], proving the viability of Rydberg mediated quantum nonlinearities at the single-photon level in strongly interacting Rydberg systems. The huge strength of dipolar Rydberg interactions can extend the blockade effect over optically resolvable distances in the tens of microns. This has lead to the demonstration of effective Rydberg-mediated photon-photon interactions between photons in spatially separate optical modes [46], and to entanglement between ensembles and atoms [47], extending applications in quantum networking.

Furthermore, demonstration [48] of dark-state polaritons, quasiparticles that can be adiabatically tuned from photonic to atomic excitations, [49] opens the possibility of light storage within atomic atomic ensembles for retrieval on demand[31, 50–55]. Slowlight techniques have been applied to store photons as Rydberg polaritons [51, 55], demonstrating a route to stationary photonic qubits, and photon memories [52, 56]. Thus a route towards the creation of stationary photonic qubits as excitations of atomic ensembles exists.

Two-qubit logic implemented through Rydberg interactions [35, 57] has been demonstrated [58–61]. Array registers based on neutral atom ensembles have also been demonstrated [62], providing a route towards scalable superatom qubits [63–65].

## 1.2 Collective Rydberg Ensembles

Underpinning modern photonic devices, quantum light-matter interactions are of fundamental interest to the scientific community. Dicke's description of the cooperative behaviour of dense quantum emitters [36] revealed the potential strength of cooperative phenomena, with an $\sqrt{N}$ enhancement of Rabi frequencies for a system of strongly coupled dipoles and a decay rate which can be $N$ times faster than the natural linewidth $\Gamma$ [3] [37]. An extension of Dicke's formalism to dilute gases [66] shortly followed revealing the density dependence of coherent emission and superradiance. Density-dependent modifications to the susceptibility of an ensemble of cold atoms have been extensively studied. Dependence of fluorescence decay upon the optical depth has been systematically reported [67–71] . superradiance has also been reported in many other systems including nuclei [72], atomic arrays [73] and coupled atom-waveguide systems [74, 75] to name but a few. *Subradiance*, the corresponding phenomena involving decay rates lower than natural $\Gamma$, due to excitation modes which couple weakly to the environment, have also been reported [76, 77]. Several studies observe sub and super-radiance in the same systems [50, 78].

The natural extension to the study of transient behavior of collective *three-level* systems are prevalent [79, 80], with characteristic features such as electromagnetically induced transparency (EIT 'overshoot' [81]) and transient modifications [82, 83]. Recent interest in the decay of three-

---

[3] Where $N$ denotes the number of coupled dipoles.

level EIT systems has been sparked by the increasing implementation of EIT in mapping light on to Rydberg excitations. This has lead to the observation of nontrivial photon statistics [42, 84, 85] within Rydberg EIT transients. These studies hint at a rich physics that can reveal information about the internal dynamics of Rydberg ensembles [86]. In this thesis, transient photon emission from two, three and four-level systems are presented, where the third and fourth level are Rydberg states linked by a microwave transition. Through application of resonant control fields, the decay rate of transient emission can be modified [84]. This transient exhibits strong Rydberg-mediated photon anti-bunching due to suppression of the underlying EIT coherences due to Rydberg interactions as reported recently in a similar system [42]. The envelope of the decay can be modulated by driving Rabi oscillations within the Rydberg manifold, to Rydberg states that do not couple to the radiative state [29]. Microwave driving replaces Van der Waals interactions with stronger resonant dipole-dipole interactions [29, 48]. Interaction induced-dephasing of the collective excitation is observed to enhance anti-bunching of photon emission in this regime [84]. Finally, *strong* dressing of the Rydberg manifold by a resonant microwave field can suppress photon emission through Autler Townes splitting. Removing this microwave field is shown to reverse this suppression, and can be used to obtain precise temporal control over a pulse of anti-bunched photons with higher efficiency than recent demonstrations of transient photon storage based on Stark-shifted subradiant excitations [50]. Enhanced interaction induced dephasing might be used to improve the photon statistics of single-photon sources based on Rydberg EIT [87].

## 1.3 Mesoscopic Rydberg Qubits

The dawn of the age of quantum computing has been heralded by the creation of Noisy Intermediate-Scale Quantum Computers (NISQCs) [88]. Existing NISQCs exploiting Rydberg interactions to implement two-qubit gates typically feature an arrays of single atoms held in far off-resonant microtraps. Recent NISQCs have relied upon optical atomic transport using movable tweezers to overcome the probabilistic loading of atomic arrays due to collisional blockade [89, 90]. This limits the stochastic loading probability to 0.5 [4]. In spite of this drawback, NISQCs based on Rydberg atoms have found significant success; demonstrating entanglement [92–95], simulating Ising Hamiltonians [96–98] and simulating spin liquids [99].

Single photons stored in atomic ensembles with strong Rydberg-mediated interactions support the implementation of collective qubits based on Rydberg polaritons [27, 35, 64, 100–103]. Multi-qubit systems based on Rydberg Superatoms in arrays of mesoscopic ensembles could overcome the need for complicated single atom loading schemes. Arrays of mesoscopic ensembles have been recently demonstrated, proving scalability to at least hundreds of ensembles [62]. These schemes might be used to achieve deterministic loading of quantum registers based on arrays of atomic ensembles with enhanced light-matter coupling. Motivated by proposals to reduce the sensitivity of the polaritons to thermal dephasing [104], this thesis reports on the implementation of qubits based on two atomic Rydberg energy states, linked via a microwave dipole transition, with a natural light-matter interface through collectively enhanced light-matter coupling in combination with the Dark State Polariton storage (DSP) protocol[5] [35, 49]. Figure 1.2 shows a schematic of the qubit implementation. Adiabatic preparation of collective Rydberg state $|0_\mathsf{R}\rangle$ is achieved through DSP storage [49]. Single qubit gates are achieved through microwave fields. Two qubit gates[6] are supported by strong Rydberg interactions [105]. Huge Rydberg dipole matrix elements support fast qubit rotations through commercial microwave sources with precise timing [65]. Issues of thermal dephasing of qubits

---

[4] with a record 0.91 by limiting pair loss [91].

[5] In this thesis, ‘polariton’, ‘spin-wave’, and ‘timed-Dicke state’ are used interchangeably to highlight various physical aspects of collective excitations.

[6] Not demonstrated in this work.

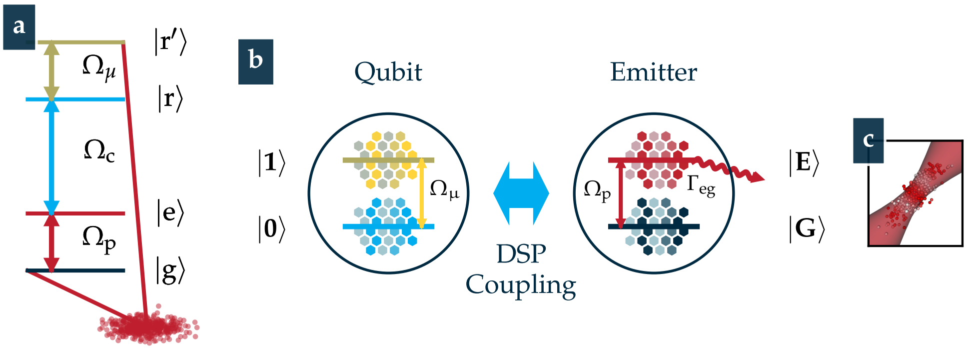

Figure 1.2: **a** The application of control fields to the ensemble of atoms causes each atom to become an effective four level system. **b** The dark state polariton (DSP) storage technique is used to transfer excitations from $|\mathsf{E}\rangle$ to $|0\rangle$. Rydberg blockade prohibits multiple excitations. Microwave fields manipulate the qubit. **c** Visualisation of a collective spin-wave excitation encoded as a Rydberg polariton in an ensemble of ultra-cold atoms trapped in an optical tweezer.

encoded in Rydberg polaritons, apparent in this thesis, can be overcome through excitation of uniform spin waves [104]. Thus ensemble arrays of collective Rydberg qubits are an interesting candidate for quantum networking and photonic interfacing [106, 107].

## 1.4 Thesis Structure

This thesis details the study of resonant light transmission through an ensemble of cold Rubidium 87. The excited state of the D2 line is coupled to a highly-excited Rydberg state via optical fields. Microwave fields provide coupling to a fourth Rydberg state. This work reports observations of nontrivial photon statistics observed in transmitted light, and upon the proof-of-principle implementation of mesoscopic Rydberg qubits as superpositions of Rydberg polariton excitations of the underlying ensemble. This work was carried out in Durham from 2016 - 2021 and follows on from previous demonstrations of controllable quantum non-linear optics and contactless photon-photon interactions by previous project members.

**Chapter 2** provides an overview of the properties of Rydberg atoms and ensembles that underpin this work, including an overview of the Rydberg blockade mechanism, polariton storage and interactions between Rydberg atoms and fields. **Chapter 3** details elements of the experimental setup that the author altered significantly in support of this work. Major upgrades were made to the experimental apparatus in order to increase experimental uptime and expand the scope of the work including the addition of a high-finesse optical cavity, novel Zeeman-shifted modulation transfer locking scheme, additional cross-dipole trap to enhance confinement and optical cooling system rebuild. **Chapter 4** showcases observations of collective effects in our system. Building on principles of coherent emission from a three-level system previously reported in the literature, we demonstrate that Rydberg dressing dramatically increases the intensity and extends the lifetime of the transient decay of a driven ensemble. Statistical analysis of transient coherent emission reveals the signature of blockade, and of interaction induced dephasing. This leads to a simple scheme for studies of Rydberg mediated photon anti-bunching and interaction-induced dephasing in mesoscopic systems. Control over the temporal envelope using strong microwave fields is also demonstrated, with applications in producing instantaneous bursts of single photons. **Chapter 5** demonstrates an experimental implementation of a collective qubit based on multilevel Rydberg polaritons. Coherent control is demonstrated using microwave pulses, culminating in the first demonstration of a Rydberg polariton interferometer to our knowledge[7]. The robustness of Rydberg polariton qubits are probed by subjecting them to electrical noise. The highly entangled nature of the polariton is shown to make the qubit robust to the loss of atoms from the ensemble. **Chapter 6** concludes this thesis and considers future directions.

---

[7] Our group is aware of a Rydberg *dressed* interferometer [63] and a polariton interferometer [108]

## 1.5 Publications

### Arising from this work

- Nicholas L. R. Spong et al. “Collectively Encoded Rydberg Qubit”. In: *Physical Review Letters* 127.6 (Aug. 2021), p. 063604. DOI: `10.1103/PhysRevLett.127.063604`

- Yuechun Jiao et al. “Single-photon stored-light Ramsey interferometry using Rydberg polaritons”. In: *Optics Letters* 45.20 (Oct. 2020), p. 5888. DOI: `10.1364/OL.405143`

- Charles Möhl et al. “Photon correlation transients in a weakly blockaded Rydberg ensemble”. In: *Journal of Physics B: Atomic, Molecular and Optical Physics* (Feb. 2020). DOI: `10.1088/1361-6455/ab728f`

### Related publications

- Robert J. Bettles et al. “Collective Mode Interferences in Light–Matter Interactions”. In: (Aug. 2018). arXiv: `1808.08415`

- Chloe So et al. “Zeeman-tunable modulation transfer spectroscopy”. In: *Optics Letters* 44.21 (Nov. 2019), p. 5374. DOI: `10.1364/OL.44.005374`

### Other publications by the author

- Jiandong Bai et al. “Autler-Townes doublet in single-photon Rydberg spectra of cesium atomic vapor with a 319 nm UV laser”. In: *Applied Physics B* 125.3 (Mar. 2019), p. 33. DOI: `10.1007/s00340-`

`019-7151-x`

- Daniel L Carr et al. “Measuring the Faraday effect in olive oil using permanent magnets and Malus’ law”. In: *European Journal of Physics* 41.2 (Mar. 2020), p. 025301. DOI: `10.1088/1361-6404/ab50dd`

# Chapter 2

# Theoretical Background

It is the purpose of this chapter to revisit the useful properties of Rydberg atoms which provide for this rich field of research, and to derive expressions characterising the mean-field optical response of an ensemble of atomic systems which is later applied to experimental data. First, an overview of relevant Rydberg physics is given, and phenomena attributable to strong Rydberg transition dipole moments including blockade and Stark shifts are traced back to a strong dependence of interactions on the position of the Rydberg valence electron and ultimately the electron energy through the principal quantum number. The optical responses of atoms are described in terms of their steady-state atomic susceptibilities which are calculated from two, three, or four-level Optical Bloch equations (OBEs). Extracted susceptibilities are used in later chapters to describe the optical response of an atomic ensemble. Several optical phenomena relevant to this thesis such as electromagnetically induced transparency, Autler Townes splitting, and modifications to this optical response by Rydberg interactions are considered. An outline of the photon storage and retrieval protocol used to store photons as collective Rydberg excitations in cold atomic ensembles is given. Particular attention is paid to the derivation of atomic susceptibilities, and implications for the interaction of light and matter.

## 2.1 Rydberg Atoms

A quantum-mechanical description of the valence electron of a Hydrogenic system like Rubidium is commonly achieved through a simple set of quantum numbers. The principal quantum number $n$ determines the binding energy of the electron. Orbital angular momentum is quantised through $L$. Electron spin is represented by $s$. Nuclear spin is described by $I$. The term 'Rydberg atom' is applied to atoms of any species, so long as the principal quantum number $n$ is large.

Rydberg physics concerns the nature of highly excited atoms with large principle quantum numbers $n$. The nomenclature is attributable to Johannes Rydberg's revision [145] of Johann Balmer's formula [146] describing emission wavelengths of Hydrogen measured by Anders Ångström. Rydberg's reformulation emphasised the transitional nature of the equation describing the Balmer series of Hydrogen.

$$\frac{1}{\lambda_{vac}} = \mathrm{Ry}_H \left( \frac{1}{n_i^2} - \frac{i}{n_f^2} \right), \tag{2.1.1}$$

where $\lambda_{vac}$ is the emission wavelength, $n_{i,f}$ are integers and $\mathrm{Ry}_H$ is the Rydberg constant for Hydrogen.

Twenty years later, the Bohr model of the atom [147] introduced a zero dimensional ionic core orbited by a zero dimensional electron under the influence of a Coulombic potential,

$$V_{\mathbf{E}} = -\frac{1}{4\pi\epsilon_0} \frac{Ze^2}{r}, \tag{2.1.2}$$

where $Z$ is the atomic number of the nucleus giving rise to nuclear charge. This provided insight that linked the $n_{i,f}$ in Rydberg's formula to electron orbitals. Bohr's model provided the theoretical insight justifying the derivation of $\mathrm{Ry}_H$ from fundamental constants.

$$\mathrm{Ry}_H = \frac{m_e e^4}{8\epsilon_0^2 h^3}, \tag{2.1.3}$$

| Element | Configuration | $n*$ | $\delta_s$ |
|---|---|---|---|
| Li | **2s** | 1.59 | 0.41 |
| Na | **3s** | 1.63 | 1.37 |
| K | **4s** | 1.77 | 2.23 |
| Rb | **5s** | 1.81 | 3.19 |
| Cs | **6s** | 1.87 | 4.13 |

Table 2.1: Ground state quantum defects $\delta_s$ ($s$ orbitals) and effective principal quantum number $n*$ of alkali-earth metals, commonly used in atomic physics due to their simple Hydrogenic structure. Shifts are largest when the orbital angular momentum is low, due to overlap between the electron wavefunction and screened charge [20, 148].

This is valid for hydrogenic atoms with a single valence electron having large orbital angular momentum $l$. Under these restrictions, the energy of the valence electron can be derived by considering that it orbits the nucleus under the action of a $V_{\mathbf{E}}$. For Hydrogenic atoms with a single valence electron, there is a significant deviation from this formula for low $l \leq 3$ states, due to penetration of the nucleus by the wavefunction of the electron [20]. Within the ionic core, deviations from the Coulomb potential cause a shift in energy level known as a 'quantum defect' which increases the binding energy of the low $l$ states. The quantum defects for common alkali metals with a single valence electron are given in table 2.1. To account for these quantum defects, the observed binding energy is commonly presented in the following form.

$$E_n = \frac{\mathrm{Ry}_H}{(n - \delta_{nlj})^2}, \tag{2.1.4}$$

where $\delta_{nlj}$ is the quantum defect of state $\langle nlj|$, and $j$ is the total angular momentum $j - l + s$. The $\delta_{nlj}$ characterise divergences of the true energy levels from Rydberg's formula. The $\delta_{nlj}$ can be represented as an expansion of even terms due to the spherical symmetry of a combined Coulomb

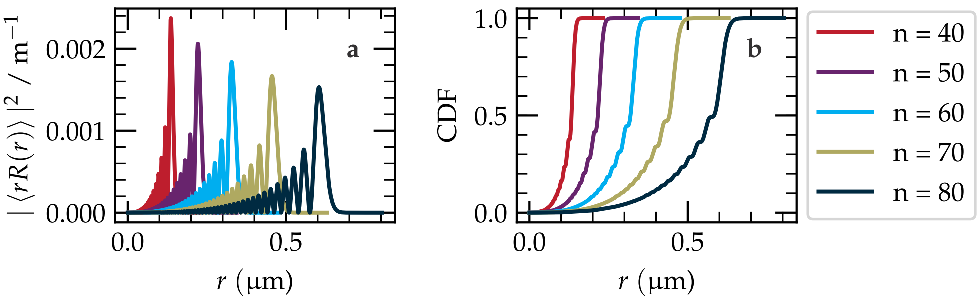

Figure 2.1: Radial Rydberg $S$ Wave Functions. **a** The wave functions of Rydberg atoms are strongly dependent on the principal quantum number. The Probability Density Function (PDF) for the electron position shows that the electron is found far from the nucleus with strong probability ($\langle r\rangle \gg a_0$). **b** The cumulative distribution function (CDF) for the radial position of the valence electron of a Rydberg atom. The CDFs show that there is a low probability of finding the electron within 0.5 μm of the nucleus for at $n = 80$. This strong scaling leads to the properties of table 2.2. Calculated using ARC [152].

potential and short-range correction [149].

$$\delta_{nlj} = \delta_0 + \frac{\delta_2}{(n-\delta_0)^2} + \frac{\delta_4}{(n-\delta_0)^4} + \cdots . \tag{2.1.5}$$

The $\delta_i$ are determined by comparison with precision measurements of atomic energy levels [150, 151]. Some $\delta_{nlj}$ for the valence electrons of alkali metals in ground $S$ states ($l = 0$) are summarised in table 2.1. States with $l > 3$ have $\delta = 0$ and are known as Hydrogenic states, with ground state energy levels matching equation 2.1.3.

## 2.1.1 Rydberg Wave Functions

The Schrödinger equation for a Hydrogenic atom in a highly excited state exposes the physical origin of many of the interesting properties of Rydberg atoms. The Hydrogenic Schröding equation in atomic units is written

$$\left[-\frac{\nabla^2}{2\mu}+V_{\mathrm{CF}}(r)\right]\psi(r,\theta,\phi)=E\psi(r,\theta,\phi), \tag{2.1.6}$$

where $r, \theta, \phi$ are the atomic coordinates, $\mu$ is the reduced mass of the electron and $V_{\mathrm{CF}}(r)$ is the potential energy of the system under the central field approximation.

The central potential relevant to this work is a modified Coulomb potential with additional potential terms. A modification due to polarisation of core electrons by the valence electron resulting in the quantum defects is made to $V_{\mathbf{E}}$. For states with low angular momentum, there is a significant probability for the electron to be found close to the nucleus. When close to the nucleus, the effect of the inner electrons can no longer be approximated to a point charge. Polarisation of the inner electrons by the valence electron is introduced to the model through the modified Coulomb potential [153].

$$-\frac{Z_{nl}(r)}{r}\rightarrow-\frac{Z_{nl}(r)}{r}-\frac{\alpha_c}{2r^4}\left[1-e^{-(r/r_c)^6}\right]+V_{so}. \tag{2.1.7}$$

Here, $\alpha_c$ describes the static dipole polarisability of the core [153]. The cutoff wavelength $r_c$ represents the spatial extent of the core, and is determined empirically. The modified Coulomb potential $Z_{nl}$ is Coulombic far from the core, but is modified for the low $l$ states due to core penetration by the valence electron at short range [153]

$$Z_l=1+(z-1)e^{-a_1r}-r(a_3+a_4r)e^{-a_2r}, \tag{2.1.8}$$

where $Z$ is the nuclear charge. The parameters $a_1, \cdots, a_4$ are be obtained through fits to precise measurements of electron energy levels [153].

The electron orbiting the nucleus creates an additional potential due to the effective magnetic field of the nucleus in the frame of the electron, which couples to the electron's intrinsic spin, through the spin-orbit interaction [154].

$$V_{\mathrm{SO}}=\frac{\alpha^2}{2r^2}\mathbf{l}\cdot\mathbf{s}, \tag{2.1.9}$$

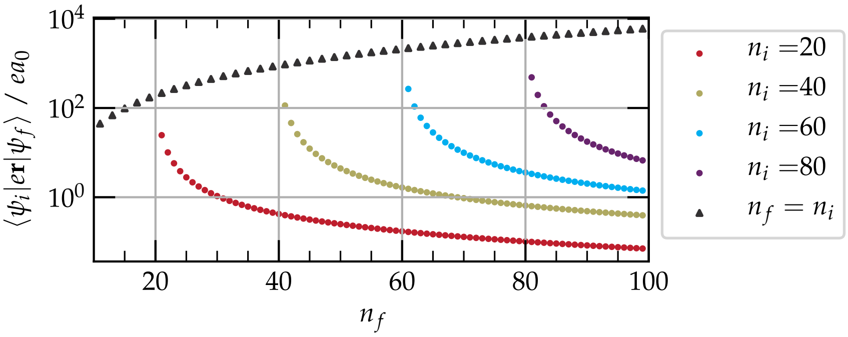

Figure 2.2: Dipole Matrix Elements $\mu_{if}$ for a $\sigma^+$ transition between $\psi_i = |n_i S_{1/2}, m_i = 0.5\rangle$ and $\psi_i = |n_f P_{3/2}, m_f = 1.5\rangle$ for $n_f > n_i$. Dipole matrix elements between states with $n_f \approx n_i$ become large as $n_{i,f}$ increases. For typical $n \in [60, 80]$ used in later chapters, the dipole matrix element approaches $10000ea_0$. For comparison, the $D2$ transition dipole moment in Rubidium is $4.227ea_0$ [155]. Matrix elements are calculated using ARC, an atomic physics package for Python [156].

where $\alpha$ is ths fine structure constant, and $\mathbf{s}, \mathbf{l}$ are the spin and angular momentum operators.

With the above modifications to the coulomb potential, the Schrödinger equation is separable in spherical coordinates $r, \theta, \phi$ as follows.

$$\begin{aligned}
\left[-\frac{1}{2\mu}\left(\frac{\mathrm{d}^2}{\mathrm{d}r^2} + \frac{2}{r}\frac{\mathrm{d}}{\mathrm{d}r}\right) - \frac{l(l+1)}{r^2} + V_{\mathrm{CF}}(r)\right] R_{nl}(r) &= E_{nlj} R(r), \\
\left[\frac{\sin\theta}{\Theta}\frac{\mathrm{d}}{\mathrm{d}\theta}\left(\sin\theta\frac{\mathrm{d}}{\mathrm{d}\theta}\right) + \frac{l(l+1)}{\Theta}\sin^2\theta\right] \Theta_l^m(\theta) &= m^2, \\
\left[-\frac{1}{\Phi}\frac{\mathrm{d}^2}{\mathrm{d}\phi^2}\right] \Phi_m(\phi) &= -m^2. \quad (2.1.10)
\end{aligned}$$

where $Y_{lm}(\theta, \phi) = \Theta_l^m(\theta)\Phi_m(\phi)$ is a spherical harmonic and $R_{nl}(r)$ are generalised Laguerre polynomials. Thus, equation 2.1.10 is fully parameterised and can be numerically integrated to obtain Rydberg wave functions with careful treatment of the range of integration due to the divergence of the Coulomb potential at $r = 0$.

### 2.1.2 Dipole Transitions

Under the dipole approximation, atoms couple to electric fields $\mathcal{E}$ through their electric dipole moment $\mathbf{d}$ [1]

$$\mathcal{E} \cdot \mathbf{d}. \tag{2.1.11}$$

Thus interaction between atomic systems and an electromagnetic field is primarily determined by the dipole matrix elements (DMEs), which governs the strength of the atomic dipole (in atomic units)

$$\mu_{if} = \langle \psi_{nlm} | \, r \, | \psi_{n'l'm'} \rangle \, . \tag{2.1.12}$$

The dipolar strength is proportional to $\langle r \rangle$, the radius of the electronic orbit. For $n = 60/80$ the mean orbital radius approaches one micron. Figure 2.1 shows the scaling of the radial wave function over the range of principal quantum numbers used in later chapters.

The electronic wave functions $R(r)Y_l^m(\theta, \phi)$ can be integrated to calculate DMEs that determine the exaggerated atomic properties of Rydberg atoms. We can simplify the computation of the dipole matrix elements $\mu_{if}$ between states through the application of the Wigner-Eckart theorem [157] which arises due to the separability of Equation 2.1.10, and the algebra of spherical harmonics, which satisfy the equations for $\theta, \phi$.

The quantity $\mu = \mathbf{r} \cdot \hat{\mathbf{e}}$ can be represented in a spherical basis

$$\mu_{-1} = \frac{1}{\sqrt{2}}(x - iy) \qquad \mu_0 = z \qquad \mu_{+1} = \frac{1}{\sqrt{2}}(x + iy). \tag{2.1.13}$$

The $\mu_q$ are defined as $\mu_q = r\sqrt{4\pi/3}Y_1^q(\theta, \phi)$ where $q = \pm 1, 0$ drive $\sigma^{\mp}, \pi$ transitions respectively. Spherical operators provide for direct application of the Wigner-Eckart theorem, stating $\langle \mu_{if} \rangle$ can be evaluated by simple algebra of spherical tensor operators combined with a reduced matrix element, which quantifies the radial dependence and depends on $l, r$ through

---

[1] Higher order electronic couplings, and magnetic couplings can also occur.

equation 2.1.10. The following general relationship for a tensor operator defines the Wigner-Eckart theorem for a tensor operator $\mu_q$

$$\langle nlm_l|\mu_q|n'l'm_l'\rangle = (-1)^{l-m_l} \langle l||\mu||l'\rangle \begin{pmatrix} l & 1 & l' \\ -m_l & q & m_l' \end{pmatrix}. \tag{2.1.14}$$

The expression in parentheses is the Wigner 3j symbol and is related to the Clebsch Gordan coefficient through

$$\langle j_1 j_2 m_1 m_2|j_1 j_2 j m\rangle = (-1)^{-j_1+j_2-m_3}\sqrt{2j_3+1} \begin{pmatrix} j_1 & j_2 & j_3 \\ m_1 & m_2 & -m_3' \end{pmatrix}. \tag{2.1.15}$$

The properties of the Wigner 3j function determine selection rules for dipole transitions, requiring $\Delta l = \pm 1, \Delta m = q$ for nonzero evaluation. With the dipole operator expressed in terms of spherical harmonics $\mu_q$ through Equations 2.1.13, the reduced matrix element can be evaluated by performing the radial integral, to determine the dependence upon the overlap of radial wavefunctions, which depends only on $l, l'$ through wavefunction[2].

$$\langle nl|r|n'l'\rangle = \int R_{n,l}(r) r R_{n',l'}(r) r^2 dr, \tag{2.1.16}$$

which can be used to define the reduced radial matrix element in the Wigner-Eckart theorem (Equation 2.1.14)

$$\langle l||\mu||l'\rangle = (-1)^l \sqrt{(2l+1)(2l'+1)} \begin{pmatrix} l & 1 & l' \\ 0 & 0 & 0 \end{pmatrix} \langle nl|er|n'l'\rangle. \tag{2.1.17}$$

Thus the calculation of matrix elements between orbital angular momentum eigenstates can be reduced through the Wigner-Eckart Theorem (Equations 2.1.14 - 2.1.17) to terms defining the dependence upon the radial wavefunction at specific $l, l'$, a coupling between orbital angular momenta through interaction with the photon and another defining the coupling between the specific $m_l, m_{l'}$.

---

[2] Typically achieved by numerical integration

The values for $\mu_{if}$ for several states $\psi_i, \psi_f$ are shown in figure 2.2 for the transitions $\psi_i = |n_i S_{1/2}, m = 0.5\rangle \leftrightarrow \psi_f = |n_f P_{3/2}, m = 1.5\rangle$. The dipole matrix elements between close lying Rydberg states used in later chapters to define a qubit $|nS_{1/2}, m = 0.5\rangle \leftrightarrow |nS_{1/2}, m = 0.5\rangle$ are shown as black data points and scale as $n^2$.

### Fine Structure

The Wigner Eckart theorem can be extended to calculate dipole matrix elements in the fine structure basis [157]. The reduced matrix element is related to equation 2.1.17 through

$$\langle j||\mu||j'\rangle = \delta_{s,s'}(-1)^{l+s+j'+1}\sqrt{(2j+1)(2j'-1)}\begin{Bmatrix} j & 1 & j' \\ l' & s & l \end{Bmatrix}\langle l||\mu||l'\rangle\,. \tag{2.1.18}$$

Where the quantity in curly braces represents the Wigner - 6j coefficient, which is defined as a sum over products of four Wigner-3j symbols. The $s, s'$ define the initial and final spin states of the system, introducing the selection rule $\delta_{ss'}$. Equations 2.1.14 through 2.1.18 can be used in conjunction to calculate the coupling between two states of the hydrogenic Hamiltonian with fine-structure interaction.

$$\begin{aligned}\langle nlj|\mu_q|n'l'j'\rangle = (-1)^{j-mj+s+j'+1}&\sqrt{(2j+1)(2j'+1)(2l'+1)(2l'+1)} \\ \ldots \times \begin{Bmatrix} j & 1 & j' \\ l' & s & l \end{Bmatrix}&\begin{pmatrix} j & 1 & j' \\ -m & q & m' \end{pmatrix}\begin{pmatrix} l & 1 & l' \\ 0 & 0 & 0 \end{pmatrix}\langle nlj|r|n'l'j'\rangle\,.\end{aligned} \tag{2.1.19}$$

### Hyperfine Structure

Atomic states often depend commonly on total angular momentum $|l, s, j, F, m_f\rangle$ due to the interaction of the electronic and nuclear spin [20]

$$\mathcal{H}_{HFS} = \boldsymbol{\mu}_I \cdot \mathbf{B}_e \equiv A\mathbf{I}\cdot\mathbf{s}. \tag{2.1.20}$$

Under the action of this Hamiltonian, $j$ is no longer a good quantum number, and instead total angular momentum $\mathbf{F} = \mathbf{J} + \mathbf{I}$, with eigenvalue $f$,

| Property | Scaling Law |
|---|---|
| Binding Energy | $n^{-2}$ |
| Energy difference of adjacent states | $n^{-3}$ |
| Orbital radius | $n^{2}$ |
| Polarisability | $n^{7}$ |
| Radiative lifetime | $n^{3}$ |
| Ionisation energy | $n^{-4}$ |
| Resonant dipole interactions ($C_3$) | $n^{4}$ |
| Resonant dipole blockade radius $r_b^{(3)}$ | $n^{4/3}$ |
| Van der Waals interactions ($C_6$) | $n^{11}$ |
| Van der Waals blockade radius $r_b^{(6)}$ | $n^{11/6}$ |

Table 2.2: Rydberg Scaling Laws. Many of the properties of Rydberg atoms are exaggerated due to the likelihood that the valence electron is predominately found far from the nucleus (see Figure 2.1). This leads to large polarisability and strong interactions through the huge dipole matrix elements $e\langle r\rangle$. Excellent background & derivations can be found in many texts including [115, 119, 156, 158].

which remains constant under the interaction, is used.

Energy splittings caused by the Hyperfine interaction are typically small for Rydberg states [151], on the order of hundreds of kilohertz for principal quantum nuumbers used in this thesis. Values for the zero field HFS and Landé $g$ factors, which determine Zeeman splitting of $m_f$ states in weak magnetic fields can be found in [155].

### 2.1.3 DC Stark Shift

DC electric fields polarise atoms, and the induced dipole-field interaction energy can cause energy shifts [159] or state mixing. The DC Stark effect was first communicated by J. Stark to Nature in 1913 [160]. The AC equivalent was observed sometime later by Bonch-Bruevich and colleagues in 1969 [161] after the development of the ruby laser. Stark shifts $\Delta E_{\text{Stark}}$ caused by applied electric fields $\mathcal{E}$ cause shifts of the the bare atomic energy levels. DC electric fields couple to atoms through the dipole moment (now in SI units)

$$\mathcal{H}_{\text{Stark}} = \mathcal{H}_0 + e\mathcal{E} \cdot \mathbf{d}. \tag{2.1.21}$$

Analysis of the above equation shows that the electric field couples to the atom through the dipole matrix operator $\mu_{i,j}$ and acts to polarise the atom for a field in the $z$ direction. The degeneracy of states with low angular momentum $l \leq 3$ is lifted by the quantum defects $\delta_{n,l}$. As such, for low values of the electric field and low $l$, the energy shift $\Delta E_{\text{Stark}}$ can also be calculated using second-order perturbation theory. Thus the selection rules for dipole transitions can again be applied to determine the states coupled by the interaction Hamiltonian.

$$\Delta E_{Stark} = e^2|\mathcal{E}|^2 \sum_{n'\ell'j' \neq n\ell j} \frac{|\langle n, \ell, j, m_j|\hat{z}|n', \ell', j', m_j'\rangle|^2}{E_{n'\ell'j'} - E_{n\ell j}}. \tag{2.1.22}$$

The summation which contains contributions to the AC Stark effect due to interactions with states $n'l'j'$ is often interpreted as the polarisability of the atom.

$$\alpha_0 = e^2 \sum_{i \neq j} \frac{|\mu_{ij}|^2}{E_i - E_j}. \tag{2.1.23}$$

Whereafter the DC stark effect can be compactly represented as.

$$\Delta E_{Stark} = \alpha_0 |\mathcal{E}|^2. \tag{2.1.24}$$

The numerator and denominator in equation 2.1.23 vanish for states with dissimilar $n$, and so the the summation is dominated by couplings between states of similar $n$. Empirical functions exist to obtain approximate values [162]. For the $S$ states with the relationship

$$\alpha_0 = 2.202(28) \times 10^{-9} n^{*6} + 5.53(15) \times 10^{-11} n^{*7} [\text{MHz / (V/cm)}^2] \tag{2.1.25}$$

The $n^7$ scaling dominates above $\sim n = 40$, as $\alpha_0$ becomes proportional to the ratio of the dipole matrix element squared ($r^4$) to state energy differences ($r^{-3}$). Stark shifts can provide extreme sensitivity to electric fields. When probing transitions shifted by the Stark effect (as in chapter 5), the *relative* shift of the transition is observed

$$\Delta_{i,f}^{Stark} = \Delta E_{1,Stark} - \Delta E_{2,Stark} = (\Delta_\alpha)|\mathcal{E}|^2, \tag{2.1.26}$$

where $\Delta_{(1,2)Stark}$ are the stark shifts of the two coupled states and thus $\Delta_\alpha = \alpha_1 - \alpha_2$.

Strong fields can not be treated perturbatively, as the basis of zero-field states $|\psi_0\rangle$ is not diagonal at high field strength. The form of the Stark Hamiltonian causes states that obey the selection rules for dipole transitions to become coupled. For the general case of strong fields, $\mathcal{H}_{Stark}$ must be diagonalised to obtain the eigenstates of the coupled basis along with their associated energy levels. This is particularly relevant at high principal quantum numbers, where dipole moments are large.

Eigenstate mixing due to strong DC Stark shifts outside of the perturbative regime is shown in Figure 2.3. The Stark map for state $|60S_{1/2}\rangle$ shown in panel **a** is initially quadratic due to state defects lifting the degeneracy of the $l = 0$ state, as opposed to the $|57, l > 3\rangle$ manifold at $-1012$ GHz with linear shift due to negligible quantum defects between states with $l > 3$.

### 2.1.4 AC Stark Shift

Describing the effect of AC fields on atomic energy levels in full generality can only be achieved numerically, and approximately [163, 164]. When the field strength is far below the saturation intensity, the Stark effect can be calculated via perturbation theory [163]. A semiclassical electric field defined by

$$\mathcal{E}(t) = \frac{\mathcal{E}}{2}\left[\exp(i\omega t) + \exp(-i\omega t)\right], \tag{2.1.27}$$

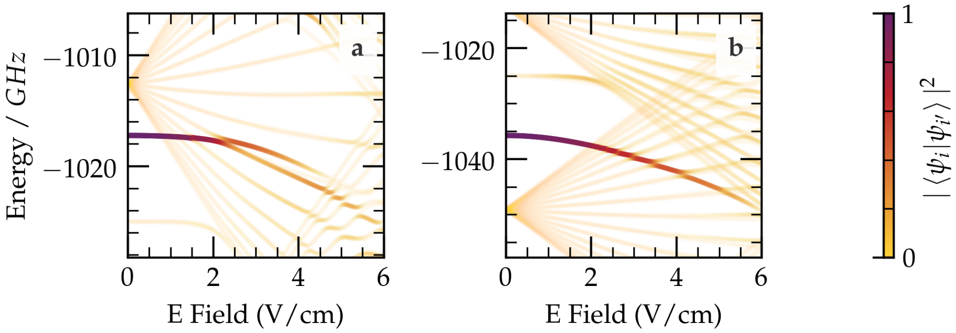

Figure 2.3: Stark maps for Rubidium 87 showing energy level shifts as a result of an applied electric field for some of the states used in later chapters. (a) Stark map for $|\psi_i\rangle = |60S_{1/2}m_j = 0.5\rangle$. A strong avoided crossing with the nearby $|n = 57\rangle$ manifold is reached at around 2 V/cm. (b) Stark map for $|\psi_i\rangle = |59P_{3/2}m_j = 1.5\rangle$. States up to $l = 20$ are diagonalised. Colour coding in **a, b** represents the inner product between $|\psi_i\rangle$, and diagonalised states $|\psi_{i'}\rangle$ which are eigenvectors of the Stark Hamiltonian (Equation 2.1.21). Matrix elements are calculated using ARC [156].

again couples to the electron through the dipole moment $\hat{\mathbf{d}} \cdot \mathbf{E} = -e|\mathcal{E}|\mu_{if}$. In general, even a perturbative approach requires complex mathematics requiring many body relativistic calculations see e.g. [165] to take account of the polarisation of core electrons by the field. A simpified derivation applies to the far detuned atom field coupling where only dispersive effects are relevant. Dressed state energies $\mathcal{E}'$ for the combined atom-field system must be used[3]. The coupled atom-field system field has $n$ photons thus energy $n\hbar\omega$. When the atom is excited by the field to state $|j\rangle$, the energy of the system is $E' = \hbar\omega_0 + (n-1)\hbar\omega$. The equation for the energy shift via second order perturbation theory is [163]

$$\Delta E_g = e^2 \frac{\mathcal{E}^2}{4} \sum_{i \neq g} |\mu_{ei}|^2 \left( \frac{1}{E_g - E_i - \omega} + \frac{1}{E_g - E_i + \omega} \right), \tag{2.1.28}$$

where the two terms in the brackets correspond to the energies of an atom having emitted or absorbed a photon at frequency $\omega$. Thus the approxi-

---

[3] for a full derivation, see [166, 167]

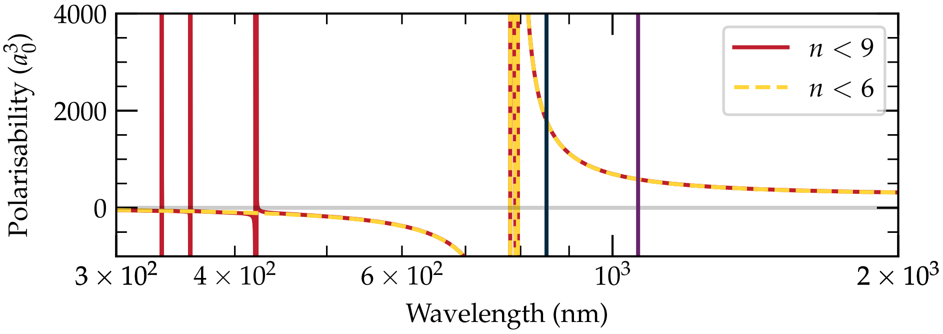

Figure 2.4: The polarisability of Rubidium 87 calculated via Equation 2.1.29. In yellow, only the D1, D2 transitions are used to calculate $\alpha_e(\omega)$. In red, transitions to $nP_{1/2}, nP_{3/2}$ are included for $n < 9$. The 852 nm trapping wavelength is identified by a vertical black line. The D1, D2 transitions dominate the polarisability at the frequency of the dipole trap laser. A common trapping frequency of 1064 nm is shown as a vertical purple line, highlighting the increased polarisability of Rubidium 87 at 852 nm.

mation is made that the atom can only absorb or emit one photon, and higher order effects corresponding to absorption and emission of multiple photons are not considered. Rearranging for the polarisability , we obtain [163]

$$\delta E_g = \frac{1}{2} \cdot \left[ e^2 |\mu_{gi}|^2 \sum_i \frac{\omega_{gi}}{\omega_{ei}^2 - \omega^2} \right] \cdot \frac{\mathcal{E}^2}{4} \equiv -\frac{1}{2} \alpha_g(\omega) \frac{\mathcal{E}^2}{4}, \tag{2.1.29}$$

where $\omega_{ei}$ is the transition frequency between the two states $E_g - E_i$. The quantity $\alpha_g(\omega)$ is known as the dynamic polarisability and characterises the polarisation of the medium in response to an AC field. This expression is valid provided that the detunings from all transitions remains large $\mu_{gi}\mathcal{E} \ll |\omega - \omega_{gi}|$. The polarisability of Rubidium 87 is shown in Figure 2.4, calculated via Equation 2.1.29. This is used to calculate trap depths in section 3.3.4.

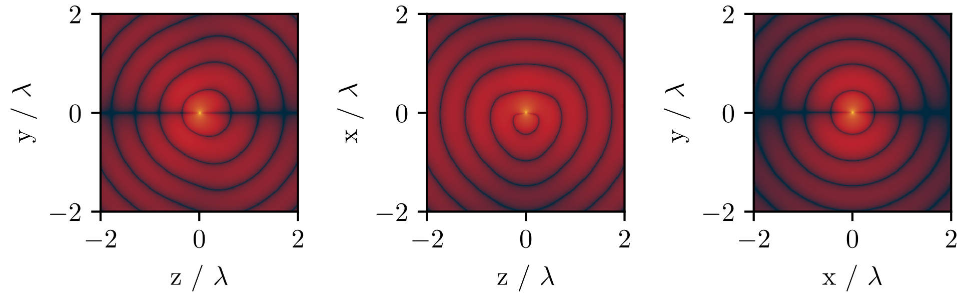

Figure 2.5: Electric field amplitudes $|\mathcal{E}|$ of dipolar radiation fields in the $x, y, z$ planes for a dipole oscillating in $z$ situated at the origin $x = 0, y = 0, z = 0$. Calculated using equation 2.1.30. The logarithm of the absolute value of the field is shown. The singularity at the origin is clipped.

### 2.1.5 Dipole - Dipole Interactions

Strong interactions with electric fields due to the huge dipole moments also lead to strong interactions between Rydberg atoms. Dipoles separated by a distance $\mathbf{r}$ interact via their dipole fields

$$\mathcal{E}_l(\mathbf{r}_j) = \frac{k^3}{4\pi\epsilon_0} e^{ikr} \left\{ (\hat{\mathbf{r}} \times \mathbf{d}_l) \times \hat{\mathbf{r}} \frac{1}{kr} + [3\hat{\mathbf{r}}\,(\hat{\mathbf{r}} \cdot \mathbf{d}_l) - \mathbf{d}_l] \left( \frac{1}{(kr)^3} - \frac{i}{(kr)^2} \right) \right\}, \tag{2.1.30}$$

where $\hat{\mathbf{r}} \equiv \mathbf{r}_a - \mathbf{r}_b$ is the position vector separating the two atomsic nuclei at positions $\mathbf{r}_a, \mathbf{r}_b$. The dipolar field is depicted in Figure 2.5. For $r \gg n^2 a_0$, where the atoms are separated by a distance much greater than the atomic radius $\langle r \rangle$, the potential of the dipolar interaction can be written as [115]

$$V_{\mathrm{dd}}(r) = \frac{e^2}{r^3} \cdot (\mathbf{r}_j \cdot \mathbf{r}_l - 3[\mathbf{r}_j \cdot \mathbf{r}][\mathbf{r} \cdot \mathbf{r}_l]) \,, \tag{2.1.31}$$

where $r$ is the inter-atomic separation as shown in Figure 2.6 and $\mathbf{r}_l, \mathbf{r}_j$ are the positions of the electrons of atom $j, l$ measured from the nuclear core. The implications of these interactions are profound and form the basis of this thesis. Assuming that the dipoles are separated along $z$, the dot products can be expanded in terms of spherical operators

$$V_{\mathrm{dd}}(R) = \frac{1}{r^3}\left(\mu_{1+}\mu_{2-} + \mu_{1-}\mu_{2+} - 2\mu_{1z}\mu_{2z}\right), \tag{2.1.32}$$

where $\mu_{iq}$ are defined in 2.1.13 and $i$ denotes one of the interacting atoms. Evaluating 2.1.32 introduces the transition dipole matrix elements and is thus dependent on the magnitude of the dipolar matrix elements $\mu_{\mathbf{ij}}$. This matrix element is almost isotropic for $|nS_{1/2}\rangle$ states, whilst for $l > 0$ there is significant angular dependence [152, 168]. This highlights the nature of the interaction as the exchange of virtual photons, which must adhere to selection rules, and does not affect the total angular momentum projection, preserving $m_{1j} + m_{2j}$.

The Hamiltonian for two pair states $|rr\rangle, |r'r''\rangle$ coupled via equation 2.1.32 is modified to include the dipolar interaction $V_{\mathrm{dd}}(R)$ between these two states

$$\mathcal{H}_{\mathrm{dd}} = \begin{bmatrix} 0 & V_{\mathrm{dd}}(R) \\ V^{*}_{\mathrm{dd}}(R) & \Delta_\infty \end{bmatrix}. \tag{2.1.33}$$

where $\Delta_\infty$ is the energy difference between pair states $|rr\rangle, |r'r''\rangle$ at infinite separation. As the atoms are brought into proximity, the energy of the interacting atoms increases and the Hamiltonian must be diagonalised, revealing modified energy levels for the coupled system.

$$E_{dd,\pm} = \frac{\Delta_\infty \pm \sqrt{\Delta_\infty^2 + 4V_{\mathrm{dd}}^2(R)}}{2}. \tag{2.1.34}$$

### First Order Resonant Dipolar Interactions ($V(r) \gg \Delta_\infty$)

The limit of strong interactions $V_{\mathrm{dd}}(r) \gg \Delta_\infty$ is known as the resonant dipole regime, where the energy scale of the system is set by the interaction potential $V_{\mathrm{dd}}$, which has a $1/r^3$ scaling. In this regime, first-order perturbation theory can be used, and the shift in energy is first order in $V_{\mathrm{dd}}$

$$\Delta E_{dd,\pm} \approx \pm V_{\mathrm{dd}}(r) = \pm \frac{C_3^{n,l,j}}{r^3}. \tag{2.1.35}$$

The $C_3$ parameter characterises the interaction strength and is a function the principal quantum number $n$, scaling $\propto n^4$ through the dipole matrix elements (c.f. Equation 2.1.31). The total energy shift scales as the underlying dipolar interaction strength $\propto r^{-3}$.

### Second Order Van der Waals Interactions $V(r) \ll \Delta_\infty$

The limit of weak interactions $V_{\mathrm{dd}}(r) \ll \Delta_\infty$ is known as the Van der Waals (VdW) regime, where the modification to the non-interacting pair state energy levels can be calculated using a perturbative approximation which results in a second order correction.

$$\Delta E_{dd,\pm} \approx \pm - \frac{V_{\mathrm{dd}}^2(r)}{\Delta_\infty} = \pm \frac{C_6^{n,l,j}}{r^6}. \tag{2.1.36}$$

The $C_6^n$ parameter characterises the interaction strength. Since $V(r) \propto n^4$ through the dipole matrix elements, and the energy separation $\propto n^{-3}$, the $C_6$ parameter scales as $n^{11}$.

The transition between resonant and VdW interactions occurs at the Van der Waals radius $R_{vdw}$ and occurs at $V_{\mathrm{dd}}(r) = \Delta_\infty$, thus scaling as $n^{7/3}$. For the excited pair state $|r'r''\rangle = |60S_{1/2}60S_{1/2}\rangle$, the interaction is characterised by a $C_6^{n,l,j}$ parameter of $C_6/h = 150$ GHz $\mu\mathrm{m}^{-6}$. The $C_6$ parameter can have positive or negative sign, and is repulsive ($C_6 < 0$) for highly excited $|nS_{1/2}\rangle$.

It is possible to use the DC stark shift to tune VdW interactions between the resonant dipolar and Van der Waals regimes through Förster resonance. Selective Stark shifts that bring two Rydberg pair states into (or out of) resonance under an applied $\mathcal{E}$ field can effect the transition. Resonant dipole couplings cause strong interactions, and an avoided crossing in the absorption profile can be observed [132, 168–170]. Alternatively, the same can be achieved through resonant interaction with microwave fields, where

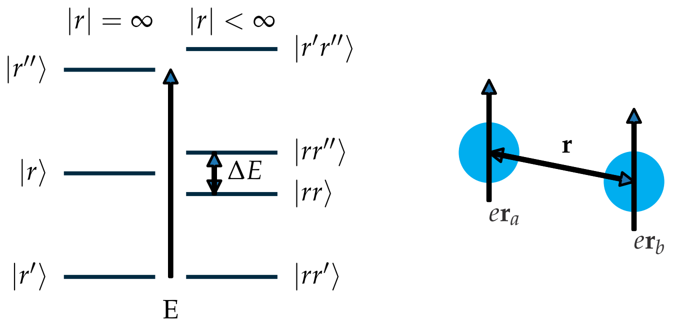

Figure 2.6: Dipole - dipole interactions between a pair of atoms lead to energy level shifts. **a** The magnitude of the energy shift $\Delta E$ can be large for near-resonant pair states coupled by the dipole-dipole interaction. **b** Geometry of interacting atoms in equation 2.1.31.

oscillations of pair state superpositions are brought in and out of resonance [48].

### 2.1.6 Blockade

Energy shifts caused by strong dipolar interactions between Rydberg atoms can modify the bulk optical response of an atomic medium [119]. In dense media, $\Delta E_{\text{dd}}$ can be large enough to shift pair states by more than the linewidth of a corresponding dipolar transition, or excitation laser. This effectively decouples the pair state from the excitation field and heavily suppresses excitation of states corresponding to multiple Rydberg excitations. This phenomenon is known as *Rydberg blockade* [35].

Conceptual Rydberg blockade is outlined in Figure 2.7 and is an extension of the consideration of two atoms separated by $\mathbf{r}$ given in section 2.1.5. Consider an ensemble of atoms driven by a probe laser. The electric field of the probe laser has Rabi frequency $\Omega_p/2\pi$, resonant with a transition between the ground state $|g\rangle$ and Rydberg state $|r\rangle$ of the non-interacting atoms ($R = \infty$). Initially, no Rydberg excitations are present in the ensemble. A resonant coupling beam seeds a single Rydberg excitation, and thus population of the symmetric state $|\mathcal{W}\rangle$ is achieved

$$|\mathcal{W}\rangle = \frac{1}{\sqrt{\mathcal{N}}} \sum_{j=1}^{\mathcal{N}} e^{-i\mathbf{k}\cdot\mathbf{r}} \left| g_1 g_2 ... r_j ... g_{n-1} g_n \right\rangle . \tag{2.1.37}$$

Excitation of multiply excited states within the blockade radius are prohibited by blockade. For the approximately isotropic Rydberg S states, the Rydberg blockade radius is defined as

$$r_b = \sqrt[i]{C_i/\hbar\Omega_p}, \tag{2.1.38}$$

where $i = 3$ for resonant dipolar interactions and $i = 6$ for Van der Waals interactions.

Evidence for this effect was initially observed in continuous wave experiments through supression of excitations [171, 172]. Blockade has since been realised in many contexts and for many purposes. Blockaded ensembles show strong, and even quantum optical nonlinearities [45, 116, 124]. The natural length scale set by $r_b$ can partition the ensemble and lead to crystalisation of excitations [173–178].

When the blockaded system is driven by $\Omega_p$, Rabi oscillations occur between the symmetric ground state and the singly excited state with a Rabi frequency $\sqrt{N}\Omega_p/2\pi$, exhibiting a collective enhancement [115]. This effective two level system has been used to implement effective free-space CQED, where strong light matter coupling is achieved without use of an optical cavity [27]. This blockade radius can extend over tens of microns leading to the demonstration of interactions between spatially separate, optically resolvable media [105]. Blockaded media with enhanced light matter coupling might find applications in quantum networking to interface 'flying qubits' [8, 9].

Suppression of multiple excitations imparts a many body character to Rydberg ensembles, and thus makes them useful for entanglement generation [129] and multi-qubit gates that rely on one-to-many interactions [142]. Rydberg interactions have further been exploited for the implemen-

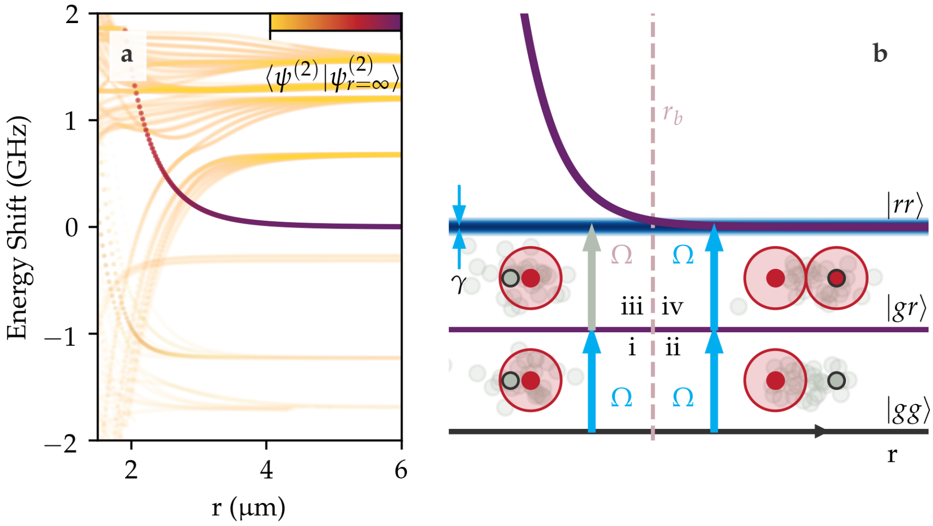

Figure 2.7: **a** Pair state energy level shift for states close in energy to $|rr(\mathbf{r})\rangle = |60S_{1/2}(\mathbf{r}_j)60S_{1/2}(\mathbf{r}_l)\rangle$. As $\mathbf{r} = \mathbf{r_j} - \mathbf{r}_l$ is decreased, VdW interactions cause energy shifts. For $r$ <4 µm, strong interactions cause state mixing. Calculated with ARC [152]. **b** Pair state energy shifts can decouple $|\phi\rangle$ from a resonant coupling $\Omega$. **i, ii** Single Rydberg excitations lacking $V_{\text{dd}}$ interactions are permissible at any $r$. **(iii)** $V_{\text{dd}}$ causes strong shifts. If the pair state shift of $|rr\rangle$ is greater than the linewidth $\gamma$ of the coupling field, excitaions are not possible (blockade regime). **d** when $r > r_b$ multiple excitations are not blockaded. Instead, small interactions cause phase shifts, which can cause dephasing. Note, that for small $r$, perturbation theory is no longer useful and strong state mixing occurs. This is known as 'Rydberg Spaghetti' [60].

tation of single photon transistors [135, 136], switches [179], phase gates [133, 180], entangling gates [181, 182], CNOT gates [92] and strong single photon non-linearities [45, 51, 183]. Rydberg blockade is extensively utilised in the creation of modern NISQCs e.g. in implementing fast gates [92], creating robust qubits from topological spin liquids [99] implementing multi-qubit gates and even solving the maximum independent set problem [184].

## 2.2 Atom Light Interactions

We now turn our attention to the semi-classical interaction between a light field and an ensemble of atoms. Whilst cooperative phenomena are absent from these models, they are useful in defining a base case against which to measure cooperative phenomena. We first derive the response of a two-level atomic ensemble and obtain the absorption and dispersion relations for a monochromatic light wave propagating in two-level media. Extensions to three and four-level media include effects such as Electromagnetically Induced Transparency (EIT) [40], Autler Townes splitting [185] and photon storage [49], which underpin work presented in chapters 4 and 5.

### 2.2.1 Electromagnetic Waves in Dielectric Media

Maxwells' equations [186] for electric fields **E** and magnetic fields **H** in dielectric media are written in terms of **D**, the electric displacement field $\mathbf{D} = \epsilon_0\mathbf{E} + \mathbf{P}$ and the magnetic field strength $\mathbf{B} = \mu_0\mathbf{H}$. In an unmagnetized medium, where the magnetisation vector **M** is assumed to have zero norm,

$$\nabla \cdot \mathbf{D} = \rho_f, \tag{2.2.39}$$

$$\nabla \cdot \mathbf{B} = 0,$$

$$\nabla \times \mathbf{E} = -\dot{\mathbf{B}}, \tag{2.2.40}$$

$$\nabla \times \mathbf{H} = \mathbf{J}_f + \dot{\mathbf{D}}. \tag{2.2.41}$$

where $\rho_f$ is the charge density and $\mathbf{J}_f$ is the free current density, both presumed to be zero in an atomic ensemble. Newtonian time derivatives are used [186]. From these equations, we obtain the equation of a monochromatic plane wave traveling in a linear dielectric medium.

$$\nabla^2\mathbf{E} = \mu\epsilon\frac{\partial^2\mathbf{E}}{\partial t^2}. \tag{2.2.42}$$

In a linear dielectric, the permittivity $\epsilon$ is given by

$$\epsilon \equiv \epsilon_0(1+\chi_e), \tag{2.2.43}$$

where $\chi_e$ is the electric susceptibility of the medium to polarisation by the electric field. Thus the polarisation is defined through

$$\mathbf{P} = \epsilon_0 \chi_e \mathbf{E}, \tag{2.2.44}$$

where $\epsilon_0$ is the electric permittivity. Assuming that the electric field is a monochromatic plane traveling wave with fixed frequency, the wave equation then becomes

$$k^2\mathbf{E} + \left(\frac{\omega}{c}\right)^2 [1+\chi_e]\,\mathbf{E} = 0, \tag{2.2.45}$$

Thus the complex $\mathbf{k}$ is defined through

$$\mathbf{k}^2 = \mathbf{k}_0^2\,[1+\chi_e]\,. \tag{2.2.46}$$

and we define an effective $\mathbf{k}$ vector through the complex refractive index

$$\mathbf{k} = (\widetilde{n} - i\kappa)\cdot \mathbf{k}_0, \tag{2.2.47}$$

where $\mathbf{k}_0$ is the wave vector of the particle in vacuum. The refractive index of the medium for this plane wave is thus $n = \sqrt{1+\chi_e}$ through equation 2.2.45. Where $\chi_e$ is small, we are able to take a Taylor expansion about $n = 1$, whence we obtain the common approximation $n \approx 1 + \chi_e/2$. The real and imaginary parts of the refractive index $\widetilde{n}$ and $\kappa$ are defined through the susceptibility as

$$\widetilde{n} = 1 + \mathfrak{Re}\,[\chi_e/2]\,, \tag{2.2.48}$$

$$\kappa = \mathfrak{Im}\,[\chi_e/2]\,. \tag{2.2.49}$$

and so a plane wave with frequency $\omega_p$ has a modified amplitude and phase after transmission through such a polarisable medium of length $l$

$$\mathbf{E}_T = \mathbf{E}_0 \exp[-k\kappa l/2]\exp[i(k\widetilde{n}l/2 - \omega t)]. \tag{2.2.50}$$

The real part of the susceptibility causes a relative phase $\Delta\phi$ shift compared to propagation through free space. Absorption into the dielectric medium also causes an exponential decay through the Beer-Lambert law.

$$I_T/I_0 = \exp[-\kappa k l], \tag{2.2.51}$$

$$\Delta\phi = \eta k l, \tag{2.2.52}$$

where $\eta = \mathfrak{Re}\left[\chi_e/2\right]$. We thus turn our attention to deriving the susceptibility of an atomic ensemble, in order to derive the effect of propagation upon light transmission.

### 2.2.2 Lindblad Dynamics

It is rarely necessary to model the full manifold of atomic states. In the field of atomic and molecular physics, it is common to reduce a multi-level atom to an $m$-level sub-system. Hamiltonians of atomic systems often naturally separate into subsystems through dipole selection rules and resonant excitation. Figure 2.8 shows how the state manifold of Rubidium 87 can be reduced to an effective four-level system, used in chapter 4. As the experimental timescale in later chapters is around 1 µs, only processes acting on timescales faster than this are included in the basic model.

The electric susceptibility determines the linear response of a medium to an electric field.

$$\mathbf{P} = \varepsilon_0 \chi_{\mathrm{e}} \mathbf{E}. \tag{2.2.53}$$

This polarization field must be equivalent to the sum of the dipolar radiation field of the individual dipoles that constitute the medium.

$$\mathbf{P} = \varrho \mathbf{d} = \frac{1}{2}\epsilon_0 \mathbf{E}\left[\chi_e e^{i\omega t} + \chi_e^* e^{-i\omega t}\right]. \tag{2.2.54}$$

Here, $\mathbf{d}$ is the atomic dipole moment and $\varrho = N/V$ is the density of $N$ atoms in a volume $V$. To calculate $\chi_e$ for an ensemble of identical atoms

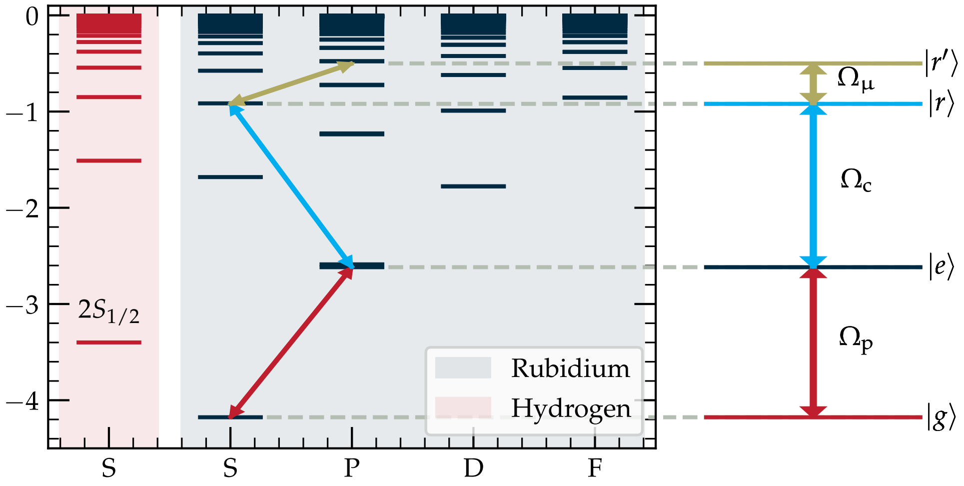

Figure 2.8: Energy landscape of atomic Rubidium 87. Real atoms have a manifold of electronic energy levels. States are isolated during modelling and experiment through resonant interactions and dipole selection rules. Above, the $m$ level Rubidium atom is reduced to a four level system of (arbitrary) ground $|g\rangle$, excited $|e\rangle$ and upper $|r\rangle$, $|r'\rangle$ states, with couplings $\Omega_i$. Note that the quantum defect of $\delta_s = 3.19$ state $5S_{1/2}$ significantly increases the binding energy of the ground state, which is energetically below the $2S_{1/2}$ state of Hydrogen. Energy levels calculated with ARC [152].

forming a macroscopic medium, we introduce the density matrix formalism. The wave-function of a single atom is

$$|\Psi\rangle = \sum_i c_i |\psi_i\rangle \approx \sum_{i\in\{e,g,r,r'\}} c_i |\psi_i\rangle\,. \tag{2.2.55}$$

These are the most natural choice for the $\{|\psi_i\rangle\}$, and are eigenstates of the Hamiltonian that describes the atomic system. Introducing the density operator,

$$\hat{\rho}_{ij} = |\Psi\rangle\langle\Psi| = |\psi_i\rangle c_i c_j^* \langle\psi_j|\,. \tag{2.2.56}$$

Moving to the ensemble picture, the $c_i c_i^*$ can be re-labelled $p_i$, and represent the probability of finding the atom in a particular state $i$. The off-diagonal terms $c_i c_j^*$ are the coherences, and represent the degree to which $\psi_i$,$\psi_j$ superpositions are present and coherent among the many atoms of the ensemble. For an ensemble of two level dipoles, these coherences are maximal when all dipoles are oscillating in phase and are minimal when there is no phase coherence between dipoles, or no superposition. The dipole operator is given by

$$\mathbf{d} = e\mu_{eg} |e\rangle\langle g| + e\mu_{eg}^* |g\rangle\langle e|\,. \tag{2.2.57}$$

Thus dipole moments only exist for states in superposition. Stationary states have no dipole moments. The expectation value of the dipole operator is

$$\mathrm{Tr}\{\hat{\rho}\mathbf{d}\} = e(\mu_{eg}\rho_{eg}e^{i\omega_p t} + \mu_{eg}^*\rho_{ge}^* e^{-i\omega_p t}), \tag{2.2.58}$$

and so we have the result that the linear susceptibility of the medium is directly attributable to coherent excitation of the underlying atoms. This adds another equivalence relation to equation 2.2.54.

$$\frac{1}{2}\epsilon_0\mathcal{E}\left[\chi e^{i\omega t} + \chi^* e^{-i\omega t}\right] = \sum_{ij} \varrho e(\mu_{ge}\rho_{ge}e^{i\omega_{ij}t} + \mu_{ge}^*\rho_{eg}e^{-i\omega_{ij}t}), \tag{2.2.59}$$

Where $\varrho$ is the atomic density $N/V$. From this equation, it is clear that the linear susceptibility is proportional to the off-diagonal matrix elements of the density matrix [116].

$$\chi = -\frac{2\varrho\mu_{eg}^2}{\epsilon_0\hbar\Omega_{ij}}\rho_{eg}, \tag{2.2.60}$$

where we have introduced the Rabi Frequency $\Omega_p = \mu_{eg} \cdot \mathcal{E}/\hbar$. Our experiments are primarily concerned with systems of $\dim(\mathcal{H}) \leq 4$. The susceptibilities to a probe beam of two [20], three [40] and four level systems [187] are well documented, and can be conveniently derived from the Lindblad equation [188],

$$\dot{\rho} = \frac{i}{\hbar}\left[\rho, \mathcal{H}\right] - \sum_{n,m} \mathcal{D}\left[\mathcal{A}_{nm}\right] = \rho\mathcal{H} - \mathcal{H}\rho - \sum_{nm} \mathcal{D}\left[\mathcal{A}_{nm}\right]. \tag{2.2.61}$$

Here, $\rho$ is the density matrix of the system, and $\mathcal{D}$ is the Lindblad dephasor which arises due to tracing over the states of the universe that are neglected from the dynamics. The dephasor acts on operators $A_n$ which form a basis of the Hilbert space under consideration.

$$\mathcal{D}_{nm} = h_{nm}\left(A_n \rho A_m^{\dagger} - \frac{1}{2}\left\{A_m^{\dagger} A_n, \rho\right\}^{+}\right), \tag{2.2.62}$$

where $A_{n,m}$ are the states of the system, and the $h_{nm}$ define the dephasing coefficients which determine the dephasing dynamics [189]. Braces represent the anti-commutator.

For cold atomic Rydberg systems, the dominant dephasing mechanism is often spontaneous emission from an excited state. The Lindblad equation can simulate this kind of dephasing by setting the $h_{mn}$ associated with the transition $|n\rangle\langle m|$ to $\sqrt{\gamma_{nm}/2}$, where $\gamma_{nm}$ is the relevant excited state lifetime. Ensemble dephasing due to Van der Waals interactions can also be simulated by a including a dephasing term proportional to the Rydberg population $h_{rr} = \sqrt{\Gamma_{dd}/2}$.

### 2.2.3 Two Level Media

One of the simplest cases of atomic dynamics concerns a single atomic electron (or ensemble of non-interacting atoms) with internal states $|g\rangle$, $|e\rangle$ interacting with a radiation field under the electric dipole approximation. The two level system is depicted inset on figure 2.10. The Schrödinger equation for the electron is [20]

$$i\hbar\frac{\partial}{\partial t}\left|\psi(\mathbf{r}t)\right\rangle = \left[\mathcal{H}_0 + e\mathbf{r} \cdot \mathcal{E}(\mathbf{r_0}, t)\right]\left|\psi(\mathbf{r}t)\right\rangle, \tag{2.2.63}$$

where $\mathcal{H}_0$ corresponds to the bare atomic Hamiltonian of Equation 2.1.6, and $\mathcal{E}(\mathbf{r_0}, t) = \mathcal{E}_0 \cos(\mathbf{k} \cdot \mathbf{r} - \omega t)$.

We now shift to the interaction picture $|g\rangle \to e^{iE_g t/\hbar} |g\rangle$, where $E_g$ are the energies of the states under the atomic Hamiltonian. The Hamiltonian of the atomic system can then be written in the interaction picture as

$$\mathcal{H}^{(2)} = \frac{\hbar}{2} \begin{bmatrix} 0 & \Omega_p^* e^{i\omega_{eg}t} \\ \Omega_p e^{-i\omega_{eg}t} & 2\omega_{eg} \end{bmatrix}. \tag{2.2.64}$$

Here, we have redefined the zero-energy point to be equal to the energy level of $|g\rangle$, thus $\omega_{eg} = E_e - E_g$, the difference in energy between states. $\omega_{eg}$ is equal to the detuning of the laser field $\omega_{eg} = \omega_p - \omega_{eg}$. The coupling

$$\Omega_p = e\mu_{eg}\mathcal{E}_0, \tag{2.2.65}$$

is also introduced, and is defined as a product of the electric field and the dipole matrix element defined in equation 2.1.12. The prefactor comes from the electric field susceptibility definition in terms of counterpropagating exponentials. In order to simplify the result, we now make a switch to a frame that rotates at the frequency of the probe beam, at which point the Hamiltonian adopts the simple form

$$\mathcal{H}^{(2)} = \frac{\hbar}{2\hbar} \begin{bmatrix} 0 & \Omega_p^* \\ \Omega_p & 2\Delta_p \end{bmatrix}. \tag{2.2.66}$$

Diagonalising this Hamiltonian gives dressed energy levels

$$E = \pm\frac{\hbar}{2} \left( \Delta \pm \sqrt{\Delta^2 - \Omega^2} \right). \tag{2.2.67}$$

We can use the Lindblad equation 2.2.61 to simulate dynamics under the action of this Hamiltonian. For the dephasing terms, we include a single dephasor

$$\sum_{ij} \mathcal{D}_{ij} \left[ A_{mn} \right] = \mathcal{D}_{eg} \left[ \sqrt{\Gamma_e/2} \, |g\rangle \langle e| \right]. \tag{2.2.68}$$

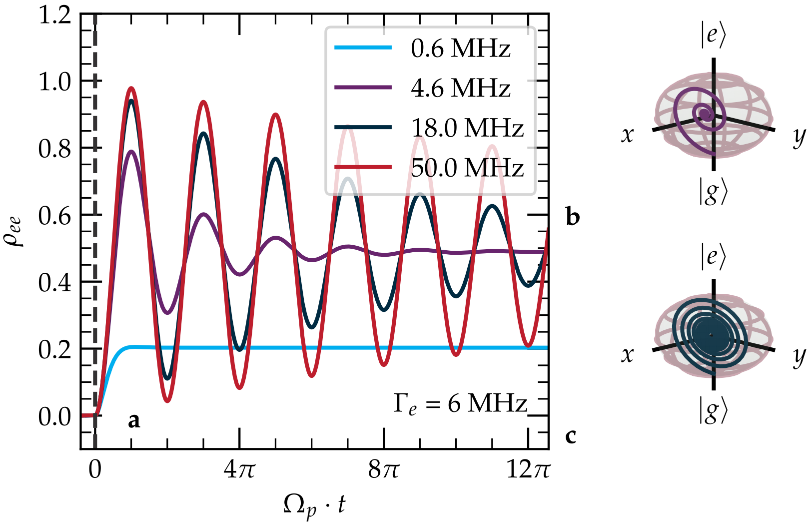

Figure 2.9: Rabi oscillations a function of rotation angle $\Omega_p t$. **a** Dephasing caused by $\Gamma_e$ causes damped Rabi oscillations. **b, c** This dephasing causes the system to relax towards $\rho_{ee} = 0.5$, when the system described by the density matrix is maximally out of phase. Figure legend shows $\Omega_p/2\pi$. Decay of oscillations due to dephasing on the Bloch sphere for $\Omega_p = 2\pi \cdot [4.6, 50]$ MHz.

Propagating this Hamiltonian and Dephasor through the Lindblad equation reveals the following equations for the time dependence of the density matrix elements $\rho_{ij}$

$$\dot{\rho}_{gg} = \frac{i\Omega_p}{2}(\rho_{ge} - \rho_{eg}) + \Gamma_e \rho_{ee}, \tag{2.2.69}$$

$$\dot{\rho}_{ge} = \frac{i\Omega_p}{2}(\rho_{gg} - \rho_{ee}) + \rho_{ge}\left(-i\Delta_p - \frac{\Gamma_e}{2}\right), \tag{2.2.70}$$

$$\dot{\rho}_{eg} = \frac{i\Omega_p}{2}(\rho_{ee} - \rho_{gg}) + \rho_{eg}\left(i\Delta_p - \frac{\Gamma_e}{2}\right), \tag{2.2.71}$$

$$\dot{\rho}_{ee} = \frac{i\Omega_p}{2}(\rho_{eg} - \rho_{ge}) - \Gamma_e \rho_{ee}. \tag{2.2.72}$$

These are the two-level Optical Bloch Equations (OBEs), governing the motion of the optical Bloch vector. The OBEs can be used to calculate the evolution of the density matrix under a certain set of initial conditions $\rho(0)$. Numerical integration can be performed to simulate the response of the system to complex, time-dependent fields.

Rabi oscillations are one simple consequence of driving the system with an electric field. Starting in the ground state, $\rho_{ij}(t = 0) = \delta_{ig}\delta_{jg}$ the dynamics can be simply solved by applying the Schrödinger equation to the two level Hamiltonian of equation 2.2.66 and matching boundary conditions. The solution shows that in the absence of dephasing, the probability that the atom is found in states the excited state $\rho_{ee}$ is

$$\rho_{ee} = \frac{\Omega_p^2}{\Omega_p^2 + \Delta^2}\left[\sin\left(\frac{\sqrt{\Omega_p^2 + \Delta^2}}{2}t\right)\right]^2 . \tag{2.2.73}$$

On resonance, this reduces to the simple formula

$$\rho_{ee}(t)\big|_{\Delta=0} = \sin\left(\Omega_p t/2\right)^2 , \tag{2.2.74}$$

where $\Omega_p t$ defines the rotation of the state vector. Resonant Rabi oscillations for various Rabi frequencies are shown in figure 2.9. The curves are calculated through numerical integration of the OBEs including a dephasing term representing the natural linewidth of the Rubidium D2 line at $\Gamma_e = 6.065$ MHz showing the transition from strongly damped oscillation at low $\Omega_c$ to coherent oscillation at high $\Omega_c$. Corresponding Bloch sphere evolution is also shown.

When the coupling $\Omega_p$ is very weak, we can make the approximations that the system remains in the ground state $\rho_{ij} = \delta_{ig}\delta_{jg}$ and that the population of the excited state remains low $\Omega \ll \Gamma \implies \rho_{ee} \approx 0$. Under these assumptions, we can rearrange the OBEs to obtain a simple form for the magnitude of the steady state atomic coherence by setting the time derivative to zero.

$$\rho_{eg} = \frac{i\Omega_p/2}{\Gamma_2 - i\Delta_p}. \tag{2.2.75}$$

The susceptibility of an atomic transition with the linewidth of the Rubidium D2 line at $\Gamma_e = 6.065$ MHz is shown in Figure 2.10.

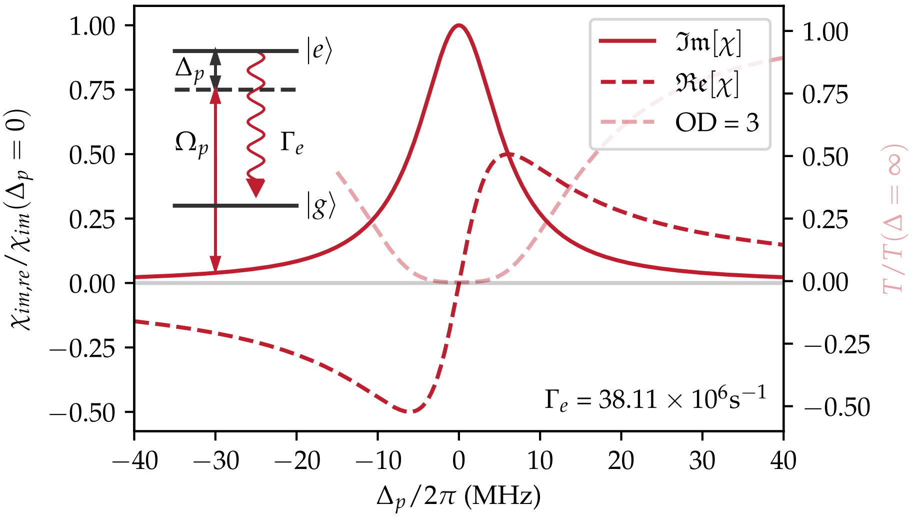

Figure 2.10: The real and imaginary parts of the susceptibility of a two level ensemble with spontaneous decay rate $\Gamma_e$, matching that of the the Rubidium 87 D2 line. The real and imaginary parts have been normalised to $\mathfrak{Im}[\chi^{(2)}](\Delta = 0) = 2\mathcal{N}d_{eg}^2/\epsilon_0\hbar\Omega$. The transmission of a media composed of such two-level scatterers having OD = 3 is also shown. Inset: The two level system considered in this section, defined by Rabi frequency $\Omega_p$, decay rate $\Gamma_e$ and detuning $\Delta_p$.

### 2.2.4 Three Level Media

In this section, we consider the same two level system coupled to an additional state state $|r\rangle$, interacting with a second electric field that couples states $|e\rangle$, $|r\rangle$ We also introduce the decay constant $\Gamma_r$, defining radiative decay from state $|r\rangle$. This system is depicted in figure 2.11. The Hamiltonian for this system in the interaction picture can be derived by following a process analogous to the derivation of the two-level system. The following three-level Hamiltonian applies to the system depicted in figure 2.11

$$\mathcal{H}^{(3)} = \frac{\hbar}{2}\begin{bmatrix} 0 & \Omega_p & 0 \\ \Omega_p & -2\Delta_p & \Omega_c \\ 0 & \Omega_c & -2(\Delta_p + \Delta_c) \end{bmatrix}. \tag{2.2.76}$$

Diagonalising this Hamiltonian gives the eigenstates of the coupled system. Making the variable substitutions

$$\tan(\theta) = \Omega_p/\Omega_c, \tag{2.2.77}$$

$$\tan(2\phi) = \sqrt{\Omega_p^2 + \Omega_c^2}/\Delta_p, \tag{2.2.78}$$

allows us to write the eigenstates of the system in the following simple forms.

$$|+\rangle = \sin\theta\sin\phi\,|g\rangle + \cos\theta\,|e\rangle + \cos\theta\sin\phi\,|r\rangle\,, \tag{2.2.79}$$

$$|D\rangle = \cos\theta\,|g\rangle - \sin(\theta)\,|r\rangle\,, \tag{2.2.80}$$

$$|-\rangle = \sin\theta\cos\phi\,|g\rangle + \sin\phi\,|e\rangle + \cos\theta\cos\phi\,|r\rangle\,. \tag{2.2.81}$$

These equations introduce the important concept of the ‘dark state’ $|D\rangle$. State $|D\rangle$ is a superposition of $|g\rangle$ and $|r\rangle$, having no $|e\rangle$ component. The dark state $|D\rangle$ is approximately stable and non-radiative. Decay from $|D\rangle$ can only occur via radiative decay of $|r\rangle$, which is often slow compared to other experimental timescales. The lack of decay via photon emission justifies the etymology of the dark state. Conversely, the bright states $|+\rangle$, $|-\rangle$ *can* decay due to their $|e\rangle$ component. The consequence of a three-level system with two rapidly decaying states leads to the phenomenon of coherent population trapping, where the state vector of the system converges upon the dark state over time.

One surprising corollary of $\mathcal{H}^{(3)}$ is the physical phenomenon of electromagnetically induced transparency (EIT). EIT is the term for a coherent phenomena that can occur when the two-photon detuning $\Delta_p + \Delta_c = 0$ of the medium is equal to zero whence the medium is rendered transparent to the probe beam. The energies of the eigenstates of $\mathcal{H}^{(3)}$ (equations 2.2.81) are

$$E_{|\pm\rangle} = E_{|D\rangle} + \frac{\hbar}{2}\left(\Delta_p \pm \sqrt{\Delta_p^2 + \Omega_p^2\Omega_c^2}\right). \tag{2.2.82}$$

The conceptual dressed atom picture is shown in Figure 2.12. For $\Omega_p \gg \Omega_c$, states $|\pm\rangle$ have equal magnitudes of the excited state $|e\rangle$, but with opposite sign. The probability amplitudes of absorption of a probe beam by $|\pm\rangle$ thus cancel and so the cross-section for probe absorption is reduced on resonance. In the weak probe regime, $\Omega_p \ll \Omega_c$, the equations for the diagonal states simplify to

$$|\pm\rangle = \frac{1}{\sqrt{2}}(|r\rangle + |e\rangle), \tag{2.2.83}$$

$$|D\rangle = |g\rangle\,. \tag{2.2.84}$$

In this regime, dipole coupling to $|\pm\rangle$ occurs with equal and opposite amplitude, thus interfering destructively on resonance. This results in zero absorption of the probe by the medium. This resonant transmission is the defining feature of electromagnetically induced transparency (EIT) [40].

When the probe is detuned such that $\Delta_p$ matches the energy level splitting of the dressed atom (equation 2.2.82), absorption reaches a maximum, as the absorption cross-sections for $|\pm\rangle$ are no longer equal and so do not cancel. Resonant transparency is the defining feature of EIT and is shown in Figure 2.12. The width of the transparency window is given by

$$\Delta_{EIT} = \frac{\Omega_c^2}{\Gamma_e}. \tag{2.2.85}$$

If the strength of the coupling beam is increased, the energy splitting of the dressed states increases. When the energy splitting is much larger than the line-width of the $|e\rangle \leftrightarrow |g\rangle$ transition, $\Omega_c \gg \Gamma_e$ then the cross-section for probe absorption by either of $|\pm\rangle$ is approximately zero on resonance, and thus trivial probe transmission occurs. In this case, however transmission is a result of the states being shifted fully out of resonance with the probe beam and is not due to the interference of probability amplitudes. It is instead a result of the large Autler-Townes splitting, depicted in Figure 2.12 [185]. In the AT regime, the peak splitting is equal to the coupling Rabi Frequency $\Delta_{AT} \approx \Omega_c$ .

In order to generate the optical Bloch equations for this system, the operators which model this dissipation are included as

$$\mathcal{D}\left[\mathcal{A}_{nm}\right] = \mathcal{D}\left[\sqrt{\Gamma_e/2}\,|e\rangle\langle g|\right] + \mathcal{D}\left[\sqrt{\Gamma_r/2}\,|e\rangle\langle r|\right]. \tag{2.2.86}$$

Propagating $\mathcal{H}^3$ and the dephasing terms through the Lindblad equation 2.2.61 results in the three-level Optical Bloch equations. In propagating the Hamiltonian, we have introduced a second dephasing term to account for decay from the excited state[4]

$$A_{mn} = \frac{\sqrt{\Gamma_r}}{2}\,|g\rangle\langle r|. \tag{2.2.87}$$

For brevity, only the equations defining the coherences are shown here.

$$\dot{\rho}_{eg} = \frac{i\Omega_p}{2}(\rho_{ee} - \rho_{gg}) + \left(i\Delta_p - \frac{\Gamma_e}{2}\right)\rho_{eg} - \frac{i\Omega_c}{2}\rho_{rg}, \tag{2.2.88}$$

$$\dot{\rho}_{rg} = \frac{i\Omega_p}{2}\rho_{re} + \left(i(\Delta_p + \Delta_c) - \frac{\Gamma_r}{2}\right)\rho_{rg} - \frac{i\Omega_c}{2}\rho_{eg}, \tag{2.2.89}$$

$$\dot{\rho}_{re} = \frac{i\Omega_c}{2}(\rho_{rr} - \rho_{ee}) - \frac{i\Omega_p}{2}\rho_{rg} + \left(i\Delta_c + \frac{\Gamma_r + \Gamma_e}{2}\right)\rho_{re}. \tag{2.2.90}$$

If $\mathcal{H}^{(3)}$ is partitioned by setting $\Omega_p = 0$, we decouple $|r\rangle$ from the dynamic Hamiltonian and the OBEs collapse to the two-level case, supporting

---

[4] For experiments reported in this thesis, decay from Rydberg states is often dominated by other, faster decay mechanisms, especially interaction-induced dephasing and thermal dephasing due to atomic motion.

all of the associated physical phenomena of the previous section. As with the two-level system, we can extract the steady-state susceptibility in the weak probe regime by assuming a small $\Omega_p \approx 0$ and negligible population of the excited states $\rho_{ee} \approx \rho_{rr} \approx 0$. Making these substitutions and setting $\dot{\rho}_{ii} = 0$, the $\rho_{rg}$ coherence is given by [190, 191].

$$0 = (i[\Delta_p - \Delta_c] - \Gamma_{rg}/2)\,\rho_{rg} - \frac{i}{2}\Omega_c\rho_{eg}, \tag{2.2.91}$$

$$\implies \rho_{rg} = \frac{1}{2}\left[\frac{\Omega_c}{([\Delta_p - \Delta_c] + i\Gamma_{ba}/2)}\right]. \tag{2.2.92}$$

And so, the susceptibility of the three-level medium is given by

$$\chi = -i\frac{\mathcal{N}|\mu_{eg}|^2}{\epsilon_0\hbar\Omega}\Bigg/\left((\Gamma_e/2 - i\Delta_p) + \left[\frac{(\Omega_c/2)^2}{(\Gamma_r/2 - i\Delta_2)}\right]\right). \tag{2.2.93}$$

Here, we have introduced the two photon detuning, $\Delta_2 = \Delta_p - \Delta_c$. Again, the real and imaginary parts of the atomic susceptibility determine the response of the optical medium through equation 2.2.46 and is shown in Figure 2.11.

This reveals a steep gradient in $\mathfrak{Re}[\chi]$ on the two photon resonance $\Delta_p = 0$. The group velocity is defined as the gradient of the dispersion relation

$$v_g = \frac{\partial\omega(k)}{\partial k}. \tag{2.2.94}$$

We can relate the group velocity to the coupling Rabi frequency $\Omega_c$ through equation 2.2.47.

$$v_g = \frac{c}{\tilde{n}} = \frac{1}{1 + \mathfrak{Re}[\chi]/2}. \tag{2.2.95}$$

The general form of the group velocity in the medium is

$$v_g = \frac{c}{1 + \mathfrak{Re}[\chi]/2 + \partial_\omega\left(\mathfrak{Re}[\chi]\right)}. \tag{2.2.96}$$

And so the group velocity is

$$\frac{6c\varrho\pi}{k^2} \cdot \frac{\Gamma_2}{\Omega_c^2 + \Gamma_r\Gamma_e}. \tag{2.2.97}$$

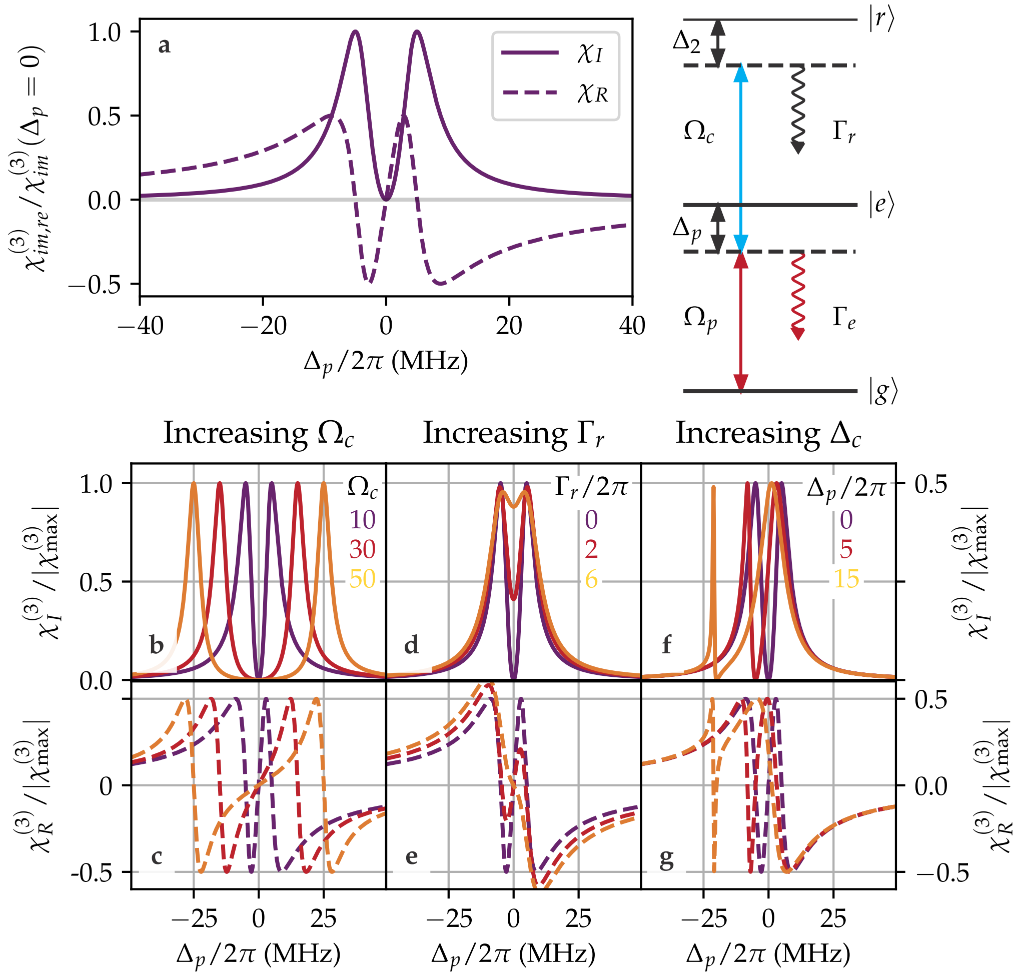

Figure 2.11: Three level atomic susceptibility and level scheme. **a** The real and imaginary parts of the susceptibility of a three level system with spontaneous decay rate $\Gamma_e$ and $\Gamma_r = 2\pi \cdot 1$ kHz, reflective of Rydberg lifetimes. $\Omega_c = 2\pi\cdot$ 10 MHz and $\Omega_p = 2\pi\cdot$ 0.1 MHz. The real and imaginary parts are normalised as with figure 2.10. The parameterisation of the three - level ladder scheme is also shown. **b, c** The effect of varying $\Omega_c = 2\pi \cdot [10, 30, 50]$ MHz is shown. Increased Rabi frequency broadens the resonant transmission window. **d, e** Upper state lifetimes of $\Gamma_r = 2\pi \cdot [0, 2, 6]$ MHz are shown. Finite Rydberg lifetime causes the dark state to decay, limiting resonant transmission. **f,g** Coupling detunings of $\Delta_p = 2\pi \cdot [5, 15]$ MHz are shown in red and orange, respectively. Probe detuning causes a shift in the two photon resonance condition where the medium is least optically thick.

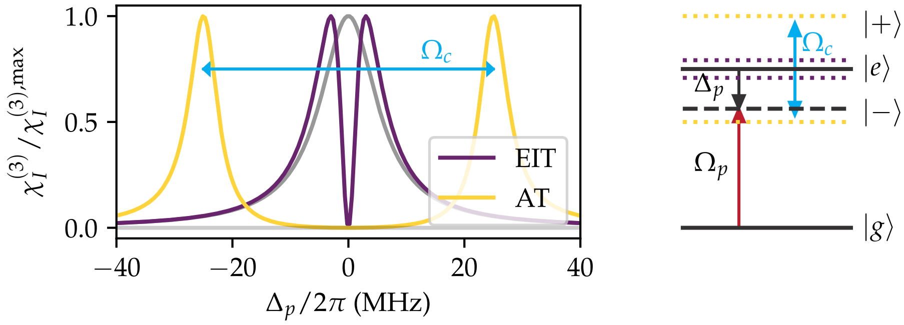

Figure 2.12: Autler-Townes Splitting vs. EIT. Diagonalisation of the three level Hamiltonian coupled by weak $\Omega_p$ and $\Omega_c \gg \Gamma_e$ leads to the emergence of dressed states $|\pm\rangle$. The medium is rendered transparent to a resonant probe $\chi_I(\Delta_p = 0)$ $= 0$. At low $\Omega_c$, this transparency arises due to cancellation of excitation amplitudes of $|\pm\rangle$, known as EIT. At larger $\Omega_c$, Autler Townes splitting of the resonance causes a transmission window due to the vanishing probability of exciting either of $|\pm\rangle$. For $\Omega_c = 0$, the susceptibility reduces to the two level system (grey line). Autler Townes splitting of $|r\rangle$ is also possible through couplings to a fourth state $|r'\rangle$, similarly detuning the coupling beam from resonance as in chapter 4.

This reveals another defining feature of EIT, that of slow light. Through tuning the coupling strength, one is able to reduce the group velocity of photons propagating in the medium [52, 191, 192]. This phenomenon is known as slow light. Group velocities on the order of $10\text{ms}^{-1}$ have been observed [193, 194]. A photon pulse travelling under slow light conditions is compressed within the medium due to change in group index.

### 2.2.5 Dark State Polariton Storage

> ... the quantum state of light is ideally transferred to collective atomic excitations and vice versa ...
>
> - M. Fleischauer & M. D. Lukin - 2000.

Dark state polaritons (DSP) were introduced in 2000 [49, 128], and provide a theoretical framework describing light storage in three-level systems of atomic dipoles through adiabatic ramping of $\Omega_c$ to zero. In their seminal articles [49, 128], Fleischauer and Lukin introduced a new quantised field composed of a superposition of atomic excitations and electric field quanta. This provides insight into the effect of the group velocity modification. The electric field is quantised as

$$\mathcal{E}(z,t) = \sum_k a_k(t) e^{ikz} e^{-i\frac{\nu}{c}(z-ct)}. \tag{2.2.98}$$

A bosonic field is then introduced through the transformation

$$|\Psi(z,t)\rangle = \cos\theta(t)\mathcal{E}(z,t) - \sin\theta(t)\sqrt{N}\hat{\sigma}_{gr}(z,t), \tag{2.2.99}$$

where $\sigma_{gr} = |g\rangle\langle r|$. Quasiparticle excitations of this field are known as *polaritons*, composed of a superposition of electric field quanta and atomic excitations. The mixing angle $\theta$ determines the relative weights of each contribution to the polariton field. The mixing angle is defined through

$$\cos\theta(t) = \frac{\Omega_c(t)}{\sqrt{\Omega_c^2(t) + g^2 N}}, \tag{2.2.100}$$

$$\sin\theta(t) = \frac{g\sqrt{N}}{\sqrt{\Omega_c^2(t) + g^2 N}}, \tag{2.2.101}$$

$$\tan\theta(t) = \frac{g\sqrt{N}}{\Omega_c(t)}. \tag{2.2.102}$$

The atom field coupling $g = \sqrt{\omega_p / 1\hbar\epsilon_0 V}$ [49], defines the coupling strength between probe beam at frequency $\Omega_p$ in quantisation volume $V$. The state mixing angle $\theta$ depends on the Rabi frequency, and the atom light coupling. Control over the mixing angle can be used to tune the field between a photonic form, with the group velocity of the photon in a vacuum, and an atomic form, with a group velocity $\propto c\cos\theta$. When the coupling field is strong, $\Omega_c \gg \sqrt{N}$, $\theta = \pi$, the polariton is a purely electric excitation, $\mathcal{E}(r,t)$. At $\theta = \pi/2$, $|\Psi\rangle$ the polariton is purely atomic $\hat{\sigma}_{gr}(z,t)$. When the coupling strength is reduced to zero, $\theta = \pi/2$ and the velocity of the polariton is zero [128], and the field is 'stored' as an atomic excitation 2.2.97. Photon storage has since been demonstrated many times in various research groups [51, 52, 195, 196].

This defines the Dark State Polariton (DSP) storage technique and is referenced throughout this work. DSP storage provides an effective light matter interface and is used in later chapters to convert excitations from photons propagating in vacuum, to excitations of an atomic ensemble.

### 2.2.6 Quantum Polariton Description

The DSP technique can be used to store an excitation as a polariton, also referred to in the literature as a spin wave [54, 55, 128] or a timed Dicke state [197]. To realise a quantum mechanical description of the spin wave, consider an optical medium composed of $N$ atoms in a macroscopic volume $V$. Each atom has three internal energy states $|g\rangle, |e\rangle, |r\rangle$ as in section

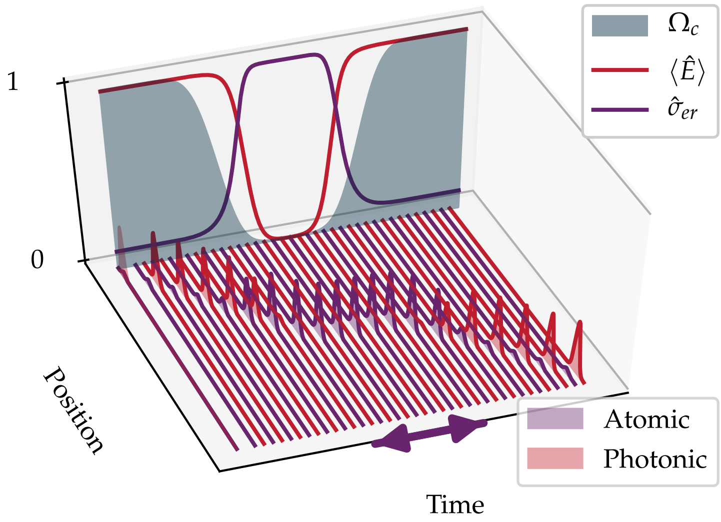

Figure 2.13: Polariton Storage Concept. With $\Omega_c$ initially high, photons pass through the medium under EIT conditions. Adiabatic ramping of the coupling beam to zero writes the photon into the ensemble, reducing the velocity of the photon to zero through equation 2.2.97. This causes excitations of the electric field $\mathcal{E}$ propagating through the medium to be coherently converted to a collective excitation of the atomic media, known as a polariton. The envelope of the atomic and photonic components of the polariton field are shown. When $\Omega_c = 0$, the polariton is stored inside the medium. The storage duration, $t_{\text{Storage}}$ is represented by a purple arrow.

2.2.4. The N particle ground state is defined as

$$|\mathsf{G}\rangle = \bigotimes_{i=1}^{\mathcal{N}} |g_i\rangle \,. \tag{2.2.103}$$

The ground state is adiabatically excited via the DSP technique to the symmetric state through application of the spin wave creation operator

$$S^\dagger = \frac{1}{\sqrt{\sum_j \mathcal{E}(\mathbf{r}_j)}} \sum_{i=1}^{\mathcal{N}} \mathcal{E}(\mathbf{r}_j) e^{\phi(\mathbf{r}_j)} |r_j\rangle \langle g_j| \,, \tag{2.2.104}$$

where $\mathcal{E}(\mathbf{r}_j)$ defines the electric field amplitude at atomic position $r_j$, and $|r_j\rangle, |g_j\rangle$ denote the ground and Rydberg states of atom $j$ [198, 199]. The local phase factors associated with each term in the summation $\phi(\mathbf{r}_j)$ define the spin wave, determined by the interference of the probe and coupling fields at the position of each atomic dipole $\phi(\mathbf{r}_j) = \mathbf{k}_{\text{eff}} \cdot \mathbf{r}_j$ and $\mathbf{k}_{\text{eff}} = \mathbf{k}_{\text{p}} - \mathbf{k}_{\text{c}}$. In the case of uniform illumination by a probe and coupling beam we obtain

$$\mathcal{S}^\dagger = \sum_{j=1}^{\mathcal{N}} e^{\phi(\mathbf{r}_j)} |r_j\rangle \langle g_j| \,. \tag{2.2.105}$$

The state of the ensemble after initialisation via DSP storage is then

$$|\mathsf{0_r}\rangle = \mathcal{S}^\dagger |\mathsf{G}\rangle \,, \tag{2.2.106}$$

where subsicript $r$ is short hand for a full set of quantum numbers and defines the Rydberg state excited by the DSP scheme. The retrieval process can be imagined as the inverse of the creation process, that which returns the spin wave to the ground state through collective emission of a photon

$$|\mathsf{G}\rangle = \mathcal{S} |\mathsf{0_r}(\mathsf{t}_{\text{Storage}})\rangle \,, \tag{2.2.107}$$

where the retrieval is performed some time $t_{\text{Storage}}$ after an initial storage event. The dynamic coupling beam ramps which are required to effect storage and later retrieval are shown in figure 2.13

It is worth remembering, that the form of $|\mathsf{R}(\mathsf{t}_{\text{Storage}})\rangle$ at the point of retrieval may have accrued global or local phase during storage, and any such phase will cause a modification to the form of collective emission at the point of retrieval [102, 200]. Dephasing of the spatial spin-wave correlations degrades the directionality of emission [37, 201]. In this work, the primary dephasing mechanism is motional dephasing, which limits storage efficiencies to $\sim 5\%$ and storage times to $\sim$1 µs. Interaction-induced dephasing also degrades the directionality of emission [116, 202]. Experimental polariton retrieval decays exponentially with time due to these effects, and the effects of thermal motion of the atomic dipoles.

### 2.2.7 Four Level Media

An effective four level medium can be obtained by introducing a fourth state $|r'\rangle$. In this thesis, we are concerned with four-level ladder-type Hamiltonians, and thus couple $|r\rangle$ to $|r'\rangle$ with Rabi frequency $\Omega_\mu$. The OBEs for the four-level system can again be obtained by solving the Lindblad equation to obtain the equations of motion for $\rho_{ij}$ under Hamiltonian

$$\mathcal{H}^{(4)} = \frac{\hbar}{2}\begin{bmatrix} 0 & \Omega_p & 0 & 0 \\ \Omega_p^* & -2\Delta_p & \Omega_c & 0 \\ 0 & \Omega_c^* & -2(\Delta_p + \Delta_c) & \Omega_\mu \\ 0 & 0 & \Omega_\mu^* & -2(\Delta_p + \Delta_c + \Delta_\mu) \end{bmatrix}. \quad (2.2.108)$$

Cranking the handle on equation 2.2.61 can be used to derive the Optical Bloch Equations of this system [185].

$$\dot{\rho}_{gg} = \frac{i\Omega_p}{2}(\rho_{ge} - \rho_{eg}) + \Gamma_e\rho_{ee}, \tag{2.2.109}$$

$$\dot{\rho}_{ee} = \frac{i\Omega_c}{2}(\rho_{er} - \rho_{re}) + \frac{i\Omega_p}{2}(\rho_{eg} - \rho_{ge}) + \Gamma_r\rho_{rr} - \Gamma_e\rho_{ee}, \tag{2.2.110}$$

$$\dot{\rho}_{rr} = \frac{i\Omega_\mu}{2}(\rho_{rr'} - \rho_{r'r}) + \frac{i\Omega_c}{2}(\rho_{re} - \rho_{er}) + \Gamma_\mu\rho_{r'r'} - \Gamma_r\rho_{rr}, \tag{2.2.111}$$

$$\dot{\rho}_{r'r'} = \frac{i\Omega_\mu}{2}(\rho_{r'r} - \rho_{rr'}) - \Gamma_\mu\rho_{r'r'}, \tag{2.2.112}$$

$$\dot{\rho}_{eg} = \frac{i\Omega_p}{2}(\rho_{ee} - \rho_{gg}) - \frac{i\Omega_c}{2}\rho_{rg} - t_e\rho_{eg}, \tag{2.2.113}$$

$$\dot{\rho}_{rg} = \frac{\Omega_p}{2}\rho_{re} - \frac{\Omega_\mu}{2}\rho_{r'g} + \frac{\Omega_c}{2}\rho_{eg} - t_r\rho_{rg}, \tag{2.2.114}$$

$$\dot{\rho}_{r'g} = \frac{i\Omega_p}{2}\rho_{r'e} - \frac{\Omega_\mu}{2}\rho_{rg} - t_\mu\rho_{r'g}, \tag{2.2.115}$$

$$\dot{\rho}_{re} = \frac{\Omega_c}{2}(\rho_{rr} - \rho_{ee}) + \frac{\Omega_p}{2}\rho_{rg} - \frac{i\Omega_\mu}{2}\rho_{r'r} - (\gamma_{re} + i\Delta_c)\rho_{re}, \tag{2.2.116}$$

$$\dot{\rho}_{r'r} = \frac{\Omega_\mu}{2}(\rho_{r'r'} - \rho_{rr}) + +\frac{\Omega_c}{2}\rho_{r'e} - (\gamma_{r'r} + i\Delta_\mu), \tag{2.2.117}$$

$$\dot{\rho}_{42} = \frac{i\Omega_p}{2}\rho_{r'g} + \frac{i\Omega_c}{2}\rho_{r'r} - \frac{i\Omega_\mu}{2}\rho_{re} - (\gamma_{r'e} + i(\Delta_c + \Delta_\mu)). \tag{2.2.118}$$

Here, the complex detunings $t_{2,3,4}$ are defined as

$$t_e = \Gamma_e + i\Delta_p, \tag{2.2.119}$$

$$t_r = \Gamma_r + i(\Delta_p + \Delta_c), \tag{2.2.120}$$

$$t_\mu = \Gamma_{r'} + i(\Delta_p + \Delta_c + \Delta_\mu). \tag{2.2.121}$$

We have also defined the $\gamma_{ij} = (\Gamma_i + \Gamma_j)/2$, and have introduced further dissipation through the operator

$$\mathcal{D}\left[\mathcal{A}_{nm}\right] = \mathcal{D}\left[\sqrt{\Gamma_{r'}/2}\,|e\rangle\,\langle r|\right]. \tag{2.2.122}$$

Once more applying the weak probe approximation, $\Omega_p \approx 0$, $\rho_{ee} \approx 0$, we can solve these equations for the coherence $\rho_{eg}$, obtaining

$$\rho_{eg} = \Omega_p \frac{\Omega_\mu^2 - t_3t_4}{\Omega_\mu^2 t_2 - t_2t_3t_4 + \Omega_c^2 t_4}. \tag{2.2.123}$$

And then the susceptibility of the four-level system is related to the coherence through equation 2.2.59. Figure 2.14 shows the form of the real and imaginary parts of the susceptibility of a four level system. The response can be understood by diagonalising the Hamiltonian $\mathcal{H}^{(4)}$ for the for level system. In the weak probe limit, $\Omega_p \sim 0$, eigenstates of the four-level system are [203]

$$|g\rangle = |g\rangle\,, \tag{2.2.124}$$

$$|+\rangle = \frac{1}{\sqrt{2}\Omega'}\left(\Omega_c\,|e\rangle + \Omega'\,|r\rangle + \Omega_\mu\,|r'\rangle\right), \tag{2.2.125}$$

$$|0\rangle = \frac{1}{\Omega'}(\Omega_c\,|r'\rangle + \Omega_\mu\,|e\rangle), \tag{2.2.126}$$

$$|-\rangle = \frac{1}{\sqrt{2}\Omega'}\left(\Omega_c\,|e\rangle - \Omega'\,|r\rangle + \Omega_\mu\,|r'\rangle\right). \tag{2.2.127}$$

Since the states $|0\rangle\,, |\pm\rangle$ have some contribution from the radiative state $|e\rangle$, transitions from $|g\rangle$ driven by the probe beam are electric dipole allowed to all three states. Thus the probe field couples to all three dressed states and as such we observe three peaks in the susceptibility. Transitions from $|g\rangle$ to $|0\rangle$, $|\pm\rangle$ are known as Autler Townes (AT) transitions.

One of the most striking changes to the three-level susceptibility by the imposition of $|r'\rangle$ is the resonant absorption, where for the three-level system we have resonant transmission. Assuming $\Gamma_{r'}$ is much smaller than the other relevant timescales ($\Omega_{c,\mu}, \Gamma_{e,r}$), we are able to split the transmission window of the three-level system in two, as shown in Figure 2.14 **a,b**.

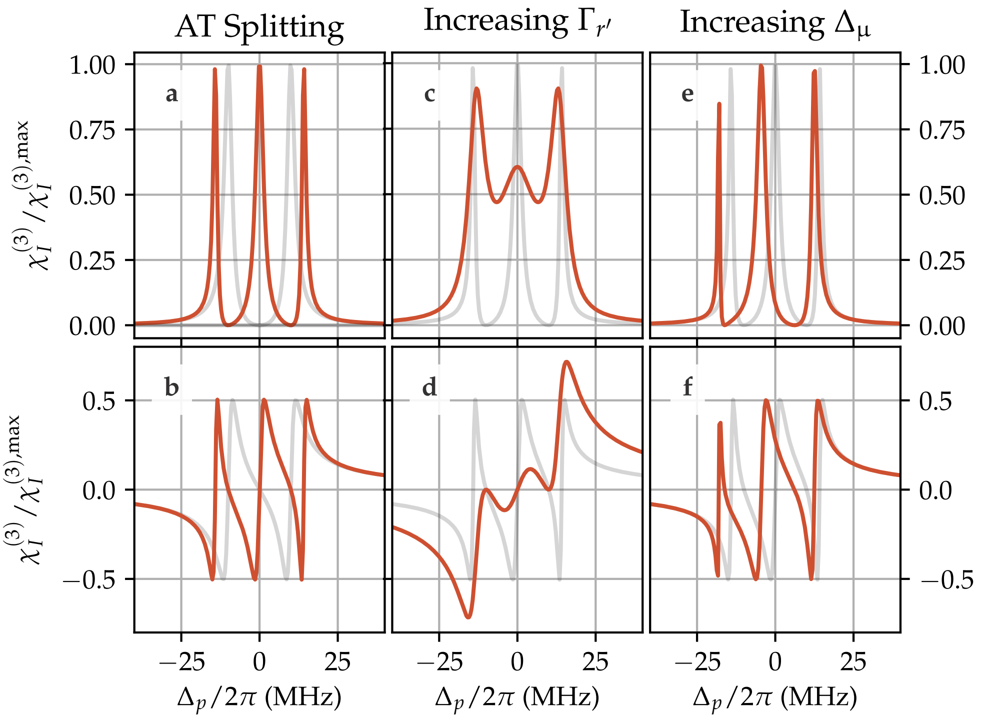

Figure 2.14: RF Splitting of EIT. Starting at the basic EIT susceptibility of Figure 2.11, the effect of applying RF dressing upon $\xi_{I,R}$ is shown. $\Gamma_e$ is the lifetime of the Rubidium 87 D2 line. $\Gamma_r \approx \Gamma_r' \approx 0$, $\Omega_c = 2\pi \cdot 20$ MHz, $\Omega_\mu = 2\pi \cdot$ 5 MHz. **a, b** $\Omega_\mu = 2\pi \cdot 20$ MHz. The case $\Omega_\mu = 0$ is shown in light gray. Increasing $\Omega_\mu$ quickly creates resonant susceptibility, and $|\pm\rangle$ appear, increasing in separation with $\Omega_\mu$ (not shown). **c, d** Increased dephasing of $|r'\rangle$ with $\gamma_{r'} = 2\pi \cdot 20$ MHz. The two transparency windows which form as a result of interference in between AT states diminish in magnitude due to fast decay via $|r'\rangle$. $|\pm\rangle$ become indistinguishable from the main susceptibility peak at large $\Gamma_{r'}$. **e,f** Increasing detuning $\Delta_\mu = 2\pi \cdot 20$ MHz causes asymmetry of the line-shape.

# Chapter 3

# Experimental Methods

As with many experimental studies of cold matter, the experimental apparatus is the culmination of the collective effort of several generations of Ph.D. students over the past decade. The current generation[1] of the experiment takes much inspiration from previous experimental hardware used in the same group for the investigation of Rydberg physics, employing a more compact experimental setup [41]. The current generation of hardware was commissioned in 2016 [204] by Hannes Busche, Paul Huillery & Simon Ball with input from many members of Durham Quantum Light & Matter group. For a more in-depth discussion of the experimental platform, the reader is referred to these references, as well as to the following theses of previous project members [41, 46, 205, 206]. Likewise, full details FPGA control hardware and software (DExTer[2]) can be found in the thesis of Tim Wiles [207]. Details of extensions to DExTer to allow for high-frequency control pulses which underpin this work can be found in the thesis of Simon Ball [205]. The experimental platform orchestrates rapid production of microscopic, ultracold ensembles of Rubidium that form the object of all later experiments. Design elements are also shared with systems found at Universität Heidelberg [208, 209].

---

[1] Loosely based upon which particular vacuum chamber was in use.

[2] Durham Experimental Terminal

Several upgrades and modifications have been made during the author's engagement with the project. Additional dipole trapping capability paves the way towards higher density ensembles needed to increase the strength of many-body Rydberg interactions. Flexible locking schemes have been added, extending the range of frequencies available to the experimentalist for atomic manipulations. The installation of an ultra-low-expansion (ULE) cavity has further improved the rate of data acquisition by improving frequency stability and allowing for longer periods of continuous operation. Figures included in this thesis rely on some 400 Gb of experimental data. A suite of data analysis software has been developed to facilitate rapid analysis and exploration of vast quantities of statistical data generated by the experiment. It is the purpose of this chapter to describe the main principles of the experiment and to document the significant upgrades that have been made to the system [41, 46, 205, 206].

In this section, use is made of the excellent SVG optics library created by Alexander Franzen [210]. The symbol key can be found in appendix A.1.

**This chapter is in part based on the following publication**

- Chloe So et al. "Zeeman-tunable modulation transfer spectroscopy". In: *Optics Letters* 44.21 (Nov. 2019), p. 5374. DOI: `10.1364/OL.44.005374`

## 3.1 Ensemble Preparation

The experimental apparatus used in this work is designed to enable the study of atom-light interactions in the pursuit of optical nonlinearities at the single-photon level. The methodology of creating samples of ultracold atomic ensembles in well-defined quantum states through laser cooling, trapping, and state preparation are well-established [20] and shared across

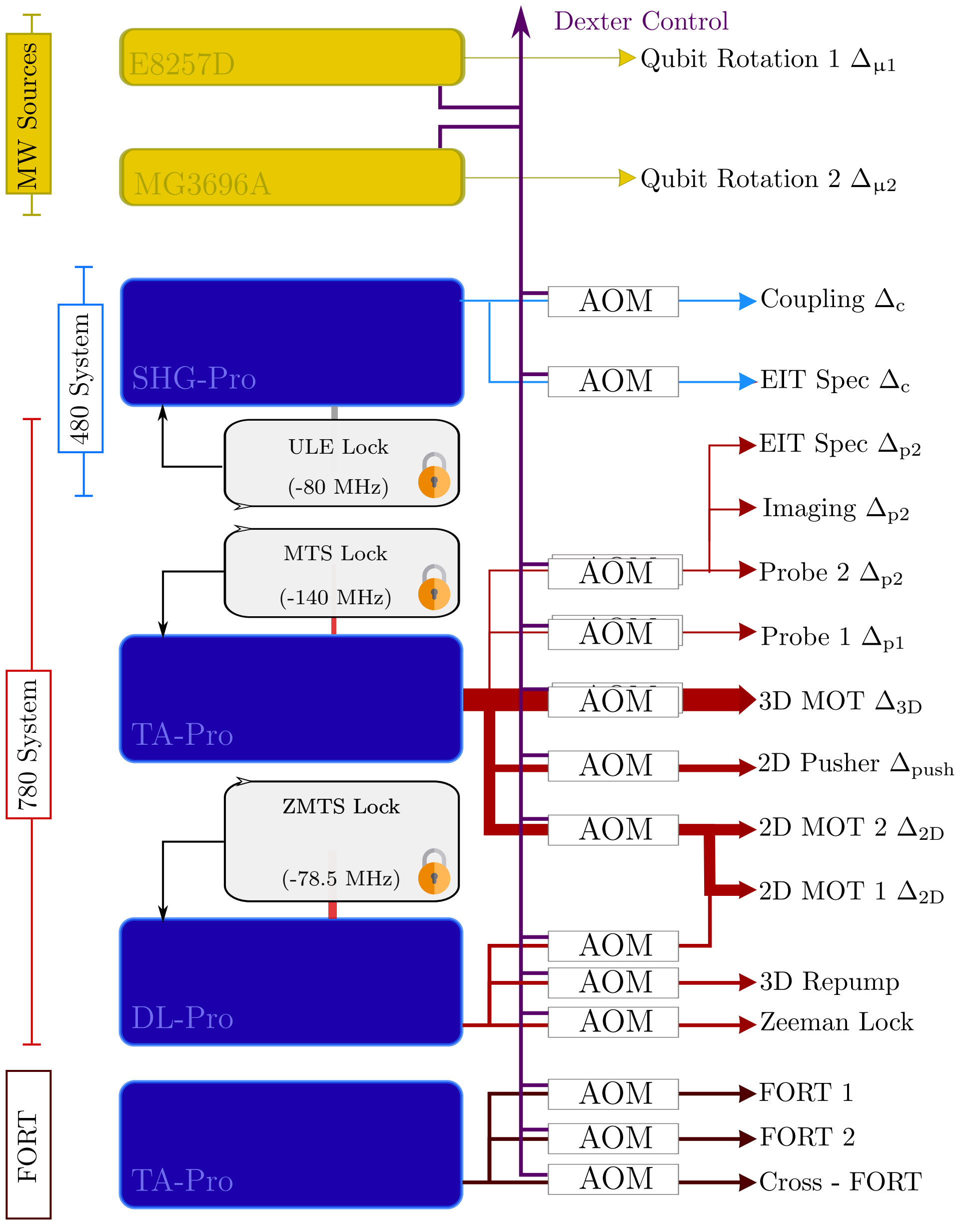

Figure 3.1: Implementation of optical control fields at 780, 480, and 852 nm discussed in the text. 480 nm light is generated in a commercial SHG system offset-locked to a ULE cavity, providing excellent frequency stability and tunable locking. The 780 cooling and repump systems are locked to atomic references via Modulation Transfer Spectroscopy (MTS) and Zeeman-tunable MTS (ZTMTS). AOMs provide optical 80/20 switching speeds of ∼ 40 ns. An FPGA controller with Labview UI (DExTer) coordinates AOMs, as discussed in the text.

a range of experiments. Magneto-optic trapping, laser cooling and the formation of FORTs requires ultra-high vacuum (UHV) conditions to limit background atomic collisions which can prohibit laser cooling. Trapped ensembles require high optical depth for strong light-matter coupling. Frequency stable control fields locked to atomic resonances or optical cavities are necessary for state manipulation and interaction. Commercial microwave sources are available for interaction with Rydberg dipole moments.

The study of single-photon nonlinearities brings some additional challenges. Sufficient statistical data to evidence optical nonlinearities at the single-photon level must be obtained [211]. This ambition conflicts with the extremely low photon numbers per experimental run $\langle n \rangle \sim 1$ required to observe sensitive quantum nonlinearities. For this reason, experiments in quantum nonlinear optics are particular in requiring high sensitivity detection schemes and ideally high repetition rates [204, 205]. For this purpose, a capable FPGA control system is implemented which interfaces to single-photon avalanche detectors to produce time-tagged photon statistics with a 5 ns timing resolution.

A functional drawing of the vacuum chamber at the heart of this system is presented in figure 3.2. Efficient loading of a 3D magneto-optic trap (MOT)[212, 213] is achieved through the pre-cooling of atoms in a 2D MOT [214]. This creates a high atomic flux for 3D MOT loading, reducing loading time to around $\sim 100$ ms and thus increasing data acquisition rates. Repeated experiments performed upon the same ensemble further increases data acquisition rates. It is possible to perform upwards of 10000 experiments upon the atomic ensemble before observing a significant reduction in optical depth. Including the loading sequence, the experimental apparatus is capable of performing automated experiments at repetition rates upwards of 100 kHz, with MOT reloads occurring at a frequency of around 10 Hz.

The assembly of this capable system was not performed by the author. This section provides an overview of the experimental apparatus and the experimental sequence required to load a macroscopic sample of ultra-cold Rubidium into an Far Off-Resonant (FORT) at the center of a UHV vacuum chamber and perform rapid manipulations via control fields. Studies of this fascinating form of matter have produced the results presented in this thesis.

### 3.1.1 2D Magneto-Optic Trap

The objective of the experimental sequence is to create an ultra-cold ensemble of atomic Rubidium confined within the FORT described in section 3.3.4 within a controlled environment. The experimental sequence used to load and pre-cool an ensemble of atoms is shown in figure 3.3. This sequence starts with cooling in two dimensions via 2D magneto-optic trap indicated on figure 3.2.

The upper 2D MOT chamber is constructed from a UHV glass cell with internal dimensions $25 \times 25 \times 150$ mm. Within this cell, a current activated Rubidium source maintains high vapor pressure[3]. The 2D MOT is similar to a traditional six-beam MOT, but with only four beams providing cooling in only two axes. The trapping volume is an elongated pencil shape [204, 214, 215].

The 2D MOT chamber is attached to the main Science chamber through a stainless steel gate valve[4] and steel junction and which connects the glass cell containing the 2D MOT trapping volume, the main science chamber containing the 3D MOT trapping volume and an ion pump. Atoms pass

---

[3] The upper chamber has two 250 mg Rubidium dispensers at natural abundance, one of which expired after approximately four years use over Christmas 2019/20.

[4] Zoning the vacuum chamber can be used to maintain vacuum conditions in one part of the system whilst the other is brought up to air, e.g. for replacing the dispensers when necessary.

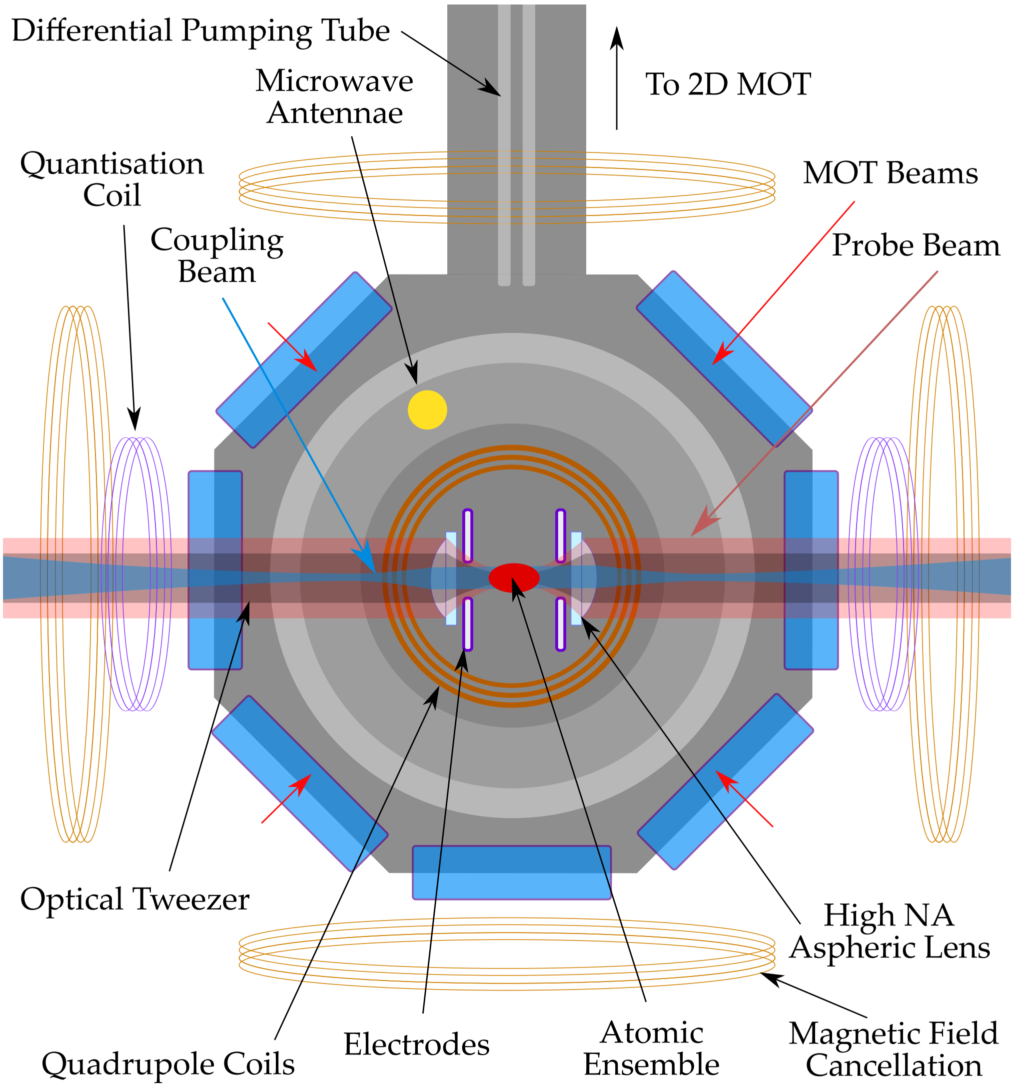

Figure 3.2: Functional drawing of the UHV vacuum chamber (internal). An ensemble of ultracold atomic Rubidium 87 is loaded into FORT at the focus of two *in-vacuo* high-NA lenses. Magnetic and electric field compensation is possible in this setup. The FORTs share a focus with the probe beam whilst the coupling beam is collimated between lenses. Microwave antennae constructed from unshielded coaxial cable drive microwave transitions. Lenses are ITO coated to reduce stray electric fields in the vicinity of the atoms. Electrodes and MOT quadrupole coils are built *in-vacuo*.

through a differential pumping tube with an aperture of 0.8 mm between the 2D MOT and 3D MOT chambers. The differential pumping tube prevents the buildup of pressure in the main chamber, which maintains a pressure of less than $1 \times 10^{-10}$ Torr. A ‘pushing’ beam [216], is directed along the axis of the 2D MOT. Photon scattering from the pushing beam forces atoms cooled by the 2D MOT through the differential pumping tube and into the main chamber. The pushing beam is red detuned to selectively address atoms with velocities directed away from the 3D chamber, towards the push beam collimator. This has the effect of enhancing the atomic flux through the differential pumping tube.

### 3.1.2 3D MOT

In the main ‘science’ chamber, a magnetic quadrupole is produced by a set of *in-vacuo* coils. The quadrupole is located directly beneath the differential pumping tube and can be offset with external shim coils. The atom flux from the 2D MOT, entering through the differential pumping tube, is caught in the 3D MOT [20, 213, 217] consisting of three red-detuned retro-reflected beams driving $\sigma^{\pm}$ transitions aligned onto the quadrupole. This light is delivered to the experiment via optical fibers from the cooling system described in section 3.3.1. Thermal fluctuations in the lab lead to polarization drifts at the output. One inch polarizing beam cubes[5] are positioned directly after the outputs of all three ports of the fiber beam splitter for polarisation purity at the MOT, reducing the need for maintenance.

The MOT quadrupole is located at the joint focus of two high numerical aperture (NA) lenses, overlapped with their common focus to prepared for dipole trap loading. The lenses have a numerical aperture of 0.6 and an effective focal length of 10 mm. The lenses are coated with an ITO coating connected to a ground reference plane. This reduces static build-up which

---

[5] Thorlabs PBS252

might perturb the atoms, and provide a resolution limit ~1 μm at 780 nm. The electronic environment about the atoms can be controlled via the four split-ring electrodes which surround each of the high NA lenses[6]. The position of the quadrupole can be controlled by a set of *ex-vacuo* magnetic field offset coils which are used to position the MOT quadrupole and to compensate background magnetic fields for the grey molasses stage[7].

### 3.1.3 Dipole Trapping

Trapping atoms in the ~ 1 mK dipole traps requires a pre-cooled, dense ensemble of atoms. FORT is positioned centrally within the MOT trapping volume and is switched on at full power throughout MOT loading. FORT positioning is optimised by maximising optical depth to the probe beam during experimental runs. The FORT loading sequence used in experiments presented in this thesis involves the following steps, with a summary of powers and timings in Figure 3.3.

1. 2D MOT and 3D MOT run at full power for ~ 100 ms achieving 3D MOT loading $2.5 \pm 0.2 \cdot 10^7$ atoms at temperatures of ~ 100 μK [218].

2. In the CMOT[8] stage, The MOT magnetic field gradient is increased and the cooling, repump powers are reduced. Cooling detuning is increased to $\sim 5\Gamma$. The MOT is compressed and phase-space density increases [212, 213].

3. In the dark molasses stage, the field gradient and repump is switched off, and the cooling powers and detunings of the CMOT stage are

---

[6] Used to apply noise fields in chapter 5

[7] There is a seven Tesla electromagnet opposite PH54. If the MOT unaccountably disappears in an instant, the magnet has probably been switched on.

[8] MOT Compression.

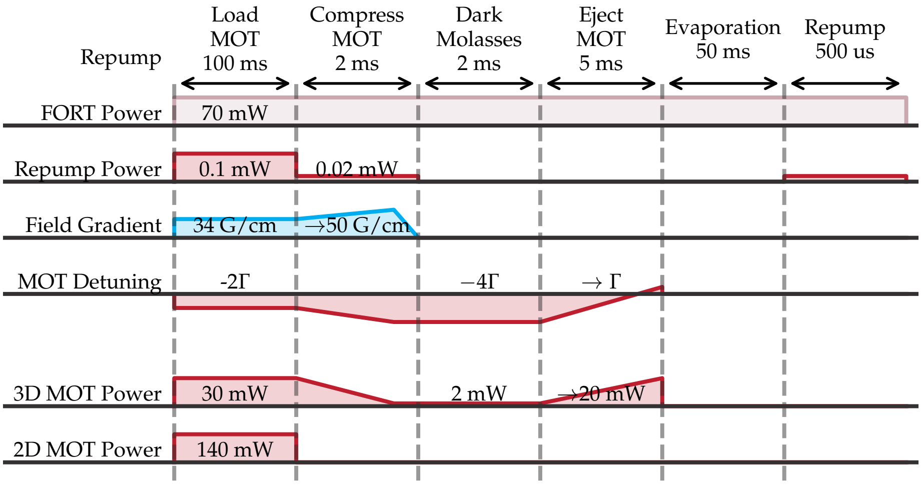

Figure 3.3: FORT Loading Sequence. After initial MOT loading, number density is increased by implementing a compression (CMOT) stage. The ensemble is then cooled via dark molasses, in the absence of repump light. Finally, the cooling light is ramped through resonance to eject the MOT, leaving only stark-shifted, trapped atoms in the FORT. A final stage of evaporative cooling further reduces the ensemble temperature.

maintained [219, 220]. Stark shifts of the bright state enact Sisyphus cooling, reducing the temperature of the MOT to $\sim 50$ μK [221]. This leaves the atoms in the $5S_{1/2}F = 1$ ground state hyperfine level.

4. The cooling beams are then ramped from negative to positive detuning, imparting momentum to atoms not held in the dipole trap, and thus not experiencing Stark shifts.

5. A variable period of evaporation further reduces the temperature of atoms in the dipole trap [222].

6. A repumping pulse is applied to transfer atoms from $5S_{1/2}F = 1$ to $5S_{1/2}F = 2$ ground-state hyperfine levels. Magnetic sublevels are not resolved at this point.

7. A quantization coil is enabled, splitting the Zeeman degeneracy giving access to well-defined energy states [9].

For a thorough analysis of the experimental application of these techniques in Durham, see the thesis of Hannes Busche [46]. These experimental stages produce optically thick ($OD \sim 4$) ensembles of Rubidium trapped within the FORTs described in section 3.3.4. Performance of FORTs is exhaustively documented [46, 68, 204, 206]. The measured MOT temperature at the end of the molasses stage via time-of-flight imaging is $\sim 50$ μK. Dipole trap temperature is expected to be significantly lower, although the elongated shape of the ensemble, exceeding the depth of field of the imaging

---

[9] Optical pumping is precluded by the lack of a suitable pumping axis, due to restrictive chamber geometry.

system available, makes direct temperature measurement challenging. Results presented throughout this thesis all rely upon the fast and efficient loading of atomic ensembles into FORTs.

Once trapped, we are able to perform up to 20,000 experiments on each ensemble[10]. During each experiment, the atomic ensemble is released from the FORT to remove unwanted AC stark shifts associated with the strong electric field of the FORT. FORT light is pulsed at $\sim$ 200 kHz with a duty cycle of 60%. In combination with the fast MOT loading facilitated by the 2D MOT, we are able to perform upwards of 100,000 experiments per second.

## 3.2 Optical Adressing & Detection

Figure 3.4 shows a reduced energy level diagram for Rubidium 87 [155], highlighting the key transitions addressed by optical fields in this experiment. The dipole trap is addressed by Gaussian control fields co- or counter-propagating with the dipole traps. Input optics for the probe and dipole traps are shown schematically in Figure 3.5. The input optics for the counter-propagating circularly polarised coupling beam addressing the $\sigma^+$ transition is shown in figure 3.6. The high NA lenses used to produce the FORTs described in section 3.3.4 focus probe light (780 nm light addressing D2 $F = 3 \rightarrow F' = 4$) onto the ensemble as shown schematically on figure 3.5 **a**, inset. The focal shift of the lens, shown on figure 3.5 **b**, can exceed the size of the dipole trap which would limit probe absorption. Thus collimation of the dipole traps is adjusted using lenses CA1, CA2 in figure 3.12 to compensate for the wavelength dependent focal shift. After compensation, we typically observe OD = 3-4.

The coupling system is designed to provide a constant Rabi frequency

---

[10] This number depends on the particular experimental sequence and associated heating, but is always more than 5,000.

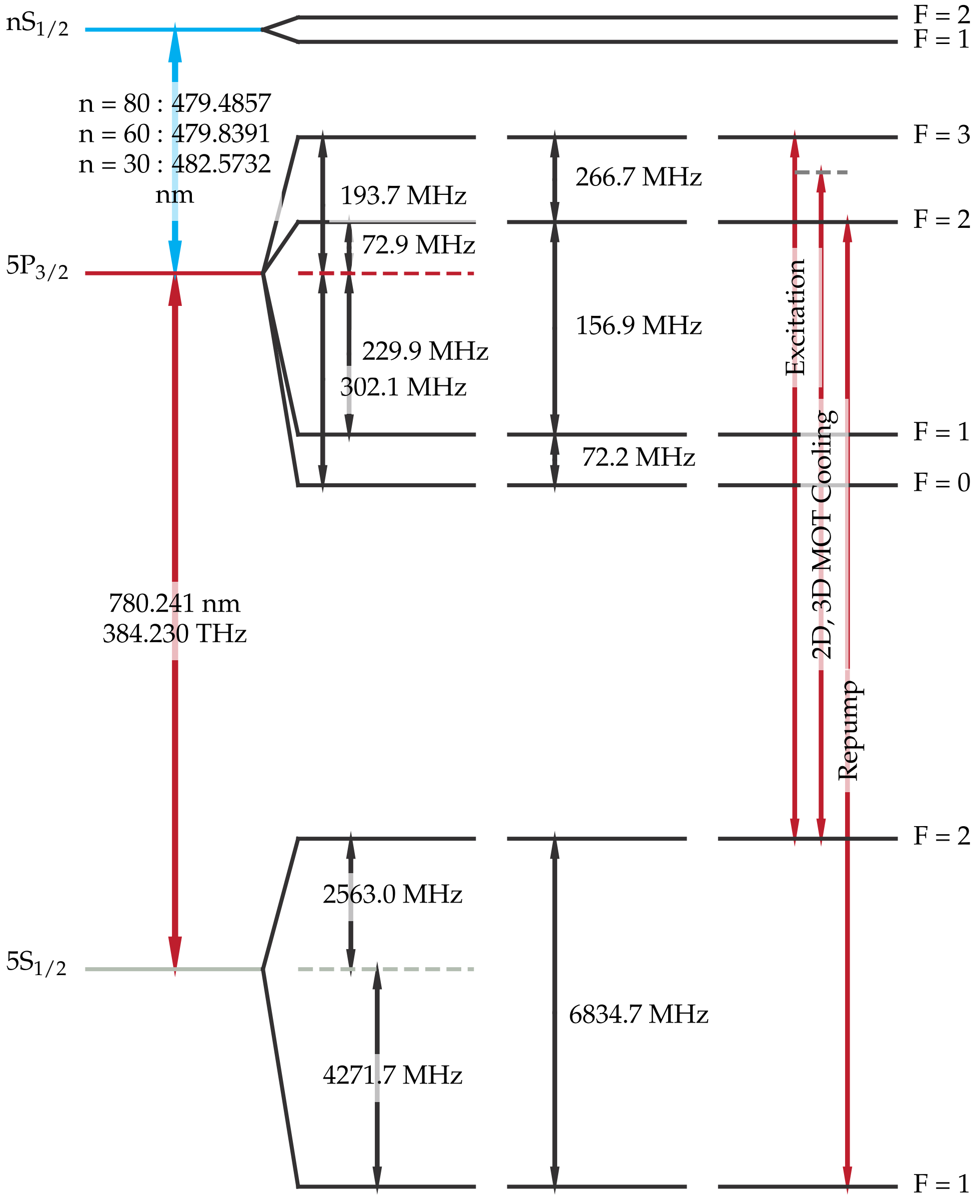

Figure 3.4: $^{87}$Rb D2 Level Diagram. Overview of optical transitions addressed. Magneto-optic trapping and cooling ares implemented using D2 line of $^{87}$Rubidium. Cooling light is detuned from the cycling transition $F = 2 \rightarrow F' = 3$ by $\sim 2\Gamma_e$ by $2\Gamma$. Repump light addresses the $F = 1 \rightarrow F' = 2$ transition returning atoms to the cycling transition and thus providing continuous cooling. Energy level data provided by D. Steck [155].

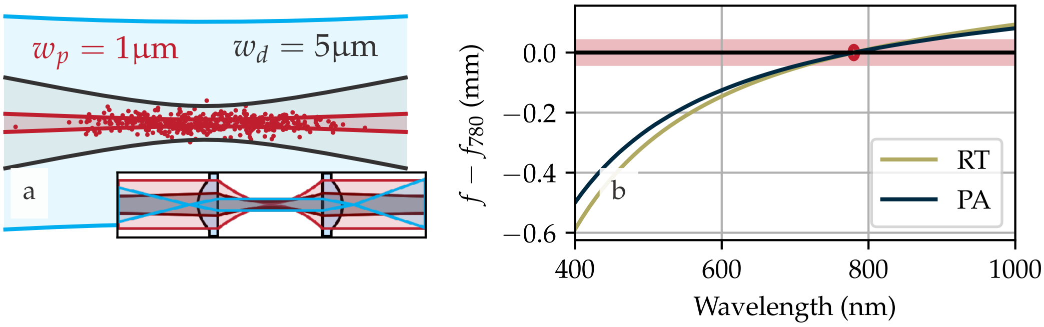

Figure 3.5: Two *in-vacuo* high NA lenses (**a** inset) at the heart of this experiment provides colinear optical addressing and FORT traps. **a** 852 nm Gaussian laser is focussed to create optical FORTs with $w_0 = 4.5\,\mu m$. A Gaussian probe beam (red) is focussed by the same lenses to $w_0 = 1\,\mu m$. A diverging 480 nm coupling beam is collimated by the in-vacuo lenses to $w_0 = 25\,\mu m$ at the position of the atoms. **b** The collimation of the dipole trap is adjusted to compensate for the focal shift of the lenses such that the dipole trap and probe beam have a common focal plane. Focal shifts shown are predicted by Zemax via the ray tracing (RT) method and propagation of paraxial Gaussian beams (PA). Ensemble length is represented by a red ellipse, projected horizontally to show the sensitivity of the experiment to wavelength-dependent focal shifts.

$\Omega_c$ across the ensemble. This is achieved by using the *in-vacuo* lenses to collimate, rather than focus the 480 nm light. Input optics for the coupling light (coupling the $5P_{3/2} \rightarrow nS_{1/2}$) are designed such that the coupling beam is divergent as it enters the *in-vacuo* lens, whereafter it is roughly collimated with a waist of $w_0 \sim 25\,\mu m$. Fine adjustment of the collimation is achieved with an ex-vacuo lens at the output of the coupling beam fiber collimator, as shown on figure 3.6, CA3.

A basic experimental sequence demonstrating single-photon spectroscopy of the ensemble is shown in Figure 3.3.

### 3.2.1 Hanbury-Brown-Twiss Detection Circuit

Figure 3.6 shows the Hanbury-Brown-Twiss (HBT) [223] detection circuit and associated optics. The experiment currently implements two FORTs at the focus of the *in-vacuo* lenses. Probe light interacting with ensembles in the FORTs is reimaged by a $4f$ setup consisting of the *in-vacuo* asphere and an external 400 mm lens providing an overall magnification of $m = 38$. Traps are separated in the reimaging plane by a D-shaped edge mirror and directed towards one of two HBT detection circuits. Probe light is split by an NPBS and fiber-coupled into a commercial single-photon avalanche module (SPAD)[11]. The reader is directed to the thesis of Simon Ball for more information on the performance and limitations of the SPADS [205].

DExTer interfaces to the HBT detector and records time-tagged photon arrival data providing for the analysis of photon statistics [211]. Figure 3.6 demonstrates the capabilities of the experimental hardware. By reducing the MOT loading time, the optical depth of the ensemble is reduced to $OD = 1.8$. The experimental sequence shown in **a** is repeated 10,000 times as described in section 3.2. The weak, coherent probe contains $\widetilde{n} = 0.25$ photons. In **b**, the HBT detector signal is shown for probe detunings $\Delta_p$ in the range -20 to 20 MHz. The single-photon absorption profile of the ensemble shows the transition from an effective two-level system to a four-level system as $\Omega_c$, $\Omega_\mu$ dress the ensemble. Solid lines represent fits to equations in chapter 2 for the susceptibility of a weakly probed system. Fits of this nature can be used to determine the values of $\Omega_c$, $\Omega_p$ experimentally. Section 4.3 shows that it is also possible to measure $\Omega_\mu$ directly.

---

[11] Currently in use are Perkin-Elmer SPCM-AQRH-14-FC and Excelitas SPCM-780-14-FC.

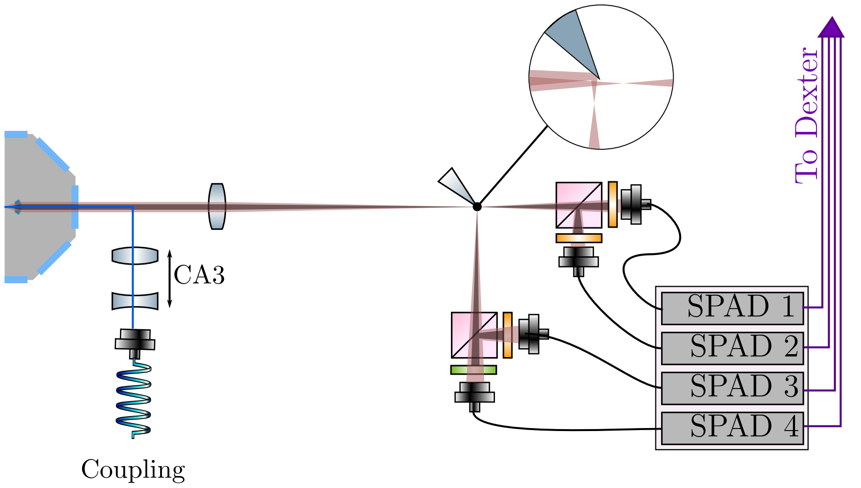

Figure 3.6: Detection and Coupling Optics. Probe waists interacting with spatially separate ensembles at the center of the chamber (far right) are re-imaged by a 400mm lens, magnifying the separation by $m = 40$. An edge mirror is used to separate probe light originating from the two ensembles at the imaging plane. Light from both traps couples to a Hanbury-Brown-Twiss detection circuit, consisting of a beam splitter and two fiber-coupled commercial SPADs. Time-tagged photon arrival data is collected by DExTer with a 5 ns resolution. Fiber inputs are protected from FORT intensity with two 780 nm bandpass filters. A coupling beam counter-propagates with the probe.

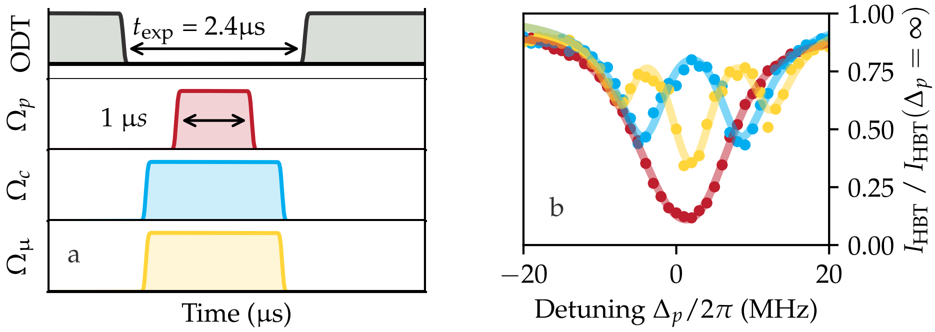

Figure 3.7: Single photon Rydberg spectroscopy. **a** Experimental pulse sequence showing 1 µs probe pulse with overlapping Rydberg couplings $\Omega_c$, $\Omega_\mu$. **b** Single photon spectroscopy. Each data point is obtained by summing photon detection events across 50,000 experiments. The transition from two level (red data, $\Omega_p$ only) to three level EIT (blue data, $\Omega_p, \Omega_c$) to four level AT (yellow data, $\Omega_p, \Omega_c, \Omega_\mu$) is observed. Fits to equations for atomic susceptibility can be used to obtain Rabi frequencies $\Omega_i$. Here, $\Omega_c/2\pi = 9.6 \pm 0.2$ MHz, $\Omega_\mu/2\pi = 13.8 \pm 0.4$ MHz. Measured OD = 1.8.

### 3.2.2 Statistical Analysis

Due to the very low incident photon numbers ($<$ 1.5/experiment) , we adopt a modified $\tau$ parameter for the analysis of photon correlations. We define a discrete $g^{(2)}(\tau)$ parameter which can be applied to situations where the average incident photon number is less than one. $g^{(2)}(\tau)$ does not compare photon arrivals across a true time delta, but instead across experimental runs. Photons propagating in the spatial mode of the probe pulse that intersects the first (second) ensemble are collected by SPADs (see Figure 3.6), with two SPADs per ensemble. Photons reaching detector 1 (3) in experimental run A, and detector 2 (4) in experimental run B are compared. The following section describes the statistical analysis of probe photons reaching two spads coupled to an ensemble. This analysis is performed in duplicate when analysing two ensembles held in two dipole traps.

We start with the usual definition

$$g^{(2)}(\tau) \equiv \frac{\langle n_1^{(A)}(n_2^{(B)} - 1)\rangle}{\langle n_1^{(A)}\rangle \langle n_2^{(B)}\rangle}. \tag{3.2.1}$$

Here, $n^{(A)}$ corresponds to the number of photons arriving in experimental run $A$, and $B = A + \tau$. Subscripts in $n_{1(2)}^{(A)}$ represent photon events registered on SPAD 1 (2). $\tau$ is thus a discrete parameter corresponding to the experimental run number, with $\tau = 1$ corresponding to a separation of roughly 5 µs, the experimental repetition period. We next restrict the formal definition of $g^{(2)}(\tau)$ to the case of very low photon numbers, where counts of greater than two photons are vanishingly rare. Disregarding possible incident photon numbers above two, we have that

$$g^{(2)}(\tau) = \frac{2 \cdot P_\tau(2)}{[P(1) + 2 \cdot P(2)]^2}. \tag{3.2.2}$$

Here, $P_\tau(2)$ compares the correlated probability of obtaining a photon detection event on both of the HBT detectors in experimental runs $A, B$, against the sum of *uncorrelated* probabilities of obtaining a photon detection event on one $P(1)$ or both $P(2)$ detectors. Thus the $g^{(2)}(\tau)$ statistic represents correlations within runs ($\tau = 0$), and between runs ($\tau \neq 0$). At the end of each experimental sequence, the atoms are left in their ground state through de-pumping by $\Omega_c, \Omega_\mu$ and spontaneous decay at rate $\Gamma_e$. Thus no correlation is expected between runs $g^{(2)}(\tau \neq 0) \approx 1$. Within a single experimental sequence ($\tau = 0$), Rydberg interactions can cause anti-bunching of emitted photons due to Rydberg blockade.

Values for $g^{(2)}$ quoted in later chapters are corrected for the relative efficiencies of the two detectors $\epsilon_\alpha, \epsilon_\beta$.

$$\epsilon_1 \equiv \frac{n_1}{n_1 + n_2}, \qquad \epsilon_\beta \equiv \frac{n_2}{n_1 + n_2}, \tag{3.2.3}$$

where $n_{1,2}$ are the number of counts received by detectors 1, 2. We can then express the probabilities in equation 3.2.2 in terms of detection events $P_1(A)$, $P_2(B)$, $P_\tau(AB)$, which are the probabilities of detector 1, 2, or both

1 and 2 registering a photon event across experimental runs $A$, $B$.

$$2\epsilon_1\epsilon_2 P(1) = \left(\epsilon_2 P_1(A) + \epsilon_1 P_1(B) - \left[2 - \frac{3}{2}(\epsilon_1 + \epsilon_2)\right] P_\tau(AB)\right), \tag{3.2.4}$$

$$2\epsilon_1\epsilon_2 P_\tau(2) = P_\tau(AB). \tag{3.2.5}$$

which can be substituted into equation 3.2.2 to give

$$g^{(2)}(0) = \frac{\epsilon_1\epsilon_2}{\left(P(A)\epsilon_2 + P(B)\epsilon_1 + 3P_\tau(AB)/2\right)^2}. \tag{3.2.6}$$

This equation is used to calculate values for $g^{(2)}$ presented in later chapters.

## 3.3 Laser System Upgrades

Stable optical and microwave fields used to manipulate atomic Rubidium 87 are fundamental to this work. Figure 3.1 shows an overview of the optical systems used to manipulate atoms in this project. Our laser system contains four subsystems, The cooling system provides optical fields addressing the ground to excited state transition $|5S_{1/2}F = 2\rangle \leftrightarrow |5P_{3/2}F' = 3\rangle$. The repump system addresses the $|5S_{1/2}F = 1\rangle \leftrightarrow |5P_{3/2}F' = 2\rangle$ transition and is used to optically pump atoms into the cycling transition addressed by the cooling system. The 480 nm laser system couples the excited state to Rydberg states, driving the transition $|e\rangle = |5P_{3/2}F' = 3\rangle \leftrightarrow |nS_{1/2}\rangle$ where $n \in [30, 100]$. A free-running ECDL at 852 nm provides seed light for the far off-resonant traps (FORT) utilised for the trapping of ensembles in this experiment.

### 3.3.1 Cooling System - 780 nm

The 780 nm cooling system provides light resonant or near-resonant with the closed $|5S_{1/2}F = 2\rangle \leftrightarrow |5P_{3/2}F' = 3\rangle$ transition in Rubidium 87 for cooling, imaging and excitation. This system was recently rebuilt to remove an aging DL-100 including the replacement of the master laser, which is now upgraded to a commercial laser system[12] consisting of a DL-Pro ECDL, a tapered amplifier, and two in-line optical isolators. Amplified light from the TA output provides $\sim 1.5$ W of 780 nm light. The system also provides $\sim 20$ mw of light directly from the ECDL via a sampler placed in between the ECDL and TA input. A double-pass AOM setup driven at the center frequency adds a blue detuning of $\Delta_{\text{lock}} = 140$ MHz. This detuned ECDL output is locked to the $|5S_{1/2}F = 2\rangle \leftrightarrow |5P_{3/2}F' = 3\rangle$ transition. Thus the ECDL output light is stable at 140 MHz below the $|5S_{1/2}F = 2\rangle \leftrightarrow |5P_{3/2}F' = 3\rangle$ resonance. Frequency stabilisation is achieved via a PID controller[13] locking to an error signal generated via modulation transfer spectroscopy (MTS) [224, 225].

An overview of the lock setup is given in figure 3.8. Frequency sidebands at ±10 MHz are added to the ECDL output by a Photonics Technologies EOM[14] driven with a 2V peak to peak electric field supplied by an arbitrary function generator[15]. This modulated pump beam then counter-propagates in a room-temperature vapor cell with an unmodulated probe beam. The 10 kHz modulation of the pump beam is transferred onto the probe beam via a four-wave mixing (FWM) process [225–227]. The modulated probe beam is detected on a fast photodiode[16]. Beats are observed where the MTS process is efficient (in the vicinity of closed transitions). The beat signal from the photodiode is downmixed to obtain an error signal using a commercial PDH module[17]. MTS produces large error signals with high SNR[18] for closed transitions. Open transitions and crossover features do not support efficient MTS due to the two-photon absorption required for FWM. For closed transitions, MTS produces error signals with lower noise

---

[12] Toptica TA-Pro

[13] Toptica FALC.

[14] Photonics Technologies EOM-02-10-V

[15] Tektronix AFG3022B

[16] Hammamatsu CI10508-01

[17] Toptica PDH 110

[18] Signal to noise ratio.

lback

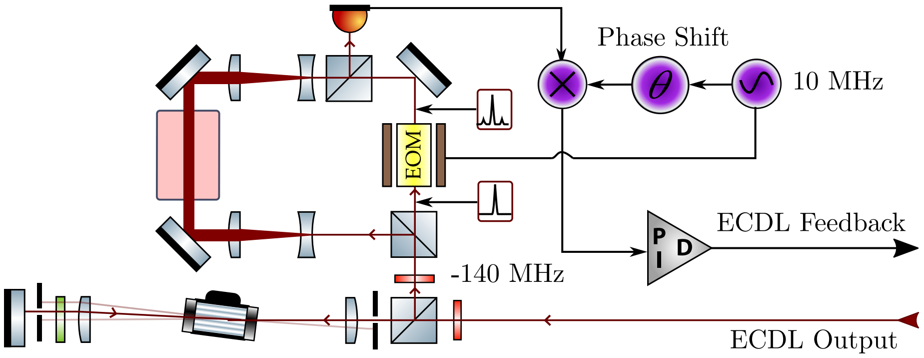

Figure 3.8: Cooling system frequency stabilisation via Modulation Transfer Spectroscopy. The ECDL output is detuned by 140 MHz by a double pass AOM and then reaches the MTS lock. The ECDL light is split into two arms. An EOM driven at 10 MHz imparts frequency sidebands to one of the arms (the pump). Both arms (pump & probe) are then expanded and are overlapped in a Rubidium vapor cell in a counter-propagating geometry. When the probe is detected on a photodiode, modulation transfer from pump to probe in the vicinity of a closed transition causes an observable beat at the modulation frequency. The signal is mixed down to extract the beat magnitude which takes the form of an error signal. This error signal is supplied to a PID controller which generates feedback, stabilising the ECDL.

and increased lock stability as compared to traditional frequency modulation (FM) spectroscopy. A commercial PID[19] controller creates piezo and current feedback from the MTS error signal which stabilises the 780 nm ECDL to the MTS transition.

IR AOMs from several suppliers[20] are used to provide frequency and amplitude control, as well as fast switching. AOMs all have similar characteristics, with a specification of 80% diffractive efficiency into the first order and a bandwidth of $\Delta_{\mathrm{AOM}} = 20$ MHz about $f_{\mathrm{AOM}}$. The AOMs shift the detuned TA light to resonance[21] or near resonance[22] when driven at the center frequency $f_{\mathrm{AOM}}$ before delivery to the experiment. In double pass configuration, light reaching the experiment can be detuned over roughly $\pm 2\Delta_{\mathrm{AOM}}$, centered on the atomic resonance. Some paths on figure 3.1 show single pass AOM configuration. Here, 110 MHz aoms are used to provide large detunings from the atomic resonance $\Delta > 30$ MHz.

Magneto-optic trapping and resonant interaction with qubits occurs at vastly different energy scales, with the former requiring hundreds of milliwatts and the latter requiring picowatts of power. Beam splitters in the probe path are not sufficient for this magnitude of attenuation. Low probe intensity also can not be obtained by reducing AOM drive power as this leads to undesirable transient effects. Thus, the intensity is reduced by a series of neutral density filters with a nominal optical depth of 7. AOMs are then driven at maximum power, achieving acceptable pulse train envelopes at low intensities. Fine intensity adjustment is performed by photon counting using the Hanbury-Brown-Twiss detection circuits described in section 3.2.1.

---

[19] Toptica FALC110

[20] AA Opto, Gooch & Housego, Isle optics.

[21] In the case of the probes and imaging light

[22] In the case of cooling light, pushing light.

### 3.3.2 Repump System - 780 nm

The 780 nm repumping system addresses the $|5S_{1/2}F = 1\rangle \leftrightarrow |5P_{3/2}F' = 2\rangle$ transition and is used to optically pump atoms out of the $F = 1$ state during magneto-optic trapping.

The repump system was previously the least stable system in the lab, and the only system locked to an FM spectroscopy signal [224]. FM spectroscopy is extremely sensitive to relative phase shifts in the modulation and demodulation signals which can cause frequent unlock events and limit experimental uptime. To stabilise the system, the technique of Zeeman - tunable MTS [110, 228] was developed to enable locking the system via the more stable MTS technique to an open transition that does not naturally support the FWM technique underlying traditional MTS. This technique was developed due to considerations of relatively low SNR [229, 230] of shifted locking schemes and previous lack of tuning in Zeeman shifted schemes [231].

Figure 3.9 shows the experimental implementation of a tunable MTS lock. As with the cooling system, an AOM imparts a 70 MHz red detuning for locking (not shown) and subsequent switching AOMs to return the system to resonance. Much of the setup is identical to a traditional MTS lock (figure 3.8)[23]. A small (2 mm thick, 22mm diameter) cell containing Rubidium at natural abundance is heated to 80 degrees centigrade by a pair of standard ceramic disk heaters[24]. The cell and heaters are held in a custom cell assembly 3D printed in Acrylonitrile Butadiene Styrene (ABS), with a glass transition temperature of 105 degrees centigrade. Heating the cell increases the negligible ambient optical depth to $\sim 5$.

The small vapor cell is held in a high magnetic field at the center of the permanent magnet assembly which can exert fields of up to 7 kG[25]. Zeeman

---

[23] EOM:Photonics Technologies EOM-02-12.5-V, Photodiode: Hamamatsu C10508-01

[24] Thorlabs HT19R

[25] Neodymium magnets were manufactured to specification by Shanghai Jinmagnets

shifts of atomic energy levels associated with the hyperfine Paschen-Back regime are observed. We apply a 4.7 kG field to shift the MTS-supporting $\mathrm{F} = 2 \rightarrow \mathrm{F}' = 3$ manifold by ±6.6 GHz, with the negative shift overlapping the repumping transition $\mathrm{F} = 1 \rightarrow \mathrm{F}' = 2$. Quarter wave plates flanking the magnet assembly select the $\sigma^-$ transition. The setup requires only 4.6 mW of power, split into a 3.5 mW pump beam and a 1.1 mW probe , each with a 500 µm beam waist. In contrast to the MTS system depicted in figure 3.8, small beams are imposed by the 3 mm aperture in the permanent magnets. Small beams do not lead to significant power or transit time broadening. Long-term stability measurements via beat note detection against a separate MTS-locked laser system show a combined instability of $< 1$ MHz which is more than sufficient to lock to the repump transition with linewidth 6.065(9) MHz [155]. The combination of Zeeman shifted MTS error signal reduces the frequency of unexpected repump lock errors to less than one per day. Zeeman shifts associated with the background magnetic fields are calculated to be less than 1 MHz.

### 3.3.3 Coupling - 480 nm

A commercial ECDL with integrated second harmonic generation (SGH) cavity[26] provides 250 mW of light over the range 479 nm - 481 nm. This system can be tuned into resonance with transitions $|5P_{3/2}\rangle \leftrightarrow |nS_{1/2}\rangle$, where $n > 30$.

Figure 3.10 shows an overview of the 480 nm laser system. The laser frequency is referenced to a ULE cavity, consisting of one flat mirror and one mirror with a radius of curvature $r_{m2}$ of 50 cm, separated by a block of zerodur with length 100 mm. The cavity has a free spectral range (FSR) of 1.5 GHz a finesse of 100,000 and a FWHM of 15 kHz. The cavity has a

---

Indistrial co. LTD, No.1602, Song Yun Shui Yuan, 1000 Wenxiang Road, Songjiang District, Shanghai, 201620,China

[26] Toptica SHG-Pro.

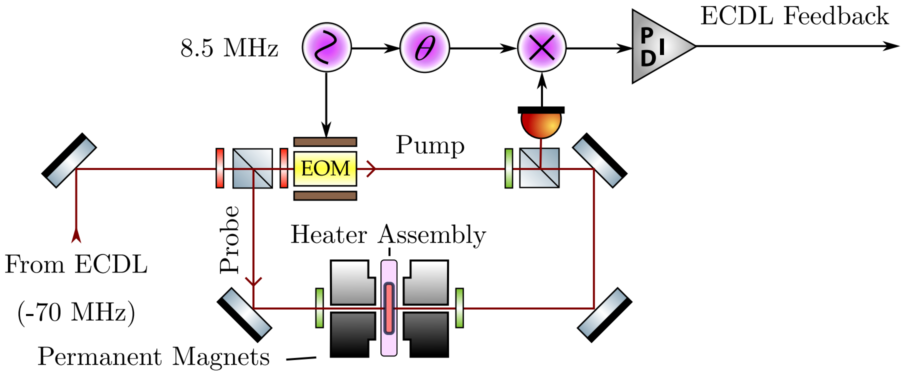

Figure 3.9: Zeeman-Tunable MTS Setup. The MTS scheme is similar to figure 3.8. The four-wave mixing process takes place in a small vapor vell with a (variable) applied **B** field of 4.7 kG derived from two powerful N52 Neodymium magnets flanking the cell. The Zeeman effect causes a shift in the position of the closed transitions and a corresponding shift in the derived MTS error signal of 6.6 GHz, whence the D2 closed transition can be used to lock to the D2 repumping transition (see text). The lock point can be tuned by adjusting the magnet separation.

quoted drift of 25 kHz / day and a shorter-term variation of 2 kHz.

The 480 nm master laser is locked to the cavity via the electronic sideband technique [232–234]. A schematic of the implementation appears in figure 3.10. Light from the master diode passes through a commercial fiber-coupled EOM[27]. The EOM is driven at two RF frequencies, $f_{\mathrm{error}}$, $f_{\mathrm{SB}}$, combined using an RF mixer. The EOM modulates the light entering the cavity, imposing sidebands. To first order, sidebands at both modulation frequencies are created. These sidebands are equally spaced about the cavity resonance at $f_0 \pm f_{\mathrm{error}}$, $f_0 \pm f_{\mathrm{SB}}$. Each of these sidebands is modulated with a set of second-order sidebands $f_0 \pm f_{\mathrm{SB}} \pm f_{\mathrm{error}}$. The reflectance from the cavity is detected using a fast photodiode and downmixed by $f_{\mathrm{error}}$. A primary error signal at the frequency of the cavity resonance is

---

[27] Jenoptic custom 980 nm fiber-coupled EOM from the PMxxx range. Two identical EOMs were purchased in anticipation of a second coupling system requiring a second lock to the same cavity following the same scheme.

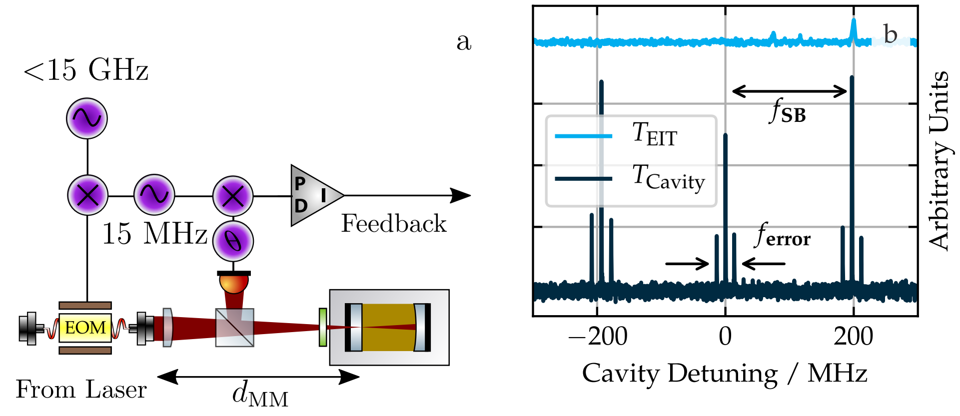

Figure 3.10: **a** Offset Locking Scheme. Sidebands at $f_{\mathrm{SB}} = \pm 200$ MHz are driven by a tunable source with $f_{\mathrm{SB}}^{\mathrm{max}}$ exceeding the lock cavity FSR. Mode matching is performed using a bare fiber and a single lens. The lens is adjusted to create a waist of the correct size, and then the lens and fiber arrangement are moved to the correct distance $d_{\mathrm{MM}}$ to couple into the cavity **b** Cavity transmission $T_{\mathrm{cavity}}$. An error signal is generated at the carrier and sideband frequencies using a PDH technique with $f_{\mathrm{error}} = 15$ MHz. Feedback stabilises the SHG system via a commercial PID controller. The ECDL is scanned 600 MHz across a cavity resonance. First and second order sidebands are observed. A vapour EIT transmission profile (cyan, offset) shows EIT resonance detuned from the carrier by $f_{\mathrm{SB}}$.

observed, with second-order error signals offset by $f_{\mathrm{SB}}$. A schematic of locking electronics as well as a typical cavity reflectance scan showing sideband alignment with the $|5P_{3/2}\rangle \leftrightarrow |60S_{1/2}\rangle$ EIT peak is shown in figure 3.10.

The position of the second-order error signal relative to the cavity resonance can be tuned by adjusting $f_{\mathrm{SB}}$ at source[28], with a range of 0.005 GHz-13.6 GHz, far exceeding the FSR of the cavity. As such, the lock point can be tuned over the full FSR of the cavity, establishing an arbitrary lock point for Rydberg EIT spectroscopy as shown in Figure 3.10. Coupling

---

[28] Commercial WindFreakTech SynthHD PRO v1.4.

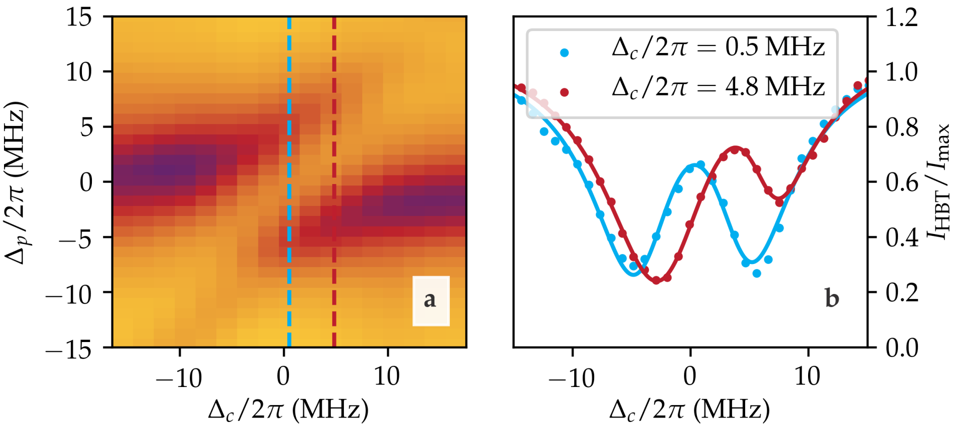

Figure 3.11: Sideband tuning demonstration. **a** An avoided crossing becomes visible in the absorption spectrum of the three level system $|5S_{1/2}F = 2\rangle \leftrightarrow |5P_{3/2}F = 3\rangle \leftrightarrow |60S_{1/2}\rangle$ when the coupling field $\Omega_c$ linking states $|5P_{3/2}F = 3\rangle \leftrightarrow |60S_{1/2}\rangle$ is swept across resonance. **b** Spectroscopy of a cold atomic ensemble held in a dipole trap with $\Omega_c/2\pi = 9 \pm 1$ MHz. Fits to the data are used to locate the resonance. Two datasets identified by dotted lines in the colour map have, $\Delta_c/2\pi = 0.5 \pm 0.4$ MHz and $4.8 \pm 0.2$ MHz, matching the detuning of the RF source supplying $f_{SB}$ (4 MHz). $I_{\mathrm{HBT}}$ is defined in section 3.2.1.

light is supplied to the experiment via a single pass, AOMs at the focus of a pair of 100mm lenses for fast switching, giving rise and fall times of 40 ns. Figure 3.11 exhibits the precision adjustment of the cavity lock point over the $|5P_{3/2}\rangle \leftrightarrow |60S_{1/2}\rangle$ through EIT spectroscopy of an ultra-cold ensemble of Rubidium 87 at 50 μK, in the weak probe limit. Fits to the data using equations developed in chapter 2 are used to locate the coupling beam resonance.

The flexible electronic sideband technique is well suited for wavelength switching to address various Rydberg states. The frequency of the 480 nm system is routinely and seamlessly tuned across the range 479 nm to 482 nm to address these transitions. Data presented in this thesis were primarily taken at principal quantum numbers $n = 30, 60, 80$.

### 3.3.4 Trapping - 852 nm

The finite Rydberg blockade radius $r_b$ for accessible principal quantum numbers is on the order of tens of microns[29]. Thus blockaded media can only be fully realised through confinement to similar dimensions. A far-off-resonance trapping (FORT) scheme common amongst experiments in atomic physics is implemented. The trapping force can be derived by considering the effect of the Gaussian laser field upon the atoms [235]. Far from resonance, the energy shifts to the atomic energy levels can be treated perturbatively as AC Stark shifts. The potential energy of the dipole force is given by Equation 3.3.7 and is quadratic in the time averaged electric $\mathcal{E}$ field [235].

$$U_{\mathrm{FORT}} = -\frac{1}{2}\left\langle \mathbf{d}\cdot\mathcal{E}\right\rangle = \frac{1}{2\epsilon_0 c}\mathfrak{Re}(\alpha)|\mathcal{E}|^2. \tag{3.3.7}$$

Trapping light for optical potentials derive from a commercial ECDL system with integrated tapered amplifier providing 2 W of power at 852 nm[30]. The power $P$ of a Gaussian beam is related to intensity $I$ through $I = 2P/\pi\omega_0^2$ and to the electric field through $I = 2\epsilon_0 c|\mathcal{E}|^2$. The equation for the trap depth at the focus is then

$$U_0 = -\mathfrak{Re}(\alpha)\frac{P}{\epsilon_0 c\pi\omega_0^2}. \tag{3.3.8}$$

Light is fiber coupled to the experiment, where it is focussed by high NA *in-vacuo* lenses to produce FORTs with $w_0 = 5\,\mu\mathrm{m}$ as shown in figure 3.13 (left). Millikelvin trap depths are achieved at relatively low powers. The 150 mW FORT traps each have trap depths of $U_0 = 2.2$ mK. Trapping frequencies are $w_r = 32$ kHz, $w_z = 1.38$ kHz, where $r$ represents the radial polar coordinate, and $z$ represents the direction of propagation of the trap, left to right on figure 3.12.

Due to the fixed scaling factor between the axial and radial lengths of the trap produced by a single focussed beam, blockade is only possible in

---

[29] For 3 MHz laser linewidth

[30] Toptica TA-Pro

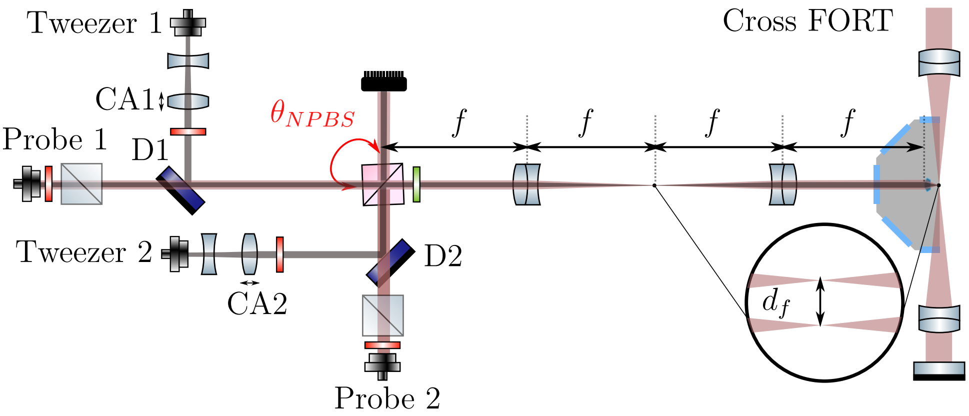

Figure 3.12: $4f$ setup providing convenient adjustment of the distance between two *in-vacuo* optical dipole traps. The $4F$ setup maps rotations of the NPBS into separations $d_f$ at the focus of the *in-vacuo* lenses. Probe and trapping beams remain overlapped when varying the distance between traps and require minimal realignment after changing $d_f$. Collimation adjustment lenses CA1, CA2 compensate for the focal shift of the *in-vacuo* lenses between 852 and 780 nm. A cross-trap consisting of a simple retro-reflected 852 nm beam exists to confine atoms in the direction of probe propagation.

the axial direction for accessible principal quantum numbers $n > 90$. The desirability of shortening the ensemble in the axial direction has prompted the installation of a cross-dipole trap [236] (also referred to as reservoir / dimple traps [237]). The cross-dipole trap intersects the FORTs to reduce the ensemble length in the direction of propagation that such that blockade can occur at lower $n$. Additionally, the larger crossed dipole trap is expected to facilitate the loading of FORTs [238]. The cross trap is formed from a focused beam which enters the chamber orthogonal to the probe beams as shown in figure 3.12. The FORT has a measured waist of $w_0 = 27 \pm 1$ μm. The additional cross dipole trap brings the total predicted trap depth to 2.5 mK as shown in figure 3.13, right. Trapping frequency in the direction of propagation is doubled to $w_z = 2.33$ kHz. The size of a thermal ensemble of atoms in a FORT with trapping frequency $w_i$ is [235]

$$\sigma_{\mathrm{i}} = \frac{1}{w_i}\sqrt{\frac{k_b T}{m}}, \tag{3.3.9}$$

thus the increased trapping frequency achieved with the crossed dipole trap is predicted to reduce the size of loaded ensembles in the direction of propagation. The ensemble length is predicted to scale as $w_1/w_2$, reducing the length of the ensemble from $\sigma_z = 8\,\mu\mathrm{m}$ to $\sigma_z = 4\,\mu\mathrm{m}$ at 50 μK. Although this reduction in length is modest, it critically reduces the size of the ensemble such that it fits within the blockade radius of accessible principal quantum numbers. This provides for the possibility of fully blockaded media in the future.

The FORT input optics have recently been upgraded to simplify the process of adjusting the lateral distance between two FORTs for future through the implementation of a $4f$ imaging system as shown in figure 3.12. The $4f$ system reimages angular deflections of the dipole trapping beam by an non-polarising beam splitter (NPBS) onto the face of the in-vacuo lens. Thus angular deflections introduced by the NPBS are mapped into lateral trap offsets at the focus of the *in-vacuo* lenses. This $4f$ setup provides a convenient method of controlling the lateral distance between the foci of

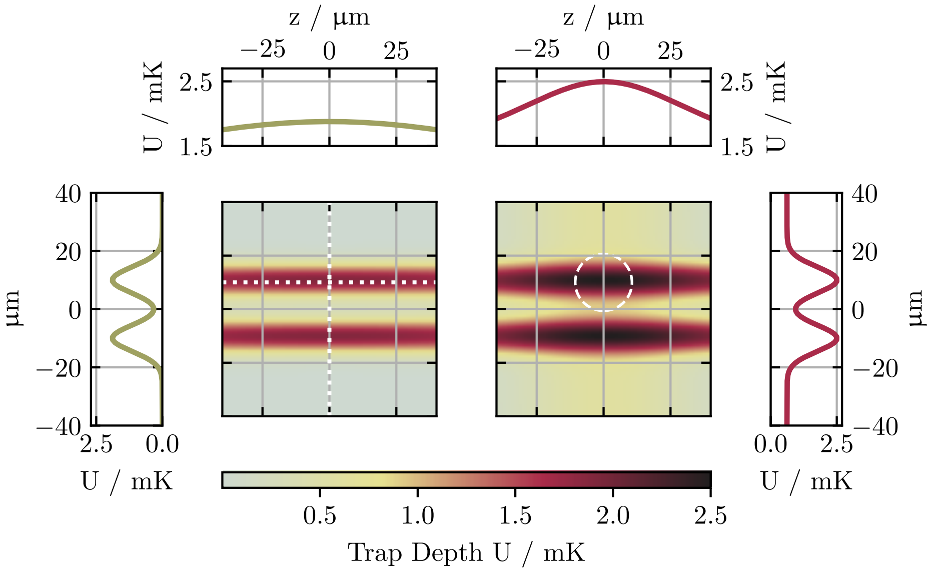

Figure 3.13: Theoretical dipole trap geometry and depth without (left) and with (right) the cross dipole trap. Color maps with upper and lateral projections show trap depth for FORTs with (left) and without (right) a cross dipole trap. Blockade radius at $n = 80$ is indicated by a dashed white circle. The cross trap was implemented to overcome the unfavourable FORT aspect ratio. The direction of propagation, $z$, is marked. The radial direction $r$ extends outward in the vertical direction from the center of each trap.

two optical dipole traps. Probe beams are combined with trapping beams using dichroic mirrors before the NPBS and are colinear at the NPBS. Thus the same lateral translation is effected for both probe and trapping beams by NPBS angular deflection. This minimises realignment of the probe onto the ensemble after lateral translation of the dipole trap.

With the crossed dipole trap in operation, an optical depth of 5.48 ±0.1 was observed. Further details on the characterisation of the crossed dipole trap can be found in the thesis of Teodora Ilieva [206]. FORTs used to obtain data for this thesis commonly achieved optical depths of 3-4.

# Chapter 4

# Cooperative Rydberg Ensembles

This chapter outlines experiments demonstrating control over the statistical and temporal nature of light through controlled interaction with an atomic ensemble. Dipolar couplings between ground and Rydberg states in two, three, and four-level systems modify optical properties of the ensemble. This becomes apparent through a study of the temporal and statistical nature of light passing through the ensemble. Observation of the density dependence of superradiant emission is described in terms of a theoretical model based on dipolar emitters coupled via dipole-dipole interactions. Interference between geometric eigenmodes of an ensemble of atoms is used to explain a density-dependent decay rate of the two-level atomic sample. This density dependence is witnessed through a study of transient optical emission which occurs immediately after the falling edge of a probe pulse, known as free-induction decay (FID) [239].

Control over the decay rate of emission from a three-level system is obtained through Rydberg dressing. Larger and more intense transient emissions are obtained with non-classical, anti-bunched photon statistics at high principal quantum numbers. The effect of interaction-induced dephasing upon the form of the decay is determined through master equation simulations of the system. Anti-bunching of transient emission is enhanced through coupling Rydberg states with a microwave field, thus injecting resonant $C_3$ interactions, effectively increasing the strength of blockade. Weaker microwave dressing is shown to modulate the temporal envelope of the transient emission. Weak measurement of Rabi oscillations between Rydberg levels is possible through monitoring the coupled optical field. This demonstrates that Rydberg transients present a new tool for the study of interaction-induced dephasing and Rydberg blockade of mesoscopic Rydberg ensembles.

## Overview

Cooperative systems are those whose properties cannot be understood by consideration of their parts in isolation. In 1954, Dicke [36] reported that emission from a dense gas of $N$ emitters could decay faster than for a single atom of the same species, assuming atomic confinement to a volume smaller than the cube of the optical wavelength of the driven transition. Emission from such gas was found to decay $N$ times faster than from a single atom. This quantum enhancement is termed 'superradiance' and has been observed in many systems since Dicke's publication including atomic ensembles [72] and Rydberg ensembles [240]. Such collective (many-body) behaviour can be used to create the entanglement which is central to the advancement of modern quantum technology. Systems exhibiting collective interactions can be used to generate entanglement [94, 241], implement single-photon sources [242] and enhance [243] or modify [244] light-matter coupling. Collective behaviour is ubiquitous among modern quantum devices including the latest NISQCs [96, 99, 245].

To utilise superpositions of collective Rydberg excitations of a cold atomic gas as a collective qubit requires a thorough understanding of cooperative excitations and interactions with the photonic pulses which carry input and output information in Rydberg systems. Moving beyond the Dicke picture to more accurately describe the emission of real systems requires a relaxation of Dicke's assumption of two-level emitters with sub-wavelength confinement [66]. The emission of a system of coupled dipoles with relatively low density requires careful consideration of the dipolar couplings between atoms [68, 243, 246, 247]. Each excited atomic dipole produces a field of dipolar radiation which couples to the dipole moment of nearby atoms. Dipole coupled systems require diagonalisation to obtain the natural modes of the system of dipoles. This process can be used to extract resonance shifts and decay rate modifications that can be expected from a driven system of coupled dipoles. We experimentally measure the transmission of our system and observe a collective enhancement of the decay rate of FID [71, 248] due to interference between the normal excitational modes of the ensemble, coupled via dipole dipole interactions [68].

Collective behaviour driven by Rydberg interactions can further modify the optical response of a medium beyond that of the coupled dipole models outlined above into the regime of Rydberg super-atoms [27]. Rydberg coupling is shown to dramatically modify both the temporal envelope of transient collective emission [76, 86, 249, 250], and the photon statistics of the emitted light [44, 45, 251] which are analyzed in line with the super-atom picture. Rabi oscillations between Rydberg states in the absence of probe light are used to enhance interactions and thus suppress $g^{(2)}$ (see chapter 3). The experimental platform used to collect data in this thesis has a rich history of research into novel Rydberg interactions. Quantum states of light have been prepared and manipulated through utilisation of Rydberg blockade [48, 51] with similar results reported elsewhere by many others in the field [43–45, 116, 135, 252–256]. Quantum non-linearities giving rise to effective photon-photon interactions have been previously observed through storage of Rydberg polaritons in two atomic ensembles in close proximity [105]. Microwave electrometry has also been extensively studied in Durham [205] and elsewhere [257, 258] due to utility in hybrid atom-resonator devices and microwave sensing. These previous experiments provide a rich physical backdrop, establishing cooperative Rydberg excitations as interesting and versatile quantum material.

This chapter extends previous work by studying the transient effects of Rydberg coupling on atomic ensembles. Many studies of the steady-state EIT condition are already available [113]. However there is now interest [82, 83] in understanding the dynamics of three (or more) level Rydberg systems to push the performance limits of Rydberg quantum devices including switches [136], transistors [135] and quantum memories [137]. In the section 4.2, Rydberg dressing is shown to dramatically modify the profile of two-level transient decay. Master equation simulations are presented showing how this modification is driven by the accumulation and dissipation of Rydberg coherences due to the Rydberg coupling. The presence of Rydberg coherences causes light transmitted by the atomic ensemble to exhibit anti-bunching, raising the possibility of using dynamic EIT pulses as single-photon sources capable of providing hundreds of single photons per second localised to a time window spanning hundreds of nanoseconds.

Whilst high $n$ Rydberg states with huge blockade radii are technically possible [259], lower principle quantum numbers around $n = \{60, 80\}$ are more commonly utilised due to their ease of preparation and reasonable coupling strengths associated with the rydberg coupling transition. The blockade strength scales with $n$, but can be increased by placing an ensemble in a superposition of $nS$ and $n'P$ Rydberg states. In section 4.3, superpositions of cooperative Rydberg excitations are used to amplify the optical nonlinearities associated with Rydberg media. Experiments showing the ability to deterministically transfer collective Rydberg excitations between Rydberg states, and to place these excitations in superpositions of Rydberg states using resonant microwave fields are reported. Then, weaker Van der Waals interactions governed by the $C_6$ parameter are replaced by a stronger resonant dipolar interaction governed by the $C_3$ parameter [30].

Light emission from the driven system carries the signature of strengthened Rydberg interactions due to stronger interaction-induced dephasing, exhibiting a lower $g^{(2)}$ parameter than for excitations stored in single-state Rydberg polaritons of similar $n$.

**This chapter is based upon the following publications:**

- Robert J. Bettles et al. "Collective Mode Interferences in Light–Matter Interactions". In: (Aug. 2018). arXiv: `1808.08415`
- Charles Möhl et al. "Photon correlation transients in a weakly blockaded Rydberg ensemble". In: *Journal of Physics B: Atomic, Molecular and Optical Physics* (Feb. 2020). DOI: `10.1088/1361-6455/ab728f`

Data presented in this chapter was taken jointly with Y. Jiao, T. Ilieva, H. Busche, S. Ball, P. Huillery, and C. Möhl, with significant input, insight, and theoretical modeling from R. Bettles.

## 4.1 Optical Transients

This section concerns the transient response of a medium composed of two-level scatterers to an incident pulse of resonant light. Early research into coherent emission of systems composed of two-level emitters borrowed terminology from NMR. Transient, coherent optical phenomena occur after a resonant probe beam propagating through an absorptive medium is extinguished. The transient phenomenon was initially termed 'free induction decay (FID)' [239] after a similar phenomenon in NMR spectroscopy. The associated phenomena occurring when a resonant probe enters a medium was first predicted in 1914 by Sommerfield and Brillouin [260, 261] in 1914, and has since been termed a 'forerunner' or 'optical precursor' [262]. The form of these transient effects in atomic gases depends on the properties of the system such as the density and number of atoms. Optical precursors and FID can thus be used to study the properties of optical media composed of two-level systems.

The scattered field can be derived from the form of dipolar radiation $\mathfrak{G}(r)$, the dipole strength $\mu_{ge}$ and the strength of coherences built between $|e\rangle$ and $|g\rangle$.

$$\mathcal{E}_{\mathrm{HBT}} = \mathcal{E}_p + \mathfrak{G}(r) d_{\mathrm{ge}} \rho_{ge}(t), \tag{4.1.1}$$

where $\rho_{\mathrm{ge}}(t)$ is a time-dependent coherence. The optical Bloch equations derived in chapter 2 can be used to show that the coherences $\rho_{eg}$ which give rise to a radiative dipolar field arise when an atom is driven by the probe. They have a complex phase associated with the laser detuning and decay due to the excited state lifetime.

$$\dot{\rho}_{ge}(t) = (i\Delta - \Gamma_0/2)\rho_{ge} + \frac{i}{\hbar}\mu_{ge}\mathcal{E}_{\mathrm{p}}. \tag{4.1.2}$$

In the weak driving limit ($\rho_{\mathrm{ee}} \approx 0$) we obtain a a solution that shows that the signal received by the photon detectors has both steady-state and transient features.

$$\rho_{\mathrm{ge}} = \rho^{ss}_{ge}(1 - e^{(i\Delta-\Gamma_0/2)t}) + e^{(i\Delta-\Gamma_0)/2}\rho^{0}_{ge}. \tag{4.1.3}$$

On resonance ($\Delta = 0$), and with all atoms initially in the ground state ($\rho^0_{ge} = 0$) we can combine with equation 4.1.1 to find the form of the electric field reaching the HBT detectors.

$$\begin{aligned}\mathcal{E}_{\mathrm{HBT}} &= \mathcal{E}_{\mathrm{p}}\left(1 + \alpha\mathfrak{G}(r)\frac{\mu_{ge}}{|\mu_{ge}|}(1 - e^{-\Gamma_0/2}t)\right), &(4.1.4)\\ &= \mathcal{E}_{\mathrm{p}}\left(1 + \alpha\mathfrak{G}(r)\frac{\mu_{ge}}{|\mu_{ge}|} - \alpha\mathfrak{G}(r)\frac{\mu_{ge}}{|\mu_{ge}|}e^{-\Gamma_0/2}t\right), &(4.1.5)\end{aligned}$$

where $\Gamma_0$ is the lifetime of the $|g\rangle, |e\rangle$ transition. In equation 4.1.5, terms are grouped. The steady-state response involves the interference of the driven field of the dipoles $\propto \rho_{ge}$ and the incident laser beam. The exponential term describes a transient electric field. By setting $\chi = \alpha\mu_{ge}\mathfrak{G}(r)/|\mu_{ge}|$ we find that upon illuminating the medium with a probe beam, the electric field recorded by the HBT detectors will be

$$|\mathcal{E}_{\mathrm{HBT}}|/|\mathcal{E}_{\mathrm{p}}| = |\chi|^2 - (\chi + \chi^*)e^{\chi e^{-\Gamma_0 t}}. \tag{4.1.6}$$

In the above equation, the first term gives the asymptotic steady state solution consisting of the laser field interfering with the field of the driven dipoles, causing the cancellation of the laser field in the forward direction and thus a steady-state optical depth. The second term governs the transient dynamics and stems from the timescale required to build coherence that establishes the dipolar field. This timescale is set by the excited state lifetime and is observed as an initial peak in intensity as the medium is transparent for a short time before coherences that cancel the field propagating toward the detectors is established.

Likewise, if the medium is initially illuminated and undergoes a rapid extinction of the probe beam at $t = 0$, the electric field received by the detectors will be

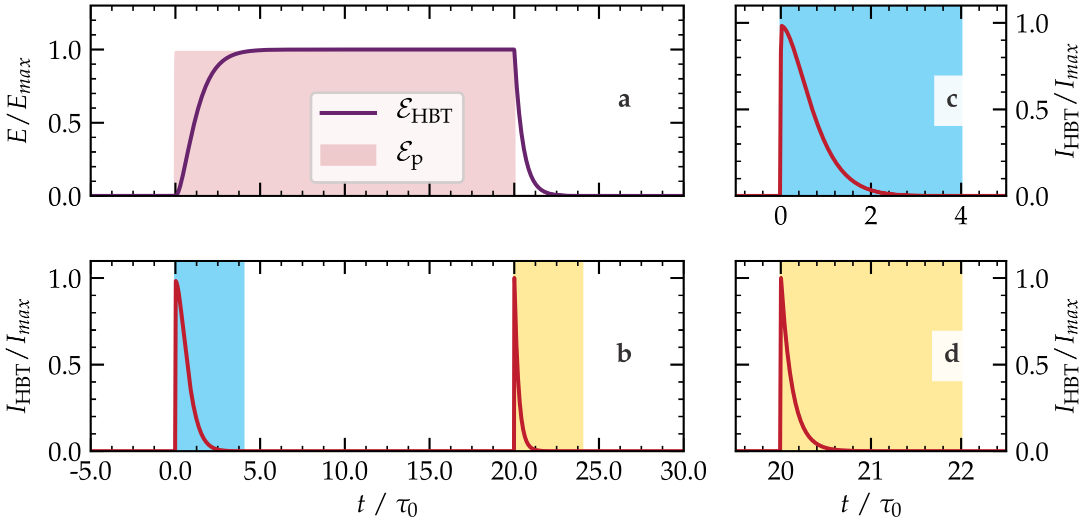

Figure 4.1: Optical Bloch Equation simulation of the optical response of a two-level atomic medium coupled with a resonant probe beam. **a** A resonant probe field $\mathcal{E}_{\mathrm{p}}$ (solid red) is applied to a dense two-level atomic medium. $\mathcal{E}_{\mathrm{p}}$ polarises the medium creating dipolar field $\mathcal{E}_{\mathrm{HBT}}$ (purple line) through equation 2.2.53. This field is out of phase with the incident field leading to destructive interference. **b** Intensity of the summed incident and dipolar field and atomic response (c.f. equation 4.1.5). The steady-state between $t = 5\tau_0, 10\tau_0$ is flanked by two transient phenomena which occur when the drive field is switched on **c** and off **d**. The final transient decays with time constant $\Gamma_0$, whereas the initial transient decays slower, at $\Gamma_0/2$ due to interference with the drive field. Background shading in **b**, **c**, **d** identify the initial (blue) and final (yellow) transient.

$$|E| = |\rho_{ge}^{ss} e^{-\Gamma_0 t/2}|^2 = e^{-\Gamma_0 t}. \tag{4.1.7}$$

This transient response of the detector signal to a probe extinguished at $t = 0$ again stems from the finite bandwidth of the medium. Once the probe beam is extinguished, atomic coherences decay over a timescale set by the excited state lifetime $\Gamma_0$. Both theoretical transient forms are shown in Figure 4.1, where the Optical Bloch equations (see chapter 2) have been integrated numerically to obtain $\rho_{ge}$ under the influence of a pulsed electric field. Study of coherent emission can provide insight to improve the latest quantum hardware [263–266]. FID has been observed in many experimental systems [67, 71, 267, 268].

Figure 4.2 (b) shows the measured response of our atomic system signal including optical precursor (equation 4.1.6) and FID (equation 4.1.7) transients. Both $\Gamma_i$ and $\Gamma_f$ are larger than predicted by the optical Bloch equations for an ensemble of non-interacting atoms [74]. This departure from the above theory is explored in the next section.

### 4.1.1 Dicke Superradiance

The interaction of light with a dense atomic gas can be remarkably different from the single atom picture. At high densities, cooperative behaviour can become the dominant factor in determining physical characteristics such as decay rates, energy levels, and light-matter coupling.

Dicke first described in 1954 [36] that spontaneous emission from a dense ensemble of excited atoms, modeled as two-level emitters, has a variable decay rate which depends upon the excitation number (Dicke's $M$). This collective effect occurs when a dense gas of $N$ two-level emitters are confined to a volume much smaller in its dimensions than the characteristic wavelength of the scatterer, and when the scatterers are all resonant with common electromagnetic field mode. In this scenario, with all scatterers indistinguishable, the atomic system is excited into a symmetric state of

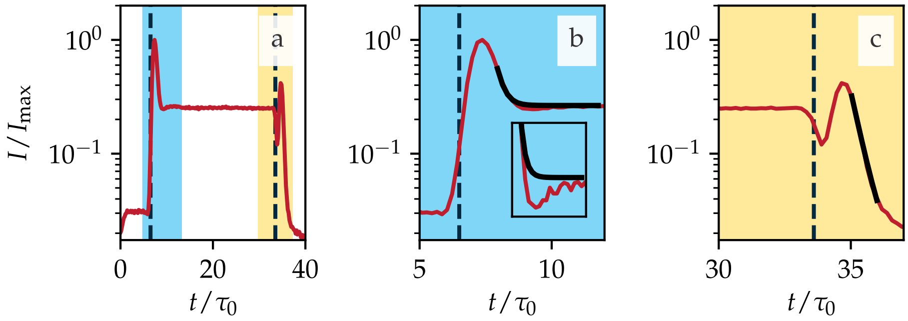

Figure 4.2: **a** The HBT signal showing normalised photon counts $I/I_{\max}$ emitted from an atomic ensemble when illuminated with a pulse from a resonant probe. The rising and falling edge of the probe are shown as dashed lines. **b** The initial transient decays with a FID $\Gamma_i = 2.49 \pm 0.13\Gamma_0$ (black line fit). **b**, inset Oscillations visible in the optical response as the coherent response that creates optical depth is established. **c** The final transient decays with decay rate $\Gamma_f = 3.9 \pm 0.3\Gamma_0$ (black line fit), roughly double that of the initial transient as per equation 4.1.5. The probe has an 80/20 switching time of $\sim \Gamma_0$. Finite probe switching reduces the visibility of the superradiant FID signal.

emitters. The full system of indistinguishable two-level emitters is modeled as a symmetric system of spin - $\frac{1}{2}$ particles.

$$\oplus_j^N \left|S = 1/2, m_s\right\rangle = \left|J = N/2, m_j\right\rangle, \tag{4.1.8}$$

with states that can be derived by repeated application of the creation operator $\sum_i \sigma_i^-$

$$\left|J, M\right\rangle = \sqrt{\frac{(J+M)!}{(N!(J-M)!)}} \left(\sum_i \sigma_i^{(J-M)} \left|g, g, g, ..., g\right\rangle\right). \tag{4.1.9}$$

When such a system of two level scatterers undergoes spontaneous emission, there is a significant increase in the emission rate as a result of the $N$ atoms acting as a macroscopic dipole [37].

$$\hat{\mathcal{D}} = \sum_{j=1}^{N} \hat{\mathcal{D}}_j = (\hat{J}^+ + \hat{J}^-)\mu_{eg}\hat{\epsilon}, \tag{4.1.10}$$

where the $J^\pm = \sum \sigma_j^\pm$ are the sum of the individual transition operators for the $N$ dipoles. The $\hat{\epsilon}$ and $\mu_{eg}$ are the normalised vectors defining the polarisation of the $|g\rangle \leftrightarrow |e\rangle$ transition and the electric dipole operator, respectively.

When such a system undergoes spontaneous emission from a fully excited state, each emitted photon corresponds to a single de-excitation (c.f. equation 4.1.9). Thus the system traverses from a fully excited state to a fully de-excited state in single-quantum jumps, passing through every possible value for $M$ as shown in Figure 4.3.

Due to the form of $\hat{\mathcal{D}}$, the macroscopic dipole, is dependent on the excitation number $M$. Dipolar radiation is much stronger when $M$ is small, because states with small $M$ have have the largest $|g\rangle \leftrightarrow |e\rangle$ coherence. The intensity of emitted photons is then proportional to $\langle J^+ J^- \rangle$.

$$\hat{J}^\pm \left|J, M\right\rangle = \sqrt{(J \mp M)(J \pm +1`)} \left|J, M \pm 1\right\rangle, \tag{4.1.11}$$

$$I \propto (J+M)(J-M+1). \tag{4.1.12}$$

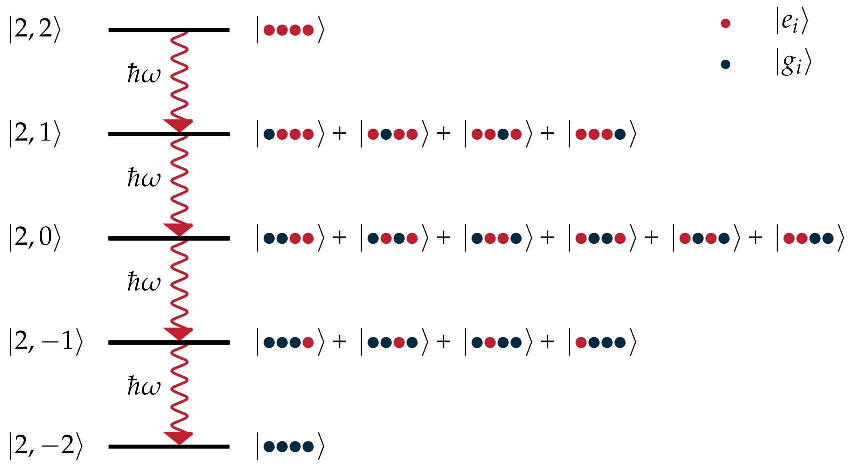

Figure 4.3: Conceptual Dicke Picture. A system of dense two-level scatterers interacting with a coherent laser field can be treated as a single coherent dipole with macroscopic state $|J, M\rangle$, where $J = N$, and $|M| < J$. The internal states of a macroscopic dipole for $J = 2$, consisting of four discrete two-level atoms, are shown. Emission from this macroscopic dipole occurs when one of four dipoles emits a photon $\hbar\omega$. When progressing from fully excited to the ground state, the system is found in a symmetric state with a certain excitation number $M$ and uncertain, symmetric configuration. This correspondence between $M$ states and underlying excitations is represented here as a sum of kets with four atoms either red (excited) or blue (ground state). The macroscopic dipole is strongest for the intermediate state $|J, 0\rangle$, where the underlying dipoles are equally split between $|g\rangle$ and $|e\rangle$, resulting in maximal $|e\rangle \leftrightarrow |g\rangle$ coherence and therefore the largest macroscopic dipole matrix element.

And so in the Dicke limit, when atoms are confined to volumes much smaller than one wavelength, the gas exhibits a modified emission rate. This rate is equal to $N\Gamma$ when all of the dipoles are excited ($|J = N/2, M = N/2\rangle$). The emission rate reaches a maximum when half of the dipoles are excited $|J = N/2, M = 0\rangle$ where the emission rate is $N^2\Gamma$, although in practice this is strongly suppressed by interactions [37]. Since the initial proposition by Dicke, this collective enhancement of the decay rate has been observed in many physical systems [70, 72, 269–271].

### 4.1.2 Dilute Gas

Dicke superradiance stems from the treatment of a tightly confined atomic sample as a coherent macroscopic dipole interacting with an EM field. The Dicke picture requires dipoles to be confined to a small volume $V^{1/3} \ll \lambda$, the so-called Dicke limit. However, this is not a necessary condition for the modification of the optical response of a medium. Rehler and Eberly's [66] theoretical treatment relaxes the requirement of the Dicke limit. Atoms are now known to exhibit collective effects when confined to volumes much larger than that imposed by the Dicke limit [272]. As noted in the previous section, this leads to observable superradiance and subradiance in cold atomic systems [50, 70, 76], Rydberg systems [27, 86] and many others [72].

When atoms in a dilute gas interact with an electromagnetic field, the action of the electromagnetic field promotes each atom into a superposition of $|\pm\rangle$, such that the state of an individual atom $|\phi_i\rangle$ after the pulse is given by

$$|\psi_i\rangle = e^{i\eta_i/2}\sin\tfrac{\theta}{2}\,|e\rangle + e^{-i\eta_i/2}\cos\tfrac{\theta}{2}\,|g\rangle\,, \tag{4.1.13}$$

where state rotation angle $\theta$ determines the likelihood that atom $i$ is excited, and the $\eta_i$ determine the phase of the dipole after excitation. The state of the full system after the excitation pulse is then

$$|\Psi\rangle = \sum_{i=1}^{N} e^{i\eta_i/2} \sin\tfrac{\theta}{2} |e\rangle + e^{-i\eta_i/2} \cos\tfrac{\theta}{2} |g\rangle . \tag{4.1.14}$$

The dipole matrix operator for a single atom in this system is given by $\mathcal{D}_i = d_{eg}(R_{i,-} + R_{i,+})\hat{z}$ (c.f. equation 4.1.10), where the $R_{\pm}$ are the raising and lowering operators of the individual atomic dipoles such that

$$R_{l,+} |e\rangle = R_{l,-} |g\rangle = 0, \tag{4.1.15}$$

$$R_{l,+} |g\rangle = |e\rangle , \tag{4.1.16}$$

$$R_{l,-} |e\rangle = |g\rangle , \tag{4.1.17}$$

$$R_{l,3} |i\rangle = E_i |i\rangle . \tag{4.1.18}$$

We can then evaluate the amplitude and phase of the atomic dipoles in state $|\psi_i\rangle$

$$\langle \mathcal{D}_l(t) \rangle = \hat{z}\mu_{eg} \sin\theta \exp\left[-i(\omega t + \phi_i - \eta_i)\right] + h.c., \tag{4.1.19}$$

where $\phi_i$ is the initial phase of the dipole and $\eta_i$ is the phase advance due to the action of the electric field. We assume that the relative phases of the dipoles are set by the phase of the incoming electromagnetic wave at the position of each dipole $\mathbf{r}_i$, then

$$\phi_i - \eta_i = -\mathbf{k} \cdot \mathbf{r_i}, \tag{4.1.20}$$

where $\mathbf{k}$ is the wave vector of the electromagnetic wave, and $\mathbf{r_i}$ is the position of the $i$'th dipole. The relationship given by equation 4.1.20 defines the spin wave which is established in a dilute optical medium by the action of a resonant plane wave. Assuming that the dephasing processes which alter the phase relationship between dipoles can be neglected, radiation from these dipoles can be calculated using the system raising and lowering operators

$$S_{\pm} = \sum_{i=0}^{N} R_{\pm} e^{\pm i(\mathbf{k}\cdot\mathbf{r_i})}. \tag{4.1.21}$$

In combination with equation 4.1.19 we obtain[66]

$$\langle I(\hat{k},t)\rangle = I_0(\hat{k})\,\langle\Psi|\,S_+S_-\,|\Psi\rangle\,, \tag{4.1.22}$$

$$= I_0(\hat{k})\frac{N}{2}\left(1-\cos\theta(t)+\frac{1}{2}\sin^2\theta(t)\left[\eta(\hat{k},\hat{k}_\mathrm{p})-1/N\right]\right). \tag{4.1.23}$$

Above, the quantity $\eta(\hat{k},\hat{k}_\mathrm{p})$ arises due to the differing phases of the individual dipoles and defines the intensity radiated in a particular direction determined by the outgoing wavevector $\mathbf{k}$. It is defined as an average over the phases of all dipoles at positions $r_i$

$$\eta(\hat{k},\hat{k}_\mathrm{p}) = \left|\sum_{j=1}^{N}\exp\left(i(\mathbf{k}-\mathbf{k}_\mathrm{p})\cdot\mathbf{r}_j\right)\right|^2. \tag{4.1.24}$$

Thus $\eta(\hat{k},\hat{k}_\mathrm{p})$ determines the degree to which dipolar radiation in direction $\hat{k}$ interferes constructively or destructively. If all dipoles are at the origin, this term is equal to one (1) and we obtain the $N^2$ dependence of intensity of the radiation field on atom number (the Dicke limit) through equation 4.1.23. We can then define the total radiation from the system in all directions by integrating equation 4.1.23

$$\int\langle I(\hat{k},t)\rangle\,d\Omega_{\hat{k}} = (\mu\hbar\omega/\tau_0)[\tfrac{1}{2}N+W(t)][\tfrac{1}{2}N-W(t)+1/\gamma]. \tag{4.1.25}$$

Here $\tau_0=\hbar\omega/I_0$ is the single atomic lifetime. We have also substituted the total energy of the system $W=-\frac{N}{2}\cos\theta$ to remove the dependence on $\theta$. The effect of dipole phase on the total radiated intensity is characterised through equation 4.1.24 by a parameter $\gamma$ which takes account of the effect the interference of the individual dipoles in the ensemble.

$$\gamma = \frac{1}{N}+\frac{1}{I_0}\int I_0(\hat{k})\eta(\hat{k},\hat{k}_\mathrm{p})d\Omega_{\hat{k}}, \tag{4.1.26}$$

where $I_0$ defines the total radiative intensity from a single dipole, $I_0 = \int I_0(\hat{k})d\Omega_{\hat{k}}$. In this way, both the decay rate and angular profile of the emission from $N$ dipoles is a function of initial arrangement of their atoms due to interference between emission from each of the dipoles which make up the extended atomic sample [66].

### 4.1.3 Coupled Dipole Model

Superradiance observed in these dilute systems can enhanced through collective mode interferences [68, 273, 274]. To further understand the collective emission of a dense ensemble of Rubidium atoms, it is necessary to examine the explicit form of the radiation field of a dipole driven by an electric field. The steady-state electric field in the vicinity of a driven electric dipole is

$$\mathcal{E}(\mathbf{r}) = \mathcal{E}_p(\mathbf{r}) + \boldsymbol{\mathfrak{G}}(\mathbf{r})\mu_{ge}\rho_{ge}, \tag{4.1.27}$$

where $\mathcal{E}_\mathrm{p}$ is the driving field, $\rho_{ge}$ is the coherence between the two energy levels of the dipole and $\boldsymbol{\mathfrak{G}}(\mathbf{r})$ is the electric field of dipole at position $\mathbf{r}$. The strength of the dipolar field created is proportional to coherence $\rho_{ge}$. In the weak driving limit, the optical Bloch equations stipulate

$$\dot{\rho}_{ge}(t) = (i\Delta_p - \Gamma_e/2)\rho_{ge} + i\Omega_p(\cancel{\rho_{ee}} - \rho_{gg}), \tag{4.1.28}$$

where $\hbar\Omega_p = \mathcal{E}_\mathrm{p} \cdot \mu_{ge}$. In the weak probe regime, $\rho_{ee} \approx 0$. On resonance, with $\Delta_p = 0$, the equation for the evolution of coherence immediately after the coupling $\Omega$ has been turned off is found by calculating equation 4.1.28 through approximating a continuous media. with $\Omega_p = 0$,

$$\rho_{ge}(t) = \int_{t=t_0}^{t} -\frac{\Gamma_e}{2}\rho_{ge}(t')\mathrm{d}t' = \rho_{eg}(t_0)(1 - e^{-\Gamma_e t/2}). \tag{4.1.29}$$

Thus the transient atomic response is determined by the decay rate of the excited state, through the exponential decay with rate $\Gamma_e/2$ (as in equation 4.1.5). Substituting this form of $\rho_{ge}(t)$ into equation 4.1.27 for the total electric field $\mathcal{E}(\mathbf{r})$ gives the intensity of the driven atomic system as

$$|\mathcal{E}(\mathbf{r})|^2 = |\mathcal{E}_\mathrm{p}(\mathbf{r})|^2 \left|1 + \frac{\alpha}{|\mu_{ge}|}\boldsymbol{\mathfrak{G}}(r)\mu_{ge}(1 - e^{-\Gamma_0 t})\right|^2, \tag{4.1.30}$$

where we have used the equation for the atomic polarisability $\mu_{ge}\rho_{ge} = \alpha\mathcal{E}$. The response of a single atomic dipole at position $\mathbf{r}_j$ to a driving field in the interaction picture (RWA) can be rewritten in terms of equation 4.1.28, again making use of the equation for the Rabi frequency $\hbar\Omega_p = \mathcal{E}_{\mathrm{p}} \cdot \mu_{ge}$.

$$\frac{\mathrm{d}}{\mathrm{dt}}\mathbf{d}_j = \mu_{ge}\dot{\rho}_{ge}, \tag{4.1.31}$$

$$= \left(i\Delta - \frac{\Gamma_e}{2}\right)\mathbf{d}_j + i\frac{|\mu_{ge}|^2}{\hbar}\left[\mathcal{E}_{\mathrm{p}}(\mathbf{r_j})\right]. \tag{4.1.32}$$

Above, $\Delta_p = \omega_p - \omega_0$ is the detuning of the probe field $\omega_p$ from the bare atomic resonance frequency $\omega_0$. $\Gamma_e$ is the bare spontaneous decay rate of an individual atom.

When multiple atoms are considered, the above expression for the evolution of a single atomic dipole becomes

$$\frac{\mathrm{d}}{\mathrm{dt}}\mathbf{d}_j = \rho_{eg}\left(\imath\Delta - \frac{\Gamma_e}{2}\right) + i\frac{|\mu_{eg}|^2}{\hbar}\left[\mathcal{E}_{\mathrm{p}}(\mathbf{r}_j) + \sum_{l\neq j}\mathfrak{G}_{jl}\mathbf{d}_l\right], \tag{4.1.33}$$

where the original expression has been modified by inclusion of a sum of contributions to the electric field at the point of dipole $j$ from the radiated fields of the remaining dipoles $l \neq j$. This coupling matrix $\mathfrak{G}$ characterises the couplings between dipoles for a specific ensemble geometry, and its elements $\mathfrak{G}_{ij}$ are defined here as the dipolar field emitted by atom $j$ evaluated at position $i$ [68]

$$\mathfrak{G}_{jl}\mathbf{d}_{jl} \equiv \mathcal{E}_l(\mathbf{r}_j), \tag{4.1.34}$$

in conjunction with the equation for the electric field of a single oscillating dipole (Equation 2.1.30) at position $\mathbf{r}_l$ evaluated at position $\mathbf{r}_j$ .

In the steady state, where $\frac{d}{dt}\mathbf{d}_j = 0$, this equation can be rearranged to give

$$\left(\frac{1}{\alpha}\mathfrak{I}^N - \sum_{l\neq j}\mathfrak{G}_{l,j}\right)\overrightarrow{\mathbf{d}} \equiv \mathfrak{M}\overrightarrow{\mathbf{d}} = \overrightarrow{\mathcal{E}}_{\mathrm{p}}. \tag{4.1.35}$$

Here, the matrix $\mathfrak{M}$ acts upon the column vector of dipoles $\overrightarrow{\mathbf{d}}$, and $\mathfrak{I}^N$ is the $N$ dimensional identity matrix corresponding to the number of dipoles $N$.

For a dilute gas, typical $R = |\mathbf{r}_i - \mathbf{r}_j|$ are large, and thus dipole-dipole interactions are small, and the matrix $\mathfrak{M}$ is contains contributions largely

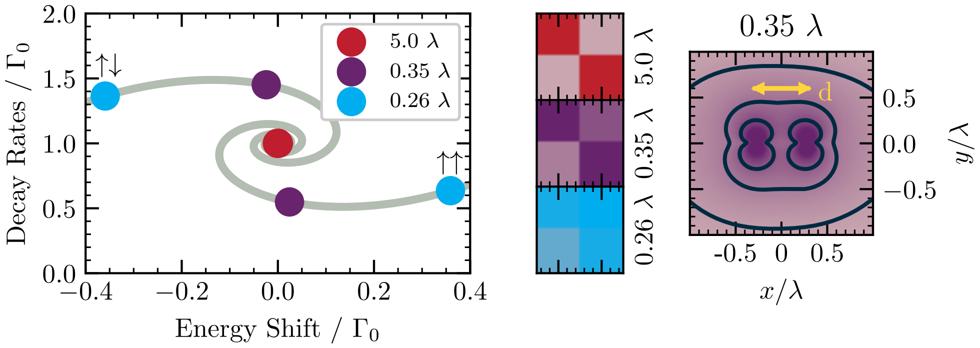

Figure 4.4: **Left:** The energy eigenmodes of two dipoles evolve as they are brought into close proximity. Energy shifts and decay rates of two dipoles at $R = [5, 0.35, 0.26]\lambda$ are shown. The continuous evolution of eigenmodes between these values is shown as a grey spiral. **Middle:** The coupling matrix $\mathfrak{M}$ is shown for the separations highlighted left demonstrating the transition from a diagonal matrix at $R = 5\lambda$ to strong coupling at $R = 0.26\lambda$, resulting in a significant eigenvalue shift. The magnitude $|\mathfrak{M}_{ij}|$ is shown. **Right:** plot of the intensity of the electric field for the intermediate ($d = 0.35\lambda$) case. Arbitrary contours are provided to highlight the form of the electric field.

from the $\frac{1}{\alpha}$ term which defines the bare polarisability. In this case, $\mathfrak{M}$ is almost diagonal and thus degenerate in the original basis of bare atomic dipoles $\overrightarrow{\mathbf{d}}$. However, for a dense sample, where the average inter-atomic spacing $|kR| < 1$, off-diagonal couplings appear due to the dipole-dipole interactions specified in equation 4.1.33 through $\mathfrak{G}$. In this case, the matrix is no longer diagonal in the original basis of $\overrightarrow{\mathbf{d}}$. Diagonalisation yields a new basis $\overrightarrow{\mathbf{d}'}$. The eigenvectors of $\overrightarrow{\mathbf{d}'}$ describe the linear combinations of dipoles contributing to the coupled geometric eigenmodes of the system. The eigenvalues of these new eigenmodes have real and imaginary parts corresponding to modified resonant frequencies and decay rates, respectively.

Figure 4.4 shows this effect on the collective modes of a system consisting of two such coupled dipoles. Three different coupling regimes are shown. At large separations $d \gg \lambda$, the dipoles have little effect upon each other. The two possible geometric modes of the system correspond to one

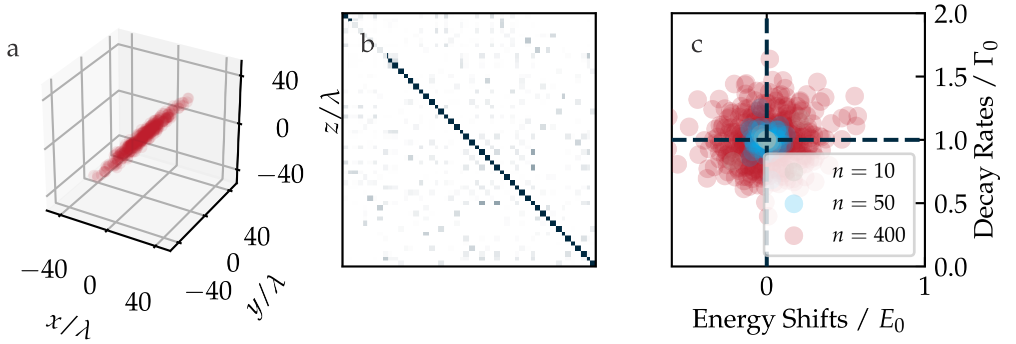

Figure 4.5: **a** Simulated ensemble, representative of our experimental geometry shown for the case $n = 400$. **b** The $50 \times 50$ coupling matrix $|\mathfrak{M}|$ for $n = 50$. The $|\mathfrak{M}|_{ij}$ show dipolar couplings between individual atoms (Equation 2.1.30). **c** Energy eigenmodes of $n$ dipoles in a Gaussian ensemble of size $\sigma_x, \sigma_y = 2\lambda$, $\sigma_z = 25\lambda$ for $n = 10, 50, 400$. Dipole-dipole coupling shifts eigenenergies and decay rates. **d** Logarithmic colour map of $|\mathfrak{M}|$ revealing many-body couplings. **e, f** Logarithmic $|\mathfrak{M}|$, with a shared color map. **e** shows $|\mathfrak{M}|$ through Equation 2.1.30. **f** shows $|\mathfrak{M}|$ with the term $\propto 1/R$ in Equation 2.1.30 omitted. Strong many body interactions due to the long range couplings $\propto 1/R$ are absent. Weaker weaker interactions $\propto R^{-2}$ or $R^{-3}$ are not sufficient for density dependent superradiance in our system.

or other of the dipoles being driven. The energies $E(r) \approx E(r = \infty) = E_e$ and decay rates $\Gamma(r) \approx \Gamma(r = \infty) = \Gamma_e$ are not significantly modified. When the dipoles are in close proximity $d \approx \lambda$, off-diagonal elements in the coupling matrix $\mathfrak{M}$ appear. In this case, the natural mode of the system is a linear superposition of the two initial dipoles, with one mode oscillating in-phase and one oscillating out of phase. Modifications to the decay rate and energies become more pronounced as the atoms are brought together. At $d = 0.25\lambda$, the fastest mode decays at $\Gamma = 1.35\Gamma_0$ and has energy $E = 1.35E_0$.

This simple picture can be easily extended to a random ensemble of atoms. Figure 4.5 shows the effect of a ensemble of 10, 100 and 400 atoms whose positions are drawn from a 3D Gaussian distribution with $\sigma_x = \sigma_y = 2\lambda$ and $\sigma_z = 25\lambda$ upon the decay rates and energy shifts of the individual geometric modes. Higher atom numbers cause stronger and more numerous dipole-dipole couplings, increasing the strength of the geometric effect.

The shifting eigenmodes and eigenenergies of these collective modes also affect the temporal envelope of emission from the system of coupled dipoles. In the coupled basis, each eigenmode has a distinct shifted frequency and decay rate. An immediate consequence is that when the excited system emits, superradiant eigenmodes decay quickly with sub radiant modes taking longer to decay. Moreover, the shifted frequencies of the individual modes cause interference upon emission. This interference causes a time-dependent overall decay rate $\Gamma(t)$, which can be defined as $\Gamma(t) = -\partial \log(P_{\text{tot}}/P_0)/\partial t$. Thus $\Gamma(t)$ is a measure of the instantaneous change in emission. Due to interference upon emission from shifted modes, $\Gamma(t)$ can be faster than the decay rate of the fastest of any of the individual eigenmodes. Once the drive field is switched off, the macroscopic dipole $\mathcal{D}$ decays as

$$\mathcal{D}(t) = \sum_{i=1}^{N} \mathbf{d}'_i \exp(-\Gamma'_i t - i\Delta'_i t). \tag{4.1.36}$$

For the case of non-interacting dipoles, where $|kR| \gg 1$, the decay rates and detunings are all equal to the bare atomic case $\Gamma'_i = \Gamma_e$, $\Delta'_j = 0$. As the density is increased, the decay rates and detunings vary as shown in Figure 4.5, giving rise to such variable decay rates.

### 4.1.4 Observation of Two-Level Transient

The experimental apparatus detailed in chapter 3 is an ideal platform to investigate coherent emission from ensembles of atomic Rubidium. Ultracold atoms held in optical dipole traps provide a means by which to freeze thermal motion and isolate optical phenomena such as superradiance [275]. The high data acquisition rate supports the study of superradiance at the single photon level, avoiding interactions that can destroy the effect [37]. Preparation of a sample of Rubidium 87 at 50 μK supports the resolution of atomic dynamics. Figure 4.6 shows an overview of the pulse sequence and trap geometry used to witness the collective superradiance of an ensemble of Rubidium 87.

An atomic ensemble is loaded into a dipole trap with waist $w_d$ =5 µm. Probe light is focused to $w_p = 1.1\,\mu\text{m}$ at the center of the atomic ensemble, having length $\sigma_z = 40\,\mu\text{m}$ in the direction of propagation and width $\sigma_x = \sigma_y = 3\,\mu\text{m}$ in the axial direction. Atoms are optically pumped into the $|5S_{1/2}F = 2,\ m_f = 2\rangle$ stretched state with $\sigma^+$ coupling light. The trap amplitude is modulated with a square wave control signal at 2.2 MHz to avoid excessive AC Stark shifts during each experimental run as shown in Figure 4.6 (c). The duty cycle is adjusted such that the trap confines the atoms for 3 µs and releases them for 1 µs of this cycle.

During the time when the trapping light is switched off a weak coherent probe pulse with circular polarisation couples states

$$|g\rangle = |5S_{1/2}F = 2,\ m_f = 2\rangle \leftrightarrow |e\rangle = |5S_{1/2}F = 3,\ m_f = 3\rangle\,, \quad (4.1.37)$$

with detuning $\Delta_p = 0$ and Rabi frequency $\Omega_p$. The probe pulse has duration $t_p = 0.35\,\mu\text{s}$ and mean photon number 1.5. This the probe beam

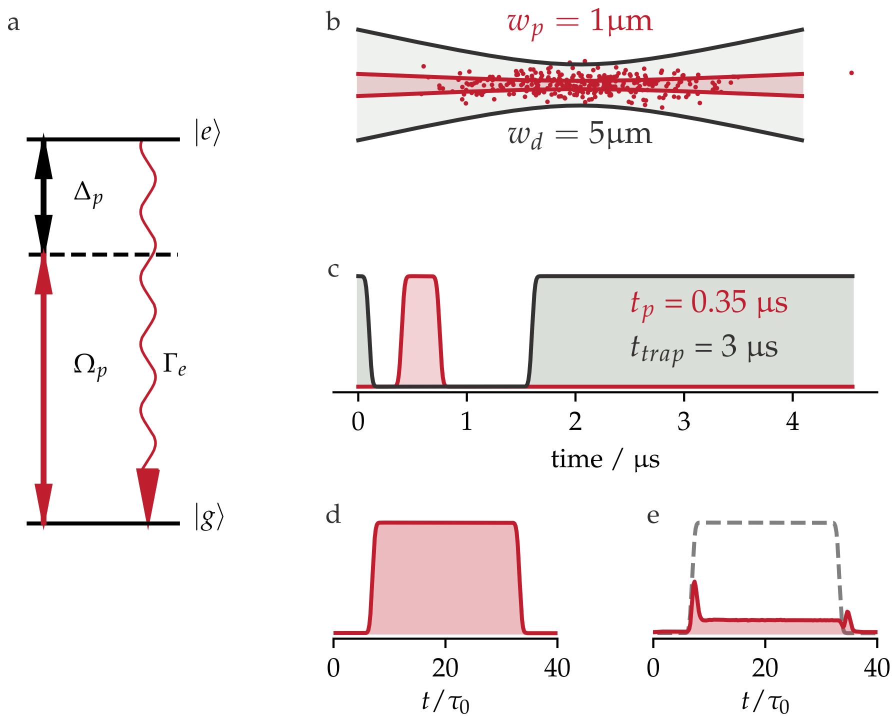

Figure 4.6: Experimental schematic for coherent FID observation. **a** The atomic ensemble is simplified to a system of two-level emitters coupled with a resonant probe beam ($\Delta = 0$) having Rabi frequency $\Omega_p$. **b** Geometry of probe (red) and dipole (black) trapping beams. The probe beam is focused into an ensemble of Rubidium atoms forming a waist of $w_p = 1.1\,\mu m$ at the center of the ensemble. The transition is the D2 line of Rubidium with decay rate $\Gamma_e = 6.065(9)$ MHz [276]. **c** Timing sequence of probe and trapping beams. The dipole trap is turned off at $t = 0.1\,\mu s$, followed by a probe pulse lasting $0.35\,\mu s$. **d, e** Histogram of photon arrivals at the HBT detection circuit, coupled to the incoming probe beam. Histograms shown in absence (**d**) and presence (**e**) of the atomic ensemble. The process of absorption causes two characteristic transient features upon the rising and falling edge of the probe pulse. $\tau_0$ is the lifetime of the $|e\rangle \leftrightarrow |g\rangle$ transition.

is coupled to the HBT detection circuit (see chapter 3) in absence of the ensemble. During the experimental sequence, the HBT detection circuit records transmission of the probe as well as emission from the ensemble. A typical histogram of photon counts extracted from the HBT detection circuit for both probe and reference pulses is shown in Figure 4.6 d & e, where the initial and final experimental transients of equations 4.1.6, 4.1.7 are observable.

Due to the density-dependent nature of this effect, the optical depth of the ensemble is monitored during experiments to ensure the validity of experimental data. Heating by the probe causes a steady loss of atoms from the trap. When the optical depth begins to decrease, the optical dipole trap is refreshed by reloading atoms from a MOT. For these experiments, the pulse sequence shown in Figure 4.6, c is implemented between 4000 and 10000 times before optical depth is degraded.

### 4.1.5 Density Dependence

To study the effects of variable atomic density without changing other experimental parameters we chose to control the number of atoms of the ensemble that interact with the probe beam by selectively pumping atoms into resonance. At the beginning of the experiment, the atoms are in the ground state $|5S_{1/2}F = 1\rangle$. To keep the ensemble parameters constant whilst varying the optical depth, we control the number of atoms addressed by the probe beam by selectively pumping atoms into the cycling transition addressed by the probe. From here, a re-pumping pulse of variable duration of between 10 and 100 μs addresses the transition $|5S_{1/2}F = 1\rangle \leftrightarrow |5P_{3/2}F' = 2\rangle$ with circular polarised light. This pulse effects optical pumping. Atoms are promoted out of the dark $|5S_{1/2}F = 1\rangle$ state, into $|5S_{1/2}F' = 2,\ m_f = 2\rangle$ where they becomeresonant with the probe beam. Thus varying the duration of this pumping process allows us to chose the number of atoms that can interact with the probe pulse

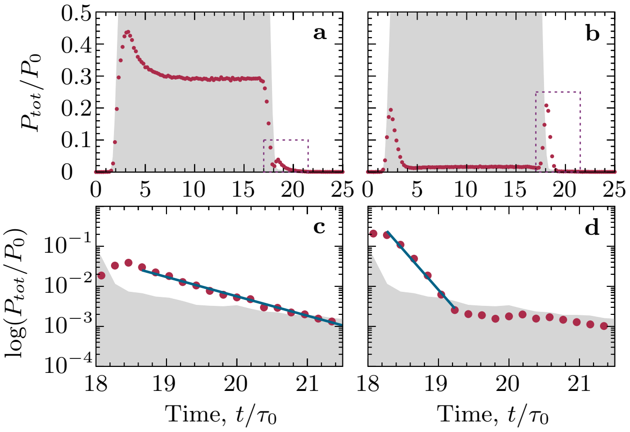

Figure 4.7: Experimental measurement of the density dependence of the response of an atomic medium to a resonant probe beam. Left panels correspond to low optical depth, $OD = 1$. Right panels correspond to high optical depth, $OD = 4$. The signal in the absence of atoms is indicated by the grey shaded region in all panels. **a, b** Total power collected by a single mode fiber during the interaction between probe and ensemble, showing initial and final two-level transients. **c, d** The decay rate of the final transient $\Gamma$ (blue line) is a strong function of optical depth. At $OD = 1$, the decay rate of the transient is $\approx \Gamma_0$ (**c**). At $OD = 4.9$, the decay rate increases to $\Gamma \approx 4\Gamma_0$ (**d**). Figure reproduced from [68], which includes an extended analysis of this density-dependent phenomenon.

and therefore select an optical depth.

Progressive absorption of photons during subsequent experiments pumps atoms into the $|5S_{1/2}F = 2m_F = 2\rangle$ state during the first few thousand experiments, which ends when atoms are predominately cycling the

$$|5S_{1/2}F = 2,\ m_F = 2\rangle \leftrightarrow |5P_{3/2}F' = 3,\ m_{F'} = 3\rangle \tag{4.1.38}$$

transition. During this pumping, the optical depth of the ensemble is seen to vary and so experimental analysis is performed on data taken after optical depth fluctuations have stabilised. Data corresponding to the first few thousand shots are discarded.

Figure 4.7 shows the result of two such experiments where a density-dependent geometric eigenmode decay is observed. Figure 4.7 (a), shows the response of the ensemble at low optical depth. The HBT reference signal is shown in grey, which corresponds to photon events due to the probe beam in absence of absorption by an atomic ensemble, coupled directly into the HBT detection circuit. Red data points show the observed response of the medium to the probe, with characteristic initial and final transient following the two edges of the reference signal.

The optical depth is characterised by the steady-state absorption of the probe beam. Figure 4.7 (a) shows the full transient optical response of the medium at low optical depth, $OD = 1$ to the resonant probe beam. The low-OD response is typified by low steady state absorption and small final transient. The $\rho_{eg}$ coherence for relatively low effective atomic density is not sufficient to cancel the drive field. Figure 4.7 (c) highlights the portion of this signal corresponding to the low OD final transient. The transient decay rate $\Gamma_f$ is calculated to match the atomic decay rate $\Gamma_f \approx \Gamma_e$. Relatively low coupling between atoms leads to a small collective enhancement of the decay rate as set out in section 4.1.5. The atomic response is not dramatically modified from the response of atoms in the absence of geometric couplings at low OD.

Figure 4.7 b & d show the atomic response at high optical depth $OD = 4.9$. In contrast to the case of low optical depth, the steady-state absorption is high, as higher atom numbers interacting with the probe pulse increase the susceptibility of the medium. The initial and final transient are well resolved and large in magnitude, being proportional to the larger $\rho_{eg}$ coherence generated at high OD due to the larger number of atoms interacting with the probe. The decay of the final transient is detailed in Figure 4.7, d and should be viewed in comparison with figure 4.7, c. The high OD transient is observed to have a much faster decay rate $\Gamma \approx 4\Gamma_0$ due to the interference of the emission from shifted geometric eigenmodes.

## 4.2 EIT Transients

In the previous section, the consideration of the geometric modes of a two-level medium leads to a modified optical response. By moving to a medium with three coupled transitions ($|g\rangle \Leftrightarrow |e\rangle \Leftrightarrow |r\rangle$), it is possible to witness a richer variety of phenomena such as electromagnetically induced transparency [40, 277], photon storage [49] and the Kerr effect [278]. Amplification of the cooperative nature of the optical response of a medium can be achieved in a three-level system by choosing the state $|r\rangle$ from amongst the Rydberg states, conferring larger dipole moments and thus achieving strong many-body interactions. Recent interest in strongly interacting Rydberg transients was sparked by proposals to use Rydberg ensembles as nodes of quantum communication networks [279] where Rydberg media might usefully interface remote quantum hardware whilst simultaneously performing gate operations [35]. Understanding of the nature of photon emission from Rydberg dressed systems is essential to achieving robust light-matter interfaces in Rydberg based network nodes [27, 280–282], which leverage existing all-optical gates [26, 134, 283]. In support of these aims, studies of three-level Rydberg transients have thus recently come to the fore [85, 284]. Three-level transients can also give insight into the internal dynamics of Rydberg systems [83, 86].

This section presents observations of the optical response of a driven three-level ensemble to resonant probe photons under a variable Rydberg dressing. The effect of Rydberg dressing on the temporal and statistical nature of light transmitted by an atomic ensemble is reported. The temporal envelope is modelled with Master equations in the superatom picture [27, 31–33, 126]. Statistical analysis of transmitted photons reveals Rydberg mediated photon anti-bunching [45, 116]. In this section 4.2, we show that by weakly dressing our atomic ensemble, we can effectively modify the temporal profile and statistical nature of light emitted from a pumped ensemble via spontaneous decay through imposition of Rydberg blockade.

By inclusion of a fourth Rydberg state $|3\rangle$, we show control over the statistical nature of light transmitted by the ensemble due to the associated increased strength of resonant-dipole interactions. In section 4.3, the blockade mechanism is enhanced through application of a resonant microwave field, introducing resonant dipolar interactions [29, 48].

Equation 4.1.1 defining the electric field of an atom interacting with an electric field can also be used to describe the response of driven three-level superatoms [27]. The master equation used to calculate $\rho_{eg}$ is solved the three-level context as set out chapter 2. Figure 4.8 shows a numerical simulation of the dynamic three-level system highlighting key features of experimentally observable dynamics. Parameters used in the model are shown in the figure caption and are representative of experimental conditions under the action of the pulse sequence set out in figure 4.11. Were $\Omega_c = 0$, this figure would match precisely the dynamics of a two-level system observed in the previous section. This section extends the analysis of two-level systems to describe dynamically driven three-level polaritons under $\Xi$-EIT (ladder) conditions where the coupling constants $\Omega_{p,c}(t)$ are time-dependent quantities.

Figure 4.8 **a, c** presents the temporal profile of the coherences $\rho_{eg}$ that arise in response to the driving with $\Omega_p, \Omega_c$. Figure 4.8 **b** shows the theoretical observable profile of the forward scattered light. Operating in the weak probe regime, the system interacts with a probe pulse lasting a few hundred nanoseconds. The initial small transient at $t = 0$ in Figure 4.8 **b** is precisely the initial transient studied in the previous section, which is followed by a short period of high optical depth, corresponding to two-level absorption. At $t = 5\tau_0$, $\Omega_c$ is rapidly increased from $\Omega_c \approx 0$ to a steady-state value of $\Omega_c \in 2\pi \cdot [0, 30]$ MHz with an 80/20 rise time of 120 ns. The resultant $|e\rangle \leftrightarrow |r\rangle$ coherences create an EIT transmission window, and thus the optical thickness of the medium is reduced. At $t = 22\tau_0$ the probe beam is rapidly extinguished such that coupling $\Omega_p = 0$, quenching the sys-

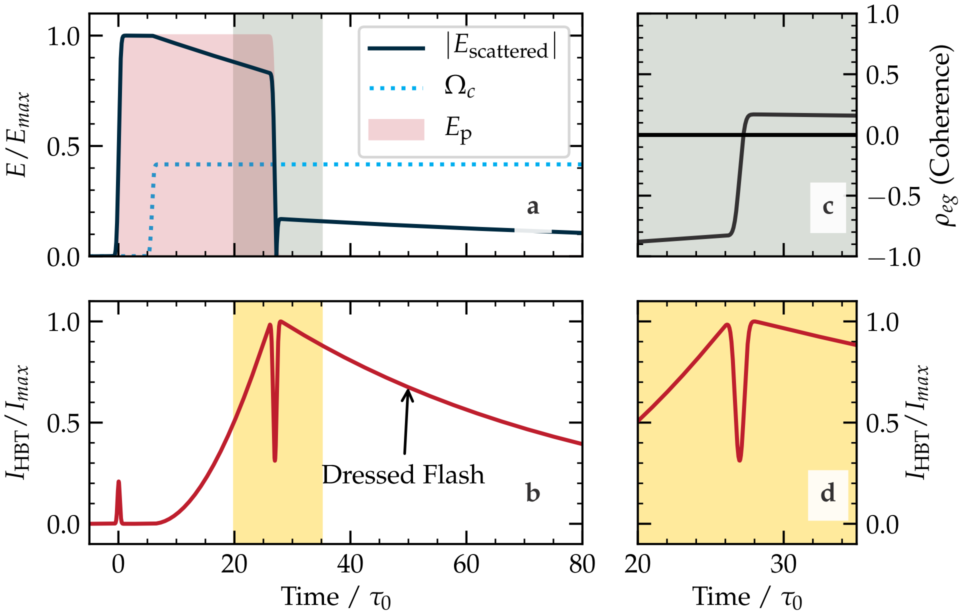

Figure 4.8: Solution of equation 4.1.1 through numerical integration of three level optical Bloch equations for the optical pulse sequence shown in 4.11, where $\Omega_c = 2\pi \cdot 2.52$ MHz, $\Omega_p = 2\pi\cdot$ 0.1 MHz and $\Gamma_e = 2\pi \cdot 6.06$ MHz. $\Omega_c$ is applied at $t = 5\tau_0$, where $\tau_0$ corresponds to the lifetime of the D2 line of Rubidium 87. Figures **a**, **b** (c.f. Figure 4.1) shows the form of the dipolar field $\mathcal{E}_{\mathrm{HBT}}$, in response to incident $\mathcal{E}_{\mathrm{p}}$ and the summed intensity that is detected by the HBT detection circuit $I_{\mathrm{HBT}}$. The extended decay observed when the atomic ensemble is weakly driven by $\Omega_c$ is identified in **b** as the *dressed flash.* **c** details the atomic coherence $\rho_{eg}$ upon the extinction of the probe propagating through a dressed media. The zero crossing gives rise to a dip in the HBT signal, followed by a revival and the slow decay associated with the dressed flash, shown in **d**. The $\rho_{eg}$ zero crossing can give rise to a $\mathcal{E}_{\mathcal{HBT}}$ transient with two intensity peaks (see Figure 4.9).

tem. Thereafter, the system exhibits a dynamic optical response. Rydberg excitations pumped into the medium decay via $|e\rangle$ due to a combination of spontaneous emission from $|r\rangle$ and resonant driving from $|r\rangle$ to $|e\rangle$ by $\Omega_c$ followed by spontaneous decay from $|e\rangle$. These processes can be significantly slower and can produce a much higher intensity transient than in the associated two-level system. In this thesis, the intense transient associated with de-pumping of Rydberg excitations is termed the *dressed flash.*

At the point that the probe beam is switched off, the EIT condition is satisfied. Under ideal steady state resonant EIT conditions, the population of $|e\rangle$ is zero, and the atomic system exists in a superposition $|\pm\rangle \propto |g\rangle \pm |r\rangle$. Thus initially $\rho_{er} > 0$ and $\rho_{eg} \approx 0$. For Rydberg systems, decay from the excited state is much faster than decay from the Rydberg state. It is also much faster than experimental timescales of 1 µs implemented in this thesis, and so we make the approximation that $0 \approx \Gamma_r \ll \Gamma_e$. After the probe beam is extinguished, we have the condition $\Omega_p = 0$. Resonant probe and coupling beams also allow us to set $\Delta_p, \Delta_c, \Delta_2 = 0$. The optical Bloch equations for $\rho_{eg}, \rho_{er}$ of the three level system as derived in chapter 2

$$\dot{\rho}_{eg} = \frac{i\Omega_p}{2}(\rho_{ee} - \rho_{gg}) - \frac{i\Omega_c}{2}\rho_{rg} + \left(i\Delta_p - \frac{\Gamma_e}{2}\rho_{eg}\right), \tag{4.2.39}$$

$$\dot{\rho}_{rg} = \frac{i\Omega_p}{2}\rho_{re} - \frac{i\Omega_c}{2}\rho_{eg} + \left(i(\Delta_p + \Delta_c) - \frac{\Gamma_r}{2}\right)\rho_{re}, \tag{4.2.40}$$

can thus be simplified to the following coupled ODEs.

$$\begin{bmatrix} \dot{\rho}_{eg} \\ \dot{\rho}_{rg} \end{bmatrix} = \frac{1}{2}\begin{bmatrix} \Gamma_e & -i\Omega_c \\ -i\Omega_c & 0 \end{bmatrix}\begin{bmatrix} \rho_{eg} \\ \rho_{rg} \end{bmatrix}. \tag{4.2.41}$$

Solving for the time dependence of the eigenstates of the density matrix we obtain the following equation for the decay rate of coherence $\rho_{eg}$.

$$\Gamma_{\text{dressed},\pm} = \frac{1}{4}\Gamma_e\left[1 \pm \sqrt{1 - C^2}\right]. \tag{4.2.42}$$

Here, $C = 2\Omega_c/\Gamma_e$. When $\Omega_c = 0$, we have that $\Gamma_{\text{dressed}} = \Gamma_e/2$, reproducing the two level dynamics. This simple picture gives rise to three dynamical regimes for the decay rate of the dressed flash determined by $C$.

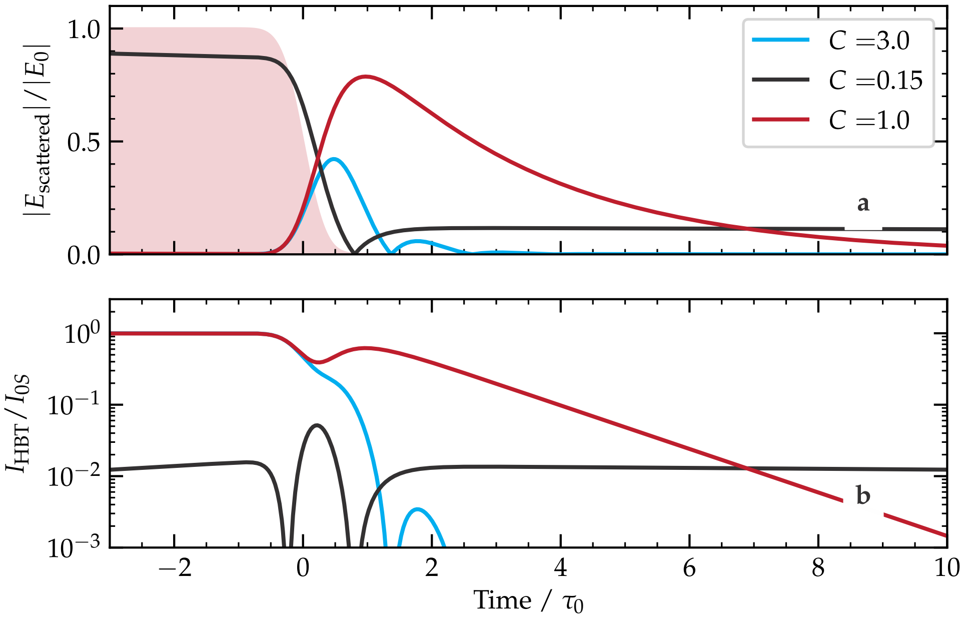

Figure 4.9: Flash dynamics are dictated by the balance of $C = 2\Omega_c/\Gamma_p$, shown above for three distinct regimes. For $C \ll 1$, $\rho_{gr}$ (black line) coherences remain small. Upon extinction of the probe, the two-level flash is visible as a sharp intensity maximum, followed by a three-level flash of low intensity and slow decay. Two and three-level flashes are separated by intensity minima due to the change in the sign of the atomic coherence term that gives rise to each flash. For $C \approx 1$, significant $\rho_{gr}$ coherence builds in the medium. $\Omega_c$ drives population from $|r\rangle$ to $|e\rangle$ where it can decay. This creates a flash that extends well beyond the initial two-level flash. For $C \gg 1$, fast de-pumping of $|r\rangle$ causes fast flash decay and can cause dressed flash oscillation. For $C \gg 0$, the initial flash is usually not observed experimentally due to the finite probe switching speed as reproduced in the above simulation.

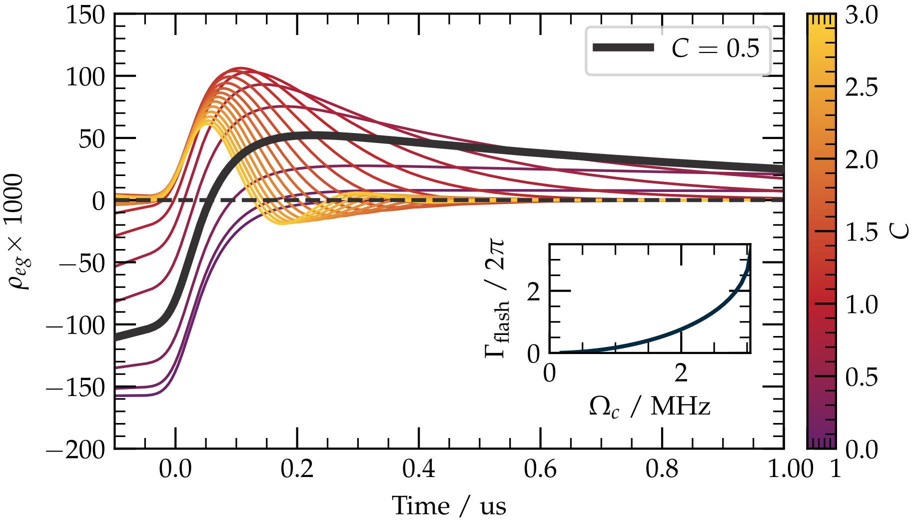

Figure 4.10: Numerical optical Bloch simulations of dressed flash coherences $\rho_{eg}$ are shown for $C \in [0, 3]$. Other parameters match Figure 4.9. For weak $\Omega_c$, the coherences closely match Figure 4.1. For intermediate $\Omega_c$, a dipolar field builds as in the previous section. Upon probe extinction, the initial negative coherence revives as a positive coherence due to de-pumping of $|r\rangle$, highlighted in black. Experimentally, this leads to a double flash. For higher $\Omega_c$, the EIT condition is better satisfied, and so little $|e\rangle, |g\rangle$ coherence is observed. In this regime, only the flash originating from Rydberg de-pumping is observed. $\Omega_c$ can dramatically extend the two-level flash, causing observable coherence well beyond that of the two-level case. **inset** The decay rates of the coherence for an atom with $\Gamma_e = 6.06$ MHz extracted from fits to optical Bloch simulations. The decay of the coherence rises to a maximum value of $\Gamma/2$ through equation 4.2.42.

- For $C \gg 1$, the Rabi frequency is the dominant factor determining the dynamics of the dressed flash, being greater in magnitude than the decay rate of the two-level flash $\frac{1}{2}\Gamma_e$. Thus weakly damped Rabi oscillations of the flash are observed. The flash lifetime is limited by the rate at which the excited state decays via spontaneous emission.

- For $C \approx 1$, this dominance is lost. Critical damping causes the loss of oscillation in the flash signal, but the flash still decays with a rate close to that of the excited state through equation 4.2.42 .

- For $C \ll 1$, $\Omega_c$, the atomic response is similar to that of the atom in the absence of dressing. The decay rate is close to that of the bare atom, with minimal contribution to the decay rate from the Rydberg dressing.

Atomic coherence and resultant dressed flashes are shown in Figure 4.9 for the three dynamical regimes, where the probe beam is extinguished at $t = 0$. Figure 4.9 **c,d** show the time evolution of $\rho_{eg}$ as well as the predicted HBT signal. In **c**, these coherences are observed to change sign at the point where the probe is extinguished. An initial negative atomic coherence counteracts the drive field during steady state EIT and causes steady state optical depth $OD > 0$ during EIT. Observation of this negative atomic coherence in the form of a two-level flash requires the experimental physicist to extinguish the coupling $\Omega_c$ enough to observe this small, fast decaying field. After extinguishing $\Omega_c$, $\rho_{eg}$, which is initially negative, again becomes positive giving rise to the dressed flash. In the two level case, the transient flash arises purely as a result of the decay of the interference field which initially cancels the probe beam due to negative $\rho_{eg}$. In the three-level case the dressed flash has its origins in positive $\rho_{eg}$ emission of photons in phase with the drive field. This positive $\rho_{eg}$ arises due to the optical pumping of excitations into state $|r\rangle$ which can decay to ground over a much longer timescale than the lifetime of the excited state due to the bottleneck at low $\Omega_c$ in state transfer from $|r\rangle$ to the radiative state $|e\rangle$.

Master equations of the atomic coherence $\rho_{eg}$ are shown in detail on figure 4.10. Parameters used for simulation are the same as figure 4.9 excepting variable $\Omega_c$ parameterised through $C$. The case $C = 0.5$ is highlighted, for which significant $\rho_{er}$ and $\rho_{eg}$ coherences build. In this regime, it is possible to obtain strong dressed flash in tandem with strong initial two-level emission. The magnitude and interplay of positive and negative $\rho_{eg}$ coherences provides for a more complete picture of the dynamics of the driven system in the three regimes for $C$

- $C \ll 1$: The sign change in transient $\rho_{eg}$ leads to two discrete flashes. The two-level flash is dominant after which a very slow flash decay due to slow de-pumping of $|r\rangle$ by weak $\Omega_c$, or $\Gamma_r$ in the limiting case. The magnitude of the dressed flash is small due to minimal EIT coherence during the probe window.

- $C \approx 1$: The Rydberg flash appears large due to significant $\rho_{eg}$ coherence during EIT. De-pumping of $|r\rangle$ by intermediate $\Omega_c$ leads to a large, extended dressed flash.

- $C \gg 1$: The magnitude of the initial flash is large, but decay is rapid due to fast de-pumping of $|r\rangle$ by strong $\Omega_c$. Emission from the ensemble can oscillate after the probe beam is extinguished through equation 4.2.42. De-pumping limited by $\Gamma_e$.

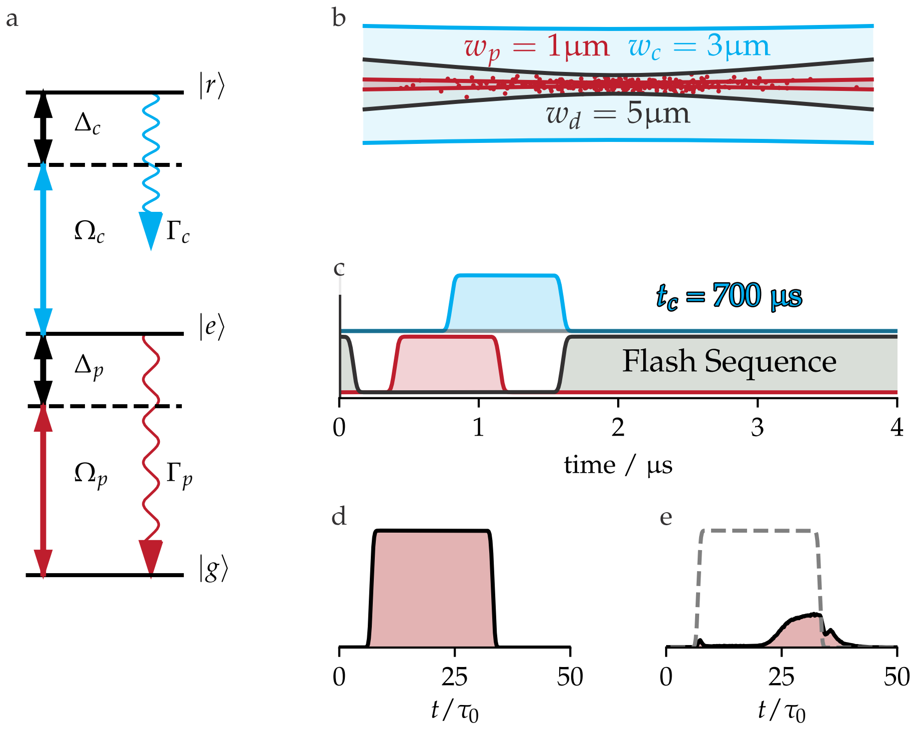

Figure 4.11: Dressed Flash Experiment Outline. **a** Probe and coupling beams $\Omega_{p,c}$ couple states $|g\rangle \leftrightarrow |e\rangle$ and $|g\rangle \leftrightarrow |r\rangle$ with single photon detunings $\Delta_{p,c}$. Spontaneous emission from $|e\rangle \rightarrow |g\rangle$ sets the timescale for the dynamic system, dominating $\Gamma_r \ll \Gamma_e$ for Rydberg systems. **b** The geometry of probe (red), trapping (black) and coupling (blue) beams. Probe and coupling beams counter-propagate. Waists are overlapped in the center of the atomic ensemble. **c** Pulse timing. The sequence is similar to that of the two-level flash. The probe pulse is bisected by the rising edge of the coupling beam creating $\rho_{eg}$ coherence. The coupling beam remains after probe extinction giving rise to the dressed flash. **d** Histogram of photon counts in the absence of an atomic ensemble revealing the shape of the probe pulse. **e** Histogram of photon counts in the presence of an ensemble showing the appearance of the dressed flash after the probe is extinguished. Steady state two-level absorption and three-level EIT are observable at $t = 15, 33\ \tau_0$, respectively. $\tau_0$ is the lifetime of the $|g\rangle \leftrightarrow |e\rangle$ transition in Rubidium 87 $\Gamma_e = 6.06$ MHz [276].

### 4.2.1 Observation of EIT Transients

Figure 4.11 **b** shows the experimental geometry used to study three-level Rydberg transients. A few thousand atoms are loaded into a dipole trap with dimensions $3\,\mu\text{m}\times 40\,\mu\text{m}$ as with the two level flash observation of figure 4.6. Figure 4.11 **c** shows the temporal profile of the probe, coupling and trapping beams. The probe beam is focused to $w_0 = 1.1\,\mu\text{m}$ into the center of the atomic ensemble. The coupling pulse is focused to $w_0 = 30\,\mu\text{m}$. This waist is large such that variation in $\Omega_c$ across the ensemble is minimised.

Trapping amplitude is modulated with a square wave amplitude profile at 2.2 MHz as with previous two-level flash experiments. Atoms experience the confining force of the dipole trap for a duration of $3\,\mu\text{s}$. The duty cycle is adjusted such that the atoms are released from the trap for $1\,\mu\text{s}$. During release, the pulse sequence shown in Figure 4.11 **c** is implemented. This experimental sequence is identical to that of the two-level flash with an additional of Rabi frequency $\Omega_c$ coupling to a Rydberg state $|r\rangle$ provided by the coupling beam. Probe photons are resonant with the

$$|g\rangle = |5S_{1/2}F = 2,\ m_f = 2\rangle \leftrightarrow |5P_{3/2}F' = 3,\ m_{f'} = 3\rangle = |e\rangle \qquad (4.2.43)$$

transition, $\Delta_p = 0$. Probe and coupling beams have opposing circular polarisation such that they both drive the $\sigma^+$ transition. A quantisation field is again applied along the propagation axis. A probe pulse lasting $0.75\,\mu\text{s}$ couples states $|g\rangle, |e\rangle$. Whilst the probe pulse is interacting with the medium, the ensemble is dynamically coupled to a Rydberg state $|r\rangle = |nS_{1/2}\rangle$ with a coupling pulse lasting $0.7\,\mu\text{s}$ and with a rising edge that bisects the probe pulse as shown in Figure 4.11, **c**. The Rabi frequency of $\Omega_c$ is variable, and we can typically obtain $\Omega_c \lesssim 30$ MHz for $n = 60$.

The transmission of the ensemble is measured using the HBT detection circuit as a series of time-tagged photon events as outlined in section 3. This allows us to obtain the temporal profile of transmitted light whilst giving simultaneous access to the underlying statistical nature of the incident photons as outlined in chapter 3. Figure 4.11 **e** shows typical histograms of the summed photon counts from both detectors of the HBT detection circuit of the ensemble during the pulse sequence shown in Figure 4.11. Photons are counted in 5 ns time bins from the start of each experimental sequence. Figure 4.12 gives a comparison between the experimentally observed $\mathcal{E}_{\mathrm{HBT}}$ for a driven three-level system and simulations of the optical response of the same system via numerical integration of equation 4.1.1. The rising edge of the probe occurs at $t = 8\tau_0$. The medium at this time is precisely that of the two-level system, and so the optical response is the same. At $t \approx$0.8 µs, an initial transient followed by high optical depth OD$\approx$ 4 as in the case of the two-level system is observed. At this time $\Omega_c = 0$. The optical dipole trap is reloaded with a fresh ensemble of atoms after every five thousand runs. Photon arrival histograms are averaged over one million experimental runs.

At $t \approx 20\tau_0$, the coupling frequency $\Omega_c(t)$ is increased to a maximum value $\Omega_c^{\max}(t)$, and an EIT transmission window opens. Steady-state EIT transmission occurs around $t \approx$30$\tau_0$. The probe beam is then switched off and slow decay of photon counts is observed, with a lifetime that is much longer than that observed in the two-level system. This transition can be seen on the raw data presented in Figure 4.12 b, the fast two-level flash at $\Omega_c = 0$ gives way to the dressed flash at $\Omega_c \approx 2\pi \cdot 5$ MHz.

The effect of varying the amplitude of $\Omega_c(t)$ between extreme values $\Omega_c \in$ [0,30] MHz upon the temporal evolution of the dressed flash is detailed in Figure 4.12 where panels **a, b** show the HBT signal histograms and panels **c, d** show a master equation simulation of the same. $\Omega_c$ is obtained from fits to EIT transmission spectra using the EIT susceptibility derived in chapter 2. For small values of $\Omega_c(t)$, we observe the optical response of a dense two-level system as described in section 4.1.4, with two characteristic emission peaks are corresponding to the rising and falling edges of the probe beam (purple data, Figure 4.12, a). As $\Omega_c$ increases, the optical response of the medium shifts towards the dressed flash picture following the progression set out in Equation 4.2.42. The presence of the coupling beam and probe beam in the medium gives rise to an EIT transparency window during the overlap of the probe and coupling beam. The time constant associated with the rising edge of this window is determined by the $\Omega_c$ coupling frequency (or, in the case of strong coupling, the form of the rising edge of $\Omega_c$) and represents the time required for the coherences that underpin EIT to build between the ground and Rydberg states $|g\rangle \leftrightarrow |r\rangle$.

Figure 4.12 **a** highlights three data sets corresponding to $C \approx 0, 0.5$ and 1. The decay rate of the excited $|e\rangle = |5P_{3/2}F = 4\rangle$ of Rubidium 87 is $\Gamma_e = 2\pi \cdot 6.065(9)$ MHz and so Rabi frequencies 1.7, 2.7 and 3.6 MHz are highlighted. Rabi frequencies are extracted from fits to EIT transmission spectra using the equation for EIT susceptibility presented in chapter 2. The red data set show low $\Omega_c^{\max}(t) = 1.7$ MHz. For such low coupling strengths, two-level dynamics are dominant. Despite a small EIT window building, insufficient $\rho_{gr}$ coherences build to produce a significant Rydberg dressed flash. The peak flash intensity exceeds the intensity of the transmission during the transparency window.

At stronger $\Omega_c = 2.7$ MHz, stronger EIT is observed due to a more significant $\rho_{gr}$ coherence. At the extinction of the probe, these coherences decay via the excited state. However, the EIT transmission is still low due to the low $\Omega_c^{\max}(t)$ , and as such, there is also significant $\rho_{eg}$ coherence suppressing probe transmission. Two flashes in intensity are observed, one from the fast decay of negative $\rho_{eg}$ coherences and one from the slower decay of positive $\rho_{eg}$ coherence which occurs after the initial probe flash has decayed. The zero crossing of the $\rho_{eg}$ coherence can clearly be seen as a dip in intensity between the initial flash associated with two-level dynamics and the longer Rydberg dressed flash associated with dressed dynamics.

At $\Omega_c = 3.6$ MHz, the EIT transmission window is large due to increased $\rho_{gr}$ coherence. The corresponding dressed flash is much larger in magnitude

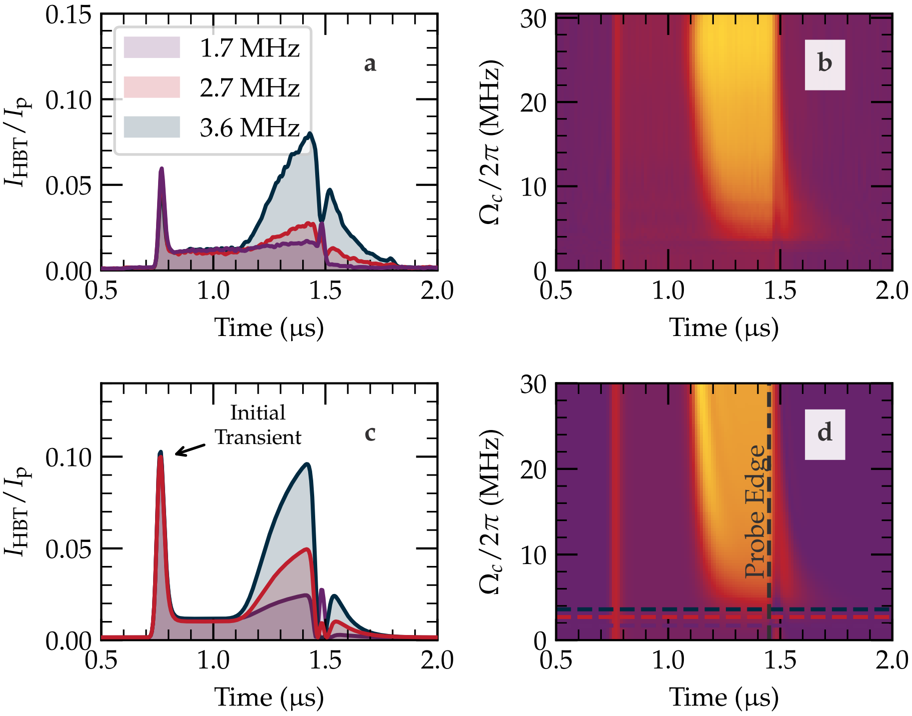

Figure 4.12: Excitation pulse dynamics vs. coupling Rabi frequency ($\Omega_c$), showing the transition from an ensemble exhibiting two-level flash to a three-level ensemble exhibiting dressed flash. **a, b** Experimentally measured transmission data in the form of photon counts detected by the HBT detection circuit binned in 5ns time intervals. **a** Data for $\Omega_c = 2\pi \cdot 1.7$ MHz (purple), $\Omega_c = 2\pi \cdot 2.7$ MHz (red) and $\Omega_c = 2\pi \cdot 3.6$ MHz (blue) corresponding to $C \approx 0, 0.5, 1$ are detailed. **b** Color plot of transmitted intensity showing the variation of the flash signal for $\Omega_c$ in the range $2\pi \cdot [0, 30]$ MHz. **c** Three-level mean-field optical Bloch Equationof the dressed flash for the same coupling strengths as described in the text. **d** Colour map showing full ME simulation of the transmitted intensity over the parameter space of **b**. The three regimes of two-level flash, mixed flash and dressed flash are present in both the experimental and theoretical data.

and the initial $\rho_{eg}$ coherence small due to stronger EIT. Thus the flash associated with two-level dynamics is not observed. Instead an intensity minimum in the HBT signal is still observed due to the time required for $\rho_{eg}$ coherence to build after probe switching. Figure 4.12 **b**, shows that an increased magnitude of $\Omega_c$ leads to more rapid flash, limited by $\Gamma_e$. Increasing $\Omega_c$ is observed to lead to faster de-pumping of the Rydberg manifold.

Figure 4.12 also shows the results of the numerical integration of three-level OBEs derived in chapter 2. The data are simulated for the same range of $\Omega_c$ as the experimental data. A superradiant excited state decay rate of $3\Gamma_0$ is used in the calculation of the Rydberg dephasor due to the geometric speedup detailed in section 4.1.5. The optical depth and pulse timings match the experimental sequence.

Rydberg interaction-induced dephasing reduces resonant optical depth under EIT conditions, which strongly depends on the coupling frequency $\Omega_c$ and principal quantum number $n$ due to the scaling of the underlying Rydberg interaction. Strong dephasing occurring for ensembles with multiple $|r\rangle$ excitations which diminishes resonant transmission [113]. In the dressed-flash context, Van der Waals dephasing causes suppression. This suppression is particularly apparent at low $\Omega_c << \Gamma_r$, where the decay rate of the dressed flash in the absence of VdW dephasing would be associated with decay from the Rydberg state $\Gamma_r$. To account for Van der Waals dephasing, the Lindblad dephasor used for master equation simulation was calculated to include a term proportional to the Rydberg population by inclusion of a mean-field Hilbert-Schmidt dephasor [285] with a jump operator [85] taking the form $\sqrt{\Gamma_{VdW}/2}\sigma_{rr}$. This term causes dephasing of the Rydberg state without population transfer out of $|r\rangle$. Figure 4.9 shows that for $C = 0.15$, where the coupling frequency does not dominate over decay from the Rydberg state, a lack of consideration of Rydberg dephasing causes an extended flash, which can only decay from the Rydberg state

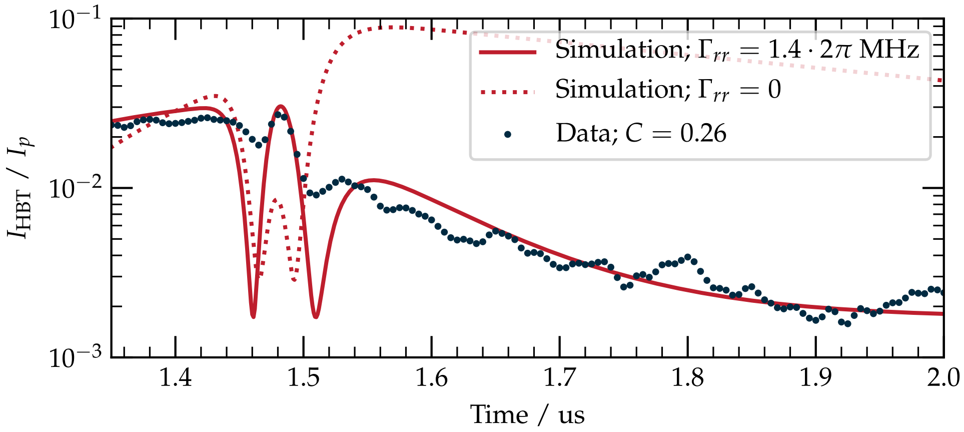

Figure 4.13: The effect of Rydberg dephasing upon the dressed flash is particularly impactful for the case $C \ll 1$ shown in the above data set and simulation. The dressed flash are well fit with master equation simulations which include a Hilbert-Schmidt VdW dephasing operator $\propto |r\rangle\langle r|$. These fits were used to determine the dephasing rate $\gamma_{VdW}/2\pi = 1.5 \pm 0.2$ MHz. Optical Bloch simulations for $\gamma_{rr} = 0$ show a prediction of incorrect magnitude and decay rate of the experimentally observed dressed flash. Data and theory are shown normalised to probe transmission with an experimentally verified optical depth of OD=3.2. An accelerated excited state decay rate of $3\Gamma_0$ was implemented to account for geometric mode interference of the two-level flash decay.

at rate $\Gamma_r$. Rydberg dephasing causes the flash to become foreshortened as shown in Figure 4.13. Where $C \ll 1$, $\Gamma_{\mathrm{VdW}} \neq 0$ causes a dramatic reduction in the extent of the Rydberg flash. The dephasing rate $\gamma_{\mathrm{VdW}}$ was obtained by fitting master equation simulations to experimental data with $\gamma_{\mathrm{VdW}}$ as a free parameter. The dephasing rate was found to be $\gamma_{\mathrm{VdW}} = (1.5 \pm 0.2) \cdot 2\pi$ MHz, which reproduces the form of the foreshortened flash. In Figure 4.13, simulations are shown for the fit value of $\gamma_{\mathrm{VdW}}$ and $\gamma_{\mathrm{VdW}} = 0$, highlighting the effect of Rydberg dephasing upon the dressed flash.

It is possible to view the dressed flash using a simplified pulse sequence, where $\Omega_c$ is never switched off. This provides the requisite condition of a coupled three-level system at the falling edge of the probe beam. Our

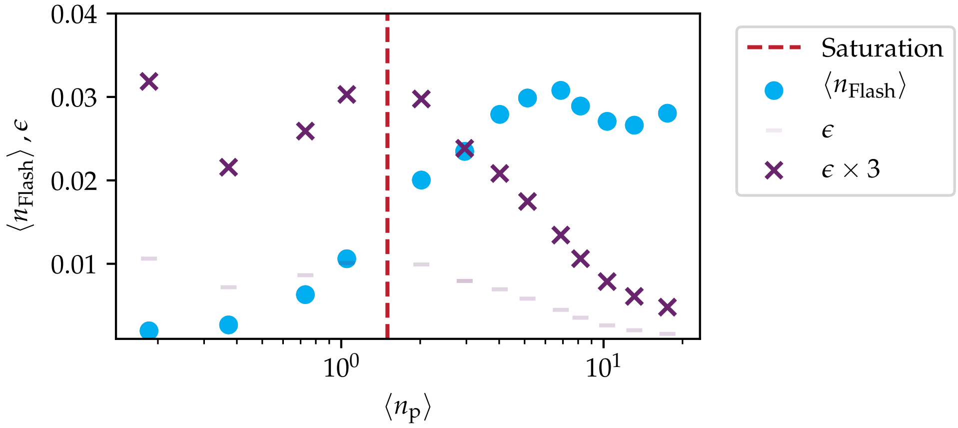

Figure 4.14: Rydberg blockade causes suppression of the dressed flash for high incident photon numbers $\langle n \rangle$. Saturation of the medium occurs at $\langle n_{\mathrm{Flash}} \rangle \approx 2$, and is marked by a dashed line. The efficiency of flash photon generation $\epsilon$ is heavily suppressed for indicent photon numbers $\langle n_{\mathrm{p}} \rangle \gg 1$, reducing the number $\langle n_{\mathrm{Flash}} \rangle$ of detected flash photons due to Rydberg dephasing and blockade. Data presented in this chapter correspond to the range $\langle n_{\mathrm{p}} \rangle \in [0, 1]$.

sequence stipulates that the coupling field is switched on during probe absorption. This is to allow monitoring of the optical depth of the ensemble during data acquisition. The optical depth of the ensemble determines the level of absorption in the steady state absorption region (between $t = 0.8\,\mu\mathrm{s}$ and $t = 1.1\,\mu\mathrm{s}$ in Figure 4.12) and $OD_b$ determines the value of $g^{(2)}$ during EIT transmission. Thus consistent data sets require a constant optical depth. The pulse sequence of Figure 4.11 enables both the optical depth of the sample and the form of the dressed flash to be monitored within a single experimental data set. The number of experimental runs that can be performed on the same ensemble is limited to that which does not significantly alter the optical depth. As such, 5000 experiments are performed on each ensemble before they are refreshed from the magneto-optic trap.

### 4.2.2 Transient Anti-Bunching

Figure 4.14 demonstrates the blockade of the flash for quantum state $|80S_{1/2}\rangle$. As the incident photon number is increased, the number of photons emitted by a superatom during the transient flash plateaus [35]. The slight reduction in emission at higher incident photon rate matched observations of this phenomenon in other experiments [85]. The observed suppression of the dressed flash was attributed to mutual dephasing of multiple excitations which are supported due to the spatial extent of the ensemble, which is larger than $r_b$. Rydberg dephasing also increases the decay rate of the dressed flash. The signature of Rydberg dephasing is also present in the supported excitation numbers in the atomic medium. These statistics are imprinted upon photons emitted by the medium which can lead to a strong modification of the statistical nature of the emission. The first optical nonlinearities induced by VdW interactions were observed in Durham by the group of Charles Adams [113]. Since that time, optical nonlinearities due to Rydberg interactions have received interest due to their projected applications in quantum technology [116, 119, 121, 286]. Statistical modifications due to a restriction of the possible geometric arrangement of excitations within optical media due to Rydberg blockade are observable as changes to the second-order correlation function of light emitted from the medium, $g^{(2)}(\tau)$.

Figure 4.15 shows the emission profile and $g^{(2)}(\tau)$ statistics of photons emitted during the dressed flash. The pulse sequence and level diagram are exactly as outlined in Figure 4.11 with the exception that Rydberg state $|r\rangle = |80S_{1/2}\rangle$ is selected to increase the blockade radius and thus increase the optical depth per blockade volume, $OD_b$. The coupling frequency is set to $\Omega_c = 1.29 \pm 0.04 \cdot 2\pi$ MHz.

Figure 4.15 shows calculated values for $g^{(2)}(\tau)$ during the dressed flash pulse sequence of Figure 4.11. The experiment produces requisite photon statistics to analyse $g^{(2)}(\tau)$ across runs for matching 50 ns time bins high-

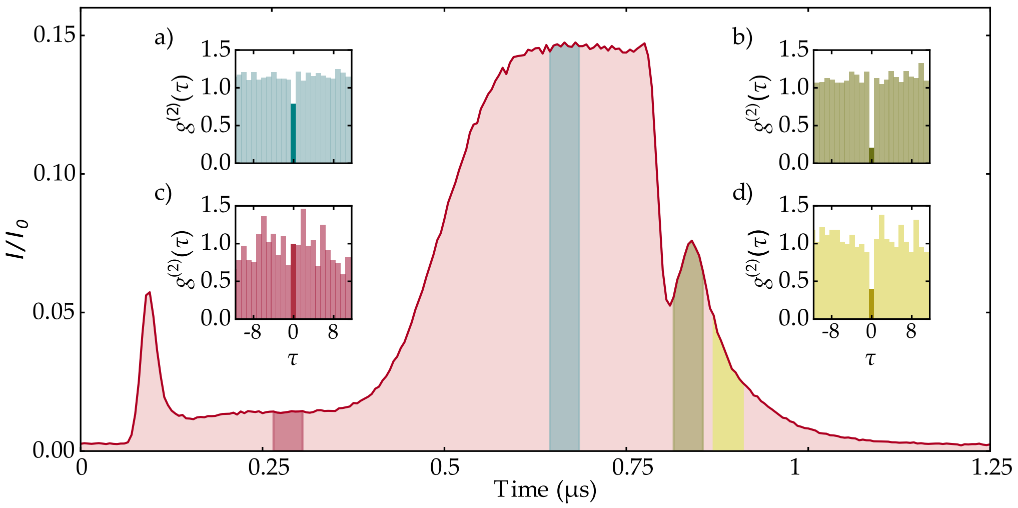

Figure 4.15: Strong VdW interactions affect transmitted photon statistics, observable through their effect on the $g^{(2)}(\tau)$ statistic as defined in the text. Inset histograms show $g^{(2)}(\tau)$ associated with two-level transmission in red ($g^{(2)}(\tau) = 1.00 \pm 0.12$), during steady-state EIT in blue ($g^{(2)}(\tau) = 0.79 \pm 0.04$), during early flash in olive ($g^{(2)}(\tau) = 0.20 \pm 0.04$) and late flash in gold ($g^{(2)}(\tau) = 0.40 \pm 0.11$) are shown. This demonstrates characteristic ($g^{(2)}(0)$) suppression during the dressed flash associated with Rydberg blockade. Suppression is weak during the EIT window due to our elongated ensemble geometry and imperfect optical depth per blockade sphere $OD_b$. (**a-d**) $g^{(2)}(\tau)$ histograms for corresponding 50 ns time bins. Figure adapted from [84].

lighted giving an insight into the evolution of $g^{(2)}(\tau)$ during the dynamical pulse sequence. Time bins used for calculation are indicated by shaded regions in red, blue, olive, and yellow. This minimum bin width is chosen to build the requisite statistics to calculate $g^{(2)}(\tau)$ with low error. A suppression of $g^{(2)}(0)$ given by Equation 3.2.2 corresponds to anti-bunching within the time bins used for calculation and within a single experimental run. Histograms of $g^{(2)}(\tau)$ are inset in Figure 4.15.

In red, the statistical nature of light transmitted by a two-level ensemble before $\Omega_c$ is applied matches that of the incident laser, with $g^{(2)}(0) \approx 1$. The data for $g^{(2)}(\tau)$ are noisy due to the high OD at this time leading to low numbers of photon events. Light detected during this time window is simply that which is not absorbed by the two-level medium with $OD \approx 4$, and has $g^{(2)}$ associated with the light source, in this case, an ECDL.

An EIT transmission window occurs from $t = 0.5\,\mu\text{s}$ to $t = 0.75\,\mu\text{s}$. In blue, the $g^{(2)}(\tau)$ statistics of continuous EIT are shown. Rydberg blockade of the two-level medium causes a weak suppression of $g^{(2)}(0)$ arising due to the suppression of the $|r\rangle$ excitations and thus $|g\rangle \to |r\rangle$ coherences that are required for EIT. In this regime the medium acts as a photon filter. Single photons pass the medium naturally under EIT conditions. Multiple photons require greater excitation of (blockaded) Rydberg population. Thus the medium becomes increasingly opaque to higher photon numbers due to the progressive detuning of multiply excited polariton states from the coupling beam. Once the medium becomes saturated with Rydberg excitations, subsequent incident photons experience an effective two-level medium and thus strong scattering occurs due to high $OD \approx 4$. During steady-state EIT, photon anti-bunching is observed ($g^{(2)}(0) < 1$).

Experimental $g^{(2)}(0)$ does not reach zero, as the finite optical depth of the medium dictates that some photons propagate without interacting with the ensemble at all. The spatial extent of the ensemble is larger than the blockade radius and multiple Rydberg excitations are supported. Thus

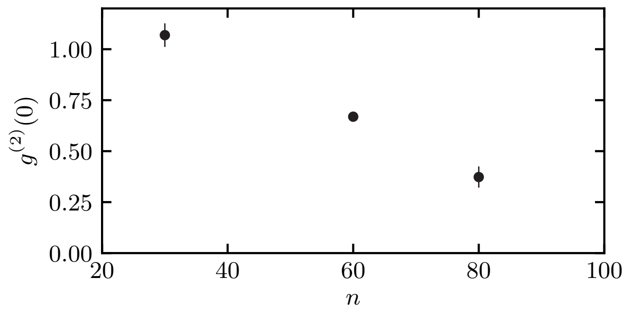

Figure 4.16: Flash $g^{(2)}(0)$ Vs. Principal Quantum Number. Photons detected during the flash are anti-bunched due to Rydberg blockade, reflected by low values of $g^{(2)}(0)$. The degree of anti-bunching scales strongly with the principal quantum number due to the strong scaling of the underlying Rydberg blockade volume. Values above reflect the average $g^{(2)}(0)$ of all photons emitted by the ensemble after the probe beam is extinguished, although at a fixed principal quantum number there is some temporal variation in $g^{(2)}$ as detailed in Figure 4.15. Data reflect average values of $g^{(2)}(\tau)$ of multiple experiments with error bars reflecting SEM.

the statistics of photons arriving at the HBT detection circuit during the EIT window are a mixed picture of the coherent input laser, and weakly blockaded EIT transmission and thus the value of $g^{(2)}(0) = 0.8 \pm 0.04$ is relatively high, a statistical mixture of the transmitted probe beam, and anti-bunched light propagating under EIT conditions.

The dressed flash gives access to the delayed release of excitations from the medium, and thus observation of photon statistics in the absence of probe light. Purple and gold histograms in Figure 4.15 show the $g^{(2)}(\tau)$ statistic for photons events recorded during two 50 ns time bins which both fall within the dressed flash. This gives access to direct observation of the statistics associated with light emitted from the blockaded Rydberg manifold in the absence of photon counts attributable to the probe beam and thus mixed photon statistics of probe and ensemble. Initially, (olive shaded region) a very low value of $g^{(2)}(0)$ is observed. The value of $g^{(2)}(0) = 0.20 \pm 0.04$ diverges from the ideal value of zero due to the atomic ensemble being larger in spatial extent than a single Rydberg blockade volume and thus supporting multiple Rydberg excitations. It was observed that the emitted flash exhibited larger values of $g^{(2)}(0)$ at later times (olive data in Figure 4.15) associated with weaker anti-bunching. This observed variation of $g^{(2)}(0)$ suggests that the dynamics for the emission of single and multiple excitations are distinct and non trivial and thus present an interesting avenue for further study. The dressed flash represents a very simple alternative to photon storage experiments allowing for simplified study of dynamic evolution of Rydberg systems as recently reported [287].

Figure 4.16 shows the value of $g^{(2)}(\tau = 0)$ for calculated for all photons counted during a dressed flash for principal quantum numbers $n \in \{30, 60, 80\}$ . The observed reduction in the value of $g^{(2)}(0)$ at high principle quantum numbers is as a direct result of $r_b$ scaling with principle quantum number. At $n = 30$, flash photon statistics are consistent with uncorrelated photon events due to the smaller Rydberg blockade radius. At $n = 80$, $g^{(2)}(\tau = 0)$ falls to $(0.38 \pm 0.03)$ at $n = 80$ when all photons retrieved after the probe is extinguished are considered. Figure 4.15 shows that this can be even lower for narrow time windows.

In the introduction, Figure 1.1 showed an idealised conceptual picture of the conversion of photon statistics from a coherent laser source due to interaction with an atomic ensemble, lowering $g^{(2)}(0)$ to zero. Photons enter the ensemble as a coherent pulse with photonic statistics. Suppression of multiple Rydberg excitations leads to the transmission of one photon. Other photons in the pulse experience a system of two-level scatterers with high optical depth and do not pass the medium. The outgoing pulse contains a single photon having $g^{(2)}(0) = 0$. A device approaching this idealised picture might be implemented using our scheme by interfacing photons emitted during the flash to fast atomic switches currently in development [288] which might be used to isolate the part of the flash where $g^{(2)}(0)$ is extremely low $\approx 0.2$. Low photon efficiency is the main draw back for this scheme. The photon efficiency of the dressed flash can be optimised to $\sim 20\%$ by matching the duration of the input probe pulse to the rise time of the EIT transmission window [289].

## 4.3 Microwave-dressed EIT Transients

Rydberg states with high principal quantum numbers converge in energy with a $n^{-3}$ scaling. Optical transitions between lower adjacent energy levels give way to microwave couplings between states of high $n, n'$. State manipulation by modern microwave sources can be powerful, accurate, and precise. Microwave transitions extend the utility of Rydberg systems by providing a convenient interface to other quantum devices [257, 290]. Microwave driving can further enhance the blockade by modifying the scale of the Rydberg-Rydberg interactions [29, 48, 114, 129]. The VdW blockade radius between states $|nS_{1/2}\rangle$, $|nS_{1/2}\rangle$ is determined by the strength of the $C_6$ parameter interaction with an $r^{-6}$ scaling. Microwave driving places the single atom system into a superposition $|\psi_1\rangle \sim |nP_{3/2}\rangle + |n'S_{1/2}\rangle$. The energy degeneracy with other excitations in $|\psi_2\rangle = |nS_{1/2}\rangle + |n'P_{3/2}\rangle$ leads to effective elimination of the pair state energy defect and thus a strong first order perturbative energy shift with $r^{-3}$ scaling. At $n = 60, n' = 59$, the strong direct dipole-dipole coupling is large between $1 - 10$ MHz for atoms separated by $10\,\mu\text{m}$ [29, 152]. This amplifies suppression of multiple excitations and the degree of anti-bunching observed in emitted light.

This subsection details precision manipulation of the optical response of a collective system of emitters using a microwave source capable of providing coupling between Rydberg states with a Rabi frequency over 100 MHz. The 80/20% switching speed of the microwave source is 10ns, and pulse timing can be controlled by gating, with a timing resolution of 5 ns.

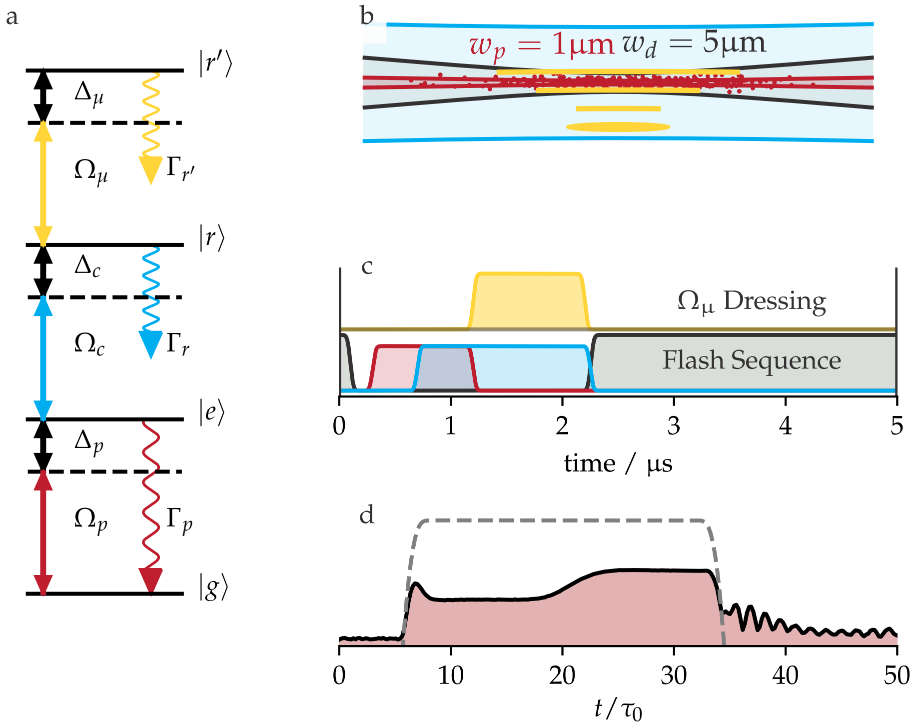

Figure 4.17: Outline of experimental pulse sequences and geometry used to investigate four-level transient dynamics of Rydberg systems. **a, b** Level diagram and beam geometry. The geometry and coupling scheme is the same as that of Figure 4.11 with the addition of a microwave field generated by an *in-vacuo* quarter wave stub antenna coupling Rydberg states $|r\rangle$, $|r'\rangle$ with Rabi frequency $\Omega_\mu$ and detuning $\Delta_\mu = 0$. **c** Representative pulse sequence. Modulated flash can be observed by applying a pulse of resonant microwaves as soon as the probe is extinguished. Microwaves are applied for a variable duration of up to 1 µs. **d** Solid line: Histogram of photon arrivals in 5 ns time bins for a typical modulated flash. Dashed line: detector signal in absence of atoms. A microwave dressing field ($\Omega_\mu$ in **c**) drives population between states $|r\rangle = |60S_{1/2}\rangle$, $|r'\rangle = |59P_{3/2}\rangle$ causing modulated flash emission. Characteristic modulation of the dressed flash emission (c.f. Figure 4.11), detected via the HBT detection circuit. The 80/20% switching speed of the microwave source is 10 ns.

### 4.3.1 Observation of Four-Level Transients

The experimental sequence used to observe the effects of microwave dressing upon the dressed flash is presented in Figure 4.17, which should be considered an extension of the dressed flash pulse sequence in figure 4.11. As with previous pulse sequences, atoms experience the confining force of the dipole trap for 3 µs between experiments. The dipole trap is switched off at $t = 0$. After 0.2 µs, a probe pulse enters the medium with mean photon number $\widetilde{n} \approx 0.5$ and duration $t_p = 0.9\,\mu\text{s}$. The probe pulse is again bisected by the rising edge of the coupling beam providing coupling Rabi frequency $\Omega_c/2\pi$. The dressed flash pulse sequence shown in Figure 4.11 is used to seed a transient Rydberg population. A microwave pulse from an *in-vacuo* quarter-wave microwave antenna is then applied as soon as the probe pulse is extinguished providing microwave Rabi frequency $\Omega_\mu/2\pi$. The variable amplitude microwave field addresses the $|nS_{1/2}\rangle \leftrightarrow |(n' \pm 1)P_{3/2}\rangle$ transition, coupling these two Rydberg states. Thus microwave coupling is initiated at the start of the transient decay witnessed in section 4.2.1. The ensemble geometry is the same as that of the dressed flash (c.f. Figure 4.11). The HBT detection circuit is again coupled to the mode of the incoming probe.

Strong microwave dressing of the $|r\rangle, |r'\rangle$ manifold drives oscillation of the super-atom population between $\rho_{rr}$ and $\rho_{r'r'}$. Population transfer out of the qubit states via spontaneous decay is negligible on the experimental timescale, with $\tau_r \approx \tau_{r'} \approx 500\ \mu\text{s} \gg t_{\text{exp}}$ for $n$=60 [152]. However continuous coupling to the bright state $|e\rangle$ via $\Omega_c$ provides a continuous, weak transfer of population between $|rS_{1/2}\rangle$ and $|e\rangle$ with lifetime 26.34(1) ns [276]. Thus photon emission due to weak coupling to the excited state is observed on the experimental timescale, with intensity proportional to the population of $|nS_{1/2}\rangle$. This provides a form of continuous weak measurement [291] which allows for the continuous monitoring of the state of the superatom. The upper state $|nP_{3/2}\rangle$ does not share the coupling via $\Omega_c$

to $|e\rangle$ and so remains dark.

Figure 4.18 shows histograms of photon arrival times registered by the HBT detection circuit during the modulated flash, exhibiting the interaction between microwave field and decaying superatom. Both microwave and coupling fields are switched off at the point at which the dipole trap is extinguished at $t_{\text{exp}}$. In order to acquire the requisite number of photon events for statistical analysis, experiments are repeated ten million times. The modulated flash extends the duration of the dressed flash and consequently the experimental duration $t_{\text{exp}}$ is extended to 2.2 µs allowing for observation of the extended flash in absence of AC Stark shifts from the dipole trap. Modulation of the $\langle n\rangle$ for the outgoing optical field is observed, as Rabi oscillations are driven between effective dark and bright states of the Rydberg manifold. Occupation number oscillations between $|0\rangle$ and $|1\rangle$ of the outgoing optical mode are observed. Modulated transient decay occuring after the probe beam is extinguished are termed *modulated flash* for this work. Modulated flash is a natural extension of the dressed flash occuring during a microwave drive.

Figure 4.18 shows a calibration of the frequency of Rabi oscillation against microwave drive frequency. The experimental pulse sequence of Figure 4.11 drives the atomic ensemble. The frequency of Rabi oscillation is observed through the modulated flash mapping. Photon emissions arriving at the HBT detection circuit are placed in 5ns time bins. Oscillations are visible up to approaching the technical limit of our detection circuit of 100 MHz[1]. The probe beam is callibrated with $\langle n\rangle = 1$ within each experimental run. The probability of photon emission during the modulated flash

---

[1] This technical limitation derives from the experimental control system which registers and time-tags photon arrival data from SPAD detectors. It is the Nyquist frequency of this system. Plans to overcome this technical limitation through the use of faster commercial photon-counting cards e.g, Becker and Hickl SPC-150NXX TCSPC FLIM Module are in motion.

within a single experimental run[2] is 1.2±0.1%. This corresponds to 78±3% of the power of the dressed flash emission. Coherent oscillations between effective bright $|r\rangle$ and dark $|r'\rangle$ states are observed as a modulation of the envelope of the decaying optical field $|\hat{0}\rangle$ at the microwave Rabi frequency $\Omega_{\mu}$, constituting a weak measurement of the state of the Rydberg manifold. No significant dephasing of the Rabi oscillations was observed during the $\sim$0.5 µs duration of $\Omega_{\mu}$ as is apparent from Figure 4.18 **a, b** (inset) demonstrating the spatial uniformity and coherence of the drive field.

The application of resonant microwaves also causes AT splitting of the Rydberg manifold $\{|r\rangle, |r'\rangle\}$. As $\Omega_{\mu}$ is increased, the energy shift of the dressed Rydberg states increases, and causes an increased detuning of the $|e\rangle \leftrightarrow |r\rangle$ transition. At the point of microwave field extinction, this transition is returned to resonance with coupling field $\Omega_c$, and ensemble emission is re-established. This provides for the storage and release of transient Rydberg excitations, similar to previous schemes exploiting natural long-lived cooperative subradiant states [50, 292]. Ideally, Rydberg population decays slowly with natural lifetime $\tau_r, \tau_{r'} \sim 0.5$ ms during this time, however the observation of such slow transient effects are limited in out experiment by thermal dephasing of the ensemble. Thermal dephasing limits us to the observation of coherent phenomena lasting less than the lifetime associated with thermal dephasing of $\tau_{\mathrm{T}} \sim 1\,\mu\mathrm{s}$.

Figure 4.19 shows the temporal envelope of the HBT detector signal $I_{\mathrm{HBT}}$ alongside single-body master equation simulations of the response of the system. The coupling frequency is obtained by fitting a master equation simulation to the measured response of the medium in the absence of microwave dressing as $\Omega_c/2\pi = 4.2 \pm 0.1$ MHz. In the same way, the linewidth induced dephasing term is determined to be $\gamma_{er} = 2.0 \pm 0.2\,\mu\mathrm{s}^{-1}$, $\gamma_{rr} = 2.35 \pm 0.5\ \mu\mathrm{s}^{-1}$. Microwaves address the transition $|e\rangle = |5P_{3/2}\rangle \leftrightarrow |r'\rangle = |60S_{1/2}\rangle$. Rabi frequency $\Omega_{\mu}/2\pi$ is varied over the range [0, 100] MHz.

---

[2] Also conversion efficiency due to incident $\langle n\rangle = 1$.

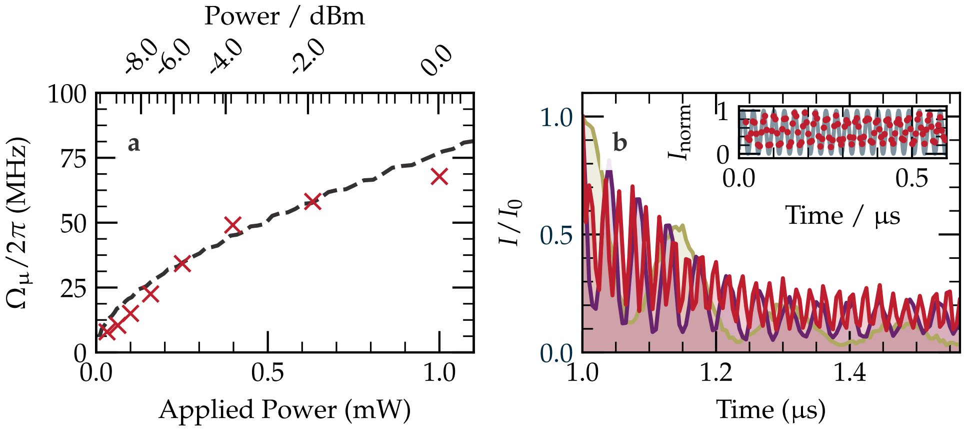

Figure 4.18: A microwave field resonant with the $|60S_{1/2}\rangle \leftrightarrow |59P_{3/2}\rangle$ transition modulates the dressed flash. **a** shows modulation frequency calibration. Data are fit to a numerical master equation simulation with power scaling as a single free parameter. Fits close to the 100 MHz Nyquist frequency are poor. **b** shows microwave modulation of the flash with a sinusoidal envelope determined by the Rabi frequency $\Omega_\mu$ is observed as Rydberg population oscillates between $|r\rangle$, $|r'\rangle$. Three data series are shown corresponding to $8, 23, 50$ MHz modulation. Rabi oscillations with a decaying envelope are observed due to spontaneous emission via $|e\rangle$, where $t = 1\,\mu$s corresponds to the start of the dressed flash. All data are normalised to peak modulated flash emission. $\Omega_c$ is fixed at $2\pi \cdot 5$ MHz. **b, inset** Rabi frequency $\Omega_\mu$ can be precisely extracted through normalised fits, producing the calibration in b. with a value of $\Omega\mu = 33.60 \pm 0.04 \cdot 2\pi$ MHz for the data inset. Error bars are derived from these fits and shown in **a** to be negligible.

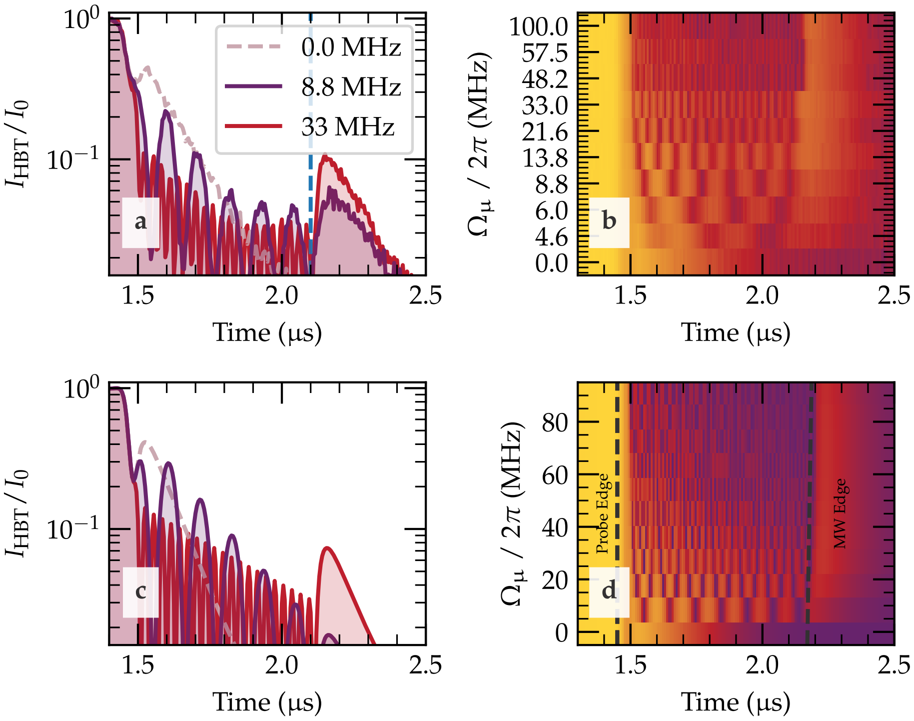

Figure 4.19: Modulation and Suppression of Dressed Flash. **a** shows dressed flash with $\Omega_c = 2\pi \cdot 5.20 \pm 0.02$ MHz modulated by $\Omega_\mu = 2\pi \cdot [0, 8.8, 33]$ MHz. The extended duration of the dressed flash is clearly shown. A vertical dashed line at 2.1 µs shows the falling edge of the microwave pulse. An emission peak is observed after the extinction of the pulse. **b** shows a colormap of the same data as in **a**, taken over an extended range of $\Omega_\mu \in [0, 100]$ MHz. Modulation and delayed emission are present across all data sets shown. Discrete $y$ axis labels represent Rabi frequencies extracted from decaying sinusoidal fits to data sets shown. $\Omega_c$ is held constant across all data sets in **a**, **b**. **c**, **d** show optical Bloch equation simulations of the modulated flash emission, using experimental parameters for pulse timings and $\Omega_{\mathrm{c,p}}$ as described in the text. $\Omega_\mu$ shown are the same as in **a**, and are a close match to observed photon emission, however the observed final emission peak is larger than the model predicts.

The coupling beam is held at a constant $\Omega_\mathrm{c}/2\pi = 13.4 \pm 0.3$ MHz. Panel **a** shows the progression from dressed flash $\Omega_c = 0$ (dashed purple line) to microwave decay supression. Panel **b** contains a colormap showing the full dataset. Master equation simulations of the same data are shown in panels **c, d**. To account for VdW dephasing, we introduce phenomenological values $\gamma_{r'r'} = 0.6\mu\mathrm{s}^{-1}$, $\gamma_{rr'} = 0.6\mu\mathrm{s}^{-1}$. Thus the size of the delayed emission depends upon the state of the Rydberg manifold[3] at $\Omega_\mu$ extinction. For the data presented in the figure, the microwave pulse duration was manually adjusted to leave population in $|r\rangle$, maximising the intensity of the final emission peak.

Figure 4.20 details the dependence of the decay rate of the stored excitation upon $\Omega_c$. The lifetime of the stored excitation is measured to be $0.50 \pm 0.01$ μs for $\Omega_\mathrm{c}/2\pi = 14$ MHz, falling to $0.4 \pm 0.041$ μs for $\Omega_\mathrm{c}/2\pi = 23$ MHz. There is dependence on $\Omega_c$ due to saturation of spontaneous emission. Ideally, Rydberg population decays slowly with natural $\Gamma_r, \Gamma_{r'} \sim 0.5$ ms during storage. However, retrieval is severely limited by thermal dephasing causing due to phase distortion due to atomic motion [128, 238]. Thus relatively low lifetimes are observed for dark state polariton storage observed in this [48, 105] and similar systems [59].

During storage, an atom with mass $m$ and temperature $T$ typically moves by $\sqrt{2k_BT/m} \cdot t$. Thus lowering the temperature of the atomic ensemble through techniques such as Raman sideband cooling might give access to longer storage times [293].

Figure 4.21 compares the experimental saturation of photon storage, which occurs at around $\Omega_\mu = 2\pi \cdot 100$ MHz. In panel **a**, Window A identifies the region of photon emission during microwave application. Window B begins at the extinction of $\Omega_\mu$, and contains the delayed emission (c.f. Figure 4.22 and associated discussion). The integrated photon counts during

---

[3] Emission is maximal (minimal) when population resides in $|r\rangle$ ($|r'\rangle$) at the end of the microwave pulse.

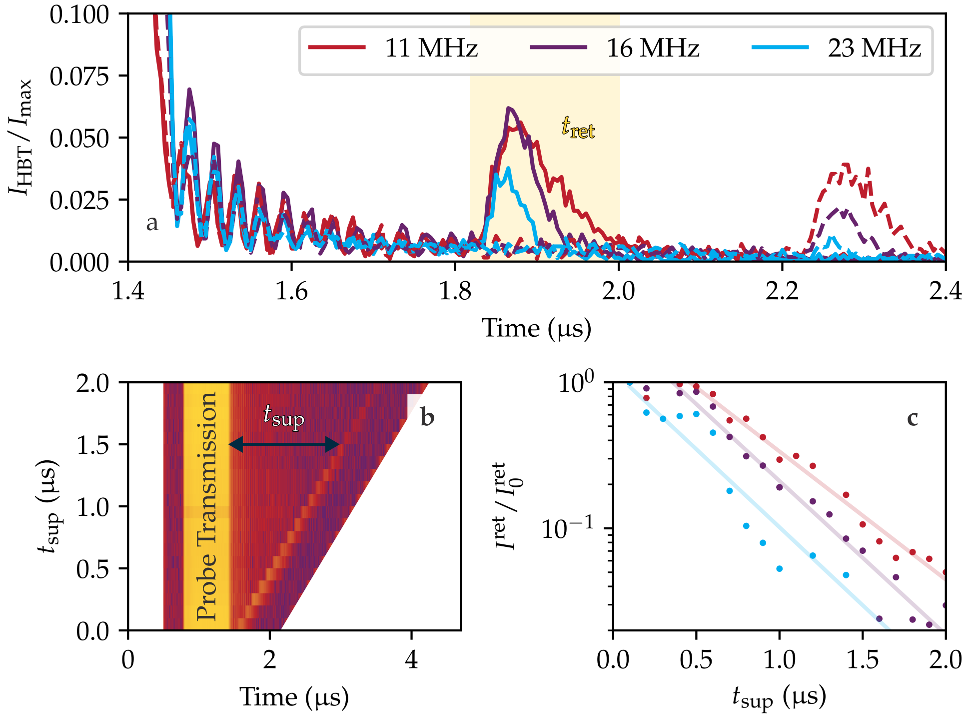

Figure 4.20: Microwave Suppression of Flash Emission. **a** A strong microwave pulse is applied immediately after the probe is extinguished during a dressed flash sequence. The microwave pulse is reinsated at $t = 1.8\,\mu\mathrm{s}$ (solid lines) or $t = 2.2\,\mu\mathrm{s}$ (dashed lines), delaying emission. Three values of $\Omega_\mu$ are shown in the range $2\pi \cdot [14, 42]$ MHz. The $|r\rangle \leftrightarrow |e\rangle$ coupling depumps Rydberg excitations faster at higher $\Omega_{\mathrm{c}}$. Red regions flanking the data represent the dipole trapping beam. **b** Colormap showing full data series for $\Omega_c = 2\pi \cdot$ 11 MHz. Decay rates are extracted by counting the photons arriving during the retrieval pulse as the microwave suppression time $t_{\mathrm{sup}}$ is varied. **c** Decay of population is exponential, and is slightly faster for higher $\Omega_c$, due to more efficient Rydberg depumping.

window A(B) is defined as the sum of the individual photon counts registered by the HBT detectors during each window and is denoted $n_{A(B)}$. The total integrated photon events in both windows are described by the quantity $\mathcal{N}_{AB} = n_A + n_B$. In **b**, the normalised photon events $n_{A(B)}/\mathcal{N}_{A+B}$ show the probability that a photon is emitted during either window. The photon counts $n_B$ are proportional to the excitations in the Rydberg manifold at the extinction of the microwaves. The corresponding quantity $n_A$ is proportional to the number of excitations emitted from the Rydberg manifold during the modulated flash.

The relative probability of emission in window A or B varies as a function of $\Omega_\mu$ shown in Figure 4.21 **b**. As $\Omega_\mu$ increases, $n_A$ is diminished as AT splitting detunes dressed states $|r\rangle \pm |r'\rangle$ from resonance with the coupling beam. Suppression of emission during window A causes an increase in emission during window B, when the Rydberg manifold is brought back into resonance with the coupling beam. Thus for $\Omega_\mu >> \Omega_c$, we observe saturation in photon storage. The colour data are ovelaid with simulation extracted from the master equation simulation presented in Figure 4.19 (solid line).

The master equation simulation predicts a higher storage efficiency for realistic dephasing rates obtained through previous analyses of the modulated flash emission as the model fails to take account of our strong thermal dephasing mechanism.

The apparent protection of the superatom from emission during strong driving opens up an interesting experimental avenue into the effects of quantum rifling [294] and weak measurement [291] in this sub-Zeno limit [295].

### 4.3.2 Interaction-Induced Dephasing

The increased interaction strength associated with $C_3$ interactions causes rapid interaction induced dephasing of multiple excitations [114, 129] due to

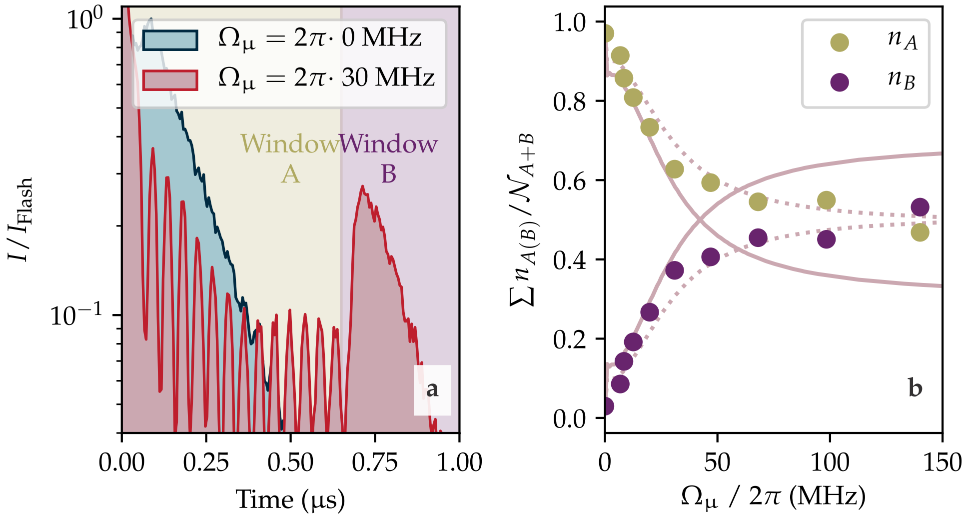

Figure 4.21: Microwave suppression of EIT transient. **a** Retrieval associated with flash ($\Omega_c = 0$) and delayed emission ($\Omega_c \gg 0$). A large number of photons are emitted from the ensemble when a strong $\Omega_\mu$ is switched off. Intensity is normalised to the peak flash intensity. **b** The degree of decoupling of Rydberg excitations from the radiative transition scales with $\Omega_\mu$, with a corresponding increase in $n_B$. Data points in **b** are normalised to the total number of photons $\mathcal{N}_{A+B}$ observed after the probe beam is switched off, $\mathcal{N}_{A+B} = n_A + n_B$. A master equation simulation (solid line) predicts higher storage efficiency for $\Omega_\mu \gg 0$. Thermal dephasing limits efficiency in practice. The dashed line shows an adjustment for thermal dephasing reducing retrieval efficiency to 0.8.

the spatial dependence of the dipolar couplings (through Equation 2.1.31). Strong dephasing with spatial dependence destroys spatial phase coherence of the ensemble and outgoing photons from the mode matched detection HBT detection circuit. This approach causes further suppression of the observation of multiple excitations leading to enhanced anti-bunching of outgoing photons and lower $g^{(2)}(0)$.

Figure 4.22 shows the timescale associated with Rydberg spin-wave dephasing associated with enhanced $C_3$ interactions through the effect on observed $g^{(2)}(0)$. Modulated flash emission is shown as a grey shaded data set, under the action of the pulse sequence matching that of Figure 4.19. This modulated flash is observed with characteristic delayed emission occurring at $t \approx 1.45\,\mu\text{s}$. The incoming probe pulse has a mean photon number $\langle n \rangle = 0.25$. This provides a sufficient number of photon events to extract values of $g^{(2)}(0)$ during 50 ns time intervals as with Figure 4.15. A representative interval is shown in Figure 4.17 highlighted in cyan. Time bin centres are indicated by the positions of the red data points, which represent the value of $g^{(2)}(0)$ evaluated for data within the respective time bin.

Upon microwave application $g^{(2)}(0)$ steadily falls from an initial value of close to $g^{(2)}(0) \approx 1$ during EIT transmission. After around 200 ns of enhanced interactions, the value of $g^{(2)}(0)$ falls to $0.38 \pm 0.2$. Comparison with Figure 4.15 shows that this level of anti-bunching is representative of a dressed flash anti-bunching at $|80S_{1/2}\rangle$, confirming enhanced anti-bunching due to resonant interactions. Despite the huge number of experimental runs, experimental SNR is too low to quote a meaningful value for $g^{(2)}(0)$ after $t \approx 200\,\text{ns}$ of microwave driving due to exponential decay of the signal once the probe beam has been switched off. This is represented by the absence of data points corresponding to $g^{(2)}(0)$ between $t = 1.1$ and $1.5\,\mu\text{s}$. Extinguishing the microwaves at later times permits an extension of this study of $g^{(2)}(0)$ to longer microwave applications. The final value

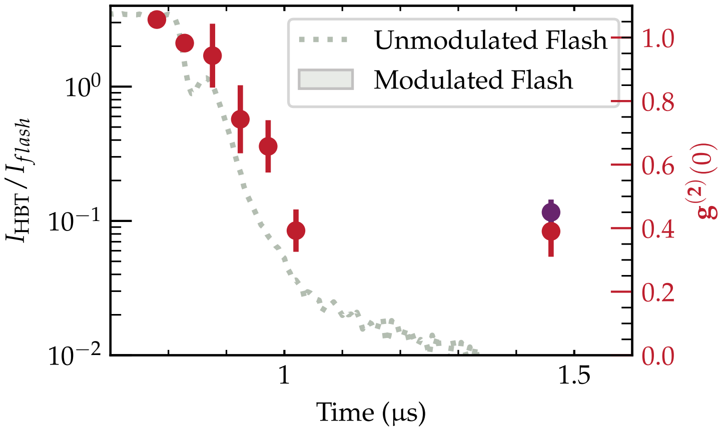

Figure 4.22: Resonant $g^{(2)}(0)$ suppression. The evolution of $g^{(2)}(0)$ for a dressed flash emission from state $|60S_{1/2}\rangle$ modulated by a microwave field providing resonant coupling to $|59P_{3/2}\rangle$ as a function of microwave duration is shown during the flash. Typical modulated and un-modulated flash envelopes are shown, normalised to the peak intensity of the un-modulated flash. The value of $g^{(2)}(0)$ quickly plummets after application of the $\Omega_\mu = 67.4 \pm 0.3$ MHz microwave field, and in less than 500ns, the value of $g^{(2)}(0)$ is reduced to $0.39 \pm 0.07$. This value of $g^{(2)}(0)$ is sustained, as can be observed by turning off the microwave coupling, whereupon a large number of photons are retrieved from the medium. Analysis of photons retrieved during this large window shows them to have a similarly low value of $g^{(2)}(0)$, here $0.39 \pm 0.08$ associated with strong resonant dipolar interactions. This is much lower than the dressed flash at the same principal quantum number. The $g^{(2)}(0)$ statistic for the dressed flash at $n = 80$ is shown as a purple data point for comparison.

for $g^{(2)}(0)$ at $t$ =1.45 µs is calculated using a 100 ns time window covering the delayed emission peak. So it is confirmed that $g^{(2)}(0)$ suppression for states $60S_{1/2}, 59P_{3/2}$ is limited at $0.38 \pm 0.2$. The atomic ensemble is larger than the blockade radius with $10\sigma_r \sim \sigma_z \sim 2r_b^{C_3}$ for $n = 60$ and is thus only partially blockaded by the interaction [28, 114].

Thus emission suppression through the application of strong microwave fields can be used to both enhance $g^{(2)}(0)$, and to exercise control over the temporal release of the excitation. Implementing microwave $g^{(2)}(0)$ suppression at a higher principal quantum numbers might achieve a useful single-photon source with an emission window of $\sim$ 100 ns, with a temporal mode tunable over several microseconds. This microwave emission suppression can be used to extend the duration of interaction-induced dephasing, enhancing $g^{(2)}(0)$ suppression. In this system, conversion efficiencies of $\sim$ 50% have been observed [289]. This conversion efficiency might be increased by engineering the mode of the incident photon to match that of emission [296].

### 4.3.3 Cleaning Pulse

The inclusion of a 'cleaning pulse'[205] was found to be essential to obtaining low values of $g^{(2)}(0)$ and for the preservation of optical depth across experimental runs. The cleaning pulse rids the medium of Rydberg pollutants; excitations remaining in the Rydberg manifold after the experiment is concluded [85, 297]. This cleaning pulse consists of a pulse of $\Omega_\mu$ lasting 0.5 µs applied at the end of each experimental run, before the reinstatement of the dipole trap. The experimental duration $t_{\text{exp}}$ is extended to accommodate this cleaning pulse where it is used. $\Omega_\mu$ is unchanged between the cleaning pulse and modulation pulse. The application $\Omega_\mu$ during $\Omega_c > 0$ again causes any population in $|r\rangle$, $|r'\rangle$ to decay via radiative state $|e\rangle$. Thus a relatively long pulse of this nature causes any Rydberg population to decay via spontaneous emission. Without this active de-pumping, Rydberg excitations promoted in one experimental run can remain in the medium and are observed to corrupt experimental data extracted from subsequent experimental runs.

# Chapter 5

# Collective Rydberg Qubits

> What kind of computer are we going to use to simulate physics?
>
> - R. Feynman - 1981

The search for systems with properties that support quantum information processing, summarised by DiVincenzo [1], is a global research effort [298]. Quantum networks are expected to hold importance in linking early quantum devices to leverage the advantages of diverse quantum hardware [279], and promise secure communication, distributed quantum computing and enhanced sensing. 'Flying' photonic qubits provide a route towards a quantum internet [7], for which collective qubits are naturally suited [64]. Collective enhancement of light-matter coupling $\propto \sqrt{N}$ confers a natural interface between a dense atomic ensemble and a photonic qubit [201]. Light storage in atomic ensembles might also underpin quantum repeaters [299]. Directional emission [199] from atomic ensembles can facilitate coupling to optical fibers for routing. Strong dipole-dipole interactions can provide coupling between ensemble qubits for the implementation of quantum logic gates [35, 179, 281, 300, 301] and interfacing [202] within computational nodes.

Collective qubits might also be applied in modern Noisy Intermediate-Scale Quantum Computers (NISQCs). Most prospective NISQCs [88] based on neutral atoms implement registers of neutral atom arrays held in far off-resonant optical dipole traps generated by Fourier imaging [120, 121]. The first demonstrations of quantum supremacy across narrow problem sets are emerging [96, 99, 144, 302]. Single atom trapping schemes rely on stochastic loading of FORT arrays , typically with a 50% stochastic load probability. Loaded traps are then rearranged to create deterministic dense arrays [303, 304]. Recent advances in the preparation of atomic ensembles and ensemble arrays [62] using acousto-optic deflectors or spatial light modulators have enabled the preparation of hundreds of individually addressable atomic ensembles. The $|\mathcal{W}\rangle$ state encoding of quantum information in collective qubits causes them to be robust against atom loss [241, 305], and information loss can be remedied by error correction [306]. These collective Rydberg qubits represent a novel and interesting qubit implementation for quantum networking and computation.

This chapter serves as the first demonstration of collectively encoded Rydberg qubits. Fast single-qubit gates are made possible through microwave control fields which couple strongly to the qubit. Gate times for $\pi/2$ rotations are limited by microwave switching to $\sim$ 20 ns. A direct photonic interface is demonstrated in the form of DSP storage/retrieval. Thermal dephasing degrades the coupling of retrieved photons to the optical retrieval mode, and therefore the fidelity of retrieval is $\sim$ 5%. In spite of lack of fidelity, rapid data acquisition and post selection enables the implementation of Ramsey interferometry. Sensing of external AC and DC electrical fields is demonstrated. Qubit decoherence matches a predicted quartic scaling with an applied noise field. Finally, the qubit is shown to be resilient to atom loss due to the nature of the underlying $|\mathcal{W}\rangle$ state.

In summary, Rydberg qubits might serve as an effective quantum interface due to the collective enhancement which provides strong coupling to directional emission in free space [201, 299]. Collective Rydberg qubits are defined as superpositions of two stationary Rydberg polaritons [49] supported by a macroscopic atomic ensemble containing a few thousand atoms

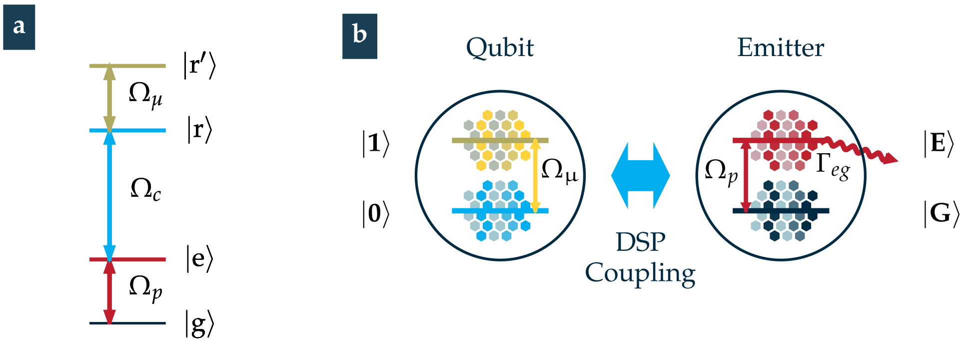

Figure 5.1: **a** Atomic states supporting a collective Rydberg qubit as described in the text. **b** Polariton states $|\mathsf{G}\rangle$ , $|\mathsf{E}\rangle$ provide a two level photonic interface via dark state polariton (DSP) light-matter interface, termed the *emitter*. Qubits are prepared in polariton state $|\mathsf{0}\rangle$ DSP. Qubit rotations are implemented through microwave fields as described in section 4.3. DSP retrieval coherently maps the qubit state on to radiative state $|\mathsf{E}\rangle$. Collective emission into the mode of the incident photon, coupled to the HBT detection circuit occurs at DSP retrieval. Bright state $|e\rangle$ decays at $\Gamma_{eg} = 38.11 \times 10^6 \mathrm{s}^{-1}$, defining the readout rate.

[48, 51, 105].

**This chapter is based upon the following publications:**

- Nicholas L. R. Spong et al. "Collectively Encoded Rydberg Qubit". In: *Physical Review Letters* 127.6 (Aug. 2021), p. 063604. DOI: `10.1103/PhysRevLett.127.063604`
- Yuechun Jiao et al. "Single-photon stored-light Ramsey interferometry using Rydberg polaritons". In: *Optics Letters* 45.20 (Oct. 2020), p. 5888. DOI: `10.1364/OL.405143`

Data presented in this chapter were acquired jointly with Y. Jiao with theoretical modeling and insight from I. Lesanovsky.

## 5.1 Light-Matter Interface

The availability of a fiducial state[1] is a pre-requisite for any qubit candidate. Direct excitation of the collective qubit with high fidelity is challenging for ensemble qubits, due to the cooperative nature of the Rabi frequency [37] which exhibits $\sqrt{N}\Omega$ dependence, where $\Omega$ is the single atom Rabi frequency and $N$ is the number of atoms in the ensemble [35, 307]. If the number of trapped atoms is unknown, population inversion by a single laser pulse is associated with a non-deterministic state preparation.

Adiabatic state transfer schemes have been demonstrated to overcome this limitation and in doing so, provide a direct photonic interface. The DSP technique facilitates coherent transfer of photonic quantum information into the collective Rydberg qubit, leveraging the dependence of the group velocity $\nu_g$ on the strength of a coupling field $\Omega_c^2$ in a three-level system (see Equation 2.2.97). Adiabatic reduction of the photonic group velocity to zero converts an incoming photonic qubit into a stationary collective Rydberg polariton $|R\rangle$. The qubit can also be initiated from a coherent laser input, whereupon a sufficiently strong blockade can enforce single excitation. The DSP technique has been demonstrated in many groups worldwide and forms the basis of several quantum technology proposals from quantum memories [256, 308, 309] and optical information processing [35, 138, 307]. Alternative schemes via STIRAP[2] have also been demonstrated which can provide deterministic loading of Rydberg qubits [307, 310].

---

[1] The DiVincenzo criteria require *The ability to initialize qubits to a simple (fiducial) state, such as* $|000\rangle$ [1].

[2] Stimulated Raman Adiabatic Passage.

### 5.1.1 DSP Storage & Retrieval

For $N$ atoms within a blockade volume [35], the polariton storage technique excites the $N$-atom ground state into the super-atom polariton [3] state [49, 105, 300]

$$|\mathsf{0}_\mathrm{r}\rangle \;=\; \frac{1}{\sqrt{N}}\sum_{j=1}^{N}\mathrm{e}^{\mathrm{i}(\boldsymbol{k}_\mathrm{eff}\cdot\boldsymbol{r}_j-\omega_\mathrm{r}t)}|\mathrm{g}_1\mathrm{g}_2\ldots\mathrm{r}_j\ldots\mathrm{g}_N\rangle\;, \tag{5.1.1}$$

where $\mathrm{g}_j$ and $\mathrm{r}_j$ denote the $j$th atom of the ensemble, with position $\mathbf{R}_j$ in states $|\mathrm{g}\rangle$ and $|\mathrm{r}'\rangle$, respectively. The effective polariton wave vector is denoted $\boldsymbol{k}_\mathrm{eff} = \boldsymbol{k}_\mathrm{p} - \boldsymbol{k}_\mathrm{c}$, and is defined as the difference between the wave vectors of probe and coupling beams due to the counter-propagating geometry. The phase at each atom contains both *local phase* terms $\boldsymbol{k}_\mathrm{eff}\cdot\mathbf{r}_\mathrm{j}$, and a *global phase* factor, $-\omega_\mathrm{r}t$, where $\omega_\mathrm{r}$ is the angular frequency of the two-photon transition $|\mathrm{g}\rangle \leftrightarrow |\mathrm{r}\rangle$. Thus $|\mathsf{0}_\mathrm{r}\rangle$ is a collective symmetric superposition of individually excited atoms interacting with the probe beam. Each term in Equation 5.1.1 contains a single excitation due to the suppression of multiple excitations provided by Rydberg blockade.

The state $|\mathsf{0}_r\rangle$ is coupled to a second polariton state $|\mathsf{1}_{r'}\rangle$

$$|\mathsf{1}_{\mathrm{r}'}\rangle \;=\; \frac{1}{\sqrt{N}}\sum_{j=1}^{N}\mathrm{e}^{\mathrm{i}(\boldsymbol{k}\cdot\boldsymbol{R}_j-\omega_{\mathrm{r}'}t)}|\mathrm{g}_0\mathrm{g}_1\ldots\mathrm{r}'_j\ldots\mathrm{g}_N\rangle\;, \tag{5.1.2}$$

where $\mathrm{r}'_j$ denotes a second Rydberg state $|\mathrm{r}'\rangle$, see Figure 5.1 **a** and **b**. The two states $[|\mathsf{0}\rangle, |\mathsf{1}\rangle]$ form fiducial states of a collective qubit, linked by a transition with frequency $\Delta\mathcal{E}_{rr'}/\hbar = \mathcal{E}_r - \mathcal{E}_{r'} = \omega_{rr'}$ [4]. For work presented in this chapter, states $|r\rangle = |60S_{1/2}\rangle$ and $|r'\rangle = |59P_{3/2}\rangle$ are used as fiducial states[5]. Arbitrary Rydberg states can be used to support the internal qubit states in principle.

---

[3] Also known as a spin-wave [198], or timed Dicke state [197]

[4] For typical dipole matrix elements, see figure 2.2.

[5] The microwave generator limits $\omega_{rr'} < 40$ GHz and therefore $r, r'$ to $n_r > 40$.

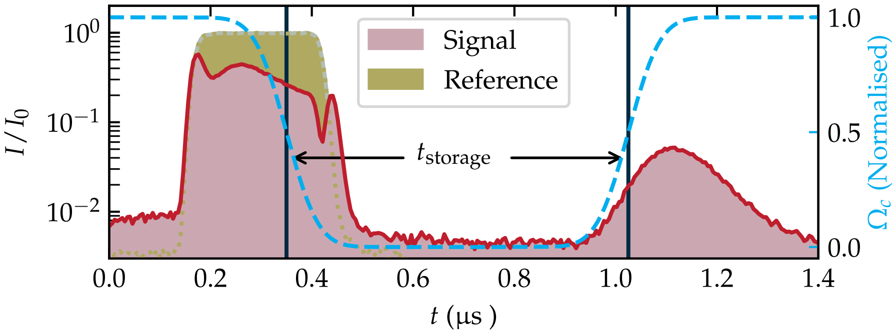

Figure 5.2: Qubit initialisation and readout via the DSP technique. Solid lines are histograms of photon counts registered by the HBT detectors. Reference data show the incoming pulse envelope. Signal data show qubit initialisation through tuning coupling $\Omega_c$ (dashed blue line). Incoming photons are stored in the medium at $t = 0.3\,\mu\text{s}$ by adiabatically reducing $\Omega_c$ to zero coherently mapping an incoming photon onto the Rydberg qubit. Polariton retrieval is achieved by reversing the DSP technique at $t = 1\,\mu\text{s}$. Retrieval of polaritons from the medium gives rise to the characteristic retrieval peak at $t = 1.1\,\mu\text{s}$. Efficiency is limited to $< 10\%$ due to thermal spin wave dephasing.

The experimental geometry used to implement polariton storage and retrieval is identical to that used for the study of modulated flash phenomena, Figure 4.17, **b**. A few thousand atoms are loaded into a FORT with waist $w_d = 5\,\mu\text{m}$. This realises an ensemble with dimensions $\sigma_x = \sigma_y = 1.5\,\mu\text{m}$, $\sigma_z = 20\,\mu\text{m}$ [311]. Ensemble loading is followed by a period of evaporative cooling to further reduce the temperature after optical pre-cooling. Probe light is focused to $w_p = 1.1\,\mu\text{m}$ at the center of the atomic ensemble. The amplitude of the FORT is modulated with a square wave control signal at 200 kHz to avoid excessive AC Stark shifts during interaction and control of the ensemble. This was achieved by rapidly switching the RF power to a dedicated switching AOM, where the first diffracted order provides light for the dipole trap. The duty cycle is adjusted such that the trap confines the atoms for $2.4\,\mu\text{s}$ and releases them for $2.6\,\mu\text{s}$ of this cycle as shown in Figure 4.17.

Figure 5.2 shows the experimental demonstration of invertable adiabatic transfer between photon and the Rydberg polariton qubit via the DSP storage protocol. A probe pulse resonant with the $|5S_{1/2}, F = 2m_f = 2\rangle \leftrightarrow |5P_{3/2}F = 3, m_f = 3\rangle$ is applied to the medium via a fast AOM switch with 80/20 switching time of 40 ns. The probe pulse is derived from a commercial laser system attenuated with neutral density filters and thus enters the medium in a coherent state. The probe beam is initially coupled into the HBT circuit which is used to adjust the intensity of the probe pulse to integrated photon number $\widetilde{n} = 0.5$ per experiment. The temporal envelope of this pulse is shown in figure 5.2. As the probe traverses the medium under EIT conditions, the coupling Rabi frequency $\Omega_c = 2\pi \cdot 30$ MHz is adiabatically tuned to zero. The DSP is fully converted to an atomic spin wave, freezing it inside the medium in state $|\mathsf{0_r}\rangle$ (Equation 5.1.1). Rydberg blockade suppresses multiple excitations of the Rydberg medium, justifying the omission of multiply excited states in the qubit definition, Equation 5.1.1. Where multiple excitations do occur, interaction-induced dephasing makes their retrieval unlikely [129]. Thus, post selecting for experiments where a photon was successfully retrieved, a single stored polariton is realised in state $|\mathsf{0}_r\rangle$.

The excitation remains in the medium for duration $t_{\text{storage}}$ whereupon the storage procedure is reversed via reinstatement of $\Omega_c = 30$ MHz. At this time, the polariton is converted back into an optical photon, and collective emission into the same optical mode as the incoming mode occurs due to coherent, directional emission [199]. The coherent nature of emission from the super-atom causes the mode of the outgoing photon to match that of the original stored photon. This couples the outgoing photon to the HBT detection circuit which registers the photon emission. The polariton retrieval process, governed by the dynamical rising edge of the coupling beam, emits photons within a time window lasting 100 ns.

Implementing qubits via the DSP storage mechanism confers a natural coherent light-matter interface via a strong measurement that takes the form of Equations 2.2.107, 2.2.106. Coupling qubit state $|\mathsf{0}_\mathsf{r}\rangle$ to the emitter via the DSP technique provides measurement of the population $\rho_{\mathsf{00}}$. Population found in $\rho_{11}$ remains dark, as it does not couple to $\Omega_c$ (See figure 5.1).

This fast photonic interface can be used to give access to strong collective Rydberg dynamics with high repetition rates [46, 204]. Ground state hyper fine qubits underpinning modern Rydberg NISQCs suffer from lengthy non-destructive state selective read-out techniques, typically achieved by detecting photons scattered from a cycling transition and requiring tens of microseconds or greater [312], whereas experimental repetition rates via the DSP protocol can be in excess of 100 kHz. The time delay between DSP storage and retrieval constitutes a photonic memory, a critical element of entanglement distribution [87, 211, 313]. Recent demonstrations of multiplexed photonic memories have proven the utility of atomic spin waves as photonic storage states through demonstrations of atom-ensemble entanglement [107, 314].

Comprehensive characterisation of the DSP retrieval interface was carried out by Simon Ball and documentation of the readout scheme can be found in his thesis [205]. This includes novel time-resolved state tomography and single-photon pulse shaping not featured in this work.

### 5.1.2 Spin Wave Dephasing

Thermal motion of the atomic ensemble represents the primary limitation to storage lifetime, limiting the experimental duration to around one microsecond. Sensitive phase information encoded in local phase factors in equation 5.1.1 decohere with thermal motion. After optical molasses, the ensemble temperature is $50\,\mu\mathrm{K}$. At this temperature, residual energy imparts a mean velocity of $\overline{v} = \sqrt{3k_BT/m_{\mathrm{Rb}}}$, where $m_{\mathrm{Rb}}$ is the mass of the rubidium atom, and $k_bB$ is the Boltzmann constant. This formula gives a mean velocity of $\overline{v}\sim 1\,\mathrm{m\,s^{-1}}$, compared to typical spin wavelengths of $\Lambda \approx 0.1\,\mu\mathrm{m}$ for $n > 30$. Atoms lose phase information over a timescale set by $\Lambda/v \sim 1\,\mu\mathrm{s}$, destroying phase information required for collective emission into the optical mode coupled to the HBT detectors.

The efficiency of the storage retrieval process is ∼5% at $n = 60$ [6] for storage times of $1\,\mu\mathrm{s}$. The measured $1/e$ lifetime of this thermal dephasing is $\gamma_{\mathrm{thermal}} = 163 \pm 8$ ns at $n = 80$ [205]. Qubit operations are limited to this duration. Recent proposals to eliminate sensitivity to atomic motion feature Doppler-free photon storage via a four wave mixing process for which the effective wavelength of the spin wave is infinite [104]. Strong coupling to engineered materials composed of atoms confined to the Lamb-Dicke regime might also be resilient to such thermal dephasing [315]. Rydberg lifetimes set an upper limit for $T_1$ type coherence, which for circular states can be more than 1000 s [316]. Storage efficiencies of up to 20% have been re-

---

[6] For details on the thorough experimental characterisation of storage/retrieval efficiencies, see the thesis of Hannes Busche [204, 218]

ported in Rydberg systems with similar principle quantum numbers [133] with higher optical depth (OD=26). The optical depth of our medium, OD=4, is a limiting factor, and the improved dipole/reservoir trap geometry is expected to improve efficiency for future experiments. Reducing ensemble temperature through Raman side-band cooling may also present an avenue for improved efficiency [317].

In principle, photon storage and retrieval is possible with near unity efficiency if thermal dephasing is controlled or absent. This is often achieved through use of lambda EIT between hyperfine levels of atomic ensembles, where the effective spin wave vector leads to lower spatial phase periodicity and thus rendering it less sensitive to motional dephasing. Optimised storage in thermal cells has been demonstrated with near unity efficiency [52]. Schemes to excite uniform spin waves promise to severely dampen sensitivity to thermal dephasing [104].

### 5.1.3 Interaction Induced Dephasing

Local phase factors are also sensitive to other dephasing mechanisms. When multiple Rydberg excitations are stored in the ensemble, their interactions are long range and inhomogenous due to the form of the dipole interaction (Equation 2.1.30). The Rydberg blockade radius is of order 10 µm for $n$ used in this work. The ensemble can not be fully blockaded by this strength of interaction due to an extended geometry which stems from the FORT optical design. This work employed an elongated trapping geometry with $\sigma_z = 20$ µm. Where multiple excitations are stored, interaction induced phase shifts [45, 51, 129, 198] are amplified due to the extended interaction time during photon storage [318], which introduces an additional pairwise interaction phase $\delta\phi_{j,k} = V(\mathbf{r}_j, \mathbf{r}_k)t_{\text{storage}}$ upon atom $k$ due to a Rydberg excitation at atom $j$ [105]. Local phase factors accrued by elements of the spin wave superposition (Equation 5.1.1) add to the effects of motional dephasing and further decouple the spin wave from the detected optical mode. This was demonstrated in chapter 4 through suppression of $g^{(2)}(0)$[7].

### 5.1.4 Rydberg Qubit Control

Interaction induced and thermal dephasing mechanisms currently prohibit access to $T_1$ coherence times on the order of the Rydberg lifetime. However, the collective Rydberg qubit is still a useful device. Fast resonant microwave operations are possible on nanosecond timescales due to exaggerated dipole matrix elements associated with Rydberg atoms. We find 1 µs more than sufficient to perform useful single-qubit gates.

Coherent interaction with the qubit is facilitated by two in-vacuo microwave antennae. These antennae are of quarter-wave type and designed for emission at 18.5 GHz. Each antenna can be independently controlled via a microwave feed-through. The feed-throughs support frequencies of DC - 40 GHz, and this limits our qubits to principle quantum numbers above $n = 46$, where the transition frequency $\Omega_\mu$ for transition between $|nS_{1/2}\rangle \leftrightarrow |nS_{3/2}\rangle$ are below this 40 GHz cutoff. Rabi frequencies greater than 100 MHz are attainable as demonstrated in chapter 4 due to the large Rydberg dipole moment >1000 Debye. Thus we are able to perform many single qubit rotations within the $\sim 1\,\mu s$ experimental timescale.

To perform single qubit gate operations, qubit states $|0_r\rangle$and $|1_{r'}\rangle$are coupled by a microwave field with angular frequency $\omega_\mu$, detuning $\Delta_\mu = \omega_\mu - (\omega_{r'} - \omega_r)$ and an amplitude characterised by a Rabi frequency $\Omega_\mu$ applied to the $|r\rangle \leftrightarrow |r'\rangle$ transition, as depicted in figure 5.1. After qubit initialisation $\Omega_c = 0$ and therefore the Rydberg qubit is decoupled from the radiative state $|e\rangle$. The decay pathways from the Rydberg manifold supporting the qubit $(|r\rangle, |r'\rangle)$ due to radiative lifetimes ($\tau_r = 252\mu s$,

---

[7] To note, whilst uncontrolled local phase factors are destructive, careful control over local phase has been leveraged for precise beam steering of the directional emission, realised through careful application of AC stark shifts [319].

$\tau_{r'} \approx 422\mu s$ [320]) are greater than $t_{\exp}$. During $t_{\exp}$ ~1 µs, blockaded states $|0_r\rangle$, $|1_{r'}\rangle$ can be treated as an effective two level system. Effective isolation of the qubit Hamiltonian subspace on the experimental timescale leads to the definition of the 'qubit', consisting of collective states of the blockaded super-atom $|0_r\rangle$, $|1_{r'}\rangle$ and the 'emitter', consisting of states $|G\rangle$, $|E\rangle$. Transfer between these two sub-spaces only occurs during the DSP protocol. During ($t_{\exp}$), there is no coupling between the sub-spaces.

An applied microwave field $\Omega_\mu$ implements single-qubit gates during DSP storage, performing qubit rotations. State tomography is performed by reversing the polariton storage technique. State $|1\rangle$ is not resonant with the DSP retrieval beam $\Omega_c$. Therefore, at the point of retrieval, population in $\rho_{rr}$ is adiabatically converted into an optical photon and counted by the HBT detection circuit. Population in $\rho_{r'r'}$ remains in the Rydberg manifold The number of counts $I_{\mathrm{HBT}}$ retrieved when implementing the polariton retrieval sequence is proportional to the population of $|0_r\rangle$. This figure is then normalised to the maximum retrieval $I_{\mathrm{HBT}^{(max)}}$ from the ensemble during qubit rotation.

At the end of an experimental sequence, any population remaining in $|1_{r'}\rangle$ experiences Rydberg anti-trapping in the field of the FORT. This rapidly degrades the optical depth of the ensemble. Rydberg excitations remaining in $|1_{r'}\rangle$ feel a ponderomotive force from the dipole trap. In the presence of the rapidly varying trapping field $\mathbf{E} = E_0 \cos \Omega_{\mathrm{trap}} t$, the charged electron of a Rydberg excitation is driven by the field, creating an extra kinetic energy term

$$\langle \mathrm{KE} \rangle = \frac{\omega_{\mathrm{trap}}}{2\pi} \frac{e^2 E_0^2}{2m_e \omega_{\mathrm{trap}}^2} \int_0^{2\pi/\omega_{\mathrm{trap}}} \sin^2 \omega_{\mathrm{trap}} t dt, \tag{5.1.3}$$

where $e, m_e$ are the charge and mass of the electron. This gives a ponderomotive energy of

$$U_p = \frac{e^2 E_0^2}{4m_e \omega_{\mathrm{trap}}^2}. \tag{5.1.4}$$

In the case where $E_0$ has some spatial dependence ($E_0 \to E_0(\mathbf{r})$), the electron experiences a force $\mathbf{F} = -\nabla U_p$, repelling the excited atom from the trap [321, 322]. This quickly degrades the optical depth of the ensemble.

The necessity of implementing a ‘cleaning pulse’ for the preservation of optical depth to overcome this issue was realised and highlighted by Simon Ball [205]. Driving the qubit with a microwave pulse after photon retrieval (whence $\Omega_c$ has been reinstated) couples population remaining in $|\mathsf{1}_{\mathsf{r}'}\rangle$ to the radiative state of the emitter $|\mathsf{E}\rangle$ via the two-photon transition $|\mathsf{1}_{\mathsf{r}'}\rangle \rightarrow |\mathsf{0}_{\mathsf{r}}\rangle \rightarrow |\mathsf{E}\rangle$. This provides a decay mechanism for the anti-trapped Rydberg population. Fast decay from $|\mathsf{E}\rangle$ returns the ensemble to ground state $|\mathsf{G}\rangle$ at the end of the experimental sequence. This extends the lifetime of the ensemble. Excited atoms that are not ejected from the dipole trap can also cause interaction-induced dephasing of subsequently initialised qubits. For a thorough treatment of the effect of Rydberg pollution’ [85, 297] as it affects this experiment, the reader is referred to the thesis of Simon Ball [205].

## 5.2 Polariton Interferometry

In this section, coherent control of the Rydberg qubit is demonstrated through the realisation of polariton interferometry. The huge dipole moment of Rydberg atoms confers a high degree of sensitivity to external fields and interaction potentials. Rydberg interferometry has many specific applications, from measuring Förster defects [323] to probing many-body dynamics [324–326]. In this section, we achieve coherent control over the Rydberg qubit through demonstrations of Rydberg polariton interferometry.

Figure 5.3 compares a polariton interferometer to a conventional optical interferometer. **a** shows a conventional Mach-Zehnder, which operates on the principle of optical interference based on an optical path length difference [327]. Photons are incident on a beam-splitter, which splits the photons into two separate paths. Light interferes at the output port of a second, output beam-splitter. Difference in the optical path lengths $\Delta_l = l_1 - l_2$

of the two arms of the interferometer causes a relative phase difference $\phi_{\Delta_l} = 2\pi\Delta_l/\lambda$, where $\lambda$ is the wavelength of the light in the interferometer. The relative phase difference is detected when the light from both paths interferes at the second beam-splitter. This interference can be constructive or destructive depending on the relative phase of the light from each arm at the point of interference. Precise measurements of variations in spatial path length between the two arms can be obtained due to the definition of $\phi_{\Delta_l}$, where a $\pi$ phase difference is measured for $\Delta_l = \lambda/2$, typically hundreds of nanometers for optical interferometers. This causes a full contrast shift in interferometer output intensity and can thus be used to accurately measure optical path length differences of order $\lambda$.

Figure 5.3 **b** shows a conceptual Ramsey interferometer based on interference between Rydberg polaritons. A quantum state is driven into an equal superposition of states differing in energy by $\Delta E$. Unitary evolution of these states causes a time-dependent phase to accumulate $\phi_{\Delta_t} = e^{i\Delta E t}$. Thus superposition time $t_{int}$ takes the place of length in the conventional interferometer. Figure 5.4 **a-e** shows the evolution of the Bloch vector of an interferometer during measurement, in a frame rotating at the angular frequency of the energy splitting. In this figure, the qubit is initially in state $|\mathsf{0}_\mathsf{r}\rangle$ (**a**). A microwave $\pi/2$ pulse about $x$ drives the polariton into an equal superposition of $|\mathsf{0}_\mathsf{r}\rangle$ and $|\mathsf{1}_{\mathsf{r}'}\rangle$, (**b**). The superposition undergoes unitary evolution. Relative phase differences between the qubit superposition and the resonant microwave field can accumulate during the period of unitary evolution $t_{\mathrm{int}}$. The figure shows evolution of the Bloch vector as it accumulates a relative difference of $\pi/2$ radians, causing the Bloch vector to point along $-x$[8]. A second microwave pulse, phase-coherent with the first pulse and rotating in resonance with the frequency of the qubit transition drives a second $\pi/2$ pulse (**d**), again rotating the qubit about $x$. The

---

[8] In general, a phase $\phi$ is acquired, rotating the Bloch vector within the Equatorial plane

qubit phase then determines the action of the final $\pi/2$ pulse. This process is commonly known as Ramsey interferometry [328, 329], and can demonstrate extreme sensitivity to perturbations of the energy levels of internal states in quantum superposition. As the superposition time occurs during the atomic polariton stage, this also gives the outgoing photon matter-like sensitivity to gravity and other inertial effects [330].

Leveraging the DSP storage protocol creates a photonic interferometer free from limitations of physical size. The maximal 450ns superposition time reported here is equivalent to a 135 m free-space interferometer path length, whilst the atomic ensemble measures just 40 µm in length. The limit to the superposition time is set by thermal dephasing, or by the maximum achievable group index [331] where this is absent. Hybrid atom-light interferometers based on atomic spin waves have previously been demonstrated [332, 333] and optical control of cavity polariton interference also exists in the literature [108]. Rydberg polaritons are particularly useful due to the sensitivity to external fields through exaggerated polarisability. Electric field detection has previously been demonstrated using individual Rydberg atoms [334], and atomic beams [335]. A similar interferometer based on collective hyperfine states of Potassium dressed with Rydberg interactions showed sensitivity to electric fields through dephasing, with a resolution of 17(1) mV/cm [63].

### 5.2.1 Experimental Implementation

The experimental pulse sequence used to perform polariton interferometry is shown in Figure 5.5. Applying these pulses realised polariton interferometry as shown in Figure 5.6. After loading the dipole trap, a storage/retrieval sequence is effected via adiabatic ramping of $\Omega_c$. The mean photon number in the incoming probe pulse is $\widetilde{n} = 1.3$. In the absence of microwaves, this stores an incoming photon in the medium in state $|0_r\rangle$. The photon is retrieved after a storage time of $t_{\text{storage}} \sim 0.5\,\mu\text{s}$. Whilst the photon is

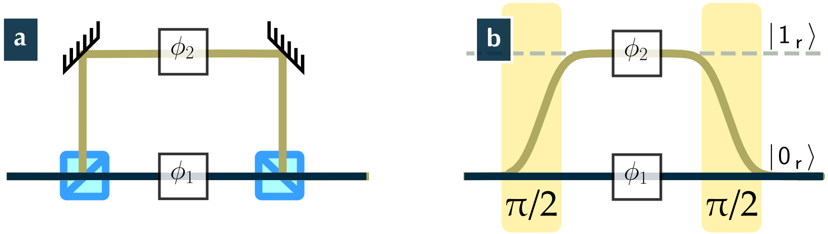

Figure 5.3: Conventional Vs. Polariton Interferometry **a.** In an optical interferometer, a relative phase difference $\Delta\phi$ occurs in light traveling via two unequal paths. Light from each path thus interferes when recombined. **b.** For polariton interferometry, a single polariton initially in state $|0_r\rangle$ is split into an equal superposition of polaritons in states $|0_r\rangle$ and $|1_{r'}\rangle$ by applying a $\pi/2$ pulse. Unequal unitary evolution leads to a relative phase difference $\Delta\phi$. Quantum interference is observed upon recombination via a second $\pi/2$ pulse.

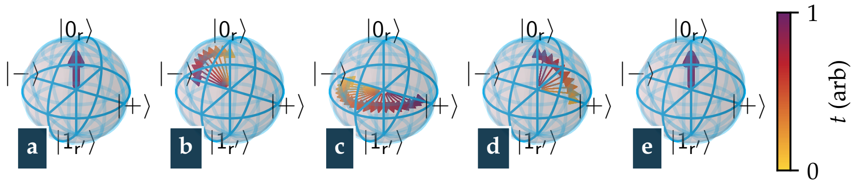

Figure 5.4: Bloch spheres showing qubit states during interferometry. **a** The interferometer is initialised in state $|0_r\rangle$. **b**. A microwave field implements a $\pi/2$ pulse. The Bloch vector is rotated to the equator, a superposition of $|0_r\rangle$, $|1_{r'}\rangle$. **c**. The relative phase of two interferometric states is sensitive to perturbations of relative energies. A shift in the energy level of either state causes an accumulation of relative phase. **d**. A microwave field drives a second $\pi/2$ pulse. **e**. The state of the qubit is read by measuring the population in $|0_r\rangle$, $|1_{r'}\rangle$via polariton retrieval.

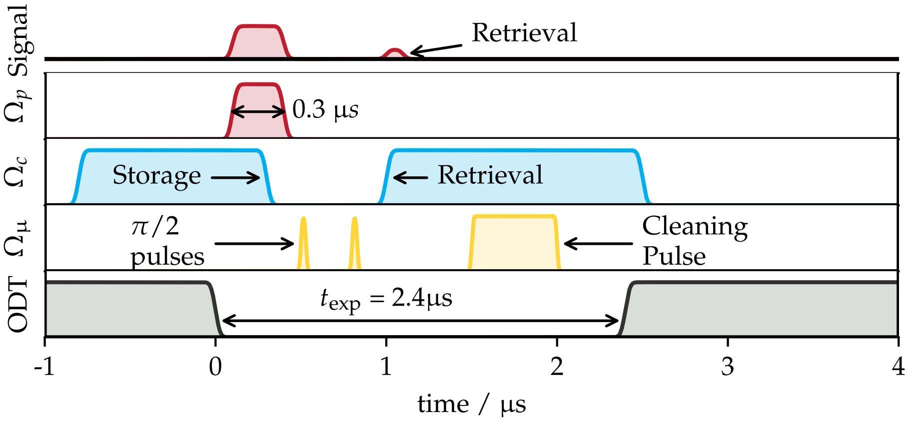

Figure 5.5: Interferometry pulse timing diagram. The DSP protocol is used to store a probe pulse lasting $t_p$ =0.3 μs. The falling edge of $\Omega_c$ bisects the probe pulse. During storage, $\Omega_\mu$ drives microwave $\pi/2$ pulses lasting 25 ns to drive the Ramsey interferometry sequence conceptualised in figure 5.4 and shown experimentally in Figure 5.6. The time between Ramsey pulses is variable such that the period of free evolution can be measured $t_{\mathrm{int}}$ <0.45 μs. After retrieval, a microwave cleaning pulse lasting 0.5 μs depumps any population left in $|1_{r'}\rangle$ at the end of the experimental sequence.

stored in the medium, two 25 ns microwave pulses address the $|0_r\rangle \leftrightarrow |1_r'\rangle$ transition and each effect $\pi/2$ rotations. The first pulse places the system into an equal superposition of the two polariton states $|0_r\rangle$, $|1_{r'}\rangle$. After a period of free evolution lasting $<\sim$ 450 ns, the second resonant $\pi/2$ pulse is applied, and the resultant population in $|0_r\rangle$ is read out via the DSP retrieval protocol. This defines the basic Ramsey interferometry sequence, built upon later in this chapter. No perturbation is applied. Oscillation in populations of $|0_r\rangle$, $|1_{r'}\rangle$ are entirely due to the relative phase accumulated between the resonant microwave source and atomic system due to unitary time evolution.

Figure 5.7 shows the use of the interferometer to locate the resonance of the $|1_{r'}\rangle$, $|0_r\rangle$transition through varying the length of the interferometer $t_{\mathrm{int}}$. Figure 5.7 **a** shows the number of photons retrieved from the

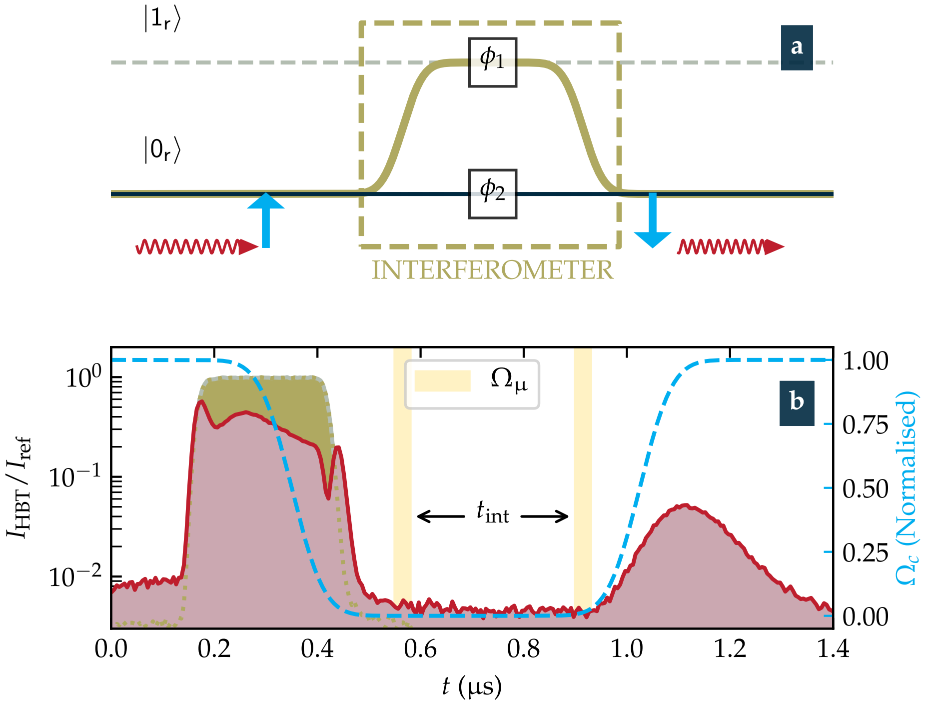

Figure 5.6: A probe photon (red arrows in **a**) is stored as a DSP by ramping coupling $\Omega_c$ to zero as shown in **b** (blue arrows in **a**). This stores the photon as a collective polariton excitation of the ensemble in state $|0_r\rangle$. Interferometry is effected with the addition of two microwave $\pi/2$ pulses during storage, separated by $t_{\rm int}$ as shown in **b**. When the first microwave $\pi/2$ pulse is applied, the polariton is placed in a superposition of $|0_r\rangle$and $|1_{r'}\rangle$as shown in **a**. Between pulses, differential phase evolution $\Delta\phi = |\phi_1 - \phi_2|$ can occur due to microwave detuning or perturbation of either qubit state energy levels. The second $\pi/2$ pulse implements interferometry, and the final state of the qubit is dependent upon this differential phase, which is driven to $|1_{r'}\rangle$ if $\Delta\phi = 0$ , or to $|0_r\rangle$ if $\Delta\phi = \pi$. The final state of the qubit detemines the magnitude of the retrieval from the medium at $t = 1$ μs, since $|1_{r'}\rangle$ is not resonant with the coupling beam.

medium upon implementing the DSP retrieval protocol as a function of the interferometer length $t_{\mathrm{int}}$. Contours show the positions of the expected maxima, which is determined by the predicted phase offset between the microwave source and interferometer $\Delta\phi = \Delta_{\mu} t_{\mathrm{int}}$ which fit experimental data well. Two data sets highlighted with arrows are shown in Figure 5.7 **b**. The data correspond to interferometric pulse sequences taken with resonant microwave pulses (purple data) and off-resonant microwave pulses ($\Delta_{\mu} = 2\pi \cdot 9$ MHz, red data). When the microwaves are resonant, there is zero differential phase evolution between states $|1_{r'}\rangle$, $|0_{r}\rangle$. The combination of two $\pi/2$ pulses driving a $\pi$ pulse on resonance is observed, and retrieval minima are indistinguishable from the noise floor. When the microwaves are set to $|\Delta_{\mu}| > 0$, characteristic oscillation of the retrieved fraction is observed, presenting a measurement of the relative phase of the qubit and the microwave field. When the phase difference is $\Delta\phi(t) \bmod 2\pi = 0$, a $\pi$ pulse is effected and no photons are retrieved from the medium. However, when $\Delta\phi(t) \bmod 2\pi = \pi$, two $\pi/2$ pulses perform zero net rotation, and a maxima of photon counts is observed upon DSP retrieval.

The relationship between microwave detuning and fringe frequency was used to locate the qubit resonance $|60S_{1/2}\rangle \leftrightarrow |59P_{3/2}\rangle$ as shown in Figure 5.7 **c**. The fringe frequencies were fit using sinusoidal fit functions as $t_{\mathrm{int}}$ was varied. This process was repeated at detunings spanning $\Delta_{\mu}/2\pi = [-12, 15]$ MHz[9]. Extracted frequencies are plotted on Figure 5.7 **c**. The fit shows that the data are highly linear, with a gradient $1.00 \pm 0.03$. Due to the maximum interferometry length of 400 ns, a full interference period is observed for detunings above 2.5 MHz. Fit values below this detuning diverge from the linear trend.

After calibrating the microwave source to the resonance of the qubit transition, the unperturbed resonant interferometric pulse sequence is implemented. Two microwave pulses separated by a time $t_{\mathrm{int}} = 0.25\,\mu\mathrm{s}$ per-

---

[9] Due to lacking ab-initio knowledge of the exact position of the resonance

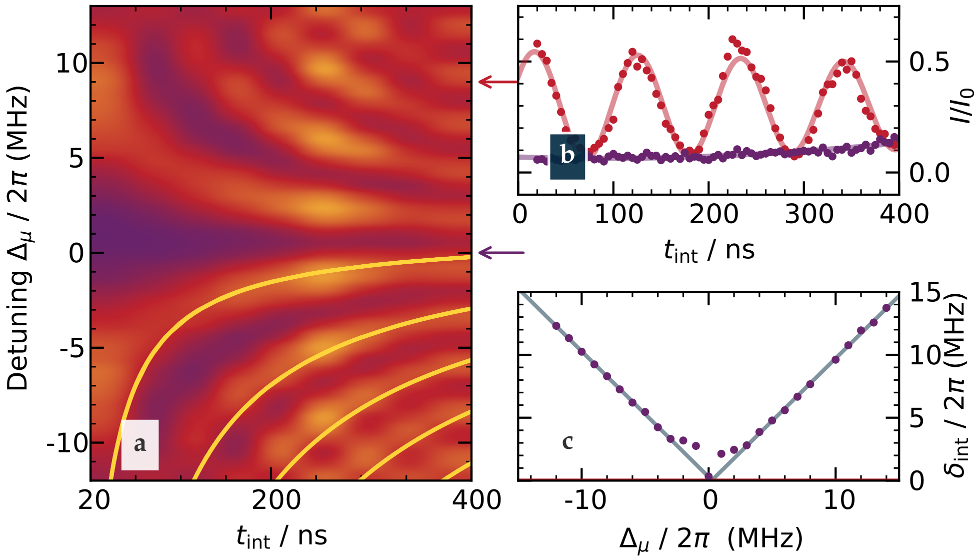

Figure 5.7: The unperturbed interferometer. Two $\pi/2$ pulses with detuning $\Delta_{\mathrm{\mu}}$ and separation $t_{\mathrm{int}}$ drive a Ramsey sequence. **a**: Varying $\Delta_{\mathrm{\mu}}$ or $t_{\mathrm{int}}$ reveals interferometric fringes. Two data sets ($\Delta_{\mathrm{\mu}} = 0\,\mathrm{MHz}, 9\,\mathrm{MHz}$) are highlighted by arrows. Some maxima of the surface $\cos(2\pi\Delta_{\mathrm{\mu}}t_{\mathrm{int}} + 0.1)$ are overlaid in yellow. **b**: Varying interferometer length $t_{\mathrm{int}}$. On resonance (purple), two $\pi/2$ pulses transfer population to $|1_{\mathrm{r}'}\rangle$, minimising retrieval for all $t_{\mathrm{int}}$. For $|\Delta_{\mathrm{\mu}}| = 9$ MHz (red), the retrieved photon number exhibits sinusoidal variation as a function of time. Sinusoidal fits are shown as solid lines. **c**: Microwave detuning $\Delta_{\mathrm{\mu}}$ causes modulation of photon retrieval as a function of interometer length, with frequency $\delta_{\mathrm{int}}$, equal to $\Delta_{\mathrm{\mu}}$. Thus the linear fit has gradient $1.00 \pm 0.03$. The resonant frequency was located at $18.517 \pm 0.001$ GHz. Low frequency fits are unreliable, due to the slowly varying nature of the experimental data (see **b**).

form single-qubit rotations in the $|0_\mathrm{r}\rangle$ and $|1_{\mathrm{r}'}\rangle$ basis. The microwave detuning is varied over the range $-50, 50$ MHz and photons are counted upon DSP retrieval. The retrieved photon counts $I$, normalised to the maximum retrieved counts $I_\mathrm{max}$, as a function of the microwave detuning, $\Delta_\mu$, for two values of the microwave pulse duration, $t_\mu$, are shown in Figure. 5.8**a** and **b**. In Fig. 5.8**a** the power, $P$, and duration, $t_\mu$, of each microwave pulse are chosen to give $\Omega_\mu t_\mu = \pi/2$. In this case the sequence of two $\pi/2$ rotations about the $x$ axis in the Bloch sphere, see Fig. 5.8**c**, separated by a rotation about $z$ (free evolution) results in familiar Ramsey fringes. In Fig. 5.8**b** the duration of the pulses is increased to give $\Omega_\mu t_\mu \sim \sqrt{2}\pi/2$. For the special case, $\Delta_\mu = \Omega_\mu$, this pulse performs a Hadamard operation ($\pi$ rotation about a Bloch vector 45° from the $z$ axis), see Fig. 5.8**d**. Consequently, the maximum fringe visibility in Fig. 5.8**c** is observed at $|\Delta_\mu| = \Omega_\mu = 2\pi(12\ \mathrm{MHz})$. Scanning the frequency of the microwave coupling field $\Omega_\mu$ across the microwave resonance breaks the simplifying assumption of a resonant coupling field in the RWA, and introduces the detuning terms into Hamiltonian 5.2.5.

$$\mathcal{H}_\mathrm{if} = \frac{1}{2}\begin{bmatrix} \Delta_\mu & \Omega_\mu(t) \\ \Omega^*_\mu(t) & -\Delta_\mu \end{bmatrix}, \tag{5.2.5}$$

where $\Delta_\mu$ defines the detuning of the microwave field, and $\Omega_\mu(t)$ defines the Rabi frequency of the microwave field The zero of energy has been defined as $\hbar(\omega_r + \omega_{r'})/2$. Thus, with $t_\mathrm{int}$ fixed, progressive detuning causes the formation of Ramsey interference fringes in the broad microwave resonance. The data are compared to the theoretical response of the interferometer through simulation of the optical Bloch equations developed in chapter 2. $\mathcal{H}_\mathrm{if}$ is used to model the output of the interferometer via numerical integration of the Lindblad Equation (2.2.61) using Qutip [120]. The amplitude of $\Omega_\mu(t)$ is set to drive two $\pi/2$ pulses with separation $t_\mathrm{int}$ as shown in Figure 5.5. using the Optical Bloch Equations for a two-level system developed in Chapter 2. Pulse timings are detailed in Figure 5.5. Only the

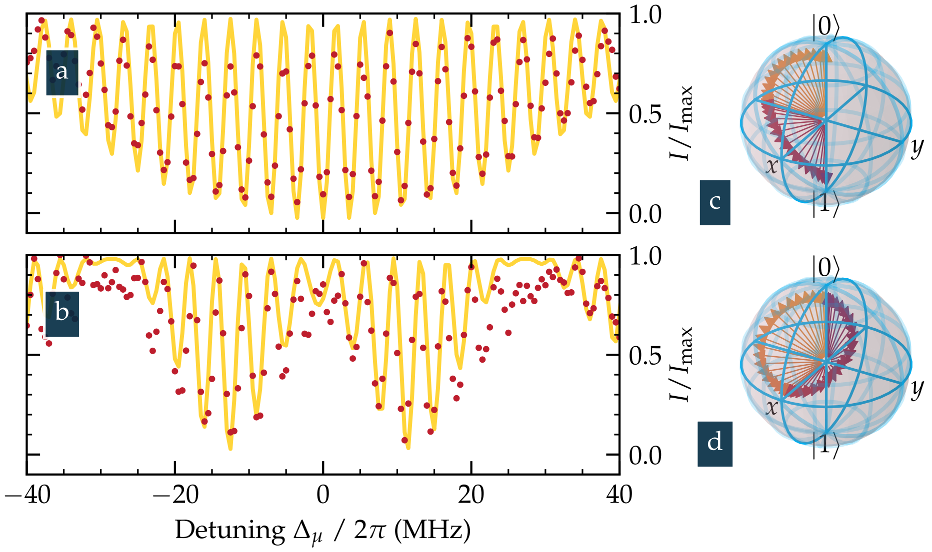

Figure 5.8: Ramsey Interference Fringes. $\Omega_\mu$ pulses separated by $t_{\text{int}} = 250\,\text{ns}$ defining the Ramsey sequence. Scanning the microwave detuning produces familiar Ramsey fringes. **a**: Normalised photon counts $I/I_{\max}$ (red circles) as a function of the $\pi/2$ pulse detuning, $\Delta_\mu$, for the case of $\Omega_\mu t_\mu = \pi/2$ at $\Delta_\mu = 0$. **c**: The same as **b** except that $\Omega_\mu t_\mu = \sqrt{2}\pi/2$, such that at $|\Delta_\mu| = \Omega_\mu = 2\pi(12\,\text{MHz})$, we obtain a Hadamard gate. **c** The evolution on the Bloch sphere for a resonant Ramsey interferometry, and **d** double Hadamard operations. Monte Carlo simulations of both data are overlaid (yellow line), described in the text. The population left in $|0_r\rangle$is measured via DSP retrieval.

Ramsey sequence is simulated and it is assumed that all excitations left in $|0_r\rangle$will be retrieved. Cleaning pulses and the DSP protocol are omitted from the simulation. For simulation, $\Omega_\mu^{\max} = 2\pi \cdot 10$ MHz during $\pi/2$ pulses, realising the observed $\pi/2$ duration of 25 ns. Realistic $|\Omega_\mu(t)|$ pulse envelopes were used for the simulation[10]. Atomic dephasing is negligible on our timescale and so are omitted from the simulation. Thermal dephasing is offset through post-selection and normalisation.

---

[10] Based on error functions, with switching speed matching the 10 ns specification of the microwave source.

### 5.2.2 DC Sensitivity

The use of Rydberg atoms in modern quantum information science has inspired interest in the interaction between electric fields (AC/DC) and cold Rydberg atoms [63, 334]. Sensitive Ramsey sequences developed in section 5.2 are ideal for measuring the effect of electric fields on Rydberg polaritons, turning them into a viable, non-invasive electric field sensor. Figure 5.9 shows a master equation simulation of resonant interferometry using the two level system defined in Equation 5.2.5. Two $\pi/2$ pulses where $\Omega_\mathrm{\mu} \neq 0$ are shown as yellow shaded regions. After the initial $\pi/2$ rotation, the system is in a superposition $|\phi\rangle = \frac{1}{\sqrt{2}}(|1_{\mathrm{r}'}\rangle + |0_\mathrm{r}\rangle)$. In the interaction picture with a resonant microwave field, there is no phase evolution. Figure 5.9**a** shows this resonant case, where two resonant $\pi/2$ pulses drive a $\pi$ pulse.

Rydberg atoms are highly polarisable, interacting with electric fields via the electric dipole moment.

$$\mathcal{H} = \mathcal{H}_\mathrm{int} + \vec{\mathbf{d}} \cdot \mathcal{E}\hat{z}, \tag{5.2.6}$$

$\mathcal{E}$ denotes the electromagnetic field magnitude, and $\hat{z}$ a unit vector in the $z$ direction. Application of this Hamiltonian results in a Stark shift $\Delta E = -\frac{1}{2}\alpha_0\mathcal{E}^2$, defined through the static polarisability $\alpha_0$. The interferometer shift is then the differential DC Stark shift of the upper and lower states of the interferometric transition.

$$\Delta(E_\mathrm{r} - E_{\mathrm{r}'}) = \frac{1}{2}\left[\alpha_{0,\mathrm{r}} - \alpha_{0,\mathrm{r}'}\right]\mathcal{E}^2, \tag{5.2.7}$$

observed through a shift of interferometric fringes. Sensitivity to the quadratic Stark shift of a nondegenerate level scales as $n^7$ through the fundamental scaling of electric dipole moment $\propto n^{2}$[11] and state energy difference, $\propto n^3$, listed in table 2.2, giving a dynamic range of three orders of magnitude for states accessible in this system.

---

[11] (squared).

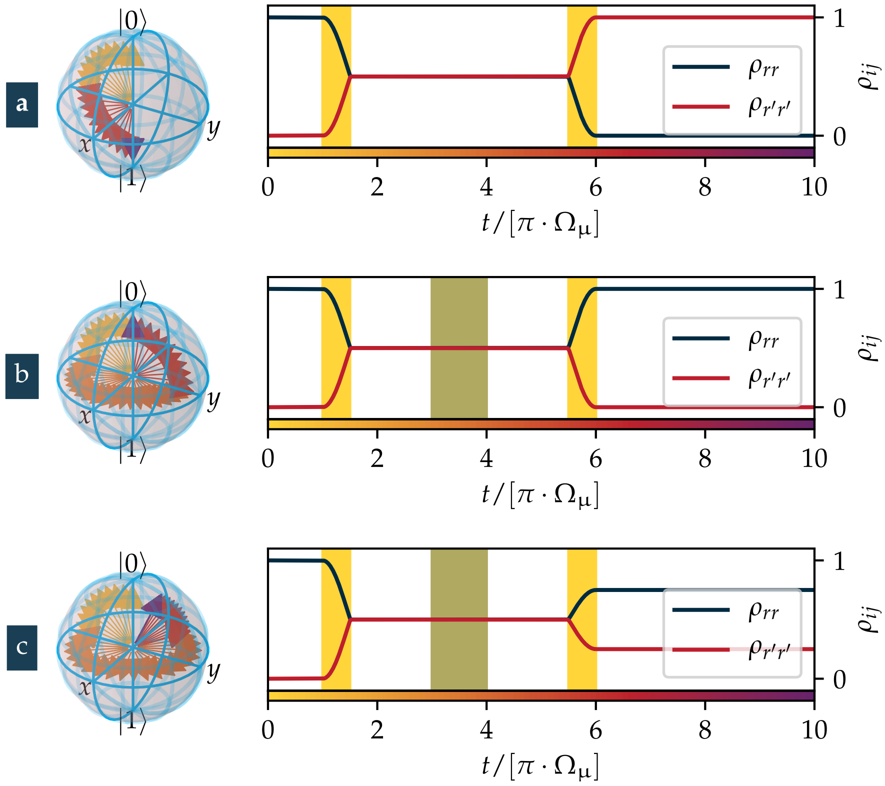

Figure 5.9: Master Equation Simulation of the perturbed interferometer. Bloch equation simulations demonstrate the principle behind the interferometer. The time evolution of populations $\rho_{rr}, \rho_{r'r'}$ are shown in the Bloch sphere (left) plotted (right). Bloch vectors are colour coded to show their timing, which can be compared to the colour bar shown beneath plots. In **a**, the interferometer is driven by two $\pi/2$ pulses about $x$ (Yellow shading) separated by time $t$. The qubit is transferred from state $|0\rangle$ to $|1\rangle$ in the absence of perturbations. In **b**, a perturbation causes detuning, and differential evolution changes the relative phase of states $|0_\mathrm{r}\rangle$, $|1_{\mathrm{r}'}\rangle$by $\pi$. The second rotation of $\pi/2$ about $x$, drives population back to $|0_\mathrm{r}\rangle$. In **c**, the perturbation is larger than in **b** and not a multiple of $\pi$. The second $\pi/2$ pulse leaves the interferometer in a superposition of $|0_\mathrm{r}\rangle$and $|1_{\mathrm{r}'}\rangle$.

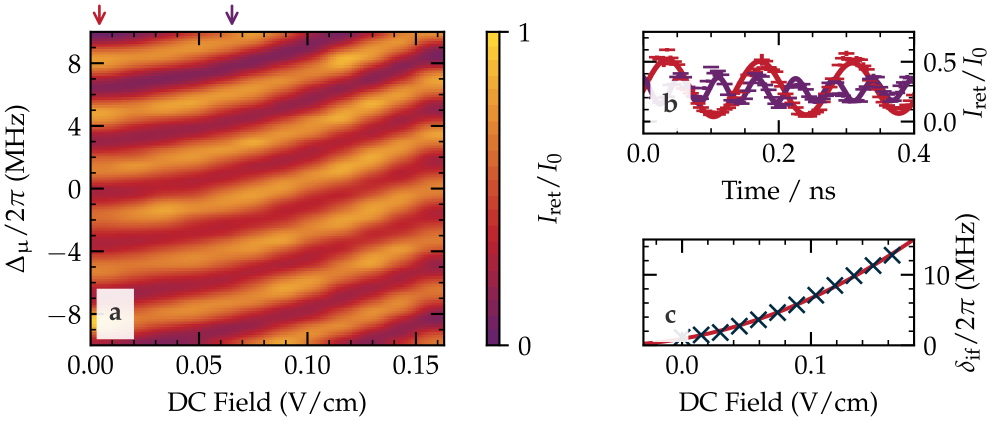

Figure 5.10: Sensing DC Electric fields with a contact-less polariton interferometer. **a** a quadratic differential Stark shift of Ramsey fringes close to the zero field microwave resonance under the influence of an applied electric field, **b**: Interference fringes obtained by varying $t_{\text{int}}$. $|\mathcal{E}|$ shifts the qubit resonance, increasing fringe frequency from an initial $7.30 \pm 0.07$ MHz in zero field, to $18.94 \pm 0.02$ MHz for the maximum applied DC field. The electric field associated with each dataset is identified by a colour coded arrow above **a**. **c** shows the expected quadratic dependence of frequency shifts $\delta_{\text{if}}$ upon DC field over the range [0, 0.163] V/cm. DC fields are calibrated through the known relative AC Stark shift of $|60S_{1/2}\rangle, |59P_{3/2}\rangle$ [152].

Figure 5.9**b** shows an Optical Bloch Equation simulation of the perturbed interferometer during the period of free evolution through application of a differential energy level shift of $\delta_{\text{if}} = \pi$, which causes phase evolution of $\pi$ radians. In this case, the second microwave pulse at $t = t_{\mu,2}$ returns population into state $|0_r\rangle$.

In this way, $\phi_{\Delta_\omega 1,2}$ at the end of the period of free evolution governs the relative population of $|0\rangle, |1\rangle$. Figure 5.9**c** shows one further example of a level shift, this time $\pi < \delta_{\text{if}} < 2\pi$. The qubit is left in a superposition of states after the second $\pi$ pulse. Perturbations effectively detune the interferometer from resonance, providing a method of measuring the strength of interactions.

Figure 5.10 shows Rydberg qubit sensitivity to electric fields during Ramsey interferometry. The qubit is initialised into $|0_r\rangle$via the DSP storage technique, and a resonant Ramsey pulse sequence was applied. An electric field of between 0 and 0.163 V/cm was applied[12] throughout the experimental sequence, shifting the atomic energy levels of the ensemble through the DC Stark shift. In **a**, a colour map shows a detail of the central (near-resonant) Ramsey fringes under the action of an applied electric field during free evolution. The quadratic level shift of the Ramsey fringes predicted by Equation 2.1.23 is observed.

Figure 5.10, **b** shows retrieval intensity fringes obtained by scanning the interferometer time and thus directly observing the relative phase of the microwave field and the qubit. Data are shown for $|\mathcal{E}| = 0$ V/cm and $|\mathcal{E}| = 0.163$ V/cm, corresponding data are indicated by the red and purple arrows at the top of panel **a**, respectively. In order to enhance sensitivity to electric fields, the interferometer is detuned when the electric field is absent, such that when $\mathcal{E}_0 = 0$, $\Delta_\mu = 7.30 \pm 2\pi \cdot 0.07$ MHz. Application of an electric field can send the interferometer towards or away from resonance, depending on the sign of the interaction. Energy level shifts are calculated by extracting the frequency shifts from this data, referenced to the frequency shift at $\mathcal{E}_0 = 0$. We observe a smooth quadratic relationship between applied electric field and level shift up to a maximum electric field strength of 0.163V/m, where the energy level shift reaches a maximum value of 18.94±0.02 MHz, giving a maximum differential shift of 11.68±0.07 MHz across the [0,0.163] V/cm range. In Figure 5.10 **c**, energy level shifts extracted from interferometric fringes obtained across the range of applied electric fields follows the predicted quadratic scaling law of Equation 2.1.23 with high precision. The data in Figure 5.10 **c** were used in combination with the known polarisability of the underlying $|59P_{3/2}\rangle$ , $|60S_{1/2}\rangle$ states,

---

[12] This range corresponds to voltages of zero to five volts applied to one plane of the in-vacuo electrodes, whilst the other plane is grounded.

$\alpha_0^{(r)}/h = 185$ MHz cm$^2$V$^{-2}$ and $\alpha_0^{(r')}/h = 1138$ MHz cm$^2$V$^{-2}$, giving a differential shift of $\Delta^{rr'}_{\text{Stark}}/h = 953$ MHz cm$^2$V$^{-2}$ [152].

The visibility $\mathbb{V}$ of Ramsey fringes is reduced when strong fields are applied. The visibility for $|\mathcal{E}| = 0$ is $\mathbb{V} = 0.89 \pm 0.02$. When subjected to the maximum applied electric field of 0.163 V/cm, the visibility is reduced to $0.14 \pm 0.03$. In this case, the interferometric superposition is not properly established. Perturbation of underlying atomic energy levels reduces $\Omega_c$ and thus efficiency of storage and retrieval. Finally, the electric field constitutes a form of global phase noise, and amplitude fluctuation thus enacts a $T_2$ type decoherence which acts across experimental runs. These effects act to reduce the visibility of interference fringes, however due to the wide range of sensitivities available to the experimental physicist, it is possible to pick a Rydberg state which has an appropriate sensitivity for the fields under measurement. In these experiments, we do not approach the regime of strong state mixing due to the Stark effect.

### 5.2.3 AC Sensitivity

Collective Rydberg Qubits are naturally sensitive to AC Stark shifts due to the underlying large dipole moments $\mu_{rr'}$ through the AC Stark effect. This strong interaction can be leveraged for wideband AC sensing [336], successfully implemented in thermal vapor cells [337] with sensitivities of less than $\sim 3[\mu\text{V/cm}]/\sqrt{\text{Hz}}$ [338].

In order to study the effects of the AC Stark shift, a polariton interferometer based on the states $|\text{r}\rangle = 60S_{1/2}$ and $|\text{r}'\rangle = 59P_{3/2}$ are implemented. A second microwave field $\Omega_{\mu_2}$ is introduced, coupling state $|59P_{3/2}\rangle$ to state $|59S_{1/2}\rangle$ with detuning $\Delta_{\mu 2} = 0$. When $\Omega_{\mu_2}$ is on resonance ($\Delta_{\mu 2} = 0$) is found at $18.512 \pm 0.001$ GHz. The dipole moment of the transition is 4107 D [152]. $\Omega_{\mu_2}$ is applied in between interferometric $\pi/2$ pulses for duration 200 ns to perturb the interferometer through the AC Stark effect. The AC Stark shift is measured in the same way as the DC Stark shift in section 5.2.2.

Figure 5.11 shows the response of the polariton interferometer to the second microwave field. The first microwave field $\Omega_\mu$ is detuned from the qubit resonance by $\Delta_\mu = 2\pi \cdot 8$ MHz to increase sensitivity as in section 5.2.2. A dotted line in **a** identifies the position of the first intensity maxima in the absence of microwaves, occurring at $t = 170$ ns. The frequency of the second microwave field is swept across the $|59P_{3/2}\rangle \leftrightarrow |59S_{1/2}\rangle$ resonance. Figure 5.11, **a** shows photon retrievals when $\Omega_{\mu 2}$ is varied over the range $2\pi \cdot [-50, 50]$ MHz. The interferometer length is also varied up to a maximum length of 400 ns. Red data show the visibility of interference fringes as a function of detuning of the second microwave source $|\Delta_{\mu 2}|$ <3 MHz in 0.5 MHz steps. A grey dashed line shows a Lorentzian fit to the data, which has a line-width of $1.3 \pm 0.1$ MHz, consistent with the Fourier transform of the pulse duration $t_{\mu 2}$. Interferometric fringes can be seen to asymptotically converge upon this line at large detunings, and diverge in opposite directions as $\Omega_{\mu 2}$ approaches resonance due to the change in sign of the dispersive shift either side of resonance (c.f. figure 2.10).

The AC field strength can be measured through the magnitude of the dispersive frequency shift, or by the destructive power of the field when tuned near to resonance which causes the visibility $\mathbb{V}$ of interferometric fringes to fall. Scattering and saturation are both increased close to resonance, invalidating the perturbative derivation of the AC Stark shift. A reduction in $\mathbb{V}$ occurs due to the polariton states $|1_{r'}\rangle$, $|0_r\rangle$becoming distinguishable in the presence of a near-resonant microwave field, which performs an effective measurement of the system. Information on the state of the system is carried by the microwave field, destroying superposition analogous to the classic decoherence experiment of Brune *et al.* [339].

At large detunings, the microwave field carries little information on the state of the interferometer. In this regime, the dispersive effect of the AC stark shift upon the interferometer can be directly extracted from the frequency shift of interference fringes, referenced to the frequency of fringes in absence of any microwave coupling. $\Omega_{\mu}$. Panel **c** shows extracted resonance shifts whilst the microwave field is scanned over a wider range of $-50, 50$ MHz (data in panel **a**). The interferometric shift $\delta_{\text{int}}$ in Panel **c** has a dispersive line shape which is a good fit to equation 2.1.29. Loss of coherence is more frequency-selective than Stark shift measurements, and could be used for high-resolution measurements of Rydberg transition frequencies, which are important in the determination of quantum defects [151].

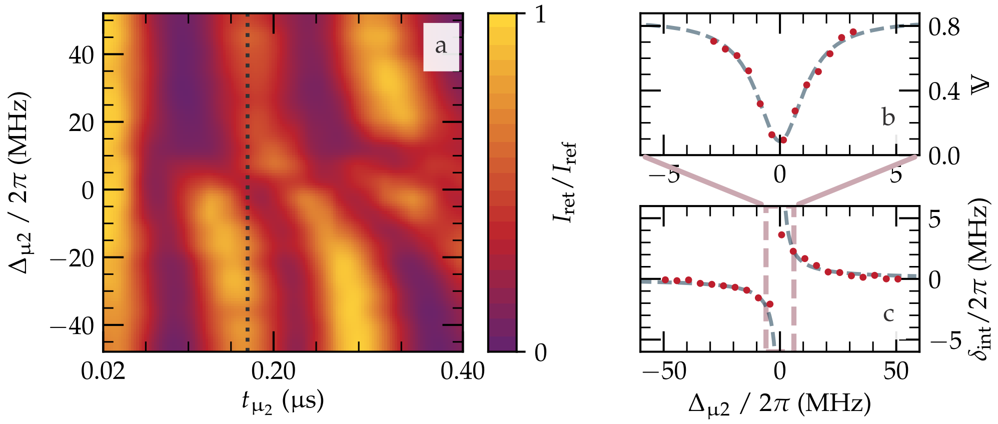

Figure 5.11: Sensing AC Electric fields with a contact-less polariton interferometer. An external microwave field couples polariton state $|1_{r'}\rangle$to a third polariton state $|2_{r''}\rangle$. **a** shows single-photon interference fringes as external field detuning $\Delta_{\mu 2}$ and superposition time, $t_{\text{int}}$ are varied. Detuning $\Delta_{\mu}/(2\pi)$ is fixed at 8 MHz. **b** Visibility $\mathbb{V}$ is destroyed by an external resonant microwave field. Red data points show the visibility of interference fringes close to resonance. The grey dotted line shows a Lorentzian fit with line-width $1.3 \pm 0.1$ MHz. **c** shows the frequency shift of Ramsey fringes $\delta_{\text{fringes}}$ has a dispersive relationship with the external microwave detuning $\Delta_{\mu 2} > 5$ MHz. The dotted line in **c** presents a good fit to Equation 2.1.29.

The current sensitivity of the experiment is limited by thermal dephasing due to a maximal superposition time of $\sim$1 μs, which diminishes photon readout. Hyperfine qubits can have longer lifetimes due to shorter effective wave vectors however these qubits have weak intrinsic interactions and must be dressed with Rydberg interactions to establish sensing. Dressed hyperfine qubits less sensitive to electric fields than the Rydberg qubit interferometer have been demonstrated [63]. To the best of our knowledge, this represents the first proof-of-principle demonstration of interferometry of Rydberg polaritons.

## 5.3 Robustness of Rydberg Qubits

Entanglement is at the heart of modern developments in quantum information and quantum technology [88, 340]. The collective Rydberg qubit is one example of a strongly entangled system, where the state of spatially separate particles defines a composite quantum state. The polariton encoding dictates that quantum information is shared between atoms of the ensemble due to the $\mathcal{W}$-like form of the polariton wavefunction (Equation 2.2.106). This sharing of quantum information confers robustness against tracing over the state of any of the individual atoms which make up the collective state, and thus exhibits multipartite entanglement [241, 305, 341] making them amenable to error correction schemes [306]. The collective system is robust against the loss of information from the ensemble due to atom loss. This section explores the loss of quantum information from the collective qubit. Electrical noise is shown to affect the qubit matching a quartic model based on theoretical dephasing of a two-level with stochastic Stark shifts. We demonstrate that quantum information stored in the qubit is robust against atom loss in a way that has no analogue in traditional atomic qubits.

### 5.3.1 Atom Loss

Collective qubits encoded in $|\mathcal{W}\rangle$ states are known to posess intrinsic robustness as a result of the distribution of quantum information over the

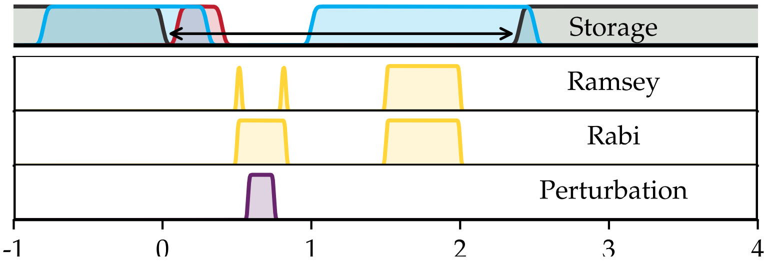

Figure 5.12: The effect of electrical noise and probe driving upon the qubit was observed through the implementation of a perturbative pulse during the superposition time of the interferometer sequence shown in Figure 5.5. The timings of the probe, coupling, microwave pulses, and dipole trap are the same as in Figure 5.5. The effect of the same perturbation upon qubit rotation is also observed by leaving the microwave drive field in-between $\pi$ pulses. Again, other parameters match Figure 5.5.

many members of the multipartite system [241, 305, 306]. To characterise the effect of atom loss on our collective qubit, we employ the pulse sequence shown in Figure 5.12, which augments the pulse sequence designed to witness Ramsey interferometry in Figure 5.5. Experiments are performed at an intermediate quantum number of $n = 60$ to maximise storage efficiency. For interferometric experiments, we operate with fixed duration $t_{\text{int}} = 0.25\,\mu\text{s}$. To observe the effect of noise upon the oscillating qubit, we operate the same interferometric pulse sequence, but do not switch the microwave pulse off during $t_{\text{int}}$, resulting in $t_{\text{Rabi}} = t_{\text{int}} = 0.3\,\mu\text{s}$. During these pulse sequences, we apply a perturbation $\mathcal{H}_{\text{p}}$ during the interferometric superposition time (or, during the corresponding Rabi oscillations for the Rabi pulse sequence).

The study of atom loss is implemented by applying a non-Hermitian perturbation in the form of resonant driving by a probe beam [342]. The density matrix of the initial state of the system is $\rho_i = |\mathsf{0}_{\mathsf{r}}\rangle\langle\mathsf{0}_{\mathsf{r}}|$. Expanding the initial state gives (c.f. Equation 5.1.1)

$$\rho_{\mathrm{i}} = \frac{1}{\sqrt{N}} \sum_{i}^{N} \sum_{j}^{N} e^{i\mathbf{K}_{\mathrm{eff}}\cdot(\mathbf{R}_j - \mathbf{R}_i)} \left|g_0, g_1..r_i..g_{n-1}, g_N\right\rangle \left\langle g_0, g_1..r_j..g_{n-1}, g_N\right| . \tag{5.3.8}$$

Examining the terms in this summation, we have that

$$\rho_{\mathrm{i}}^{(i,j)} \propto \left|g_0, g_1..r_i..g_{n-1}, g_N\right\rangle \left\langle g_0, g_1..r_j..g_{n-1}, g_N\right| . \tag{5.3.9}$$

This multipartite system can be decomposed into product terms

$$\rho_{\mathrm{i}}^{(i,j)} \propto \left|g_0\right\rangle \left\langle g_0\right| \otimes \left|g_1\right\rangle \left\langle g_1\right| \otimes ... \otimes \left|r_i\right\rangle \left\langle r_j\right| \otimes ... \otimes \left|g_n\right\rangle \left\langle g_n\right| \otimes \left|g_{n-1}\right\rangle \left\langle g_{n-1}\right| . \tag{5.3.10}$$

Each atom in the superposition undergoes dissipative dynamics as determined by the Lindblad dephasor 2.2.62 under the action of a scattering Hamiltonian

$$\mathcal{H}_p = \frac{\Omega_s}{2} \left[\left|g\right\rangle \left\langle e\right| + \left|e\right\rangle \left\langle g\right|\right], \tag{5.3.11}$$

and decay via spontaneous emission from $\left|e\right\rangle$

$$\mathcal{D} = \Gamma_e \left|g\right\rangle \left\langle e\right| . \tag{5.3.12}$$

As discussed in previous sections, the long lifetimes of the Rydberg states and absence of coupling to $\left|g\right\rangle$ during qubit operation means that the elements $\left|r_i\right\rangle \left|r_j\right\rangle$ do not evolve when $i = j$. Likewise, the 6 MHz linewidth of the excited state dictates that any population in $\left|e\right\rangle \left\langle e\right|$ does evolve in time, but will decay back to the ground state by the end of the experimental sequence, as this decay process is much faster than the experimental timescale of 2.4 µs. Thus it does not contribute to the Rydberg spin wave after the interaction is complete. Thus the only element in the summation with nontrivial dynamics are the Rydberg coherences, which evolve as

$$\partial_t \left|g\right\rangle \left\langle r\right| = -i\Omega \left|e\right\rangle \left\langle r\right| , \tag{5.3.13}$$

$$\partial_t \left|e\right\rangle \left\langle r\right| = -i\Omega \left|g\right\rangle \left\langle r\right| - \frac{\Gamma_e}{2} \left|e\right\rangle \left\langle r\right| . \tag{5.3.14}$$

These differential equations are solved subject to the initial condition that the adiabatic polariton storage protocol is effective in transferring all excited state population to the Rydberg state $|r\rangle$, $|e\rangle\langle r|_{t=0} = 0$. The time evolution of the Rydberg coherences is then given by

$$|g\rangle\langle r|_{\mathrm{t_s}} = \mathrm{e}^{-\frac{\gamma}{4}t_\mathrm{s}}\left(\cosh(\omega_\mathrm{s}t_\mathrm{s}) + \frac{\gamma}{4\omega_\mathrm{s}}\sinh(\omega_\mathrm{s}t_\mathrm{s})\right)|g\rangle\langle r| \ldots \tag{5.3.15}$$

$$- \mathrm{i}e^{-\gamma t_\mathrm{s}}\frac{\Omega}{\omega_\mathrm{s}}\sinh(\omega_\mathrm{s}t_\mathrm{s})\,|e\rangle\langle r|, \tag{5.3.16}$$

where $\omega_\mathrm{s} = \frac{1}{4}\sqrt{\gamma^2 - 16\Omega^2}$. Under the assumption that the population of the excited state is negligible due to fast decay, the scattering beam affects the critical ground-Rydberg coherences as

$$|g(t)\rangle\langle r(t)| \to \alpha(t_\mathrm{s})\,|g\rangle\langle r| = e^{-\frac{\Gamma_e}{4}t_\mathrm{s}}\left(\cosh(\omega_\mathrm{s}t_\mathrm{s}) + \frac{\gamma}{4\omega_\mathrm{s}}\sinh(\omega_\mathrm{s}t_\mathrm{s})\right)|g\rangle\langle r|. \tag{5.3.17}$$

And so equation 5.3.8, under the influence of the scattering field becomes

$$\rho_\mathrm{i} = \frac{1}{\sqrt{N}}\sum_i^N\sum_j^N e^{i\mathbf{K}_\mathrm{eff}\cdot(\mathbf{R}_j - \mathbf{R}_i)}\,|g_0, g_1..r_i..g_{n-1}, g_N\rangle\langle g_0, g_1..r_j..g_{n-1}, g_N|$$

$$\cdot\,(1 - \delta_{ij})\alpha(t). \tag{5.3.18}$$

Represented as an N-particle density matrix, the system evolves from a coherent entangled collective excitation towards a mixed state,

$$\rho_\mathrm{f} = \frac{1}{N}|\alpha(t)|^2\begin{pmatrix}1 & . & . & 1\\ . & 1 & . & .\\ . & . & 1 & .\\ 1 & . & . & 1\end{pmatrix} + \frac{1}{N}\left(1 - |\alpha(t)|^2\right)\begin{pmatrix}1 & . & . & 0\\ . & 1 & . & .\\ . & . & 1 & .\\ 0 & . & . & 1\end{pmatrix}. \tag{5.3.19}$$

As time increases, $\alpha(t)$ evolves from $\alpha(0) = 0$ towards $\alpha(t \to \infty) = 1$. The left hand matrix represents the maximally entangled $|\mathcal{W}\rangle$ state which is established as the photon is stored as a polariton[13]. As the qubit

---

[13] Note that this conceptual picture would not account for variations in Rabi frequencies $\Omega_c, \Omega_p$ across the ensemble, the effects of optical depth and of geometric modes.

scatters probe photons, multipartite entanglement is diminished due to the exponent in $\alpha(t)$ in equation 5.3.17 and the system asymptotically approaches a mixed state represented by the right hand matrix.

The read-out fidelity $\mathcal{F}$ can be calculated as the overlap between the state of the polariton after it is written into the medium $|i\rangle$, and the state of the qubit before retrieval $|f\rangle$, such that

$$\mathcal{F} = \langle i|\rho_\mathrm{f}|f\rangle \,. \tag{5.3.20}$$

Diminishing the coherence between the qubit and the emitter diminishes the readout fidelity.

$$\mathcal{F}(t) = \frac{1}{N} + \frac{N-1}{N}|\alpha(t)|^2. \tag{5.3.21}$$

The effect of this scattering field on the collective qubit Rabi oscillation and Ramsey fringes are shown in Figs. 5.13**b** and **c**, respectively. Increasing the amplitude of the scattering field is observed to reduce the visibility of both the Rabi oscillations and the Ramsey fringes. Figure 5.13**d** demonstrates the reduction in interferometric fringe amplitude due to progressive atom loss. The scattering field is varied between $\Omega_c \in 2\pi\cdot[0,2]$ MHz. Data corresponding to $\Omega_s \in 2\pi\cdot[0,1,2]$ MHz are shown. The scattering field causes atom loss which reduces the fidelity of the read-out. For $\Omega_s \gg \Gamma_e$ and a many atom ensemble $N \gg 1$, the readout fidelity is simplified to

$$\mathcal{F}(t) = \exp\left(-4\frac{\Omega_\mathrm{p}^2}{\Gamma_\mathrm{e}}t\right)\,, \tag{5.3.22}$$

where $\Omega_\mathrm{p}$ is the amplitude of the scattering field and $\Gamma_\mathrm{e}$ is the lifetime of the emitter. Note that the dephasing due to the scattering field does not depend on the number of atoms $N$ in the limit of a large $N$ due to the increasingly negligible effect of tracing over a single degree of freedom in a large, multipartite system [241, 305].

Figure 5.14 (**a**) shows the effect of scattering from the probe beam upon the optical depth of the medium. The probe beam has duration $t_\mathrm{p}$ =0.25 µs and Rabi frequency $\Omega_\mathrm{p} \in [0,2]$ MHz. Data are extracted from five million

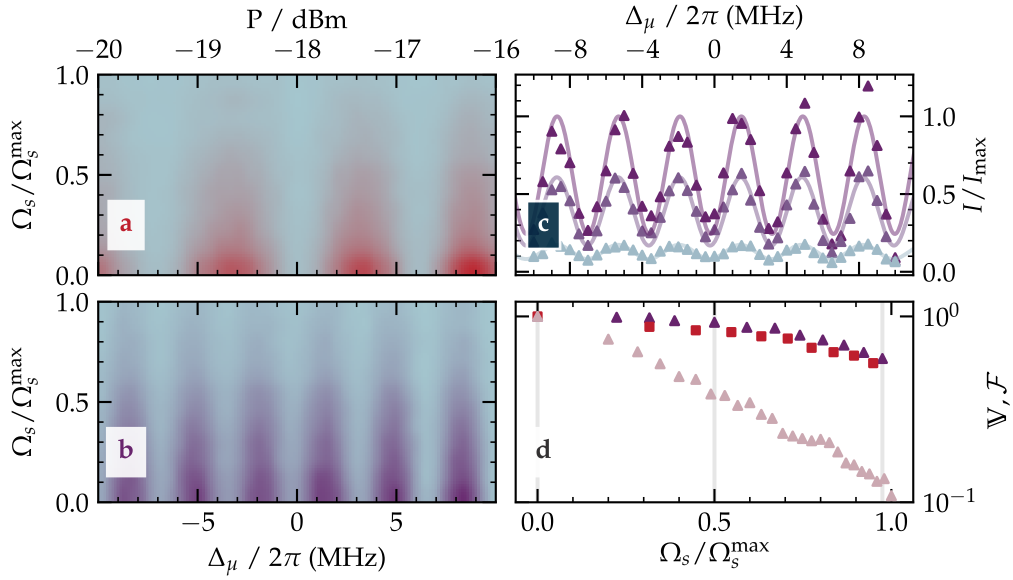

Figure 5.13: **Robustness of the collectively-encoded qubit to atom loss**: The effect of light scattering on the $|g\rangle \rightarrow |e\rangle$ transition upon Rydberg qubit dynamics. **a**, **b** show colourmaps of both Rabi oscillations and Ramsey fringes respectively, under the action of an applied scattering field $\Omega_s$ as it is increased up to a maximum value $\Omega_s^{\max}/2\pi = 2$ MHz. **c** Shows Ramsey fringes for three scattering amplitudes indicated in **d** by vertical lines. **d** The visibility of the Rabi oscillations (red squares) and Ramsey fringes (purple diamonds) as function of $\Omega_s$. $\mathcal{F}$ is also shown, integrated across all experiments (pink diamonds). $\mathcal{F}$ is reduced to $\sim 0.1$, whilst $\mathbb{V}$ remains above 0.6 for strong scattering. This provides proof of the robustness of the multipartite encoding offered by by the $|\mathcal{W}\rangle$ state. Figure adapted from [65].

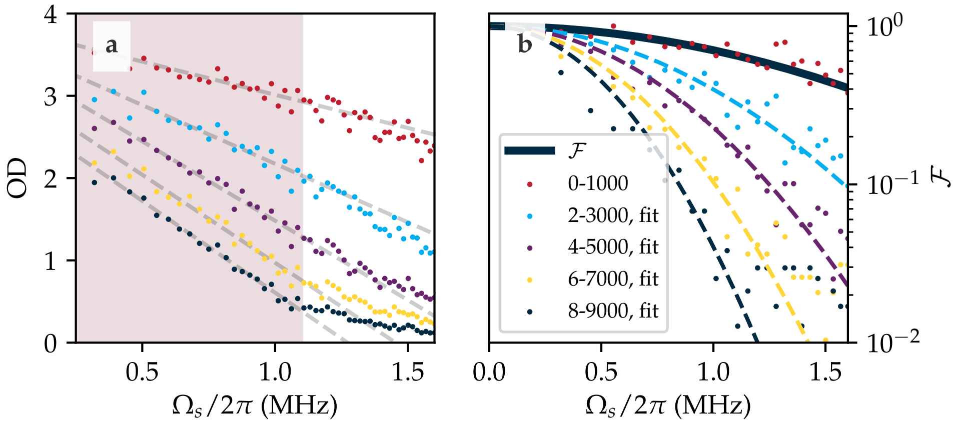

Figure 5.14: Photon scattering diminishes OD and $\mathcal{F}$ (Equation 5.3.2) due to atom loss. **a** High $\Omega_s$ causes nonlinear reduction of OD due to total atom loss for high shot numbers $> 6000$ and scattering fields $\Omega_s > 1$. Dashed lines represent linear fits to the highlighted data. In **b** scattering is observed to diminish $\mathcal{F}$. This is in line with for low shot numbers $< 1000$ where the optical depth remains high (black line). Dashed lines represent fits of $\mathcal{F}(\Gamma_e)$ to the data.

experimental runs, corresponding to one hundred thousand runs for each data point. The experiment is repeated ten thousand times in between dipole trap reloading, and OD is shown as a function of experimental run number $n_{\text{exp}}$, measured from the dipole trap reloading. As the experimental run number increases, OD is diminished due to compound scattering events of previous experimental runs. The analysis of the first two thousand experimental runs reveals an initial OD of $\sim 3.4$. Atom loss is severe for large $\Omega_s$, saturating at the highest incident photon rates.

Figure 5.14 (**b**) shows a comparison between Equation 5.3.2 for $\mathcal{F}$ and experimental data. Experimental $\mathcal{F} = I_{\text{ret}}/I_0$ are determined by normalising observed photon retrieval counts $I_{\text{ret}}$ by the number of counts observed in the absence of any scattering beam $I_0$. The data are again analysed as a function of the experimental run number. The effect of diminished optical depth causes the fidelity to diminish much faster than predicted for larger scattering fields. However, for low $n_{\text{exp}}$, experimental $\mathcal{F}$ are a good fit to equation 5.3.2, shown as a solid line.

Figure 5.13 shows the effect of $\Omega_\mathrm{s}$ on both Rabi and Ramsey sequences presented in Figure 5.12. Colormap 5.13 **a** shows retrieval amplitude during a Rabi sequence across the range $\Omega_\mu \in 2\pi \cdot [2.0, 5.3]$ MHz. Data are normalised to the retrieval at $\Omega_\mathrm{s} = 0$. Colormap 5.13 **b** shows a similar effect during a Ramsey sequence, again normalised to retrieval at $\Omega_\mathrm{s} = 0$. Central Ramsey fringes ($|\Delta_\mu| < 10$) are shown for $t_\mathrm{int}$ =0.25 µs. The Rabi frequency of the scattering field is varied over the range range $\Omega_\mathrm{s} \in 2\pi \cdot [0, 2]$ MHz. In both panels, retrieval fidelity $\mathcal{F}$ is reduced under the action of the resonant scattering beam. The qubit and emitter become dephased as per equation 5.3.17.

Rabi oscillations and central Ramsey fringes are shown in Figure 5.13 **a**, **b**. Simple sinusoidal fits with free parameters of frequency, $\omega$, phase $\phi$, amplitude $A$ and offset $O$ are used to obtain visibility $\mathbb{V} = A/O$. Figure 5.13 **c** shows these fits for a subset of data from **b**. Corresponding scattering amplitudes are represented by vertical lines on **d**. Each data point corresponds $n_\mathrm{exp} = 10000$, and so each sinusoidal data set represents four million experiments. Extracted $\mathbb{V}$ of both Rabi oscillations (red squares) and Ramsey fringes (purple triangles) are shown in Figure 5.13 **d** as a function of $\Omega_s$. Pink triangles show corresponding $\mathcal{F}$ extracted from data presented in Figure 5.14, **a** and averaged over all colour runs. Fidelity $\mathcal{F}$ is shown normalised to the case where $\Omega_\mathrm{s} = 0$. Visibility $\mathbb{V}$ of both Rabi oscillations and Ramsey fringes versus the amplitude of the scattering field $\Omega_\mathrm{s}$ is shown.

This brings us to one of the most interesting outcomes of this work. The visibility of Ramsey interference fringes and Rabi oscillations of Rydberg polariton qubits are persistent even under the action of destructive photon scattering. Figure 5.14 shows the loss of optical depth as a function of the shot number, which proves atom loss during the experimental sequence. In fact, the ensemble is effectively destroyed across experimental runs for

$\Omega_\mathrm{s} = {\Omega_\mathrm{s}}^{max}$. At the largest $\Omega_\mathrm{s}$, this causes a reduction in $\mathcal{F}$ of an order of magnitude. However, even in this extreme case, $\mathbb{V}$ is reduced by less than a factor of two across both Rabi and Ramsey sequences. Thus this polariton qubit state is robust to atom loss due to multipartite encoding [241, 305], which can be further mitigated through error correction schemes that advantage the collective nature of these qubits [306]. This provides an advantage over similar schemes based on single atoms which are much more sensitive to qubit loss [343], requiring expensive loss correction schemes [344].

### 5.3.2 Environmental Noise

Many schemes exist to overcome decoherence and dissipation in open quantum systems such as those used to implement qubits in NISQCs [345, 346]. To assess the feasibility of collective Rydberg qubits in modern NISQs, it is important to understand the degree of coupling between the qubit and the environment, causing decoherence. A stochastic Hamiltonian can be used to simulate environmental coupling, revealing the susceptibility of the collective encoding scheme to environmental noise [342].

Dissipation is introduced through the application of a stochastic electric field exploiting the strong electric dipole moment of Rydberg atoms to simulate environmental noise

$$\mathcal{H}_\mathrm{stochastic}(t) = -\mathbf{d} \cdot \mathcal{E}(t), \tag{5.3.23}$$

where $\mathcal{E} = E_0\hat{z}$. The noise field can be expanded as a sum of static field terms. In the perturbative regime, this gives rise to an average quadratic Stark shift through the polarisability as described in chapter 2, and a stochastic dephasing term. Assuming alignment between dipole and field, the square of the time averaged electric field can be obtained from the integral[14]

$$\langle E^2(t)\rangle = \frac{1}{2E_0}\int_{-E_0}^{E_0} E^2(t)\,dE(t) = \frac{E_0^2}{3}. \tag{5.3.24}$$

Thus equation 5.3.23 can be rewritten as

$$\mathcal{H}' = \frac{E_0^2}{6}\begin{pmatrix}\alpha_{\mathrm{r}'} & 0\\ 0 & \alpha_{\mathrm{r}}\end{pmatrix} + \frac{1}{2}\begin{pmatrix}\alpha_{\mathrm{r}'} & 0\\ 0 & \alpha_{\mathrm{r}}\end{pmatrix}\xi^2(t), \tag{5.3.25}$$

where $\alpha_j$ is the polarizability of state $|j\rangle$, and $\xi^2(t) = E^2(t) - \langle E^2(t)\rangle$ represents the stochastic fluctuations of the squared electric field amplitude about the average value $E_0^2/6$. Since each of the terms in the definition of the polariton qubit (Equations 5.1.1, 5.1.2) contains a single Rydberg excitation, Equation 5.3.23 acts globally on all terms in the summation.

Temporal correlations at times $t, t'$ can be written

$$\begin{aligned}\langle \xi^2(t)\xi^2(t')\rangle &= \langle (E^2(t) - \langle E^2(t)\rangle)(E^2(t') - \langle E^2(t')\rangle)\rangle\\ &= \langle E^2(t)E^2(t')\rangle - 2\langle E^2(t)\rangle\langle E^2(t')\rangle + \langle E^2(t)\rangle\langle E^2(t')\rangle\\ &= \langle E^2(t)E^2(t')\rangle - \langle E^2(t)\rangle^2.\end{aligned}$$

To evaluate this equation, we calculate the value of $\langle E^2(t)E^2(t')\rangle$ as in equation 5.3.24.

$$\langle E^2(t)E^2(t')\rangle = \frac{1}{2E_0}\int_{-E_0}^{E_0} E^2(t)E^2(t')dE(t) = \frac{E_0^4}{5}. \tag{5.3.26}$$

Then, for $t = t'$, we have that

$$\langle \xi^2(t)\xi^2(t)\rangle = \eta E_0^4, \tag{5.3.27}$$

where $\eta = \frac{4}{45}$ is a proportionality factor arising from the calculation of the strength of fluctuations of $E(t)$ about the average value. We assume that the exponential decay of correlations for unequal times $t \neq t'$ such that

$$\langle \xi^2(t)\xi^2(t')\rangle \approx \langle \xi^2(t)\xi^2(t)\rangle \exp\left[-\frac{|t-t'|}{\tau_{\mathrm{corr}}}\right] = \eta E_0^4 \exp\left[-\frac{|t-t'|}{\tau_{\mathrm{corr}}}\right]. \tag{5.3.28}$$

---

[14] For a stochastic electric field amplitude over the interval ($[-E_0, E_0]$) with equal probability such that $P(\mathcal{E}) = \frac{1}{2\mathcal{E}_0}; \mathcal{E} \in [-\mathcal{E}_0, \mathcal{E}_0]$

where $\tau_{\text{corr}}$ represents the timescale associated with the temporal decay of noise correlations. If the noise correlation time is much shorter than other experimental ($t_{\text{exp}}$) decay ($\Gamma_e, \Gamma_r$) and dephasing ($\gamma_{\text{thermal}}$) mechanisms, we can approximate $\tau_{\text{corr}} \approx 0$, then

$$\langle \xi^2(t)\xi^2(t')\rangle \approx 2\eta\tau_{\text{corr}}E_0^4\,\delta(t-t'). \tag{5.3.29}$$

We next calculate the Lindblad dynamics of this physical system. The form of the Lindblad dissipator in Equation 2.2.61 is given through Equation 10 in [342].

$$\begin{aligned}\mathcal{D}(\rho(t)) &= -\frac{2\eta}{\hbar^2}\tau_{\text{corr}}E_0^4\left[\frac{1}{2}\begin{pmatrix}\alpha_{\text{r}'} & 0\\ 0 & \alpha_{\text{r}}\end{pmatrix}, \left[\frac{1}{2}\begin{pmatrix}\alpha_{\text{r}'} & 0\\ 0 & \alpha_{\text{r}}\end{pmatrix}, \rho(t)\right]\right]\\ &= -\frac{2\eta}{\hbar^2}\tau_{\text{corr}}E_0^4\delta_\alpha^2\hat{\sigma}_x.\end{aligned} \tag{5.3.30}$$

We have introduced the relative polarisability of the two states $\delta_\alpha = \alpha_{\text{r}'} - \alpha_{\text{r}}$. Thus evolution of atomic coherence is proportional to Pauli operator $\sigma_x$

$$\frac{\partial}{\partial t}\sigma_x(t) = -\frac{\gamma_{\text{deph}}}{2}\hat{\sigma}_x(t), \tag{5.3.31}$$

where we have defined the dephasing rate of atomic coherences under the action of $\mathcal{H}_{\text{Stochastic}}$ through Equations 2.2.61, 5.3.30, 5.3.31 as

$$\gamma_{\text{deph}} = \eta\cdot\tau_{\text{corr}}\cdot\frac{\delta_\alpha^2}{\hbar^2}\cdot E_0^4. \tag{5.3.32}$$

Qubit dephasing is proportional to $E_0^4$ under the action of the applied electrical noise field with stochastic amplitude drawn from a uniform distribution spanning $[-E_0, E_0]$.

To simulate the effect of a stochastic electric field, we employ the pulse sequence of Figure 5.12, where the perturbation takes the form of the applied noise Hamiltonian of Equation 5.3.25[15]. The noise pulse is applied in between the $\pi/2$ pulses for duration 250 ns.

---

[15] Electrical noise with a Gaussian probability distribution generated using a Tektronix AFG3252 arbitrary function generator with a bandwidth of 240 MHz.

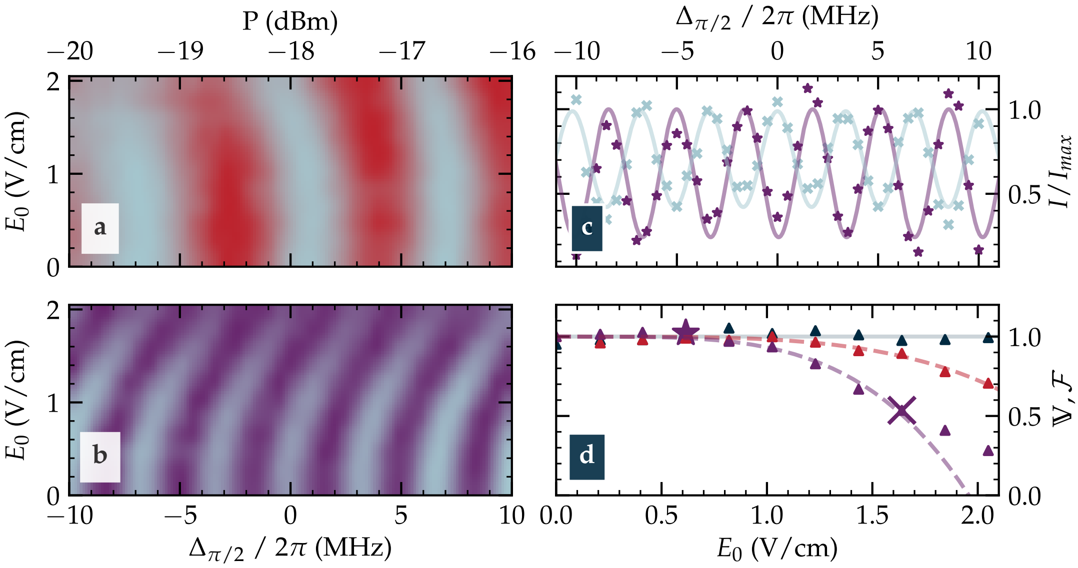

Figure 5.15: Driving the qubit with a noise field during Rabi (**a**) or Ramsey (**b**) pulse sequences leads to both dephasing and Stark shifts. **a** The collective qubit is driven with the Ramsey pulse sequence as in Figure 5.12, with the addition of a stochastic perturbation due to an electric field as per equation 5.3.25. Colourmaps show retrievals from the ensemble normalised to their peak value. **c** Central Ramsey fringes low noise, ($E_0 = 0.6$ )V (purple stars) and high noise, $E_0 = 1.6$ V (blue crosses) with sinusoidal fits. **d** Visibility $\mathbb{V}$ normalised to $\mathbb{V}(E_0 = 0)$ as a function of the noise amplitude for Ramsey fringes (purple) and Rabi oscillations (red) data. The star and the cross correspond to the datasets detailed in **c**. $\mathcal{F}$ is not degraded by noise [black triangles, normalised to $\mathcal{F}(E_0 = 0)$]. $\mathcal{H}_{\text{Stochastic}}$ degrades $\mathbb{V}$, following the quartic relationship as per Equation 5.3.32 (dotted lines). For $E > 1.6$ V/cm, the model fails due to the breakdown of the perturbative approach.

The noise perturbation is applied to the qubit during both Ramsey and Rabi sequences. A simulated noise pulse with a peak-to-peak amplitude $2E_0$ is applied to *in-vacuo* electrodes described in chapter 3. The effect on the Ramsey fringes is shown in Figure 5.15**b**. Both the quadratic level shift and the dephasing caused by the two terms in Equation 5.3.25 are observed.

The global perturbation causes a $T_1$ type dephasing which imparts no significant reduction in readout fidelity $\mathcal{F}$ (see equation ), in contrast to previous measurements of progressive $T_2$ type dephasing due to gradual loss of local coherence in section 5.3.1. Thus the electric field is truly global in nature, causing no significant decoherence of the Rydberg spin-wave during $t_{\text{exp}}$. Therefore we conclude that the reduction in $\mathbb{V}$ shown in figure 5.12 **c** can be attributed to the dephasing as per Equation 5.3.32. The predicted $E_0^4$-scaling is a good fit to experimental $\mathbb{V}$, see Figure 5.15. Panel **b** highlights two sets of Ramsey fringes taken at different noise amplitudes. Figure 5.15**c** shows retrieval efficiency remains constant under application of $\mathcal{H}'$. Thus, dephasing of local phase factors is not observed. However, in the same Figure, the pulse of electronic white noise is seen to reduce the visibility of Rabi and Ramsey oscillations. The visibility of both Rabi and Ramsey fringes is found to have a quartic dependence on field amplitude, c.f. equation (5.15).

The experimental data diverges slightly from the model for large $E_0$. At high field strength, the foundational assumption of a quadratic Stark shift in equation 5.3.25 loses validity. An analysis of the breakdown of the model is presented in figure 5.16. Panel **a** shows fits to the data for quartic ($\mathbb{V} = 1 - aE_0^4$) and quadratic ($\mathbb{V} = 1 - bE_0^2$) models, where $a, b$ are fit parameters. Data points for $E_0 < 1.6$ V/cm (indicated by the yellow shaded regions) were used to fit the data and the quartic model performs better in this region. Panel **b** shows the average residual for both quartic and quadratic fits when only the first $N$ data points are included in the

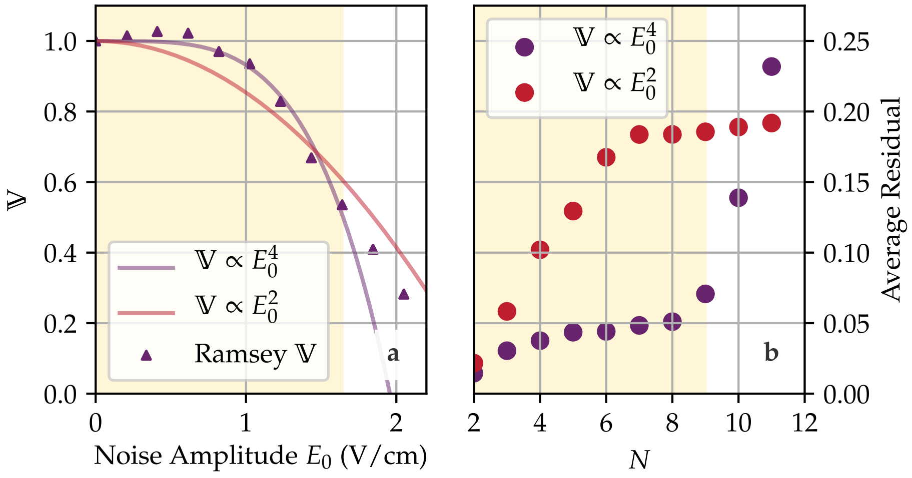

Figure 5.16: Analysis of quadratic noise dephasing evidencing quartic scaling. **a** Fringe visibilities $\mathbb{V}(E_0)$ are fit well by a quartic scaling (purple line) and are not accurately described by a quadratic (red line) model. **b** A quadratic model is a better fit to the full dataset as large $E_0$, showing the breakdown of the perturbative model. Fits are made to the first $N$ data points from **a**. The perturbative assumptions of equation 5.3.32 are satisfied in the region $E_0 < 1.6$ V/cm where the goodness of fits to $\mathbb{V} \propto E_0^4$ exceeds fits to $\mathbb{V} \propto E_0^2$. The breakdown of the perturbative assumption can also be clearly seen in the divergence from $\mathbb{V} \propto E_0^4$ in the region $E_0 < 1.6$.

fit. The quartic model vastly outperforms the quadratic model at low field strengths. The strong departure from the quartic model at field strengths $E_0 > 1.6$ V/cm is apparent as a dramatic increase of the residuals of the quartic fit. Thus collective qubit coherence is robust against this kind of noise to second order.

### 5.3.3 Conclusion

In summary, we have described an implementation of a collective Rydberg qubit [64, 65]. We find the qubit to have excellent coherence properties allowing for the implementation of fast Rabi oscillations, Ramsey interferometry, and Hadamard gates. We have shown that collective atomic qubits encoded in Rydberg polaritons are robust against atom loss and global phase distortions due to environmental noise [241, 305]. For the latter, we observe a quartic dependence on the noise amplitude profile that matches theoretical predictions. Further resilience might be obtained by utilising ‘magic’ Rydberg states [347], where the polarizabilities of the Rydberg states are matched. Qubit sensitivity to AC and DC fields may also have applications in sensing [63, 334].

This work prepares for the implementation of quantum gates between collective qubits mediated by Rydberg interactions. Tunable, contactless interactions between collective Rydberg excitations have previously been reported [105] and phase gate proposals implemented with collective qubits are also available [138, 348]. The emitter-qubit coupling provides a photonic interface to the qubit, making collective encoding useful for the creation of flying qubits, plus hybrid light-matter interfaces for quantum computing and communication.

# Chapter 6

# Conclusion

This thesis reports on the coherent collective response of driven Rydberg polaritons. A new method for the study of blockade phenomena through slow decay of Rydberg EIT transients is introduced. Fast microwave pulses are used to suppress the decay of Rydberg EIT transients entirely through Autler Townes splitting of Rydberg states, leading to a new method of photon storage. Microwave pulses are also shown to enhance interaction induced dephasing of the stored excitations through injection of resonant dipole interactions, enhancing outgoing photon anti-bunching. Thus driven Rydberg transients present opportunities for the analysis of interaction induced dephasing of Rydberg spin-waves. A novel implementation of a collective Rydberg qubit, a superposition of polariton excitations of an ultracold ensemble of Rubidium 87, is demonstrated through several proof-of-principle experiments. Coherent control of the qubit is demonstrated. Manipulation of the qubit Hamiltonian is achieved through Rabi oscillations and applied electric fields. A study of the response of the qubit to stochastic noise reveals a quartic dependence matching theoretical modeling. The distributed nature of the qubit encoding is demonstrated through studies of atom loss, revealing the high degree of entanglement inherent in multipartite qubits. Qubit readout is critically limited by thermal dephasing, however recent proposals aim to remove this limitation, making

Rydberg qubits worthy of further study.

## 6.1 Cooperative Rydberg Ensembles

Coherent manipulation of an atomic ensemble of Rubidium 87 was demonstrated through a series of experiments that extend knowledge of transient phenomena in three and four-level ensembles. Three-level Rydberg ensembles are shown to exhibit transient decay with a decay rate governed by the strength of the coupling field. This transient decay was found to be many orders of magnitude more intense than the corresponding two-level transient observable in the same system [263]. The susceptibility of the ensemble was successfully modelled through mean-field, non-interacting optical Bloch equations. Divergences from mean-field behavior were observed through studies of the statistical nature of outgoing photons. Photon blockade of the transient decay is demonstrated through intensity saturation [85]. Statistical analysis of the emitted light showed strong anti-bunching [84]. Thus the EIT transient gives access to sub-Poissonian light due to Rydberg-mediated effective photon-photon interactions [105] without the complexity of storage and retrieval protocols [51]. This technique may find applications in the analysis of collective dynamics through observation of EIT transients [86].

Further control over the EIT transient was achieved through the introduction of a fourth level through microwave coupling to a second Rydberg state [205]. Modulation of the flash due to Rabi oscillations within the Rydberg manifold was observed, with a concomitant increase in anti-bunching as the transition from VdW interactions to resonant dipole-dipole interactions imparts enhanced interaction-induced dephasing [29]. Dressing the system with resonant microwaves detunes the Rydberg manifold from the dominant decay mechanism via coupling to the excited state. Control over the timing of photon emission from the ensemble is achieved through the application of strong microwave pulses. Photon emission can be separated from the probe pulse by several microseconds. This adds a new method of photon storage similar to previous schemes based on photon storage [51, 128], weaker subradiant states [50, 292] or AT splitting of EIT [349, 350].

## 6.2 Collective Rydberg Qubits

Demonstration of collective Rydberg qubits [65] complement previous demonstrations of collective hyperfine qubits [300], Rydberg dressed qubits [63], and similar Rydberg superatoms based on atomic arrays [126]. Photons were stored as long-lived collective Rydberg excitations of an ensemble of Rubidium 85 [49, 51]. Coupling between collective Rydberg states was implemented via resonant microwave fields. Coherent control of the qubit was established and Bloch sphere rotations were implemented. Ramsey interferometry of Rydberg polaritons was demonstrated, confirming sensitivity to DC fields and constituting the first such demonstration of interferometry using Rydberg polaritons[1] [109]. Dispersive energy level shifts and resonant exchanges were observed via interferometric sensing of near-resonant AC electric fields. The sensitivity of the qubit to many-body decoherence was investigated through the controlled application of an electric field with a simulated stochastic amplitude applied during interferometric superposition. Qubit dephasing was found to scale with the fourth power of the applied noise field, matching theoretical predictions. These results are in agreement with the theoretical model presented in the text [342]. Progressive removal of atoms from the ensemble during qubit operation was found to reduce readout fidelity, attributable to the sensitivity of local atomic phase factors encoding quantum information in the determination of the outgoing optical mode of the stored photon [199]. Conversely, due to the highly entangled nature of the $|\mathcal{W}\rangle$-like blockaded polariton [241, 305], qubit coherence was not significantly degraded after adjustment for loss of

---

[1] To the knowledge of this research group.

read-out fidelity [306].

## 6.3 Experimental Upgrades

The experimental setup carefully prepared by previous generations of students has been extended and stabilised. A cross dipole trap has been installed, intersecting a set of optical tweezers at a ninety-degree angle. Enhanced trapping prepares for the future realisation of fully blockaded media. This should enable experiments to be performed in fully blockaded regimes, and preliminary results show an improvement in optical depth and $g^{(2)}$[2]. The technique of Zeeman-tunable MTS [110] has been developed and implemented, conferring increased stability to the optical pumping system upon which this experiment relies and increasing experimental uptime. Offset-locking [232] the coupling system to an optical cavity has increased the number of addressable principal quantum numbers by circumventing the power requirements associated with Rydberg spectroscopy [152]. It also provides a tunable lock point for subsequent experiments. The experimental analysis steps have been formalised, and automated analysis code was written by the author currently facilitates rapid data analysis is crucial to the agile use of this capable system.

## 6.4 Outlook

This thesis presents proof of the feasibility of the implementation of collective Rydberg qubits following on from previous demonstrations of Rydberg superatoms [27] and collective hyperfine qubits [102, 103, 300]. The qubit implementation in this thesis does not yet pass DiVinchenzo's five criteria for a useful qubit [1]. Addressing the first criteria of scalability, several recent demonstrations of hundreds of ensembles trapped in optical tweezers

---

[2] Detailed in [206].

are present in the literature [62]. These schemes seek to simplify complex single atom loading protocols based on light assisted collisions [90] and rearrangement using optical tweezers [351]. Simplified ensemble loading combined with Rydberg blockade might produce hundreds of identical superatoms for quantum information processing [35]. A route to scalability exists. Much progress has been made in the optical engineering methodology required for the generation of larger arrays of optical potentials which might facilitate the implementation of hundreds of Rydberg qubits. Traps might be generated via Fourier imaging of spatial light modulators [352] or acousto-optic deflectors.

Allowing for post-selection, the system is initialised into a well defined fiducial state fulfilling the second of DiVinchenzo's criteria. The efficiency of the qubit storage and retrieval (DSP) process is intolerably low for efficient two-qubit gates. Higher efficiencies approaching unity [353, 354] have been reported for lower principal quantum numbers due to the the shorter effective wavelength of the polariton spin-wave. However, storage at lower principal quantum numbers does not confer the Rydberg character without dressing schemes [355–359]. This presents the most glaring need for innovation. A recent scheme for storage in spin waves with uniform phase [104] suggests that it may be possible to mitigate thermal dephasing by implementing storage based on four-wave mixing, with the light fields arranged at angles of incidence such that the effective wave vector is zero. This is expected to dramatically increase storage efficiencies of these systems and may overcome the dominant loss mechanism of Rydberg qubits based on photon storage.

Successful implementation of Doppler-free storage and retrieval would also address shortcomings of this system when measured against the fourth criteria. A Doppler-free configuration would dramatically reduce the scrambling of phase information contained in the qubit spin-wave due to thermal motion. This would greatly extend the effective coherence time of collective Rydberg qubits. If spin-wave dephasing can be mitigated, coherence times might be expected to be limited by the Rydberg lifetime, a dramatic improvement over lifetimes observed for qubits presented in this thesis.

The fifth criteria of effective qubit readout is demonstrated in this thesis and by others on this project via polariton retrieval [51, 65, 105]. If the efficiency of the storage and retrieval process can be improved, mapping the polariton state onto a well defined optical mode via polariton retrieval might demonstrate an efficient readout process.

Photonic readout conveniently satisfies DiVinchenzo's criteria for quantum communication. The minimal coupling between 'flying' photonic qubits and the environment allows them to be transmitted across large distances via optical fiber networks [9, 10, 360]. Thus interacting collective Rydberg qubits and associated gate schemes may be useful in interfacing existing quantum hardware for quantum networking [57]. Extensions of this scheme to qutrits and qudits [103] can be easily achieved using additional microwave fields.

# Appendix A

# Supplementary Material

## A.1 Symbol Key for Optics Drawings

This thesis makes use of the excellent SVG optics library created by Alexander Franzen [210]. Symbol meanings are as below. Dichroic mirrors are signified by any coloured mirror. The symbols are provided under an Attribution-NonCommercial 3.0 Unported (CC BY-NC 3.0) license. Some changes were made to colors used in symbols and so these symbols may differ from those available elsewhere in this regard.

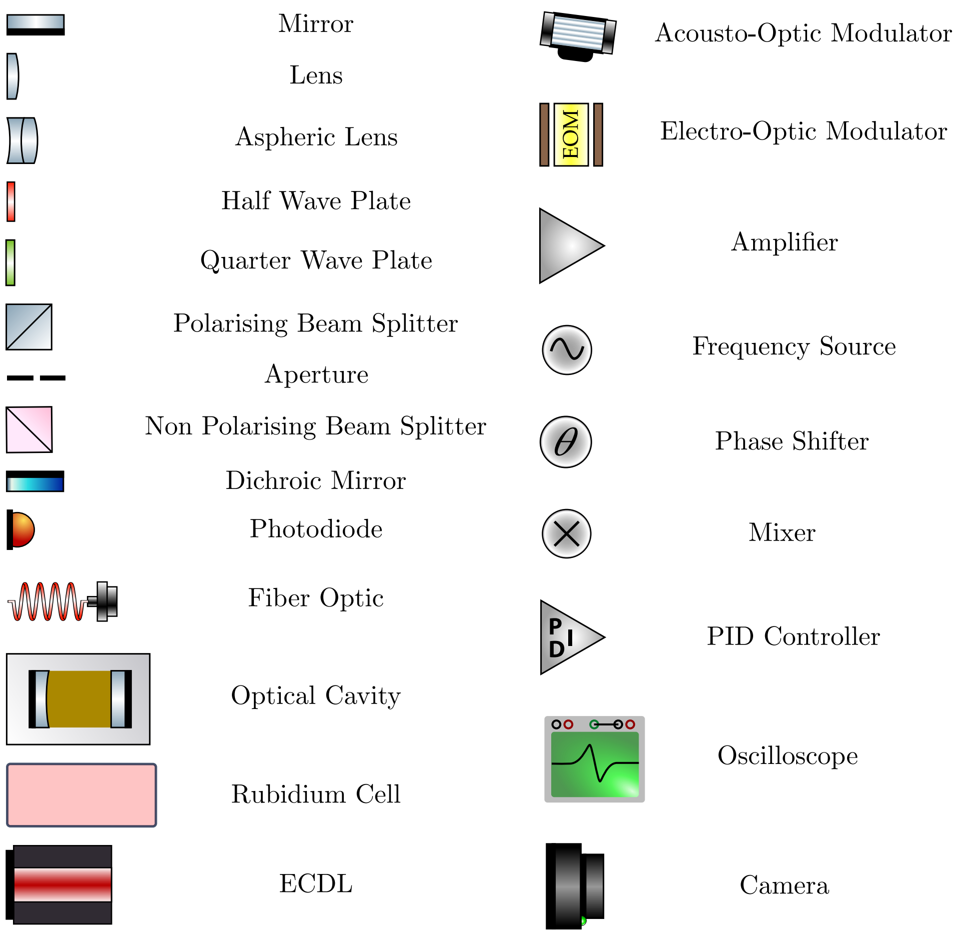

## A.2 Double Pass AOM Description

Double pass AOMs in the cooling, repump system are positioned at the focus of two 150 mm lenses to increase switching speed. Probe and 3D MOT AOMs are measured to have 80/20 rise time of 40 ns. An overview of

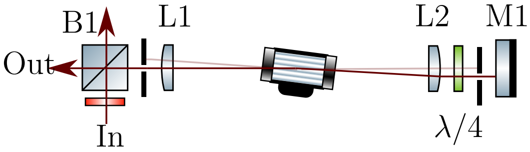

Figure A.1: Principle of double pass AOM. Placing an AOM at the focus of two lenses (L1, L2) corrects the angular deflection and causes the output beam of the lens pair to propagate parallel to the the input beam. Use of a quarter wave plate ($\lambda/4$) and a beam cube can then separate the beams, whereafter the output beam does not change pointing as a function of AOM drive frequency.

the 780 system is presented in Figure 3.1. The double pass configuration has the added advantage of stabilising the beam pointing when changing AOM frequency. Figure A.1 shows a schematic of our double pass AOMs. The AOM diffractive element is sited at the focus of a lens pair, and so the beam is brought to a focus inside the AOM by lens L1. Deflection $\phi_{aom}$ caused by the AOM originates from the focus of lens L2, and is made to propagate in the $z$ direction after collimation by lens L2. Light reflects from mirror M1 and is again brought to a focus within the AOM diffractive element by lens L2. This diffractive element then corrects the initial deflection by causing second, equal deflection to the beam $-\phi_{aom}$. Thus the output beam is ideally colinear with ths input beam. Due to passing twice through the AOM, the beam picks up a frequency shift equal to twice the drive frequency of the AOM $\Delta_{\text{out}} = 2f_{\text{AOM}}$.

The beam passes the $\Lambda/4$ twice, and so picks up a total polarization rotation of $\pi/2$. Thus the beam is transmitted by beam cube B1. With this arrangement, we are able to maintain sufficient colinearity of the output beam to achieve a 50% variation in fiber coupling efficiency across a 30 MHz range of probe beam detunings.

# Bibliography

[1] David P. DiVincenzo. “The Physical Implementation of Quantum Computation”. In: *Fortschritte der Physik* 48.9-11 (Sept. 2000), pp. 771–783. DOI: `10.1002/1521-3978(200009)48:9/11<771::AID-PROP771>3.0.CO;2-E`.

[2] Sergei Slussarenko and Geoff J. Pryde. “Photonic quantum information processing: A concise review”. In: *Applied Physics Reviews* 6.4 (2019). DOI: `10.1063/1.5115814`. arXiv: `1907.06331`.

[3] W. Heisenberg and H. Euler. “Folgerungen aus der Diracschen Theorie des Positrons”. In: *Zeitschrift fur Physik* 98.11-12 (Nov. 1936), pp. 714–732. DOI: `10.1007/BF01343663`.

[4] Victor Frederick. Weisskopf. “Über die elektrodynamik des vakuums auf grund des quanten-theorie des elektrons.” In: *Dan. Mat. Fys. Medd.* 14 (1936), pp. 3–39.

[5] Ben King, Antonino Di Piazza, and Christoph H. Keitel. “A matterless double slit”. In: *Nature Photonics* 4.2 (Feb. 2010), pp. 92–94. DOI: `10.1038/nphoton.2009.261`.

[6] Mattias Marklund. “Fundamental optical physics: Probing the quantum vacuum”. In: *Nature Photonics* 4.2 (Feb. 2010), pp. 72–74. DOI: `10.1038/nphoton.2009.277`.

[7] T. E. Northup and R. Blatt. “Quantum information transfer using photons”. In: *Nature Photonics* 8.5 (May 2014), pp. 356–363. DOI: `10.1038/nphoton.2014.53`.

[8] W. J. Munro et al. “From quantum multiplexing to high-performance quantum networking”. In: *Nature Photonics* 4.11 (Nov. 2010), pp. 792–796. DOI: `10.1038/nphoton.2010.213`.

[9] T. Pellizzari. “Quantum Networking with Optical Fibres”. In: *Physical Review Letters* 79.26 (Dec. 1997), pp. 5242–5245. DOI: `10.1103/PhysRevLett.79.5242`.

[10] K.C. Kao and G.A. Hockham. “Dielectric-fibre surface waveguides for optical frequencies”. In: *Proceedings of the Institution of Electrical Engineers* 113.7 (July 1966), pp. 1151–1158. DOI: `10.1049/piee.1966.0189`.

[11] Stephanie Wehner, David Elkouss, and Ronald Hanson. “Quantum internet: A vision for the road ahead”. In: *Science* 362.6412 (Oct. 2018), eaam9288. DOI: `10.1126/science.aam9288`.

[12] T. D. Ladd et al. “Quantum computers”. In: *Nature* 464.7285 (2010), pp. 45–53. DOI: `10.1038/nature08812`.

[13] S. Takeda and A. Furusawa. “Toward large-scale fault-tolerant universal photonic quantum computing”. In: *APL Photonics* 4.6 (2019). DOI: `10.1063/1.5100160`.

[14] Pieter Kok et al. “Linear optical quantum computing with photonic qubits”. In: *Reviews of Modern Physics* 79.1 (2007), pp. 135–174. DOI: `10.1103/RevModPhys.79.135`.

[15] E. Knill, R. Laflamme, and G. J. Milburn. “A scheme for efficient quantum computation with linear optics”. In: *Nature* 409.6816 (Jan. 2001), pp. 46–52. DOI: `10.1038/35051009`.

[16] Jianwei Wang et al. “Integrated photonic quantum technologies”. In: *Nature Photonics* 14.5 (2020), pp. 273–284. DOI: `10.1038/s41566-019-0532-1`. arXiv: `2005.01948`.

[17] M.G. Thompson et al. “Integrated waveguide circuits for optical quantum computing”. In: *IET Circuits, Devices & Systems* 5.2 (2011), p. 94. DOI: `10.1049/iet-cds.2010.0108`.

[18] A. Politi, J. C. F. Matthews, and J. L. O’Brien. “Shor’s Quantum Factoring Algorithm on a Photonic Chip”. In: *Science* 325.5945 (Sept. 2009), pp. 1221–1221. DOI: `10.1126/science.1173731`.

[19] Mario Arnolfo Ciampini et al. “Path-polarization hyperentangled and cluster states of photons on a chip”. In: *Light: Science & Applications* 5.4 (Apr. 2016), e16064–e16064. DOI: `10.1038/lsa.2016.64`.

[20] Chris Foot. *Atomic Physics*. 2005.

[21] D. Meschede, H. Walther, and G. Müller. “One-Atom Maser”. In: *Physical Review Letters* 54.6 (Feb. 1985), pp. 551–554. DOI: `10.1103/PhysRevLett.54.551`.

[22] J M Raimond, M Brune, and S Haroche. “Manipulating quantum entanglement with atoms and photons in a cavity”. In: *Reviews of Modern Physics* 73.3 (Aug. 2001), pp. 565–582. DOI: `10.1103/RevModPhys.73.565`.

[23] K. M. Birnbaum et al. “Photon blockade in an optical cavity with one trapped atom”. In: *Nature* 436.7047 (2005), pp. 87–90. DOI: `10.1038/nature03804`.

[24] H. J. Kimble. “Strong Interactions of Single Atoms and Photons in Cavity QED”. In: *Physica Scripta* T76.1 (1998), p. 127. DOI: `10.1238/Physica.Topical.076a00127`.

[25] Christoph Hamsen et al. “Two-Photon Blockade in an Atom-Driven Cavity QED System”. In: *Physical Review Letters* 118.13 (2017), pp. 1–6. DOI: `10.1103/PhysRevLett.118.133604`. arXiv: `1608.01571`.

[26] Bastian Hacker et al. “A photon-photon quantum gate based on a single atom in an optical resonator”. In: *Nature* 536.7615 (Aug. 2016), pp. 193–196. DOI: `10.1038/nature18592`.

[27] Asaf Paris-Mandoki et al. “Free-Space Quantum Electrodynamics with a Single Rydberg Superatom”. In: *Physical Review X* 7.4 (Oct. 2017), p. 041010. DOI: `10.1103/PhysRevX.7.041010`.

[28] L. Béguin et al. “Direct Measurement of the van der Waals Interaction between Two Rydberg Atoms”. In: *Physical Review Letters* 110.26 (June 2013), p. 263201. DOI: `10.1103/PhysRevLett.110.263201`.

[29] Sylvain de Léséleuc et al. “Optical Control of the Resonant Dipole-Dipole Interaction between Rydberg Atoms”. In: *Physical Review Letters* 119.5 (Aug. 2017), p. 053202. DOI: `10.1103/PhysRevLett.119.053202`.

[30] Antoine Browaeys, Daniel Barredo, and Thierry Lahaye. “Experimental investigations of dipole-dipole interactions between a few Rydberg atoms”. In: *Journal of Physics B: Atomic, Molecular and Optical Physics* 49.15 (Aug. 2016), p. 152001. DOI: `10.1088/0953-4075/49/15/152001`.

[31] Hanxiao Zhang et al. “Single-photon-level light storage with distributed Rydberg excitations in cold atoms”. In: *Frontiers of Physics* 17.2 (Apr. 2022), p. 22502. DOI: `10.1007/s11467-021-1105-6`.

[32] T. M. Weber et al. “Mesoscopic Rydberg-blockaded ensembles in the superatom regime and beyond”. In: *Nature Physics* 11.2 (Feb. 2015), pp. 157–161. DOI: `10.1038/nphys3214`.

[33] Y. O. Dudin et al. “Observation of coherent many-body Rabi oscillations”. In: *Nature Physics* 8.11 (Nov. 2012), pp. 790–794. DOI: `10.1038/nphys2413`.

[34] Rolf Heidemann et al. “Evidence for Coherent Collective Rydberg Excitation in the Strong Blockade Regime”. In: *Physical Review Letters* 99.16 (Oct. 2007), p. 163601. DOI: `10.1103/PhysRevLett.99.163601`.

[35] M. D. Lukin et al. “Dipole blockade and quantum information processing in mesoscopic atomic ensembles”. In: *Physical Review Letters* 87.3 (2001), pp. 37901–1–37901–4. DOI: `10.1103/PhysRevLett.87.037901`. arXiv: `0011028`.

[36] R. H. Dicke. “Coherence in Spontaneous Radiation Processes”. In: *Physical Review* 93.1 (Jan. 1954), pp. 99–110. DOI: `10.1103/PhysRev.93.99`.

[37] M. Gross and S. Haroche. “Superradiance: An essay on the theory of collective spontaneous emission”. In: *Physics Reports* 93.5 (Dec. 1982), pp. 301–396. DOI: `10.1016/0370-1573(82)90102-8`.

[38] I. I. Beterov et al. “Jaynes-Cummings dynamics in mesoscopic ensembles of Rydberg-blockaded atoms”. In: *Physical Review A* 90.4 (Oct. 2014), p. 043413. DOI: `10.1103/PhysRevA.90.043413`.

[39] Christine Guerlin et al. “Cavity quantum electrodynamics with a Rydberg-blocked atomic ensemble”. In: *Physical Review A* 82.5 (Nov. 2010), p. 053832. DOI: `10.1103/PhysRevA.82.053832`.

[40] Michael Fleischhauer, Atac Imamoglu, and Jonathan P Marangos. “Electromagnetically induced transparency: Optics in coherent media”. In: *Reviews of Modern Physics* 77.2 (July 2005), pp. 633–673. DOI: `10.1103/RevModPhys.77.633`.

[41] J.D. Pritchard. “Cooperative Optical Non-linearity in a blockaded Rydberg Ensemble”. PhD thesis. Durham University, 2011.

[42] Auxiliadora Padrón-Brito et al. “Transient dynamics of the quantum light retrieved from Rydberg polaritons”. In: *New Journal of Physics* 23.6 (2021). DOI: `10.1088/1367-2630/abfc19`. arXiv: `2011.12585`.

[43] Ofer Firstenberg et al. “Attractive photons in a quantum nonlinear medium”. In: *Nature* 502.7469 (Oct. 2013), pp. 71–75. DOI: `10.1038/nature12512`.

[44] Thibault Peyronel et al. “Quantum nonlinear optics with single photons enabled by strongly interacting atoms”. In: *Nature* 488.7409 (Aug. 2012), pp. 57–60. DOI: `10.1038/nature11361`.

[45] Y. O. Dudin and A. Kuzmich. “Strongly Interacting Rydberg Excitations of a Cold Atomic Gas”. In: *Science* 336.6083 (May 2012), pp. 887–889. DOI: `10.1126/science.1217901`.

[46] H. Busche. “Contactless quantum non-linear optics with cold Rydberg atoms”. PhD thesis. Durham University, 2017.

[47] Jun Li et al. “Semideterministic Entanglement between a Single Photon and an Atomic Ensemble”. In: *Physical Review Letters* 123.14 (Oct. 2019), p. 140504. DOI: `10.1103/PhysRevLett.123.140504`.

[48] D. Maxwell et al. “Microwave control of the interaction between two optical photons”. In: *Physical Review A* 89.4 (Apr. 2014), p. 043827. DOI: `10.1103/PhysRevA.89.043827`.

[49] M Fleischhauer and M D Lukin. “Dark-state polaritons in electromagnetically induced transparency”. In: *Phys. Rev. Lett.* 84.22 (2000), pp. 5094–5097. DOI: `10.1103/PhysRevLett.84.5094`. arXiv: `0001094`.

[50] Giovanni Ferioli et al. “Storage and Release of Subradiant Excitations in a Dense Atomic Cloud”. In: *Physical Review X* 11.2 (May 2021), p. 021031. DOI: `10.1103/PhysRevX.11.021031`.

[51] D. Maxwell et al. “Storage and control of optical photons using Rydberg polaritons”. In: *Physical Review Letters* 110.10 (2013). DOI: `10.1103/PhysRevLett.110.103001`. arXiv: `1207.6007`.

[52] I. Novikova, R.L. Walsworth, and Y. Xiao. "Electromagnetically induced transparency-based slow and stored light in warm atoms". In: *Laser & Photonics Reviews* 6.3 (May 2012), pp. 333–353. DOI: `10.1002/lpor.201100021`.

[53] Nathaniel B. Phillips, Alexey V. Gorshkov, and Irina Novikova. "Optimal light storage in atomic vapor". In: *Physical Review A - Atomic, Molecular, and Optical Physics* 78.2 (2008), pp. 1–10. DOI: `10.1103/PhysRevA.78.023801`. arXiv: `0805.3348`.

[54] Alexey V. Gorshkov et al. "Photon storage in ¡math display="inline"¿ ¡mi¿Λ¡/mi¿ ¡/math¿ -type optically dense atomic media. I. Cavity model". In: *Physical Review A* 76.3 (Sept. 2007), p. 033804. DOI: `10.1103/PhysRevA.76.033804`.

[55] Alexey V. Gorshkov et al. "Universal Approach to Optimal Photon Storage in Atomic Media". In: *Physical Review Letters* 98.12 (Mar. 2007), p. 123601. DOI: `10.1103/PhysRevLett.98.123601`.

[56] Karsten B. Dideriksen et al. "Room-temperature single-photon source with near-millisecond built-in memory". In: *Nature Communications* 12.1 (Dec. 2021), p. 3699. DOI: `10.1038/s41467-021-24033-8`.

[57] M Saffman. "Quantum computing with atomic qubits and Rydberg interactions: progress and challenges". In: *Journal of Physics B: Atomic, Molecular and Optical Physics* 49.20 (Oct. 2016), p. 202001. DOI: `10.1088/0953-4075/49/20/202001`.

[58] T. M. Graham et al. "Rydberg-Mediated Entanglement in a Two-Dimensional Neutral Atom Qubit Array". In: *Physical Review Letters* 123.23 (Dec. 2019), p. 230501. DOI: `10.1103/PhysRevLett.123.230501`.

[59] Daniel Tiarks et al. "A photon-photon quantum gate based on Rydberg interactions". In: *Nat. Phys.* 15.2 (2019), pp. 124–126. DOI: `10.1038/s41567-018-0313-7`.

[60] Y.-Y. Jau et al. "Entangling atomic spins with a Rydberg-dressed spin-flip blockade". In: *Nature Physics* 12.1 (Jan. 2016), pp. 71–74. DOI: `10.1038/nphys3487`.

[61] L Isenhower et al. "Demonstration of a Neutral Atom Controlled-NOT Quantum Gate". In: *Physical Review Letters* 104.1 (Jan. 2010), p. 10503. DOI: `10.1103/PhysRevLett.104.010503`.

[62] Yibo Wang et al. "Preparation of hundreds of microscopic atomic ensembles in optical tweezer arrays". In: *npj Quantum Information* 6.1 (Dec. 2020), p. 54. DOI: `10.1038/s41534-020-0285-1`.

[63] A. Arias et al. "Realization of a Rydberg-Dressed Ramsey Interferometer and Electrometer". In: *Physical Review Letters* 122.5 (Feb. 2019), p. 053601. DOI: `10.1103/PhysRevLett.122.053601`.

[64] Chao-Wei Yang et al. "Single-shot measurement of a Rydberg superatom via collective photon burst". In: (2021), pp. 1–6. arXiv: `2106.10858`.

[65] Nicholas L. R. Spong et al. "Collectively Encoded Rydberg Qubit". In: *Physical Review Letters* 127.6 (Aug. 2021), p. 063604. DOI: `10.1103/PhysRevLett.127.063604`.

[66] Nicholas E. Rehler and Jo9h H. Eberly. "Superradiance". In: *Physical Review A* 3.5 (May 1971), pp. 1735–1751. DOI: `10.1103/PhysRevA.3.1735`.

[67] G. Ferioli et al. "Laser driven superradiant ensembles of two-level atoms near Dicke's regime". In: (July 2021). arXiv: `2107.13392`.

[68] Robert J. Bettles et al. "Collective Mode Interferences in Light–Matter Interactions". In: (Aug. 2018). arXiv: `1808.08415`.

[69] Michelle O. Araújo et al. “Superradiance in a Large and Dilute Cloud of Cold Atoms in the Linear-Optics Regime”. In: *Physical Review Letters* 117.7 (Aug. 2016), p. 073002. DOI: `10.1103/PhysRevLett.117.073002`.

[70] S. J. Roof et al. “Observation of Single-Photon Superradiance and the Cooperative Lamb Shift in an Extended Sample of Cold Atoms”. In: *Physical Review Letters* 117.7 (Aug. 2016), p. 073003. DOI: `10.1103/PhysRevLett.117.073003`.

[71] C. C. Kwong et al. “Cooperative Emission of a Coherent Superflash of Light”. In: *Physical Review Letters* 113.22 (Nov. 2014), p. 223601. DOI: `10.1103/PhysRevLett.113.223601`.

[72] R. Rohlsberger et al. “Collective Lamb Shift in Single-Photon Superradiance”. In: *Science* 328.5983 (June 2010), pp. 1248–1251. DOI: `10.1126/science.1187770`.

[73] Z. Meir et al. “Cooperative Lamb Shift in a Mesoscopic Atomic Array”. In: *Physical Review Letters* 113.19 (Nov. 2014), p. 193002. DOI: `10.1103/PhysRevLett.113.193002`.

[74] Riccardo Pennetta et al. “Collective radiative dynamics of an ensemble of cold atoms coupled to an optical waveguide”. In: (Sept. 2021). DOI: `arXiv:2109.00860`. arXiv: `2109.00860`.

[75] A. Goban et al. “Superradiance for Atoms Trapped along a Photonic Crystal Waveguide”. In: *Physical Review Letters* 115.6 (2015). DOI: `10.1103/PhysRevLett.115.063601`. arXiv: `1503.04503`.

[76] William Guerin, Michelle O. Araújo, and Robin Kaiser. “Subradiance in a Large Cloud of Cold Atoms”. In: *Physical Review Letters* 116.8 (Feb. 2016), p. 083601. DOI: `10.1103/PhysRevLett.116.083601`.

[77] A. Cipris et al. “Subradiance with Saturated Atoms: Population Enhancement of the Long-Lived States”. In: *Physical Review Letters* 126.10 (Mar. 2021), p. 103604. DOI: `10.1103/PhysRevLett.126.103604`.

[78] Tom Bienaimé, Nicola Piovella, and Robin Kaiser. “Controlled Dicke Subradiance from a Large Cloud of Two-Level Systems”. In: *Physical Review Letters* 108.12 (Mar. 2012), p. 123602. DOI: `10.1103/PhysRevLett.108.123602`.

[79] J. F. Chen et al. “Optical coherent transients in cold atoms: From free-induction 12ay to optical precursors”. In: *Physical Review A - Atomic, Molecular, and Optical Physics* 81.3 (2010), pp. 1–11. DOI: `10.1103/PhysRevA.81.033844`.

[80] Dong Wei et al. “Optical precursors with electromagnetically induced transparency in cold atoms”. In: *Physical Review Letters* 103.9 (2009), pp. 1–4. DOI: `10.1103/PhysRevLett.103.093602`.

[81] H. X. Chen et al. “Observation of transient electromagnetically induced transparency in a rubidium Λ system”. In: *Physical Review A* 58.2 (Aug. 1998), pp. 1545–1548. DOI: `10.1103/PhysRevA.58.1545`.

[82] Qi Zhang, Zhengyang Bai, and Guoxiang Huang. “Fast-responding property of electromagnetically induced transparency in Rydberg atoms”. In: *Physical Review A* 97.4 (Apr. 2018), p. 043821. DOI: `10.1103/PhysRevA.97.043821`.

[83] Ya-Wei Guo et al. “Transient optical response of cold Rydberg atoms with electromagnetically induced transparency”. In: *Physical Review A* 101.2 (Feb. 2020), p. 023806. DOI: `10.1103/PhysRevA.101.023806`.

[84] Charles Möhl et al. “Photon correlation transients in a weakly blockaded Rydberg ensemble”. In: *Journal of Physics B: Atomic, Molec-*

*ular and Optical Physics* (Feb. 2020). DOI: `10.1088/1361-6455/ab728f`.

[85] Przemyslaw Bienias et al. “Photon propagation through dissipative Rydberg media at large input rates”. In: *Physical Review Research* 2.3 (2020), pp. 1–17. DOI: `10.1103/physrevresearch.2.033049`. arXiv: `1807.07586`.

[86] Nina Stiesdal et al. “Observation of collective 12ay dynamics of a single Rydberg superatom”. In: *Physical Review Research* 2.4 (Dec. 2020), p. 043339. DOI: `10.1103/PhysRevResearch.2.043339`.

[87] Jonathan Simon et al. “Interfacing collective atomic excitations and single photons”. In: *Physical Review Letters* 98.18 (2007), pp. 2–5. DOI: `10.1103/PhysRevLett.98.183601`. arXiv: `0702013`.

[88] John Preskill. “Quantum Computing in the NISQ era and beyond”. In: *Quantum* 2 (Aug. 2018), p. 79. DOI: `10.22331/q-2018-08-06-79`.

[89] N. Schlosser, G. Reymond, and P. Grangier. “Collisional Blockade in Microscopic Optical Dipole Traps”. In: *Physical Review Letters* 89.2 (June 2002), p. 023005. DOI: `10.1103/PhysRevLett.89.023005`.

[90] Nicolas Schlosser et al. “Sub-poissonian loading of single atoms in a microscopic dipole trap”. In: *Nature* 411.6841 (June 2001), pp. 1024–1027. DOI: `10.1038/35082512`.

[91] Yin Fung, Pimonpan Sompet, and Mikkel Andersen. “Single Atoms Preparation Using Light-Assisted Collisions”. In: *Technologies* 4.1 (Jan. 2016), p. 4. DOI: `10.3390/technologies4010004`.

[92] K. M. Maller et al. “Rydberg-blockade controlled-not gate and entanglement in a two-dimensional array of neutral-atom qubits”. In: *Physical Review A* 92.2 (Aug. 2015), p. 022336. DOI: `10.1103/PhysRevA.92.022336`.

[93] Harry Levine et al. “Parallel Implementation of High-Fidelity Multiqubit Gates with Neutral Atoms”. In: *Physical Review Letters* 123.17 (Oct. 2019), p. 170503. DOI: `10.1103/PhysRevLett.123.170503`.

[94] A. Omran et al. “Generation and manipulation of Schrödinger cat states in Rydberg atom arrays”. In: *Science* 365.6453 (Aug. 2019), pp. 570–574. DOI: `10.1126/science.aax9743`.

[95] T Wilk et al. “Entanglement of Two Individual Neutral Atoms Using Rydberg Blockade”. In: *Physical Review Letters* 104.1 (Jan. 2010), p. 10502. DOI: `10.1103/PhysRevLett.104.010502`.

[96] Pascal Scholl et al. “Programmable quantum simulation of 2D antiferromagnets with hundreds of Rydberg atoms”. In: (Dec. 2020). arXiv: `2012.12268`.

[97] Hannes Bernien et al. “Probing many-body dynamics on a 51-atom quantum simulator”. In: *Nature* 551.7682 (2017), pp. 579–584. DOI: `10.1038/nature24622`.

[98] Henning Labuhn et al. “Tunable two-dimensional arrays of single Rydberg atoms for realizing quantum Ising models”. In: *Nature* 534.7609 (June 2016), pp. 667–670. DOI: `10.1038/nature18274`.

[99] Giulia Semeghini et al. “Probing Topological Spin Liquids on a Programmable Quantum Simulator”. In: (2021). DOI: `arXiv:2104.04119`. arXiv: `2104.04119`.

[100] Shannon Whitlock, Alexander W Glaetzle, and Peter Hannaford. “Simulating quantum spin models using Rydberg-excited atomic ensembles in magnetic microtrap arrays”. In: *Journal of Physics B: Atomic, Molecular and Optical Physics* 50.7 (Apr. 2017), p. 074001. DOI: `10.1088/1361-6455/aa6149`.

[101] V. Y.F. Leung et al. “Microtrap arrays on magnetic film atom chips for quantum information science”. In: *Quantum Information Processing* 10.6 (2011), pp. 955–974. DOI: `10.1007/s11128-011-0295-1`. arXiv: `1104.3067`.

[102] Line Hjortshøj Pedersen and Klaus Mølmer. “Few qubit atom-light interfaces with collective encoding”. In: *Physical Review A* 79.1 (Jan. 2009), p. 012320. DOI: `10.1103/PhysRevA.79.012320`.

[103] E. Brion, K. Mølmer, and M. Saffman. “Quantum Computing with Collective Ensembles of Multilevel Systems”. In: *Physical Review Letters* 99.26 (Dec. 2007), p. 260501. DOI: `10.1103/PhysRevLett.99.260501`.

[104] N. Šibalić et al. “Dressed-state electromagnetically induced transparency for light storage in uniform-phase spin waves”. In: *Physical Review A* 94.3 (Sept. 2016), p. 033840. DOI: `10.1103/PhysRevA.94.033840`.

[105] Hannes Busche et al. “Contactless nonlinear optics mediated by long-range Rydberg interactions”. In: *Nature Physics* 13.7 (July 2017), pp. 655–658. DOI: `10.1038/nphys4058`.

[106] Stefan Langenfeld et al. “A network-ready random-access qubits memory”. In: *npj Quantum Information* 6.1 (2020), pp. 1–5. DOI: `10.1038/s41534-020-00316-8`. arXiv: `2011.00811`.

[107] N. Jiang et al. “Experimental realization of 105-qubit random access quantum memory”. In: *npj Quantum Information* 5.1 (2019). DOI: `10.1038/s41534-019-0144-0`. arXiv: `1904.09643`.

[108] C. Sturm et al. “All-optical phase modulation in a cavity-polariton Mach-Zehnder interferometer”. In: *Nature Communications* 5.1 (May 2014), p. 3278. DOI: `10.1038/ncomms4278`.

[109] Yuechun Jiao et al. “Single-photon stored-light Ramsey interferometry using Rydberg polaritons”. In: *Optics Letters* 45.20 (Oct. 2020), p. 5888. DOI: `10.1364/OL.405143`.

[110] Chloe So et al. “Zeeman-tunable modulation transfer spectroscopy”. In: *Optics Letters* 44.21 (Nov. 2019), p. 5374. DOI: `10.1364/OL.44.005374`.

[111] Jiandong Bai et al. “Autler-Townes doublet in single-photon Rydberg spectra of cesium atomic vapor with a 319 nm UV laser”. In: *Applied Physics B* 125.3 (Mar. 2019), p. 33. DOI: `10.1007/s00340-019-7151-x`.

[112] Daniel L Carr et al. “Measuring the Faraday effect in olive oil using permanent magnets and Malus’ law”. In: *European Journal of Physics* 41.2 (Mar. 2020), p. 025301. DOI: `10.1088/1361-6404/ab50dd`.

[113] J. D. Pritchard et al. “Cooperative atom-light interaction in a blockaded Rydberg ensemble”. In: *Physical Review Letters* (2010). DOI: `10.1103/PhysRevLett.105.193603`.

[114] M. Tanasittikosol et al. “Microwave dressing of Rydberg dark states”. In: *Journal of Physics B: Atomic, Molecular and Optical Physics* 184020 (2011), p. 184020. DOI: `10.1088/0953-4075/44/18/184020`. arXiv: `1102.0226`.

[115] M Saffman, T G Walker, and K Mølmer. “Quantum information with Rydberg atoms”. In: *Reviews of Modern Physics* 82.3 (Aug. 2010), pp. 2313–2363. DOI: `10.1103/RevModPhys.82.2313`.

[116] Ofer Firstenberg, Charles S Adams, and Sebastian Hofferberth. “Nonlinear quantum optics mediated by Rydberg interactions”. In: *Journal of Physics B: Atomic, Molecular and Optical Physics* 49.15 (2016), p. 152003. DOI: `10.1088/0953-4075/49/15/152003`. arXiv: `1602.06117`.

[117] Iris Cong et al. “Hardware-Efficient, Fault-Tolerant Quantum Computation with Rydberg Atoms”. In: (May 2021). arXiv: `2105.13501`.

[118] Xiaoling Wu et al. “A concise review of Rydberg atom based quantum computation and quantum simulation*”. In: *Chinese Physics B* 30.2 (Feb. 2021), p. 020305. DOI: `10.1088/1674-1056/abd76f`.

[119] C S Adams, J D Pritchard, and J P Shaffer. “Rydberg atom quantum technologies”. In: *Journal of Physics B: Atomic, Molecular and Optical Physics* 53.1 (Jan. 2020), p. 12002. DOI: `10.1088/1361-6455/ab52ef`.

[120] Loïc Henriet et al. “Quantum computing with neutral atoms”. In: *Quantum* 4 (Sept. 2020), p. 327. DOI: `10.22331/q-2020-09-21-327`.

[121] Antoine Browaeys and Thierry Lahaye. “Many-body physics with individually controlled Rydberg atoms”. In: *Nature Physics* 16.2 (Feb. 2020), pp. 132–142. DOI: `10.1038/s41567-019-0733-z`.

[122] S. E. Harris, J. E. Field, and A. Imamoglu. “Nonlinear optical processes using electromagnetically induced transparency”. In: *Physical Review Letters* 64.10 (Mar. 1990), pp. 1107–1110. DOI: `10.1103/PhysRevLett.64.1107`.

[123] S. Sevinçli et al. “Nonlocal Nonlinear Optics in Cold Rydberg Gases”. In: *Physical Review Letters* 107.15 (Oct. 2011), p. 153001. DOI: `10.1103/PhysRevLett.107.153001`.

[124] Alexey V. Gorshkov et al. “Photon-Photon Interactions via Rydberg Blockade”. In: *Physical Review Letters* 107.13 (Sept. 2011), p. 133602. DOI: `10.1103/PhysRevLett.107.133602`.

[125] L. A. Williamson, M. O. Borgh, and J. Ruostekoski. “Superatom Picture of Collective Nonclassical Light Emission and Dipole Blockade in Atom Arrays”. In: *Physical Review Letters* 125.7 (Aug. 2020), p. 073602. DOI: `10.1103/PhysRevLett.125.073602`.

[126] “Microscopic characterization of scalable coherent rydberg superatoms”. In: *Physical Review X* (2015). DOI: `10.1103/PhysRevX.5.031015`.

[127] K J Weatherill et al. “Electromagnetically induced transparency of an interacting cold Rydberg ensemble”. In: *Journal of Physics B: Atomic, Molecular and Optical Physics* 41.20 (Oct. 2008), p. 201002. DOI: `10.1088/0953-4075/41/20/201002`.

[128] M. Fleischhauer and M. D. Lukin. “Quantum memory for photons: Dark-state polaritons”. In: *Physical Review A* 65.2 (Jan. 2002), p. 022314. DOI: `10.1103/PhysRevA.65.022314`.

[129] F. Bariani et al. “Dephasing of Multiparticle Rydberg Excitations for Fast Entanglement Generation”. In: *Physical Review Letters* 108.3 (Jan. 2012), p. 030501. DOI: `10.1103/PhysRevLett.108.030501`.

[130] Sylvain Ravets et al. “Coherent dipole-dipole coupling between two single Rydberg atoms at an electrically-tuned Förster resonance”. In: *Nature Physics* 10.12 (Dec. 2014), pp. 914–917. DOI: `10.1038/nphys3119`.

[131] T. F. Gallagher et al. “Resonant Rydberg-atom – Rydbert-atom collisions”. In: *Physical Review A* 25.4 (Apr. 1982), pp. 1905–1917. DOI: `10.1103/PhysRevA.25.1905`.

[132] Thibault Vogt et al. “Dipole Blockade at Förster Resonances in High Resolution Laser Excitation of Rydberg States of Cesium Atoms”. In: *Physical Review Letters* 97.8 (Aug. 2006), p. 083003. DOI: `10.1103/PhysRevLett.97.083003`.

[133] Daniel Tiarks et al. “Optical $\pi$ phase shift created with a single-photon pulse”. In: *Science Advances* 2.4 (Apr. 2016), e1600036. DOI: `10.1126/sciadv.1600036`.

[134] Simon Baur et al. “Single-Photon Switch Based on Rydberg Blockade”. In: *Physical Review Letters* 112.7 (Feb. 2014), p. 073901. DOI: `10.1103/PhysRevLett.112.073901`.

[135] H. Gorniaczyk et al. “Single-Photon Transistor Mediated by Interstate Rydberg Interactions”. In: *Physical Review Letters* 113.5 (July 2014), p. 053601. DOI: `10.1103/PhysRevLett.113.053601`. arXiv: `/doi.org/10.1103/PhysRevLett.113.053601`.

[136] Daniel Tiarks et al. “Single-Photon Transistor Using a Förster Resonance”. In: *Physical Review Letters* 113.5 (July 2014), p. 053602. DOI: `10.1103/PhysRevLett.113.053602`.

[137] Lin Li and A Kuzmich. “Quantum memory with strong and controllable Rydberg-level interactions”. In: *Nature Communications* 7.1 (Dec. 2016), p. 13618. DOI: `10.1038/ncomms13618`.

[138] D. Paredes-Barato and C. S. Adams. “All-optical quantum information processing using rydberg gates”. In: *Physical Review Letters* 112.4 (2014), pp. 1–5. DOI: `10.1103/PhysRevLett.112.040501`. arXiv: `1309.7933`.

[139] T. M. Graham et al. “Rydberg-Mediated Entanglement in a Two-Dimensional Neutral Atom Qubit Array”. In: *Physical Review Letters* 123.23 (Dec. 2019), p. 230501. DOI: `10.1103/PhysRevLett.123.230501`.

[140] D Jaksch et al. “Fast Quantum Gates for Neutral Atoms”. In: *Physical Review Letters* 85.10 (Sept. 2000), pp. 2208–2211. DOI: `10.1103/PhysRevLett.85.2208`.

[141] Mohammadsadegh Khazali, Khabat Heshami, and Christoph Simon. “Photon-photon gate via the interaction between two collective Rydberg excitations”. In: *Physical Review A* 91.3 (Mar. 2015), p. 030301. DOI: `10.1103/PhysRevA.91.030301`.

[142] L. Isenhower, M. Saffman, and K. Mølmer. “Multibit C k NOT quantum gates via Rydberg blockade”. In: *Quantum Information Processing* 10.6 (Dec. 2011), pp. 755–770. DOI: `10.1007/s11128-011-0292-4`.

[143] Mohammadsadegh Khazali and Klaus Mølmer. “Fast Multiqubit Gates by Adiabatic Evolution in Interacting Excited-State Manifolds of Rydberg Atoms and Superconducting Circuits”. In: *Physical Review X* 10.2 (June 2020), p. 021054. DOI: `10.1103/PhysRevX.10.021054`.

[144] Sepehr Ebadi et al. “Quantum Phases of Matter on a 256-Atom Programmable Quantum Simulator”. In: (Dec. 2020). arXiv: `2012.12281`.

[145] Johannes Robert Rydberg. “Recherches sur la constitution des spectres d’émission des éléments chimiques”. In: *Kungliga vetenskapsakademiens handlingar* 23.11 (1890).

[146] J. J. Balmer. “Notiz über die Spectrallinien des Wasserstoffs”. In: *Annalen der Physik* 261.5 (1885), pp. 80–87. DOI: `10.1002/andp.18852610506`.

[147] N. Bohr. “I. On the constitution of atoms and molecules”. In: *The London, Edinburgh, and Dublin Philosophical Magazine and Journal of Science* 26.151 (July 1913), pp. 1–25. DOI: `10.1080/14786441308634955`.

[148] Greg A. Smith et al. “Efficient quantum-state estimation by continuous weak measurement and dynamical control”. In: *Physical Review Letters* 97.18 (2006), pp. 1–4. DOI: `10.1103/PhysRevLett.97.180403`. arXiv: `0606115`.

[149] D. R. Hartree. “The Wave Mechanics of an Atom with a Non-Coulomb Central Field. Part I. Theory and Methods”. In: *Mathematical Proceedings of the Cambridge Philosophical Society* 24.1 (Jan. 1928), pp. 89–110. DOI: `10.1017/S0305004100011919`.

[150] Jianing Han et al. "Rb nf quantum defects from millimeter-wave spectroscopy of cold Rb85 Rydberg atoms". In: *Physical Review A - Atomic, Molecular, and Optical Physics* 74.5 (Nov. 2006), p. 054502. DOI: `10.1103/PhysRevA.74.054502`.

[151] Wenhui Li et al. "Millimeter-wave spectroscopy of cold Rb Rydberg atoms in a magneto-optical trap: Quantum defects of the ns , np , and nd series". In: *Physical Review A* 67.5 (May 2003), p. 52502. DOI: `10.1103/PhysRevA.67.052502`.

[152] N. Šibalić et al. "ARC: An open-source library for calculating properties of alkali Rydberg atoms". In: *Computer Physics Communications* 220 (Nov. 2017), pp. 319–331. DOI: `10.1016/j.cpc.2017.06.015`.

[153] M Marinescu, H R Sadeghpour, and A Dalgarno. "Dispersion coefficients for alkali-metal dimers". In: *Physical Review A* 49.2 (Feb. 1994), pp. 982–988. DOI: `10.1103/PhysRevA.49.982`.

[154] F. Nez et al. "Optical frequency determination of the hyperfine components of the two-photon transitions in rubidium". In: *Optics Communications* 102.5-6 (Oct. 1993), pp. 432–438. DOI: `10.1016/0030-4018(93)90417-4`.

[155] Daniel Adam Steck. *Rubidium 87 D Line Data*. 2019.

[156] Nikola Sibalic. *Rydberg Physics*. IOP Publishing, 2018. DOI: `10.1088/978-0-7503-1635-4ch1`.

[157] Mitchel Weissbluth. *Atoms and Molecules*. Elsevier., 2012, pp. 159–167.

[158] Jonathan D Pritchard. *Cooperative Optical Non-Linearity in a Blockaded Rydberg Ensemble*. Springer Theses. Berlin, Heidelberg: Springer Berlin Heidelberg, 2012. ISBN: 978-3-642-29711-3. DOI: `10.1007/978-3-642-29712-0`.

[159] Myron L Zimmerman et al. “Stark structure of the Rydberg states of alkali-metal atoms”. In: *Physical Review A* 20.6 (Dec. 1979), pp. 2251–2275. DOI: `10.1103/PhysRevA.20.2251`.

[160] J. STARK. “Observation of the Separation of Spectral Lines by an Electric Field”. In: *Nature* 92.2301 (Dec. 1913), pp. 401–401. DOI: `10.1038/092401b0`.

[161] NN; Bonch-Bruevich, AM; Kostin and V V Khodovoi, VA; Khromov. “Changes in the atomic absorption spectrum in the field of a light wave I”. In: *Sov. Phys. JETP* 29 (1969), p. 82.

[162] M. S. O’Sullivan and B. P. Stoicheff. “Scalar polarizabilities and avoided crossings of high Rydberg states in Rb”. In: *Physical Review A* 31.4 (Apr. 1985), pp. 2718–2720. DOI: `10.1103/PhysRevA.31.2718`.

[163] N B Delone and Vladimir P Krai11. “AC Stark shift of atomic energy levels”. In: *Physics-Uspekhi* 42.7 (July 1999), pp. 669–687. DOI: `10.1070/PU1999v042n07ABEH000557`.

[164] Michèle Crance. “Nonperturbative ac Stark shifts in hydrogen atoms”. In: *Journal of the Optical Society of America B* 7.4 (Apr. 1990), p. 449. DOI: `10.1364/JOSAB.7.000449`.

[165] M. S. Safro11a, Carl J. Williams, and Charles W. Clark. “Relativistic many-body calculations of electric-dipole matrix elements, lifetimes, and polarizabilities in rubidium”. In: *Physical Review A* 69.2 (Feb. 2004), p. 022509. DOI: `10.1103/PhysRevA.69.022509`.

[166] M. Haas, U. D. Jentschura, and C. H. Keitel. “Comparison of classical and second quantized description of the dynamic Stark shift”. In: *American Journal of Physics* 74.1 (Jan. 2006), pp. 77–81. DOI: `10.1119/1.2140742`.

[167] Claude Cohen-/Tannoudji, Jacques Dupont-/Roc, and Gilbert Grynberg. *Atom–Photon Interactions.* Wiley, Apr. 1998. ISBN: 9780471293361. DOI: `10.1002/9783527617197`.

[168] Sylvain Ravets et al. “Measurement of the angular dependence of the dipole-dipole interaction between two individual Rydberg atoms at a Förster resonance”. In: *Physical Review A* 92.2 (Aug. 2015), p. 020701. DOI: `10.1103/PhysRevA.92.020701`.

[169] J. Nipper et al. “Highly Resolved Measurements of Stark-Tuned Förster Resonances between Rydberg Atoms”. In: *Physical Review Letters* 108.11 (Mar. 2012), p. 113001. DOI: `10.1103/PhysRevLett.108.113001`.

[170] I. I. Ryabtsev et al. “Observation of the Stark-Tuned Förster Resonance between Two Rydberg Atoms”. In: *Physical Review Letters* 104.7 (Feb. 2010), p. 073003. DOI: `10.1103/PhysRevLett.104.073003`.

[171] D. Tong et al. “Local Blockade of Rydberg Excitation in an Ultracold Gas”. In: *Physical Review Letters* 93.6 (Aug. 2004), p. 063001. DOI: `10.1103/PhysRevLett.93.063001`.

[172] Kilian Singer et al. “Suppression of Excitation and Spectral Broadening Induced by Interactions in a Cold Gas of Rydberg Atoms”. In: *Physical Review Letters* 93.16 (Oct. 2004), p. 163001. DOI: `10.1103/PhysRevLett.93.163001`.

[173] P Schauss et al. “Crystallization in Ising quantum magnets”. In: *Science* 347.6229 (Mar. 2015), pp. 1455–1458. DOI: `10.1126/science.1258351`.

[174] Michael Höning et al. “Steady-state crystallization of Rydberg excitations in an optically driven lattice gas”. In: *Physical Review A - Atomic, Molecular, and Optical Physics* 87.2 (2013), pp. 1–5. DOI: `10.1103/PhysRevA.87.023401`. arXiv: `1208.2911`.

[175] Peter Schauß et al. “Observation of spatially ordered structures in a two-dimensional Rydberg gas”. In: *Nature* 491.7422 (2012), pp. 87–91. DOI: `10.1038/nature11596`.

[176] R M W van Bijnen et al. “Adiabatic formation of Rydberg crystals with chirped laser pulses”. In: *Journal of Physics B: Atomic, Molecular and Optical Physics* 44.18 (Sept. 2011), p. 184008. DOI: `10.1088/0953-4075/44/18/184008`.

[177] T. Pohl, E. Demler, and M. D. Lukin. “Dynamical Crystallization in the Dipole Blockade of Ultracold Atoms”. In: *Physical Review Letters* 104.4 (Jan. 2010), p. 043002. DOI: `10.1103/PhysRevLett.104.043002`.

[178] Hendrik Weimer et al. “Quantum critical behavior in strongly interacting rydberg gases”. In: *Physical Review Letters* 101.25 (2008), pp. 1–4. DOI: `10.1103/PhysRevLett.101.250601`. arXiv: `0806.3754`.

[179] Wenlan Chen et al. “All-Optical Switch and Transistor Gated by One Stored Photon”. In: *Science* 341.6147 (Aug. 2013), pp. 768–770. DOI: `10.1126/science.1238169`.

[180] Sumanta Das et al. “Photonic controlled-phase gates through Rydberg blockade in optical cavities”. In: *Physical Review A* 93.4 (Apr. 2016), p. 040303. DOI: `10.1103/PhysRevA.93.040303`.

[181] X. L. Zhang et al. “Deterministic entanglement of two neutral atoms via Rydberg blockade”. In: *Physical Review A* 82.3 (Sept. 2010), p. 030306. DOI: `10.1103/PhysRevA.82.030306`.

[182] Chi Zhang et al. “Submicrosecond entangling gate between trapped ions via Rydberg interaction”. In: *Nature* 580.7803 (2020), pp. 345–349. DOI: `10.1038/s41586-020-2152-9`. arXiv: `1908.11284`.

[183] C. Tresp et al. "Single-Photon Absorber Based on Strongly Interacting Rydberg Atoms". In: *Physical Review Letters* 117.22 (Nov. 2016), p. 223001. DOI: `10.1103/PhysRevLett.117.223001`.

[184] Hannes Pichler et al. "Computational complexity of the Rydberg blockade in two dimensions". In: (Sept. 2018). arXiv: `1809.04954`.

[185] Harish Singh Rawat, Satya Kesh Dubey, and Vijay Narain Ojha. "Distinction between double electromagnetically induced transparency and double Autler-Townes splitting in RF-driven four-level ladder 87 Rb atomic vapor". In: *Journal of Physics B: Atomic, Molecular and Optical Physics* 51.15 (Aug. 2018), p. 155401. DOI: `10.1088/1361-6455/aacdd9`.

[186] David J. Griffiths. *Introduction to electrodynamics.* 2005.

[187] M G Bason et al. "Narrow absorptive resonances in a four-level atomic system". In: *Journal of Physics B: Atomic, Molecular and Optical Physics* 42.7 (Apr. 2009), p. 75503. DOI: `10.1088/0953-4075/42/7/075503`.

[188] G. Lindblad. "On the generators of quantum dynamical semigroups". In: *Communications in Mathematical Physics* 48.2 (June 1976), pp. 119–130. DOI: `10.1007/BF01608499`.

[189] Daniel Manzano. "A short introduction to the Lindblad master equation". In: *AIP Advances* 10.2 (Feb. 2020), p. 025106. DOI: `10.1063/1.5115323`.

[190] A K Mohapatra, T R Jackson, and C S Adams. "Coherent Optical Detection of Highly Excited Rydberg States Using Electromagnetically Induced Transparency". In: *Physical Review Letters* 98.11 (Mar. 2007), p. 113003. DOI: `10.1103/PhysRevLett.98.113003`.

[191] Min Xiao et al. "Measurement of dispersive properties of electromagnetically induced transparency in rubidium atoms". In: *Physical Re-*

*view Letters* 74.5 (1995), pp. 666–669. DOI: `10.1103/PhysRevLett.74.666`.

[192] D. Budker et al. “Nonlinear Magneto-optics and Reduced Group Velocity of Light in Atomic Vapor with Slow Ground State Relaxation”. In: *Physical Review Letters* 83.9 (Aug. 1999), pp. 1767–1770. DOI: `10.1103/PhysRevLett.83.1767`.

[193] Michael M. Kash et al. “Ultraslow Group Velocity and Enhanced Nonlinear Optical Effects in a Coherently Driven Hot Atomic Gas”. In: *Physical Review Letters* 82.26 (June 1999), pp. 5229–5232. DOI: `10.1103/PhysRevLett.82.5229`.

[194] Lene Vestergaard Hau et al. “Light speed reduction to 17 metres per second in an ultracold atomic gas”. In: *Nature* 397.6720 (Feb. 1999), pp. 594–598. DOI: `10.1038/17561`.

[195] D. F. Phillips et al. “Storage of Light in Atomic Vapor”. In: *Physical Review Letters* 86.5 (Jan. 2001), pp. 783–786. DOI: `10.1103/PhysRevLett.86.783`.

[196] Chien Liu et al. “Observation of coherent optical information storage in an atomic medium using halted light pulses”. In: *Nature* 409.6819 (Jan. 2001), pp. 490–493. DOI: `10.1038/35054017`.

[197] Marlan O. Scully. “Collective lamb shift in single photon dicke superradiance”. In: *Physical Review Letters* 102.14 (2009), pp. 1–4. DOI: `10.1103/PhysRevLett.102.143601`.

[198] F. Bariani, Paul M. Goldbart, and T. A. B. Kennedy. “Dephasing dynamics of Rydberg atom spin waves”. In: *Physical Review A* 86.4 (Oct. 2012), p. 041802. DOI: `10.1103/PhysRevA.86.041802`.

[199] Marlan O. Scully et al. “Directed spontaneous emission from an extended ensemble of N atoms: Timing is everything”. In: *Physical Review Letters* 96.1 (2006), pp. 1–4. DOI: `10.1103/PhysRevLett.96.010501`.

[200] M. Saffman and T. G. Walker. “Creating single-atom and single-photon sources from entangled atomic ensembles”. In: *Physical Review A* 66.6 (Dec. 2002), p. 065403. DOI: `10.1103/PhysRevA.66.065403`.

[201] Klemens Hammerer, Anders S. Sørensen, and Eugene S. Polzik. “Quantum interface between light and atomic ensembles”. In: *Reviews of Modern Physics* 82.2 (Apr. 2010), pp. 1041–1093. DOI: `10.1103/RevModPhys.82.1041`.

[202] M. Saffman and T. G. Walker. “Entangling single- and N-atom qubits for fast quantum state detection and transmission”. In: *Physical Review A - Atomic, Molecular, and Optical Physics* 72.4 (2005), pp. 1–6. DOI: `10.1103/PhysRevA.72.042302`. arXiv: `0402111`.

[203] Rejjak Laskar, Md Mabud Hossain, and Jayanta K Saha. “The analysis of coherent phenomena for both linear and non-linear interactions in a four-level ladder (Ξ)-type configuration using density matrix formalism in dressed state representation”. In: *Physica Scripta* 96.3 (Mar. 2021), p. 035108. DOI: `10.1088/1402-4896/abdbf3`.

[204] Hannes Busche, Simon W Ball, and Paul Huillery. “A high repetition rate experimental setup for quantum non-linear optics with cold Rydberg atoms”. In: *The European Physical Journal Special Topics* 225.15-16 (Dec. 2016), pp. 2839–2861. DOI: `10.1140/epjst/e2015-50338-3`.

[205] Simon William Ball. “A coherent microwave interface for manipulation of single optical photons”. PhD thesis. Durham Unviersity, 2017, p. 102.

[206] Teodora Ilieva. “Collective Behaviour in Cold Rubidium Atoms”. PhD thesis. Durham University, 2019.

[207] T. P. Wiles. “Dynamics of bright solitary matter-waves”. PhD thesis. Durham Unviersity, 2013.

[208] Vladislav Gavryusev. “Imaging of Rydberg Impurities in an Ultracold Atomic Gas”. PhD thesis. Ruperto-Carola-University of Heidelberg, 2016.

[209] C. S. Hofmann et al. “An experimental approach for investigating many-body phenomena in Rydberg-interacting quantum systems”. In: *Frontiers of Physics* 9.5 (Oct. 2014), pp. 571–586. DOI: `10.1007/s11467-013-0396-7`.

[210] Alexander Franzen. *ComponentLibrary.* 2006.

[211] Darrick E. Chang, Vladan Vuletić, and Mikhail D. Lukin. “Quantum nonlinear optics – photon by photon”. In: *Nature Photonics* 8.9 (Sept. 2014), pp. 685–694. DOI: `10.1038/nphoton.2014.192`.

[212] Wolfgang Petrich et al. “Behavior of atoms in a compressed magneto-optical trap”. In: *Journal of the Optical Society of America B* 11.8 (Aug. 1994), p. 1332. DOI: `10.1364/JOSAB.11.001332`.

[213] C. G. Townsend et al. “Phase-space density in the magneto-optical trap”. In: *Physical Review A* 52.2 (Aug. 1995), pp. 1423–1440. DOI: `10.1103/PhysRevA.52.1423`.

[214] K. Dieckmann et al. “Two-dimensional magneto-optical trap as a source of slow atoms”. In: *Physical Review A - Atomic, Molecular, and Optical Physics* 58.5 (1998), pp. 3891–3895. DOI: `10.1103/PhysRevA.58.3891`.

[215] Matthew T. Hummon et al. “2D magneto-optical trapping of diatomic molecules”. In: *Physical Review Letters* 110.14 (2013), pp. 1–5. DOI: `10.1103/PhysRevLett.110.143001`. arXiv: `1209.4069`.

[216] Sung Jong Park, Jiho Noh, and Jongchul Mun. “Cold atomic beam from a two-dimensional magneto-optical trap with two-color pushing laser beams”. In: *Optics Communications* 285.19 (Sept. 2012), pp. 3950–3954. DOI: `10.1016/j.optcom.2012.05.041`.

[217] E. L. Raab et al. “Trapping of Neutral Sodium Atoms with Radiation Pressure”. In: *Physical Review Letters* 59.23 (Dec. 1987), pp. 2631–2634. DOI: `10.1103/PhysRevLett.59.2631`.

[218] Hannes Busche. “Contactless quantum non-linear optics with cold Rydberg atoms”. PhD thesis. Durham Unviersity, 2017.

[219] Paul D. Lett et al. “Observation of Atoms Laser Cooled below the Doppler Limit”. In: *Physical Review Letters* 61.2 (July 1988), pp. 169–172. DOI: `10.1103/PhysRevLett.61.169`.

[220] M Weidemüller et al. “A Novel Scheme for Efficient Cooling below the Photon Recoil Limit”. In: *Europhysics Letters (EPL)* 27.2 (July 1994), pp. 109–114. DOI: `10.1209/0295-5075/27/2/006`.

[221] P. D. Lett et al. “Optical molasses”. In: *Journal of the Optical Society of America B* 6.11 (Nov. 1989), p. 2084. DOI: `10.1364/JOSAB.6.002084`.

[222] Saptarishi Chaudhuri, Sanjukta Roy, and C S Unnikrishnan. “Evaporative Cooling of Atoms to Quantum Degeneracy in an Optical Dipole Trap”. In: *Journal of Physics: Conference Series* 80 (Sept. 2007), p. 012036. DOI: `10.1088/1742-6596/80/1/012036`.

[223] R. Hanbury Brown and R.Q. Twiss. “LXXIV. A new type of interferometer for use in radio astronomy”. In: *The London, Edinburgh, and Dublin Philosophical Magazine and Journal of Science* 45.366 (July 1954), pp. 663–682. DOI: `10.1080/14786440708520475`.

[224] Gary C. Bjorklund. “Frequency-modulation spectroscopy: a new method for measuring weak absorptions and dispersions”. In: *Optics Letters* 5.1 (Jan. 1980), p. 15. DOI: `10.1364/OL.5.000015`.

[225] D J McCarron, S A King, and S L Cornish. “Modulation transfer spectroscopy in atomic rubidium”. In: *Measurement Science and Technology* 19.10 (Oct. 2008), p. 105601. DOI: `10.1088/0957-0233/19/10/105601`.

[226] Tilman Preuschoff, Malte Schlosser, and Gerhard Birkl. "Optimization strategies for modulation transfer spectroscopy applied to laser stabilization". In: *Optics Express* 26.18 (Sept. 2018), p. 24010. DOI: `10.1364/OE.26.024010`.

[227] Jon H. Shirley. "Modulation transfer processes in optical heterodyne saturation spectroscopy". In: *Optics Letters* 7.11 (Nov. 1982), p. 537. DOI: `10.1364/OL.7.000537`.

[228] Chloe So. "Zeeman-tunable Modulation Transfer Spectroscopy". PhD thesis. Durham University, 2020.

[229] Anna L. Marchant et al. "Off-resonance laser frequency stabilization using the Faraday effect". In: *Optics Letters* 36.1 (Jan. 2011), p. 64. DOI: `10.1364/OL.36.000064`.

[230] D. J. Reed et al. "Low-drift Zeeman shifted atomic frequency reference". In: *OSA Continuum* 1.1 (Sept. 2018), p. 4. DOI: `10.1364/OSAC.1.000004`.

[231] Jin-Bao Long et al. "Magnetic-enhanced modulation transfer spectroscopy and laser locking for 87 Rb repump transition". In: *Optics Express* 26.21 (Oct. 2018), p. 27773. DOI: `10.1364/OE.26.027773`.

[232] Remy Legaie, Craig J. Picken, and Jonathan D. Pritchard. "Sub-kilohertz excitation lasers for quantum information processing with Rydberg atoms". In: *Journal of the Optical Society of America B* 35.4 (Apr. 2018), p. 892. DOI: `10.1364/JOSAB.35.000892`.

[233] P D Gregory et al. "A simple, versatile laser system for the creation of ultracold ground state molecules". In: *New Journal of Physics* 17.5 (May 2015), p. 055006. DOI: `10.1088/1367-2630/17/5/055006`.

[234] J. I. Thorpe, K. Numata, and J. Livas. "Laser frequency stabilization and control through offset sideband locking to optical cavities". In:

*Optics Express* 16.20 (Sept. 2008), p. 15980. DOI: `10.1364/OE.16.015980`.

[235] Rudolf Grimm, Matthias Weidemüller, and Yurii B. Ovchinnikov. "Optical Dipole Traps for Neutral Atoms". In: *Advances in Atomic, Molecular and Optical Physics* 42.C (2000), pp. 95–170. DOI: `10.1016/S1049-250X(08)60186-X`. arXiv: `9902072`.

[236] Charles S. Adams et al. "Evaporative Cooling in a Crossed Dipole Trap". In: *Physical Review Letters* 74.18 (May 1995), pp. 3577–3580. DOI: `10.1103/PhysRevLett.74.3577`.

[237] D Jacob et al. "Production of sodium Bose-Einstein condensates in an optical dimple trap". In: *New Journal of Physics* 13.6 (2011), p. 065022. DOI: `10.1088/1367-2630/13/6/065022`. arXiv: `1104.1009`.

[238] D. Sofikitis et al. "Loading a dipole trap from an atomic reservoir". In: *The European Physical Journal D* 61.2 (Jan. 2011), pp. 437–442. DOI: `10.1140/epjd/e2010-10261-5`.

[239] Richard G. Brewer and R. L. Shoemaker. "Optical Free Induction Decay". In: *Physical Review A* 6.6 (Dec. 1972), pp. 2001–2007. DOI: `10.1103/PhysRevA.6.2001`.

[240] J. M. Raimond et al. "Collective Absorption of Blackbody Radiation by Rydberg Atoms in a Cavity: An Experiment on Bose Statistics and Brownian Motion". In: *Physical Review Letters* 49.2 (July 1982), pp. 117–120. DOI: `10.1103/PhysRevLett.49.117`.

[241] W. Dür, G. Vidal, and J. I. Cirac. "Three qubits can be entangled in two inequivalent ways". In: *Physical Review A* 62.6 (Nov. 2000), p. 062314. DOI: `10.1103/PhysRevA.62.062314`.

[242] M. M. Müller et al. "Room-temperature Rydberg single-photon source". In: *Physical Review A - Atomic, Molecular, and Optical Physics* 87.5 (2013). DOI: `10.1103/PhysRevA.87.053412`. arXiv: `1212.2811`.

[243] N. J. Schilder et al. “Polaritonic modes in a dense cloud of cold atoms”. In: *Physical Review A* 93.6 (June 2016), p. 063835. DOI: 10.1103/PhysRevA.93.063835.

[244] Yutaka Yoshikawa, Yoshio Torii, and Takahiro Kuga. “Superradiant Light Scattering from Thermal Atomic Vapors”. In: *Physical Review Letters* 94.8 (Mar. 2005), p. 083602. DOI: 10.1103/PhysRevLett.94.083602.

[245] Stuart J Masson and Ana Asenjo-Garcia. “Universality of Dicke superradiance in atomic arrays”. In: (2021). DOI: arXiv:2106.02042. arXiv: 2106.02042.

[246] N. J. Schilder et al. “Near-Resonant Light Scattering by a Subwavelength Ensemble of Identical Atoms”. In: *Physical Review Letters* 124.7 (Feb. 2020), p. 073403. DOI: 10.1103/PhysRevLett.124.073403.

[247] David Petrosyan and Klaus Mølmer. “Collective emission of photons from dense, dipole-dipole interacting atomic ensembles”. In: *Physical Review A* 103.2 (Feb. 2021), p. 023703. DOI: 10.1103/PhysRevA.103.023703.

[248] M. Chalony et al. “Coherent flash of light emitted by a cold atomic cloud”. In: *Physical Review A* 84.1 (July 2011), p. 011401. DOI: 10.1103/PhysRevA.84.011401.

[249] Jan Kumlin et al. “Nonexponential 12ay of a collective excitation in an atomic ensemble coupled to a one-dimensional waveguide”. In: *Physical Review A* 102.6 (Dec. 2020), p. 063703. DOI: 10.1103/PhysRevA.102.063703.

[250] Stewart D. Jenkins et al. “Many-Body Subradiant Excitations in Metamaterial Arrays: Experiment and Theory”. In: *Physical Review Letters* 119.5 (Aug. 2017), p. 053901. DOI: 10.1103/PhysRevLett.119.053901.

[251] Fabian Ripka et al. “A room-temperature single-photon source based on strongly interacting Rydberg atoms”. In: *Science* 362.6413 (Oct. 2018), pp. 446–449. DOI: `10.1126/science.aau1949`.

[252] C. S. Hofmann et al. “Sub-Poissonian Statistics of Rydberg-Interacting Dark-State Polaritons”. In: *Physical Review Letters* 110.20 (May 2013), p. 203601. DOI: `10.1103/PhysRevLett.110.203601`.

[253] L. Li, Y. O. Dudin, and A. Kuzmich. “Entanglement between light and an optical atomic excitation”. In: *Nature* 498.7455 (June 2013), pp. 466–469. DOI: `10.1038/nature12227`.

[254] E. Distante et al. “Storage Enhanced Nonlinearities in a Cold Atomic Rydberg Ensemble”. In: *Physical Review Letters* 117.11 (Sept. 2016), p. 113001. DOI: `10.1103/PhysRevLett.117.113001`.

[255] Jeff D. Thompson et al. “Symmetry-protected collisions between strongly interacting photons”. In: *Nature* 542.7640 (Feb. 2017), pp. 206–209. DOI: `10.1038/nature20823`.

[256] Emanuele Distante et al. “Storing single photons emitted by a quantum memory on a highly excited Rydberg state”. In: *Nature Communications* 8.1 (Apr. 2017), p. 14072. DOI: `10.1038/ncomms14072`.

[257] A. A. Morgan and S. D. Hogan. “Coupling Rydberg Atoms to Microwave Fields in a Superconducting Coplanar Waveguide Resonator”. In: *Physical Review Letters* 124.19 (May 2020), p. 193604. DOI: `10.1103/PhysRevLett.124.193604`.

[258] Manuel Kaiser et al. “Cavity driven Rabi oscillations between Rydberg states of atoms trapped on a superconducting atom chip”. In: (2021). DOI: `arXiv:2105.05188`. arXiv: `2105.05188`.

[259] X. Zhang et al. “Rydberg blockade effects at ¡math¿ ¡mrow¿ ¡mi¿n¡/mi¿ ¡mo¿ ¡/mo¿ ¡mn¿300¡/mn¿ ¡/mrow¿ ¡/math¿ in strontium”. In: *Physical Review A* 92.5 (Nov. 2015), p. 051402. DOI: `10.1103/PhysRevA.92.051402`.

[260] A. Sommerfeld. “Über die Fortpflanzung des Lichtes in dispergierenden Medien”. In: *Annalen der Physik* 349.10 (1914), pp. 177–202. DOI: `10.1002/andp.19143491002`.

[261] L. Brillouin. “Über die Fortpflanzung des Lichtes in dispergierenden Medien”. In: *Annalen der Physik* 349.10 (1914), pp. 203–240. DOI: `10.1002/andp.19143491003`.

[262] Shanchao Zhang et al. “Optical Precursor of a Single Photon”. In: *Physical Review Letters* 106.24 (June 2011), p. 243602. DOI: `10.1103/PhysRevLett.106.243602`.

[263] Robert J. Bettles, Simon A. Gardiner, and Charles S. Adams. “Enhanced Optical Cross Section via Collective Coupling of Atomic Dipoles in a 2D Array”. In: *Physical Review Letters* 116.10 (Mar. 2016), p. 103602. DOI: `10.1103/PhysRevLett.116.103602`.

[264] Ephraim Shahmoon et al. “Cooperative Resonances in Light Scattering from Two-Dimensional Atomic Arrays”. In: *Physical Review Letters* 118.11 (Mar. 2017), p. 113601. DOI: `10.1103/PhysRevLett.118.113601`.

[265] W. Guerin, M.T. Rouabah, and R. Kaiser. “Light interacting with atomic ensembles: collective, cooperative and mesoscopic effects”. In: *Journal of Modern Optics* 64.9 (May 2017), pp. 895–907. DOI: `10.1080/09500340.2016.1215564`.

[266] William Guerin and Robin Kaiser. “Population of collective modes in light scattering by many atoms”. In: *Physical Review A* 95.5 (May 2017), p. 053865. DOI: `10.1103/PhysRevA.95.053865`.

[267] Diptaran1 Das, B. Lemberger, and D. D. Yavuz. “Subradiance and superradiance-to-subradiance transition in dilute atomic clouds”. In: *Physical Review A* 102.4 (Oct. 2020), p. 043708. DOI: `10.1103/PhysRevA.102.043708`.

[268] K. Toyoda et al. “Optical free-induction 12ay of laser-cooled ¡math display=”inline”¿ ¡mrow¿ ¡msup¿ ¡mrow/¿ ¡mrow¿ ¡mn¿85¡/mn¿ ¡/mrow¿ ¡/msup¿ ¡/mrow¿ ¡/math¿ Rb”. In: *Physical Review A* 56.2 (Aug. 1997), pp. 1564–1568. DOI: `10.1103/PhysRevA.56.1564`.

[269] Michael Scheibner et al. “Superradiance of quantum dots”. In: *Nature Physics* 3.2 (Feb. 2007), pp. 106–110. DOI: `10.1038/nphys494`.

[270] N. Skribanowitz et al. “Observation of Dicke Superradiance in Optically Pumped HF Gas”. In: *Physical Review Letters* 30.8 (Feb. 1973), pp. 309–312. DOI: `10.1103/PhysRevLett.30.309`.

[271] M. Gross et al. “Observation of Near-Infrared Dicke Superradiance on Cascading Transitions in Atomic Sodium”. In: *Physical Review Letters* 36.17 (Apr. 1976), pp. 1035–1038. DOI: `10.1103/PhysRevLett.36.1035`.

[272] M. O. Scully and A. A. Svidzinsky. “The Super of Superradiance”. In: *Science* 325.5947 (Sept. 2009), pp. 1510–1511. DOI: `10.1126/science.1176695`.

[273] S. D. Jenkins et al. “Collective resonance fluorescence in small and dense atom clouds: Comparison between theory and experiment”. In: *Physical Review A* 94.2 (Aug. 2016), p. 023842. DOI: `10.1103/PhysRevA.94.023842`.

[274] J. Pellegrino et al. “Observation of Suppression of Light Scattering Induced by Dipole-Dipole Interactions in a Cold-Atom Ensemble”. In: *Physical Review Letters* 113.13 (Sept. 2014), p. 133602. DOI: `10.1103/PhysRevLett.113.133602`.

[275] Rafael A. de Oliveira et al. “Single-photon superradiance in cold atoms”. In: *Physical Review A* 90.2 (Aug. 2014), p. 023848. DOI: `10.1103/PhysRevA.90.023848`.

[276] Daniel Adam Steck. *Rubidium 87 D Line Data.* Tech. rep. 2015. arXiv: `0612314`.

[277] C. Ates, S. Sevinçli, and T. Pohl. “Electromagnetically induced transparency in strongly interacting Rydberg gases”. In: *Physical Review A* 83.4 (Apr. 2011), p. 041802. DOI: `10.1103/PhysRevA.83.041802`.

[278] Josiah Sinclair et al. “Observation of a large, resonant, cross-Kerr nonlinearity in a cold Rydberg gas”. In: *Physical Review Research* 1.3 (Dec. 2019), p. 033193. DOI: `10.1103/PhysRevResearch.1.033193`.

[279] H. J. Kimble. “The quantum internet”. In: *Nature* 453.7198 (June 2008), pp. 1023–1030. DOI: `10.1038/nature07127`.

[280] Neal Solmeyer, Xiao Li, and Qudsia Quraishi. “High teleportation rates using cold-atom-ensemble-based quantum repeaters with Rydberg blockade”. In: *Physical Review A* 93.4 (Apr. 2016), p. 042301. DOI: `10.1103/PhysRevA.93.042301`.

[281] Y. M. Hao et al. “Quantum controlled-phase-flip gate between a flying optical photon and a Rydberg atomic ensemble”. In: *Scientific Reports* 5.March (2015), pp. 1–7. DOI: `10.1038/srep10005`.

[282] M. Müller et al. “Mesoscopic Rydberg Gate Based on Electromagnetically Induced Transparency”. In: *Physical Review Letters* 102.17 (Apr. 2009), p. 170502. DOI: `10.1103/PhysRevLett.102.170502`.

[283] Y. M. Hao et al. “Single-photon transistor based on cavity electromagnetically induced transparency with Rydberg atomic ensemble”. In: *Scientific Reports* 9.1 (Dec. 2019), p. 4723. DOI: `10.1038/s41598-019-41185-2`.

[284] Emil Zeuthen et al. “Correlated Photon Dynamics in Dissipative Rydberg Media”. In: *Physical Review Letters* 119.4 (July 2017), p. 043602. DOI: `10.1103/PhysRevLett.119.043602`.

[285] Heinz-Peter Breuer and Francesco Petruccione. *The Theory of Open Quantum Systems*. Oxford University Press, Jan. 2007. ISBN: 9780199213900. DOI: `10.1093/acprof:oso/9780199213900.001.0001`.

[286] C. Murray and T. Pohl. "Quantum and Nonlinear Optics in Strongly Interacting Atomic Ensembles". In: *Advances in Atomic, Molecular and Optical Physics* 65 (2016), pp. 321–372. DOI: `10.1016/bs.aamop.2016.04.005`. arXiv: `1710.08547`.

[287] Adam Gali. "Theory of the neutral nitrogen-vacancy center in diamond and its application to the realization of a qubit". In: *Physical Review B - Condensed Matter and Materials Physics* 79.23 (2009). DOI: `10.1103/PhysRevB.79.235210`.

[288] Mohammad Reza Jalali Azizpour et al. "All-Optical Ultra-Fast Graphene-Photonic Crystal Switch". In: *Crystals* 9.9 (Sept. 2019), p. 461. DOI: `10.3390/cryst9090461`.

[289] "Photon correlation transients in a weakly-blockaded Rydberg ensemble". PhD thesis. Universitat Heidelberg \& Durham University.

[290] J. D. Pritchard et al. "Hybrid atom-photon quantum gate in a superconducting microwave resonator". In: *Physical Review A* 89.1 (Jan. 2014), p. 010301. DOI: `10.1103/PhysRevA.89.010301`.

[291] Greg A. Smith et al. "Continuous Weak Measurement and Nonlinear Dynamics in a Cold Spin Ensemble". In: *Physical Review Letters* 93.16 (Oct. 2004), p. 163602. DOI: `10.1103/PhysRevLett.93.163602`.

[292] G. Facchinetti, S. D. Jenkins, and J. Ruostekoski. "Storing Light with Subradiant Correlations in Arrays of Atoms". In: *Physical Review Letters* 117.24 (Dec. 2016), p. 243601. DOI: `10.1103/PhysRevLett.117.243601`.

[293] Chang Huang, Shijie Chai, and Shau-Yu Lan. “Dark-state sideband cooling in an atomic ensemble”. In: *Physical Review A* 103.1 (Jan. 2021), p. 013305. DOI: `10.1103/PhysRevA.103.013305`.

[294] Daniel Szombati et al. “Quantum Rifling: Protecting a Qubit from Measurement Back Action”. In: *Physical Review Letters* 124.7 (Feb. 2020), p. 070401. DOI: `10.1103/PhysRevLett.124.070401`.

[295] T. M. Stace and S. D. Barrett. “Continuous Quantum Measurement: Inelastic Tunneling and Lack of Current Oscillations”. In: *Physical Review Letters* 92.13 (Apr. 2004), p. 136802. DOI: `10.1103/PhysRevLett.92.136802`.

[296] Shanchao Zhang et al. “Coherent Control of Single-Photon Absorption and Reemission in a Two-Level Atomic Ensemble”. In: *Physical Review Letters* 109.26 (Dec. 2012), p. 263601. DOI: `10.1103/PhysRevLett.109.263601`.

[297] Auxiliadora Padrón-Brito et al. “Probing the indistinguishability of single photons generated by Rydberg atomic ensembles”. In: (Nov. 2020). arXiv: `2011.06901`.

[298] Ehud Altman et al. “Quantum Simulators: Architectures and Opportunities”. In: *PRX Quantum* 2.1 (2021), pp. 1–19. DOI: `10.1103/prxquantum.2.017003`. arXiv: `1912.06938`.

[299] L.-M. Duan et al. “Long-distance quantum communication with atomic ensembles and linear optics”. In: *Nature* 414.6862 (Nov. 2001), pp. 413–418. DOI: `10.1038/35106500`.

[300] M. Ebert et al. “Coherence and Rydberg Blockade of Atomic Ensemble Qubits”. In: *Physical Review Letters* 115.9 (Aug. 2015), p. 093601. DOI: `10.1103/PhysRevLett.115.093601`.

[301] Chen Yue Guo et al. “Optimized geometric quantum computation with a mesoscopic ensemble of Rydberg atoms”. In: *Physical Review*

*A* 102.4 (2020), pp. 1–17. DOI: `10.1103/PhysRevA.102.042607`. arXiv: `2009.03718`.

[302] Frank Arute et al. “Quantum supremacy using a programmable superconducting processor”. In: *Nature* 574.7779 (Oct. 2019), pp. 505–510. DOI: `10.1038/s41586-019-1666-5`.

[303] F. Nogrette et al. “Single-Atom Trapping in Holographic 2D Arrays of Microtraps with Arbitrary Geometries”. In: *Physical Review X* 4.2 (May 2014), p. 021034. DOI: `10.1103/PhysRevX.4.021034`.

[304] Manuel Endres et al. “Atom-by-atom assembly of defect-free one-dimensional cold atom arrays”. In: *Science* 354.6315 (Nov. 2016), pp. 1024–1027. DOI: `10.1126/science.aah3752`.

[305] Ryszard Horo12ki et al. “Quantum entanglement”. In: *Reviews of Modern Physics* 81.2 (June 2009), pp. 865–942. DOI: `10.1103/RevModPhys.81.865`.

[306] E. Brion et al. “Error Correction in Ensemble Registers for Quantum Repeaters and Quantum Computers”. In: *Physical Review Letters* 100.11 (Mar. 2008), p. 110506. DOI: `10.1103/PhysRevLett.100.110506`.

[307] I I Beterov et al. “Application of adiabatic passage in Rydberg atomic ensembles for quantum information processing”. In: *Journal of Physics B: Atomic, Molecular and Optical Physics* 53.18 (Sept. 2020), p. 182001. DOI: `10.1088/1361-6455/ab8719`.

[308] Keyu Su et al. “Synchronization and phase shaping of single photons with high-efficiency quantum memory”. In: (July 2021). arXiv: `2107.08742`.

[309] Mehdi Namazi et al. “Free-Space Quantum Communication with a Portable Quantum Memory”. In: *Physical Review Applied* 8.6 (2017). DOI: `10.1103/PhysRevApplied.8.064013`. arXiv: `1609.08676`.

[310] Daniel Cano. “Conditional STIRAP based on Rydberg blockade: entanglement fidelities in three- and four-level schemes”. In: *Journal of Physics B: Atomic, Molecular and Optical Physics* 54.4 (Feb. 2021), p. 045502. DOI: `10.1088/1361-6455/abdf18`.

[311] Robert J. Bettles. “Cooperative Interactions in Lattices of Atomic Dipoles”. PhD thesis. Durham University, 2016.

[312] Minho Kwon et al. “Parallel Low-Loss Measurement of Multiple Atomic Qubits”. In: *Physical Review Letters* 119.18 (Oct. 2017), p. 180504. DOI: `10.1103/PhysRevLett.119.180504`.

[313] Alexander I. Lvovsky, Barry C. Sanders, and Wolfgang Tittel. “Optical quantum memory”. In: *Nature Photonics* 3.12 (2009), pp. 706–714. DOI: `10.1038/nphoton.2009.231`. arXiv: `1002.4659`.

[314] C. Li et al. “Quantum Communication between Multiplexed Atomic Quantum Memories”. In: *Physical Review Letters* 124.24 (2020), pp. 1–9. DOI: `10.1103/PhysRevLett.124.240504`. arXiv: `1909.02185`.

[315] Robert J. Bettles, Simon A. Gardiner, and Charles S. Adams. “Enhanced Optical Cross Section via Collective Coupling of Atomic Dipoles in a 2D Array”. In: *Physical Review Letters* 116.10 (Mar. 2016), p. 103602. DOI: `10.1103/PhysRevLett.116.103602`.

[316] T. L. Nguyen et al. “Towards Quantum Simulation with Circular Rydberg Atoms”. In: *Physical Review X* 8.1 (Feb. 2018), p. 011032. DOI: `10.1103/PhysRevX.8.011032`.

[317] Y Li et al. “Enhanced Raman sideband cooling of caesium atoms in a vapour-loaded magneto-optical trap”. In: *Laser Physics Letters* 12.5 (May 2015), p. 055501. DOI: `10.1088/1612-2011/12/5/055501`.

[318] E. Distante et al. “Storage Enhanced Nonlinearities in a Cold Atomic Rydberg Ensemble”. In: *Physical Review Letters* 117.11 (Sept. 2016), p. 113001. DOI: `10.1103/PhysRevLett.117.113001`.

[319] Michał Parniak et al. “Quantum Optics of Spin Waves through ac Stark Modulation”. In: *Physical Review Letters* 122.6 (2019). DOI: 10.1103/PhysRevLett.122.063604. arXiv: 1804.05854.

[320] I. I. Beterov et al. “Erratum: Quasiclassical calculations of blackbody-radiation-induced depopulation rates and effective lifetimes of Rydberg ¡math display=”inline”¿ ¡mrow¿ ¡mi¿n¡/mi¿ ¡mi¿S¡/mi¿ ¡/mrow¿ ¡/math¿ , ¡math display=”inline”¿ ¡mrow¿ ¡mi¿n¡/mi¿ ¡mi¿P¡/mi¿ ¡/mrow¿ ¡”. In: *Physical Review A* 80.5 (Nov. 2009), p. 059902. DOI: 10.1103/PhysRevA.80.059902.

[321] Kelly Cooper Younge, Sarah Elizabeth Anderson, and Georg Raithel. “Adiabatic potentials for Rydberg atoms in a ponderomotive optical lattice”. In: *New Journal of Physics* 12.2 (Feb. 2010), p. 023031. DOI: 10.1088/1367-2630/12/2/023031.

[322] S. E. Anderson. “Trapping Rydberg Atoms in Ponderomotive Optical Lattices”. PhD thesis. 2014.

[323] J. Nipper et al. “Atomic Pair-State Interferometer: Controlling and Measuring an Interaction-Induced Phase Shift in Rydberg-Atom Pairs”. In: *Physical Review X* 2.3 (Aug. 2012), p. 031011. DOI: 10.1103/PhysRevX.2.031011.

[324] Kaden R. A. Hazzard et al. “Many-Body Dynamics of Dipolar Molecules in an Optical Lattice”. In: *Physical Review Letters* 113.19 (Nov. 2014), p. 195302. DOI: 10.1103/PhysRevLett.113.195302.

[325] Nobuyuki Takei et al. “Direct observation of ultrafast many-body electron dynamics in an ultracold Rydberg gas”. In: *Nature Communications* 7.1 (Dec. 2016), p. 13449. DOI: 10.1038/ncomms13449.

[326] Johannes Zeiher et al. “Many-body interferometry of a Rydberg-dressed spin lattice”. In: *Nature Physics* 12.12 (Dec. 2016), pp. 1095–1099. DOI: 10.1038/nphys3835.

[327] Charles S. Adams and Ifan G. Hughes. *Optics f2f*. Oxford University Press, Dec. 2018. ISBN: 9780198786788. DOI: `10.1093/oso/9780198786788.001.0001`.

[328] Norman F. Ramsey. "A Molecular Beam Resonance Method with Separated Oscillating Fields". In: *Physical Review* 78.6 (June 1950), pp. 695–699. DOI: `10.1103/PhysRev.78.695`.

[329] N. F. Ramsey. "Experiments with Separated Oscillatory Fields and Hydrogen Masers". In: *Science* 248.4963 (June 1990), pp. 1612–1619. DOI: `10.1126/science.248.4963.1612`.

[330] C.S Adams, M Sigel, and J Mlynek. "Atom optics". In: *Physics Reports* 240.3 (May 1994), pp. 143–210. DOI: `10.1016/0370-1573(94)90066-3`.

[331] Zhimin Shi et al. "Slow-Light Fourier Transform Interferometer". In: *Physical Review Letters* 99.24 (Dec. 2007), p. 240801. DOI: `10.1103/PhysRevLett.99.240801`.

[332] Bing Chen et al. "Atom-Light Hybrid Interferometer". In: *Physical Review Letters* 115.4 (July 2015), p. 043602. DOI: `10.1103/PhysRevLett.115.043602`.

[333] Cheng Qiu et al. "Atom-light superposition oscillation and Ramsey-like atom-light interferometer". In: *Optica* 3.7 (July 2016), p. 775. DOI: `10.1364/OPTICA.3.000775`.

[334] Adrien Facon et al. "A sensitive electrometer based on a Rydberg atom in a Schr{ö}dinger-cat state". In: *Nature* 535.7611 (July 2016), pp. 262–265. DOI: `10.1038/nature18327`.

[335] J. E. Palmer and S. D. Hogan. "Electric Rydberg-Atom Interferometry". In: *Physical Review Letters* 122.25 (June 2019), p. 250404. DOI: `10.1103/PhysRevLett.122.250404`.

[336] David H Meyer et al. “Assessment of Rydberg atoms for wideband electric field sensing”. In: *Journal of Physics B: Atomic, Molecular and Optical Physics* 53.3 (Feb. 2020), p. 034001. DOI: `10.1088/1361-6455/ab6051`.

[337] Haoquan Fan et al. “Atom based RF electric field sensing”. In: *Journal of Physics B: Atomic, Molecular and Optical Physics* 48.20 (Oct. 2015), p. 202001. DOI: `10.1088/0953-4075/48/20/202001`.

[338] Santosh Ku3 et al. “Rydberg-atom based radio-frequency electrometry using frequency modulation spectroscopy in room temperature vapor cells”. In: *Optics Express* 25.8 (Apr. 2017), p. 8625. DOI: `10.1364/OE.25.008625`.

[339] M. Brune et al. “Observing the Progressive Decoherence of the ”Meter” in a Quantum Measurement”. In: *Physical Review Letters* 77.24 (Dec. 1996), pp. 4887–4890. DOI: `10.1103/PhysRevLett.77.4887`.

[340] John Preskill. “Quantum computing and the entanglement frontier”. In: (Mar. 2012). DOI: `arXiv:1203.5813`. arXiv: `1203.5813`.

[341] Nicolai Friis et al. “Entanglement certification from theory to experiment”. In: *Nature Reviews Physics* 1.1 (2019), pp. 72–87. DOI: `10.1038/s42254-018-0003-5`. arXiv: `1906.10929`.

[342] A. Chenu et al. “Quantum Simulation of Generic Many-Body Open System Dynamics Using Classical Noise”. In: *Physical Review Letters* 118.14 (Apr. 2017), p. 140403. DOI: `10.1103/PhysRevLett.118.140403`.

[343] C.-Y. Lu et al. “Experimental quantum coding against qubit loss error”. In: *Proceedings of the National Academy of Sciences* 105.32 (Aug. 2008), pp. 11050–11054. DOI: `10.1073/pnas.0800740105`.

[344] Roman Stricker et al. “Experimental deterministic correction of qubit loss”. In: *Nature* 585.7824 (Sept. 2020), pp. 207–210. DOI: `10.1038/s41586-020-2667-0`.

[345] Lorenza Viola, Emanuel Knill, and Seth Lloyd. “Dynamical Decoupling of Open Quantum Systems”. In: *Physical Review Letters* 82.12 (Mar. 1999), pp. 2417–2421. DOI: `10.1103/PhysRevLett.82.2417`.

[346] Emanuel Knill, Raymond Laflamme, and Lorenza Viola. “Theory of Quantum Error Correction for General Noise”. In: *Physical Review Letters* 84.11 (Mar. 2000), pp. 2525–2528. DOI: `10.1103/PhysRevLett.84.2525`.

[347] Michael Peper et al. “Magic Rydberg-Rydberg transitions in electric fields”. In: *Physical Review A* 100.3 (Sept. 2019), p. 032512. DOI: `10.1103/PhysRevA.100.032512`.

[348] Mohammadsadegh Khazali, Callum R. Murray, and Thomas Pohl. “Polariton Exchange Interactions in Multichannel Optical Networks”. In: *Physical Review Letters* 123.11 (Sept. 2019), p. 113605. DOI: `10.1103/PhysRevLett.123.113605`.

[349] Erhan Saglamyurek et al. “Single-photon-level light storage in cold atoms using the Autler-Townes splitting protocol”. In: *Physical Review Research* 1.2 (2019), pp. 1–6. DOI: `10.1103/physrevresearch.1.022004`. arXiv: `1905.05856`.

[350] Erhan Saglamyurek et al. “Coherent storage and manipulation of broadband photons via dynamically controlled Autler-Townes splitting”. In: *Nature Photonics* 12.12 (Dec. 2018), pp. 774–782. DOI: `10.1038/s41566-018-0279-0`.

[351] Daniel Barredo et al. “An atom-by-atom assembler of defect-free arbitrary two-dimensional atomic arrays”. In: *Science* 354.6315 (Nov. 2016), pp. 1021–1023. DOI: `10.1126/science.aah3778`.

[352] Donggyu Kim et al. “Large-scale uniform optical focus array generation with a phase spatial light modulator”. In: *Optics Letters* 44.12 (June 2019), p. 3178. DOI: `10.1364/OL.44.003178`.

[353] Yi-Hsin Chen et al. “Coherent Optical Memory with High Storage Efficiency and Large Fractional Delay”. In: *Physical Review Letters* 110.8 (Feb. 2013), p. 083601. DOI: `10.1103/PhysRevLett.110.083601`.

[354] Ya-Fen Hsiao et al. “Highly Efficient Coherent Optical Memory Based on Electromagnetically Induced Transparency”. In: *Physical Review Letters* 120.18 (May 2018), p. 183602. DOI: `10.1103/PhysRevLett.120.183602`.

[355] Anupam Mitra et al. “Robust Mølmer-Sørensen gate for neutral atoms using rapid adiabatic Rydberg dressing”. In: *Physical Review A* 101.3 (Mar. 2020), p. 030301. DOI: `10.1103/PhysRevA.101.030301`.

[356] X. Q. Shao et al. “Ground-state blockade of Rydberg atoms and application in entanglement generation”. In: *Physical Review A* 96.1 (July 2017), p. 012328. DOI: `10.1103/PhysRevA.96.012328`.

[357] Tyler Keating et al. “Robust quantum logic in neutral atoms via adiabatic Rydberg dressing”. In: *Physical Review A* 91.1 (Jan. 2015), p. 012337. DOI: `10.1103/PhysRevA.91.012337`.

[358] Matthias M. Müller et al. “Implementation of an experimentally feasible controlled-phase gate on two blockaded Rydberg atoms”. In: *Physical Review A* 89.3 (Mar. 2014), p. 032334. DOI: `10.1103/PhysRevA.89.032334`.

[359] Tyler Keating et al. “Adiabatic quantum computation with Rydberg-dressed atoms”. In: *Physical Review A* 87.5 (May 2013), p. 052314. DOI: `10.1103/PhysRevA.87.052314`.

[360] Alessio Serafini, Stefano Mancini, and Sougato Bose. “Distributed Quantum Computation via Optical Fibers”. In: *Physical Review Letters* 96.1 (Jan. 2006), p. 010503. DOI: `10.1103/PhysRevLett.96.010503`.